Roma Tre University
Department of Structures

Scuola Dottorale in Ingegneria /
Ph.D. School of Engineering

Sezione di Scienze dell'Ingegneria Civile /
Section of Civil Engineering

XXIII Ciclo / XXIII Cycle

Tesi di Dottorato / Doctoral Thesis

Load-carrying capability and seismic assessment of masonry bridges

Dottorando / Ph.D. Student: Stefano De Santis

Docente guida / Tutor: Prof. Gianmarco de Felice

Coordinatore del dottorato / Ph.D. Coordinator: Prof. Leopoldo Franco

Rome, February 2011

THE PRESENT DOCTORAL THESIS HAS RECEIVED A SPECIAL MENTION IN THE FINAL JUDGEMENT OF THE JURY OF THE EDOARDO BENVENUTO PRIZE (10TH EDITION, YEAR 2012).

Collana delle tesi di Dottorato di Ricerca
in Scienze dell'Ingegneria Civile
Università degli Studi Roma Tre
Tesi n° 27

I wish to dedicate this Thesis to my family

Abstract

The present work contributes to the knowledge of the structural behaviour of masonry bridges and proposes a modelling approach for their assessment under exercise loads and seismic actions. As a first step, an experimental investigation on brickwork specimens is carried out to define the material properties; the tests are performed under cyclic centred and eccentric compression with displacement control. Secondly, a fiber beam model is used to simulate eccentric compression experiments: the fiber constitutive relation is determined and calibrated according to centred tests and the feasibility in predicting the cross-section response of brick arches and piers under axial load and bending moment is demonstrated. The simplicity of a 1-D model, combined with its accuracy in taking into account the mechanical properties of the material, makes it suitable for the structural analysis of masonry bridges. Then, a representative sample of existing large-span rail viaducts is considered, for which the load-carrying capability under travelling load is estimated. Numerical simulations highlight the effect of the constitutive assumptions on the overall resistance estimate and the reliability of yield design-based approaches; the safety level and expected damage under exercise load are also provided. Finally, the dynamic behaviour of masonry bridges is examined starting from the response of a single arch to base impulse acceleration and earthquake motion, considering the influence of arch geometry and material properties. The safety of a multi-span viaduct towards different earthquake scenarios is then assessed by means of push-over analyses and non-linear dynamic simulations under sets of suitable natural accelerograms. The reliability of earthquake engineering conventional procedures, based on non-linear static methods, is evaluated when applied to masonry bridges and a framework for performance-based seismic assessment is outlined.

Keywords: Experimental investigation; Historic brickwork; Masonry bridges; Load-carrying capability; Seismic assessment.

Sommario

Il lavoro fornisce un contributo alla conoscenza dei ponti in muratura, per i quali viene sviluppato un approccio per la valutazione della sicurezza rispetto ai carichi di esercizio e all'azione sismica. In prima battuta vengono determinate le caratteristiche della muratura attraverso una campagna sperimentale con prove cicliche di compressione, condotte con carico centrato ed eccentrico in controllo di spostamento. Le prove di pressoflessione sono poi simulate utilizzando un modello di trave con sezione a fibre, da adottare per la rappresentazione del comportamento di archi e pile, in cui la relazione costitutiva della fibra è calibrata sulla base delle prove centrate. Il confronto con la sperimentazione dimostra l'attendibilità dell'approccio proposto e, d'altra parte, la semplicità di un modello monodimensionale, unita alla sua accuratezza nel tenere conto delle proprietà meccaniche del materiale, lo rende adatto per l'analisi strutturale dei ponti in muratura. Successivamente, viene preso in esame un insieme di dodici viadotti ferroviari esistenti di grande luce, per i quali si valuta la capacità portante al variare delle ipotesi costitutive adottate, verificando l'attendibilità di approcci basati sull'analisi limite e stimando il livello di sicurezza e di sollecitazione in condizioni di esercizio. Infine, viene analizzato il comportamento dinamico dei ponti in muratura studiando innanzitutto la risposta di un singolo arco ad azioni impulsive e sismiche e valutando successivamente il comportaemento sismico di ponti a più arcate attraverso analisi di push-over e analisi dinamiche non lineari con accelerogrammi naturali. Il confronto tra le diverse simulazioni per un caso di studio consente di mettere a fuoco alcune problematiche legate all'applicazione ai ponti in muratura delle metodologie attualmente impiegate per la verifica delle costruzioni in zona sismica basate su metodi statici non lineari e di evidenziare i criteri di base per l'impostazione di una procedura di valutazione della sicurezza nei confronti del terremoto su base prestazionale.

Parole chiave: Indagine sperimentale; Muratura storica; Ponti in muratura; Capacità portante; Sicurezza sismica.

Contents

List of Figures

List of Tables

List of Symbols

Roman symbols

a	Impulse amplitude
A	Diagonal matrix containing the areas of the fibers
a(x)	Deformation interpolation matrix
AB, BC, CD, DA	Length of the links of the four-bars linkage
B	Brickwork specimen width
B	Reference transformation matrix
b(x)	Force interpolation matrix
b_1	Strength degradation rate in "Masonry02" constitutive law
b_2	Strength loss after infinite cycles in "Masonry02" constitutive law
C	Rayleigh damping matrix
C_U	Functional type coefficient
d	Brickwork specimen depth
d(x), $\Delta\mathbf{d}^i$(x)	Deformation field along the element and its increment at step *i*
D(x), $\Delta\mathbf{D}^i$(x)	Force field along the element and its increment at step *i*
d_h	Amplitude of hysteretic cycles
d_k	Control displacement
$\mathbf{D}_R$(x)	Section resisting forces
e	Eccentricity in eccentric compression tests on masonry
e′	Initial imposed eccentricity in eccentric compression tests on masonry
e″	Second order rotation-dependent eccentricity in eccentric compression tests on masonry
E(x)	Fiber section resisting stresses vector
e(x), $\Delta\mathbf{e}^j$(x)	Fiber section strain vector and its increment at step *j*
E	Elastic modulus in ENT and EP constitutive laws
E	Young modulus
E_b	Brick elastic modulus
E_{c0}	Initial tangent stiffness in the constitutive law for brickwork
E_m	Mortar elastic modulus
$E_{M,s}$	Slope of the softening branch of the response curve for masonry under uniform compression tests
$E_{M,u\text{-}r}$	Average slope of the unloading-reloading branches of the response curve for masonry under uniform compression tests
E_{M0}	Masonry initial elastic stiffness

E_{rel}	Stiffness of the reloading branches in the constitutive law for brickwork
E_{soft}	Slope of the softening branch in the constitutive law for brickwork
$\mathbf{E}_{tan}$	Diagonal matrix containing the elastic moduli of the fibers
$\mathbf{F}$	Element flexibility matrix
F	Applied load
f	Frequency
$\mathbf{f}(x)$	Section flexibility matrix
F_0, F_0^{exp}	Maximum axial load in eccentric compression tests
F_0^{num}	Maximum axial load in numerical predictions
f_b^c	Brick strength in compression
f_b^t	Brick strength in tension
f_{cp}	Compressive strength in the constitutive law for brickwork
f_{cu}	Compressive residual strength in the constitutive law for brickwork
f_M	Experimental strength in compression of brickwork
f_m^c	Mortar strength in compression
f_m^t	Mortar strength in tension
g	Gravity acceleration
G_{AB}, G_{BC}, G_{CD}	Centers of mass of links AB, BC and CD
H	Brickwork specimen height
h_p	Height of the steel beam used in eccentric compression tests on masonry specimens
H_p	Pier height
i	Imaginary unit
I_{AB}, I_{BC}, I_{CD}	Centroidal moments of inertia of links AB, BC and CD
IL	Intensity level
$\mathbf{K}$	Element stiffness matrix
$\mathbf{K_S}$	Structure stiffness matrix
$\mathbf{l}(x)$	Linear geometric matrix containing the position of the fibers
L_0, L	Length of the beam finite element in the undeformed and deformed configuration
$\mathbf{M}$	Structure mass matrix
M	Applied bending moment
m	Modal participating mass of the structure
m*	Modal participating mass of the equivalent SDOF system
M_0	Maximum bending moment in eccentric compression tests
M_0^{num}	Maximum bending moment in numerical predictions
M_E	Magnitude
n	Number of unloading-reloading cycles
p	Probability of exceedence
P	Thickness of the top section of the pier
$\mathbf{p}$, $\Delta\mathbf{p}^i$	Structure displacement vector and its increment at step *i*
$\mathbf{P}$, $\Delta\mathbf{P}^i$	External load vector at the structure level and its increment at step *i*
$\mathbf{P_R}$	Structure resisting forces
$Q(\theta)$	Forcing function
$\mathbf{q}$, $\Delta\mathbf{q}^i$	Vector of element deformation and its increment at step *i*
$\mathbf{Q}$, $\Delta\mathbf{Q}^i$	Vector of element force and its increment at step *i*

Q_u	Ultimate load
r	Rise
R	Radius
$\mathbf{r}(x)$	Residual section deformation vector
$\mathbf{R_{AB}}$, $\mathbf{R_{BC}}$, $\mathbf{R_{CD}}$, $\mathbf{R_{DA}}$	Position of the second end of the links link with respect to the first one (polar form)
R_E	Distance from the source
R_μ	Reduction factor
s	Thickness of the vault section at the crown
S	Span
S_a	Spectral acceleration
S_{ae}	Elastic spectral acceleration
S_d	Spectral displacement
S_{de}	Elastic spectral displacement
SF	Safety factor
t	Influence vector
t	Time
T	Period
$T(\theta, \dot{\theta})$	Kinetic energy
t_b	Brick thickness
T_C	Characteristic period of the ground motion
t_m	Mortar layer thickness in masonry specimens
T_R	Return period
u	Distance between axial load and compressed edge of the specimen in eccentric compression tests on masonry
u′	Initial distance between axial load and compressed edge of the specimen in eccentric compression tests on masonry
$V(\theta)$	Potential energy
$\mathbf{v_{AB}}$, $\mathbf{v_{BC}}$, $\mathbf{v_{CD}}$, $\mathbf{v_{DA}}$	Absolute linear velocity of the second end of the links link with respect to the first one (polar form)
V_b	Resultant base shear
V_N	Nominal life
V_R	Reference period
W	Self weight
W	Vector of element basic force
x_i, x_j, y_i, y_j	Coordinates of the end nodes *i* and *j* of the beam in the deformed configuration with respect to the global reference system
y*	Depth of the stress block
y_c	Distance of the neutral axis from the sample compressed edge

Greek symbols

α	Skewback angle
β	Angle of embrace
β_c	Chord rotation in the beam finite element

γ	Self weight
Γ	Modal participating factor
δ	Displacement of the point of force application
ε	Axial strain
ε_{c0}	Strain corresponding to compressive strength in the constitutive law for brickwork
ε_{cu}	Strain correspondent to compressive residual strength in the constitutive law for brickwork
ζ_1, ζ_2	Rayleigh damping constants
η	Ductility
θ	Lagrange parameter of the four-bar linkage
θ_{AB}, θ_{BC}, θ_{CD}, θ_{DA}	Rotation of the links of the four-bar linkage
θ_d	Diffusion angle of stresses within the fill soil
Θ	Rotation of the steel plates in experimental tests on masonry specimens
κ^c_i, κ^c_j	Rotation of the end nodes *i* and *j* of the beam with respect to the chord
κ_i, κ_j	Absolute rotation of the end nodes *i* and *j* of the beam
λ	Relative slope of the reloading branch in Masonry01 and Masonry02 constitutive laws
μ	Ductility factor
ν_b	Brick Poisson ratio
ν_{eq}	Equivalent Poisson ratio for layers provided with head joints
ν_m	Mortar Poisson ratio
ξ	Viscous damping ratio
ξ_1	Relative initial slope of the unloading branch in Masonry01 constitutive law
ξ_2	Relative final slope of the unloading branch in Masonry01 constitutive law
φ	Friction angle
$\mathbf{\Phi}$	Eigenvector
ρ_1	Ratio between brick and mortar layer thickness
ρ_2	Ratio between brick and mortar elastic moduli
σ	Normal stress
τ	Impulse duration
χ	Curvature
ψ_{AB}, ψ_{BC}, ψ_{CD}	Angular offsets of links AB, BC and CD
ω	Pulsation
ω_{AB}, ω_{BC}, ω_{CD}, ω_{DA}	Rotational velocity of the links of the four-bars linkage
Ω, $\Omega*$	Quantity of the MODF system and of the equivalent SDOF one

1. Introduction

1.1. Motivation and aims

The infrastructural networks of several Countries all over the world present a rich heritage of masonry bridges, spacing from small single-span overpasses to large multi-span viaducts. Most of the thousands of Italian masonry bridges belonging to rail and road lines are almost coeval, being built in the second half of XIX Century and in the very first years of XX Century. They show comparable geometries, materials, building techniques and design criteria, diffused all over the national territory after the unification of Italy. Thus, analogous features and issues often recur.

Historic bridges constitute a precious cultural heritage and evidence of the past, and specialized analysis and intervention methodologies are needed to ensure their safety level. Indeed, the activities of knowledge and valorization, conservation and assessment, inspection and diagnosis, repair, strengthening and retrofitting of existing bridges have recently experienced a wider and wider interest.

The design rules adopted in the past for the construction of masonry arches and multi-span bridges were based on empirical criteria or graphical methods. The expected traffic loads were lower than the actual ones and the seismic action was not explicitly included in the calculations; moreover, material degradation processes, foundation settlements, structural damages, transformations or partial demolitions could have occurred with the passing of time. Anyway, masonry bridges generally show an extremely long life and, thanks to the large self-weight, high strength and stiffness under exercise conditions. At present time, an accurate assessment towards both traffic and earthquake loads is needed according to the safety standard requested by actual codes. Nevertheless, no detailed instructions are provided by guide-lines and technical regulations to professional engineers for the structural analysis and reliability evaluation.

Despite their importance, a deep awareness of the real safety level offered by existing masonry bridges is still lacking and a lot of work has still to be done by the scientific community to better understand their structural

behaviour; several issues, such as for example the seismic response, even seem to be almost unexplored. Researchers have now to face the challenge of developing tools and procedures to carry out analysis, perform reliability assessment and design interventions that offer a satisfactory compromise between accuracy and simplicity.

A well-founded structural model has to include, among the other things, an accurate description of the material properties and of the effect induced by the interaction between structural elements on the whole response. Moreover, an adequate representation of the external actions has to be provided. At the same time, computational sustainability and robustness, as well as clearness and simplicity in the determination of the parameters, have to be ensured, since the professional utilization asks for low modelling and calculus time, and comprehensible, verifiable and, of course, reliable results.

Several alternative approaches are available nowadays for the structural analysis of masonry bridges. Limit analysis-based methods start from the simplifying assumptions proposed by Heyman (1966; 1982) that brickwork in compression is infinitely resistant or has finite strength with unlimited ductility, that it has no tensile resistance, and, finally, that no sliding between voussoirs occurs. They are widely used (see, among others: Harvey, 1988; Harvey and Smith, 1991; Gilbert and Melbourne, 1994; Clemente et al., 1995; Boothby, 1997; Gilbert, 2007; Clemente, 2010) but may lead to an overestimate of the effective strength. Otherwise, applications of incremental finite element analysis have been proposed, making use of 1-D (Molins and Roca, 1998; Boothby, 2001; Brencich and De Francesco, 2004a; 2004b; Brencich et al., 2004; de Felice, 2009), 2-D elements (Cavicchi and Gambarotta, 2005; 2007; Gilbert et al., 2007a) and 3-D elements (Fanning and Boothby, 2001; Fanning et al., 2005; Harvey et al., 2005; Domède and Sellier, 2010). As an alternative, expeditious empirical methodologies have been developed providing a quick estimate of the safety level of a bridge, such as the MEXE Method (UK Department of Transport, 1997; Wang et al., 2010) and the SMART Method (Melbourne et al., 2007).

In dynamics, static equivalent analyses based on the mechanism method are typically performed (Oppenheim, 1992; Clemente, 1998; De Luca et al., 2004; De Lorenzis et al., 2007), but the effective reliability of these approaches has still to be wholly verified. On the other hand, 3-D elasto-plastic finite elements (Pelà et al., 2009) and 1-D non-linear macro-elements (Resemini and Lagomarsino, 2007) have also been used. Finally, reliable assessment criteria towards earthquakes are lacking and should be included in a general performance-based approach.

The research work presented in this Thesis aims at giving a contribution in the field of the structural analysis of existing masonry bridges, facing some of the most important features of this complex issue; in detail the main purposes are:

- giving a contribution to the knowledge of existing masonry bridges, starting from the mechanical properties of adopted materials;
- deeply understand some issues of the response of historic brickwork, such as the characteristics of the components (mortar and bricks), the behaviour under cyclic centered and eccentric loading, the cross-section deformation;
- developing an approach for the structural modelling based on beam elements with fiber cross-section that offers a good compromise between accuracy (which results from an adequate description of the material properties experimentally derived) and simplicity, and is therefore suitable for a practical use;
- deepening some features of the evaluation of the safety level offered by existing masonry bridges under exercise conditions, such as the effect of the material characteristics on the whole load-carrying capability, the feasibility of yield design-based approaches, the load models to adopt, the response of different bridge typologies in terms of resistance, expected damage, collapse mechanisms;
- facing the issue of the seismic response, starting from the identification of advantages and limits of available methodologies, based on non-linear static analysis methods and conceived for the design of r.c. and steel buildings;
- discussing the criteria and the procedures needing wariness in modal, non-linear static, and incremental non-linear dynamic analyses, such as the interpretation of modal frequencies and shapes; the load distribution to adopt within push-over methods, and, finally, the definition of damping parameters and the selection and manipulation of accelerograms within time-step integration simulations;
- outlining a first proposal of a performance-based seismic assessment methodology.

1.2. Organization of the Thesis

The Thesis is organized as follows. In Chapter 2 the results of an experimental campaign carried out on brick, mortar and masonry specimens, representative of Italian rail bridges, is presented. Monotonic and cyclic displacement-controlled tests, as well as three-point bending tests, are carried out on cubic and prismatic samples to determine the main mechanical properties of brick and mortar, then used to build brickwork prisms. The

mechanical response of historic brick masonry (resistance, stiffness, cyclic and softening behaviour) in terms of Force-Displacement and Moment-Curvature relations are derived on the base of cyclic centered and eccentric compression tests. The results are reported and discussed, together with the observed damage evolution. The cross-section behaviour of a brickwork element under compression and bending is examined, and a criterion for the estimate of the maximum load and an analytical estimate of the response after several load cycles are proposed.

In Chapter 3 the fiber beam element is presented and the possibility of using it to represent vaults and piers of masonry bridges is investigated. Two constitutive relations are defined, implemented and calibrated on the base of experimental results with the purpose of representing the global effective behaviour of historic brickwork under cyclic eccentric compression. Tests under axial force and bending moment are then simulated and numerical predictions are compared with experimental data in terms of strength domain and peak values, as well as of whole response curve.

In Chapter 4 the modelling of masonry bridges is described and applied to some case studies. First of all, a laboratory test carried out on a three-span large scale specimen in Bolton Institute (Melbourne et al., 1997) is simulated to validate the proposed approach. Two Italian historic multi-span viaducts are modelled and their load-carrying capability is evaluated under travelling load. The agreement between the results provided by the fiber beam simulations and limit analysis under the same constitutive assumptions is checked. The effective material properties are then taken into account and the effect of the constitutive law on overall resistance and collapse mechanism are discussed to establish to what extent the results of a yield design-based approach are reliable. Finally, the safety level offered by a wider sample of Italian large-span rail bridges is assessed under exercise conditions.

In Chapter 5 the seismic assessment is treated. First of all, the problem of a single arch under impulse base motion is considered: numerical simulations are compared to the solution provided by the mechanism method to validate the fiber beam-based approach in dynamics; size and slenderness effects on the resistance, as well as the influence of the material properties, are also investigated. Then the response of the arch under earthquake motion is investigated, and modal, push-over and dynamic analyses are performed. The main features of the analysis methods for the seismic assessment are presented and discussed, underlining some issues related to their application to masonry bridges: push-over analyses (distribution of horizontal loads, cyclic response), non-linear dynamic simulations (viscous damping, selection and scaling of records, choice of the structural state variables), earthquake engineering conventional procedures (reliability of push-over analysis-based methods). An existing viaduct is then analyzed: its natural frequencies and modal shapes are compared to the ones provided by an elastic model built with 3-D finite elements and then push-over analyses and incremental non-

linear dynamic analyses under suitable natural accelerograms are performed; the N2 method is also applied for the evaluation of the seismic safety level. Finally, some basic concepts of a framework for the performance-based seismic assessment are proposed.

In Chapter 6 the conclusions of the Thesis and the basis for future developments are illustrated.

2. Experimental investigation on historic brickwork

2.1. State-of-the-art

Masonry vaults, arches, pillars and walls may experiment similar load conditions characterized by a concentration of compressive stress due to the eccentricity of the axial load acting on the cross-section. The collapse of these structural elements may be induced by loss of equilibrium as well as by crushing failure of the material; anyway, the compressive strength is not the only significant parameter, since the structural response to a cyclic loading history (such as traffic loads or seismic actions) is strongly influenced by the stiffness, and the post-peak, cyclic and hysteretic behaviour. For this reason, the investigation of the material mechanical properties is a primary issue for the structural assessment of masonry constructions.

The behaviour of brick masonry subjected to centered and eccentric axial load has been widely investigated over a long period of time. The first works date back to the Seventies and the Eighties. In (Francis et al., 1971; Shrive, 1985; McNary and Abrams, 1985; Page, 1981; 1983; Shubert, 1988) the parameters influencing the compressive strength and the stiffness of brickwork (such as the lateral strength of the units, and the lateral deformation mismatch between units and mortar) were studied.

In the last twenty years several works have been devoted to the experimental testing on masonry. An extensive campaign carried out to characterize the mechanical response of brick masonry under compression along both material directions, as well as in tension along horizontal mortar joint direction, is presented in (Olivito and Stumpo, 2001). Similar experimental tests have been carried out to investigate the compressive strength and the failure mechanism of brickwork loaded parallel to the bed joints in (Hoffman and Schubert, 1994). The influence of test sample geometry, including the presence of mortar head joints, on the compressive strength has been investigated in (Mann and Betzler, 1994). The bond effect

on the response under compression has been studied also in (Vermeltfoort, 1994).

Again speaking of monotonic axial loading, in (Ewing and Kowalsky, 2004) an experimental campaign on unconfined and confined clay brick masonry prisms leads to the identification of the parameters of one of the first constitutive models for masonry to predict the experimental response. In (Oliveira et al., 2006) an experimental campaign on masonry under pure compression is presented, in which tests are carried out on both stone and brickwork masonry specimens, as well as on their components (sandstone and clay bricks); the main properties (strength, stiffness, brittleness, energy dissipation, degradation) are achieved from displacement controlled monotonic and cyclic tests.

The cyclic behaviour of masonry under axial load has been investigated in (Roberts et al., 2006) and in (AlShebany and Sinha, 1999); in the latter paper an analytical macroscopic constitutive relation (named stability curve) is proposed to describe the response after several unloading-reloading cycles. In (Tomor and Wang, 2010) the deterioration process of masonry under fatigue loading is investigated with the help of acoustic emission technique, and the fatigue strength is assessed.

The condition of combined axial load and bending moment is investigated by several authors, starting from (Drysdale and Hamid, 1982) and (Ding, 1997). A wide experimental campaign is described in (Brencich and Gambarotta, 2005), (Brencich et al., 2002) and (Brencich et al., 2006) in which the tests are carried out on clay brick masonry specimens, as well as on their components; crack pattern evolution, acoustic emissions and cross-section deformation are monitored; moreover, experimental data are compared with the predictions of a 3-D finite element model. Finally, in (Cavalieri et al., 2005) an analytical law for masonry in compression is defined on the base of centered and eccentric tests and is used to predict experimental response curves and strength properties.

Having in mind the effective loads experimented by masonry elements, and aiming at reproducing in the laboratory similar stress conditions, other combined actions have been investigated in addition to the eccentric axial load. Among others, in (Mojsilović and Marti, 1997) brickwork walls have been subjected to in-plane and out-of-plane loads, in (Mojsilović, 2005) and in (Mojsilović and Marti, 2002) shear and normal forces have been considered, and, finally, in (Litewka and Szojda, 2006) the collapse under triaxial state of stress has been investigated.

Although several studies have been carried out to experimentally determine its mechanical response, most contributions deal with contemporary, rather than historic, masonry. Apart from some studies on the behaviour of old brickwork under compression (Venu Madhava Rao et al., 1997; Aprile et al., 2001, de Felice and Carbone, 2006), or under overload phenomena (Anziani et al., 2000), with a view towards strengthening

techniques, such as in (Valluzzi et al., 2005), only a few papers have been devoted to historic masonry, which, however, may behave completely differently from contemporary one, due to both brick and mortar properties (Brencich and de Felice, 2009), as well as to the material degradation. The latter paper presents three different experimental campaigns carried out on historic brickwork elements under centered and eccentric compression; the limit domains gathered from laboratory data are estimated by means of a 1-D model and its reliability is investigated with the change in the global constitutive law (perfectly brittle, elasto-plastic, Kent&Park relation) as well as of the available ductility.

Regarding the materials used in the construction of old masonry bridges, some data on the mechanical properties of bricks and mortar may be found in historic treatises, like (Rondelet, 1802; Curioni, 1874; Séjourné, 1913; Gay, 1924); more recent experimental results can be found in (Barbi et al., 2002), where the behaviour of historic bricks under compression is presented, in (Sala et al., 2008) where the mechanical properties of lime mortar enriched with natural pozzolana are derived from experimental tests, and, finally, in (Binda et al., 1988), where the influence of mortar types on the compressive strength of masonry is underlined. In some cases, laboratory tests are performed on extracted samples from historic constructions in order to characterize chemical, physical and mechanical characteristics of original materials (Baronio et al., 2003), as well as on new materials, to be adopted for the repair or reconstruction of damaged buildings, to investigate their compatibility with historic ones (Binda et al., 2003).

In this chapter, an experimental campaign on historic brick masonry is presented, directed to assess the mechanical properties of the brickwork used in rail arch bridges built in Italy at the end of XIX Century. The starting point is the consideration that the behaviour of masonry under compression plays a non-negligible role in the bridge load-carrying and seismic capacity. In fact, the structural response, when close to failure, may widely change depending on the effective material properties (Brencich and De Francesco, 2004a; 2004b); for instance, the classical four-hinge mechanism takes place only when masonry exhibits an adequate ductility capacity; otherwise, failure is reached with crushing within the critical cross-section (de Felice, 2007; 2009). Moreover, the post peak behaviour was quite recently discovered to play a crucial role in the inelastic response of masonry (Lourenço, 1998).

With this in mind, some viaducts built between 1890 and 1894 along the rail line between Rome and Viterbo have been surveyed and the masonry properties assessed, to reproduce in the laboratory specimens having characteristics similar to the brickwork used in the bridges.

The significance of this experimental campaign and the scientific contribute represented by its results arise from the consideration that most of the rail Italian masonry bridges were built in a relatively short period of time

(mainly, in the second half of the XIX Century), using almost everywhere the same materials and with similar construction rules (Brencich and Morbiducci, 2007). This is the reason why bridges with comparable overall dimension, material properties and structural details may be found, without distinction, in different regions. Their structural assessment has to start from the knowledge of the effective properties of the brickwork they are made of.

2.2. Experimental set-up

The whole experimental investigation presented in this work is carried out in the Experimental Laboratory of the Department of Structures of University Roma Tre. The tests are made using an MTS hydraulic load frame (Figure 2.1) with 500kN load rating; most of the experiments are displacement controlled, with a velocity of displacement of the load plates equal to 0.01mm/sec, while when the control is made on the load the rate of application of the force is equal to 50N/sec, as suggested by the European Standards (UNI EN 772-1). The acquisition frequency is always equal to 10Hz.

In the unloading branches of the displacement controlled cyclic tests, a testing procedure is implemented *ad hoc*, provided with a minimum load threshold to avoid the complete unloading of the specimen.

Except for the applied load data, directly acquired by the load cell integrated in the MTS testing machine, displacements and strains are acquired by linear potentiometers and resistive strain-gauges, and collected by a National Instruments NI PCI 6281 Multifunction Data Acquisition (DAQ) system. It is provided with 3 units NI SCXI 1520 Universal Strain-Gauge Input Module, with 8 Channels each; the acquisition software is developed in LabView environment.

Figure 2.1. MTS testing machine (left) and detail of the oil control device (right, up) and of the data acquisition device (right, bottom).

2.3. Masonry components

Before testing masonry specimens, the mechanical properties of bricks and mortar used for their construction are investigated; monotonic and cyclic compression tests and three-point bending tests are performed to determine the compressive and tensile strength of the materials together with the correspondent strain values, their stiffness, and, thanks to the displacement control, their whole response curve, including the post-peak softening phase and the unloading-reloading cycles.

This first part of the experimental campaign leads to a deeper knowledge of the mechanical behaviour of historic materials, whose response shows some important differences if compared with those in use nowadays, and to useful information for the interpretation of the response of brickwork specimens.

2.3.1. Bricks

In the construction of the bridge vaults of the rail line built between 1890 and 1894 from Rome to Viterbo, clay bricks were used also called *original bricks* hereafter; they measure 270×130×55mm^3. In order to determine their mechanical properties, 20 cubic samples with side 45÷50mm are extracted from 6 bricks and submitted to monotonic and cyclic compression tests. The experiments are performed in direction normal to the face of the bed joints, which are previously carefully leveled by means of a grinding machine (Figure 2.2) in order to guarantee the parallelism of the loaded surfaces and avoid initial stress concentrations. No devices are employed to reduce the friction between the specimen surface and the plates of the load frame.

For the purpose of reproducing masonry specimens to be tested in the laboratory, a stock of old clay bricks (also called *historic bricks* hereafter) with the same characteristics and dimensions as the original samples is found; the bricks were produced at the beginning of the XX Century in a clink situated in Monterotondo, not far from the bridge locations. Their mechanical properties are determined by testing 11 cubic specimens of approximately 48mm side, extracted from 6 bricks.

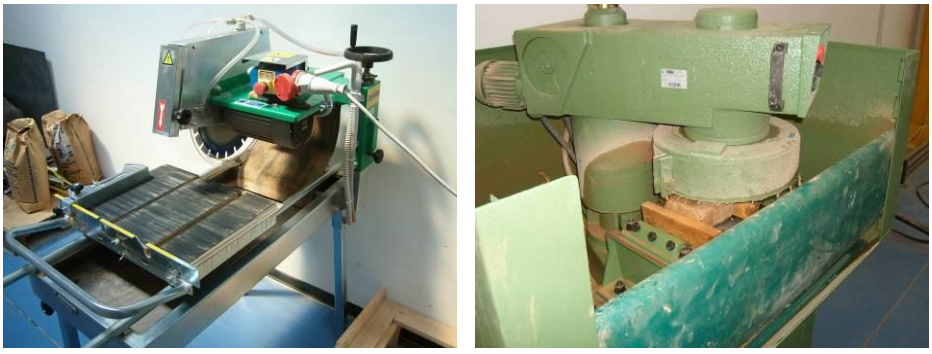

Figure 2.2. Cutting machine (right) and grinding machine (left).

The stress-strain curves are reported in Figures 2.3 and 2.4 for original and historic bricks, respectively: both brick stocks show very similar properties in terms of strength and post-peak behaviour, with a slightly higher stiffness of old bricks.

The maximum stress is approximately 30MPa, and the correspondent strain is in the order of 1%. Looking at the response curves, an apparent stiffness increase is observed in the first branch, resulting from the bedding effect induced by the asperities and the unavoidable non-perfect parallelism of the loaded surfaces; however, a linear branch can be clearly identified from the end of this bedding phase until about 70% of the maximum load; the elastic stiffness is estimated by a linear interpolation of this linear branch,

giving an average value of about 3100MPa and 3900MPa for original and historic bricks, respectively.

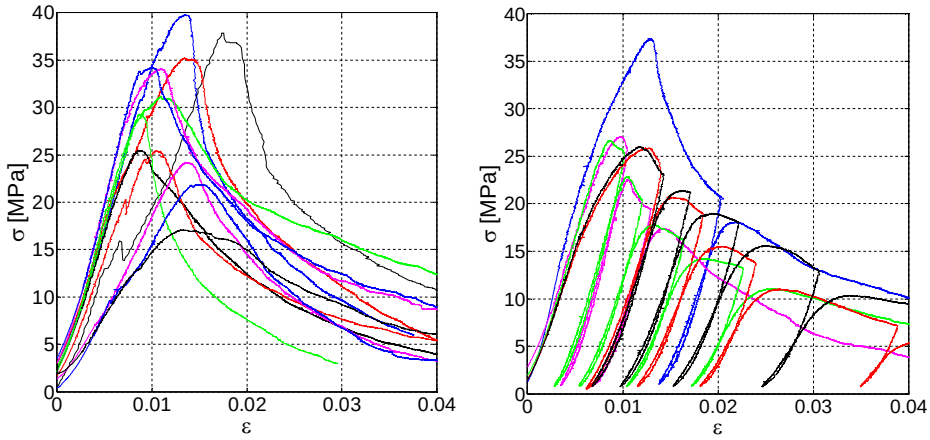

Figure 2.3. Experimental stress-strain curves of monotonic (left) and cyclic (right) compression tests on original brick cubic samples belonging to the masonry arch bridges of Rome-Viterbo rail line.

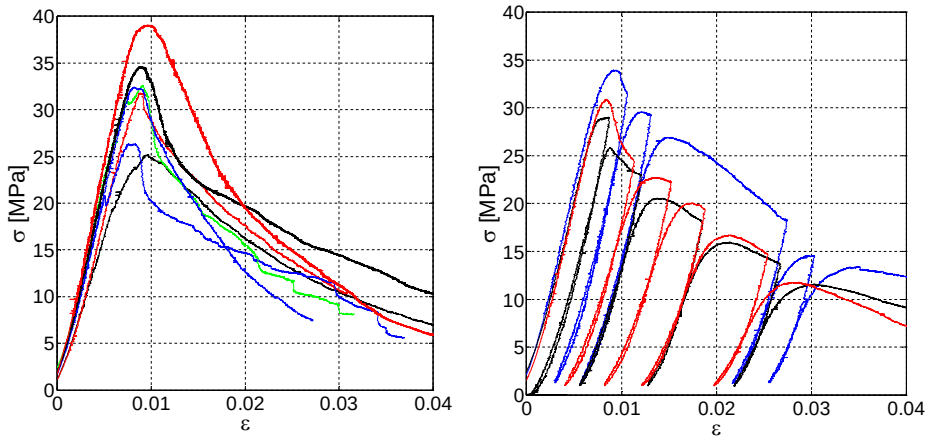

Figure 2.4. Experimental stress-strain curves of monotonic (left) and cyclic (right) compression tests on historic brick cubic samples (bricks manifactured in Monterotondo clink).

Both the stocks of bricks behave comparably under cyclic loading, showing a good capability in sustaining loading-unloading cycles even when they are performed in the softening branch, without appreciable stiffness degradation in spite of the high level of deformation and damage reached.

Figure 2.5 shows the evolution of damage during a compression test on a brick sample: the first cracks occur at about 75%÷85% of the maximum load, together with the expulsion of fragments from the corners; at peak load the cracks involve the whole height of the specimen and then increase in size and number during the softening phase, inducing a progressive lateral dilatation; finally, under very high strains, slices or scraps are discharged from one or more lateral faces.

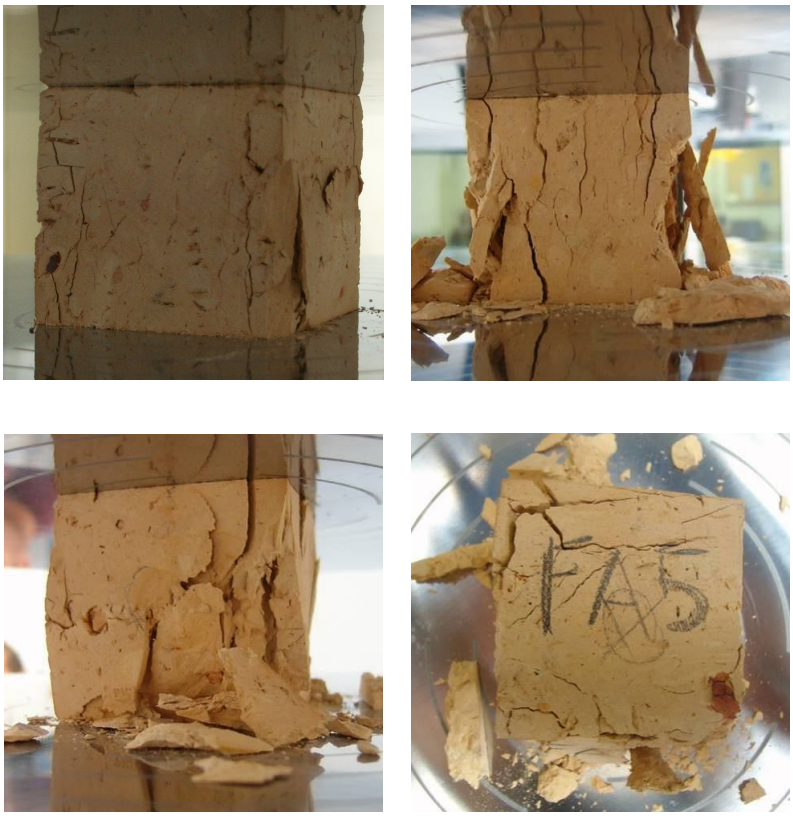

Figure 2.5. Failure pattern of an cubic brick sample during a compression test.

The tensile strength of historic bricks is indirectly estimated throughout 14 three point bending tests (3PBT), carried out on two different prismatic specimen types (having dimensions 100×40×40mm^3 and 160×40×40mm^3), extracted from 5 bricks. The test set-up consists of two steel bars with diameter ∅=10mm and 100mm far from each other, on which the specimen is placed, and a third bar (identical to the other ones) by means of which the load is applied in the center section. The device to perform the tests is designed on purpose (Figure 2.6) to be used with the MTS testing machine

(Figure 2.7). The tests are load controlled with 50N/sec loading rate, in agreement with the UNI 8943-3 Standard.

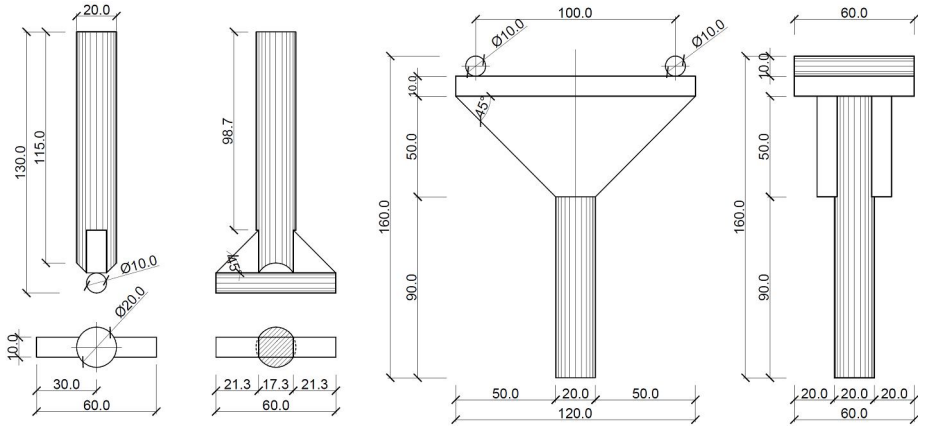

Figure 2.6. Testing device for three-point bending test.

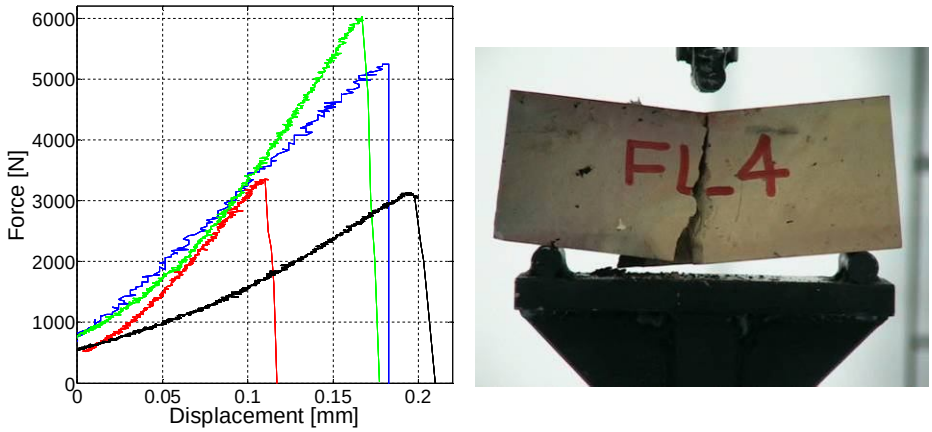

Figure 2.7. Three-point bending test on brick specimens: force-displacement response curves (left) and sample after the end of the test (right).

The tensile strength can be determined from the ultimate load directly from Navier's formula, giving the stress value in the intrados of the centre section (UNI 8943-3) starting from the force value that produces the brittle collapse of the specimen (Figure 2.7). Anyway, this may lead to overestimate the effective tensile resistance, since the horizontal forces due to the friction between specimen intrados and bottom steel bars result in the arising of a strut&tie mechanism, as can be easily identified through an elastic 3-D FE analysis (Figure 2.8). The lower constraints give an eccentric horizontal

reaction, producing a bending moment which is opposed to the one due to the vertical load (Figure 2.9).

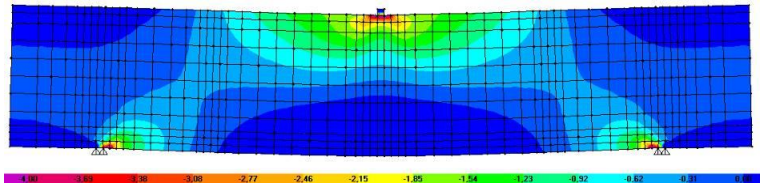

Figure 2.8. Elastic FE analysis of a brick sample under a three-point bending test: horizontal stresses indentifying the strut&tie mechanism.

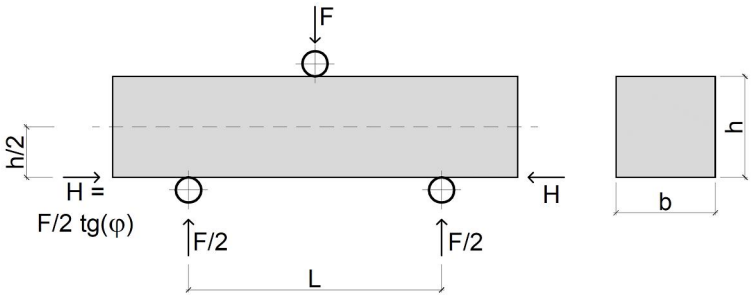

Figure 2.9. Additional bending moment due to specimen-steel bar friction in three-point bending test.

Considering the effective stress field in the specimen, a more realistic estimate of the tensile strength can be achieved by expression (2.1), which takes into account the friction contribute and contains the friction angle (φ). The latter is experimentally determined by means of tests on reclining table (Figure 2.10) and, in this case, is found to be equal to 26°.

$$f_b^t = 1.5\frac{F \cdot L}{b \cdot h^2}\left(1 - \frac{2h}{L} \cdot tg(\varphi)\right) \qquad (2.1)$$

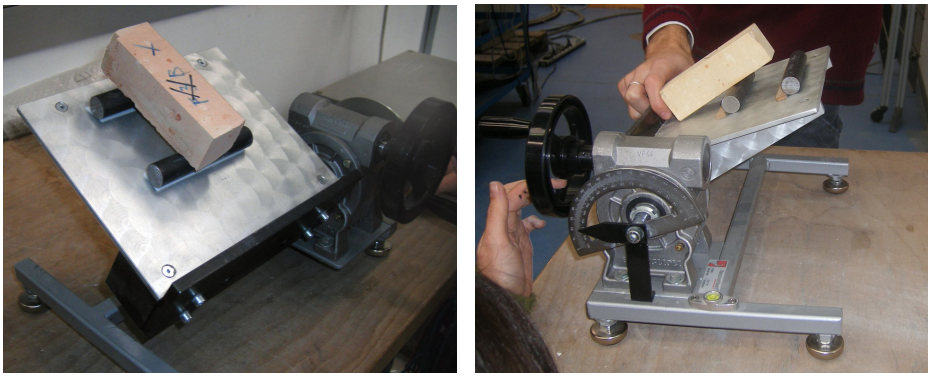

Figure 2.10. Experimental tests on reclining table, before (left) and after (right) the sliding onset.

The value of the tensile strength is evaluated to be 3.79MPa, while the overestimate achieved without considering the friction contribute is approximately 20%.

The average properties and the corresponding standard deviations of the experimental tests on both original and historic brick samples are collected in Table 2.1.

	Compression strength f_b^c [MPa]	Deformation at peak stress $\varepsilon(f_b)$	Tangent stiffness E_b [MPa]	Tensile strength f_b^t [MPa]
	Original brick samples (compression tests: 18 samples)			
Mean value	29.85	$11.1 \cdot 10^{-3}$	3067	-
Standard deviation	7.33	$3.2 \cdot 10^{-3}$	731	-
	Historic brick samples (compression tests: 11 samples – 3PBT: 7 samples)			
Mean value	30.51	$9.4 \cdot 10^{-3}$	3918	3.79
Standard deviation	5.24	$2.1 \cdot 10^{-3}$	395	0.24

Table 2.1. Experimental properties of original and historic bricks.

2.3.2. Mortar

Some mortar original samples are taken from one bridge of Rome-Viterbo rail line and petrographical, microstratigraphical and microchemical analyses are performed on it (Figure 2.11).

These tests aim at providing a knowledge base for the interpretation of building techniques and structural response (Middendorf et al., 2005), as well as at producing a new mortar with the same properties.

The original mortar is made with lime and pozzolana; the samples contain several grey mortar fragments, with a low cohesion level, immersed in a large quantity of powder coming from mortar disaggregation, and dark grey round pozzolana particles (probably coming from a volcanic deposit in the Sabatini Mountains, not far from Rome).

The bonding element is a light grey carbonated lime, characterized by a homogeneous structure (few fragments can be observed); its total porosity (whose estimated average value is 20÷40%) is essentially due to the drying process of the lime. The aggregate is made of volcanic fragments and is characterized by a granulometry variable from silt to fine gravel, with granules of dimensions comprised between 0.01 and 4.50mm. The sorting ratio is very low and its distribution into the binder is homogenous; the granules are not oriented and from their high thickening (more than 50%) the estimated volumetric ratio binder/aggregate is approximately equal to 1:4.

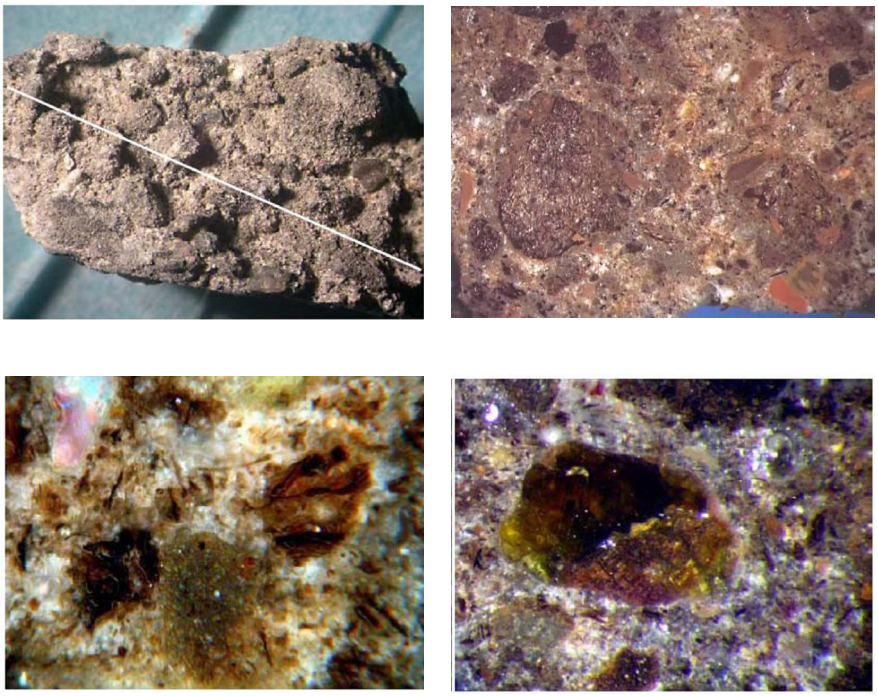

Figure 2.11. Extracted mortar sample (up, left) and enlargements of its bright section: 40× (up, right) and 100× (bottom).

A mortar with similar characteristics is prepared in the laboratory to be used with the previously described bricks for building masonry specimens, to obtain samples that are representative of the effective brickwork of the bridges. Cubic and prismatic samples are realized (Figure 2.12) and tested.

Figure 2.12. Cubic and prismatic mortar specimens before and after the extraction from the formworks.

Totally, 11 cubic mortar samples having 40mm side and 8 prismatic samples having 40×40mm^2 base dimensions and slenderness ratio height to width (H/W) equal to 2 and 4, are tested under compression. The response curves (Figure 2.13) are characterized by an initial elastic phase, where a linear branch can be clearly identified; a linear regression in this interval is used to determine the material elastic stiffness, as already done for bricks. When 70÷80% of the maximum load is reached, a significant loss of linearity occurs; finally, the post-peak response is characterized by a softening branch with constant slope, up to the end of the test. Similarly to brick samples, during the tests on mortar an initial bedding phase is recognizable with an apparent stiffness increase, which has to be attributed to the asperities and non-prefect parallelism of the loaded surfaces.

The cyclic behaviour is characterized by low energy dissipation: the unloading-reloading branches display high stiffness values, probably as a result of the material compaction. The skeleton curve can be clearly seen as the envelope of the cyclic ones and no significant degradation occurs in the continuation of the test after an unloading-reloading cycle, even if it is performed in the softening phase.

The comparison between the response curves of cubic and prismatic samples shows the confining effect of the loading plates; in fact, the more slender is the specimen, the lower is the compressive strength gathered from the experiment, passing from 1.62MPa (cubic specimens, H/L=1) to 1.46MPa (H/L=2) and 1.27MPa (H/L=4) (Figure 2.13, Table 2.2); the strength reduction is also associated to a higher slope of the softening branch, indicating the dependence of confinement on ductility. Anyway, no devices are used to reduce this effect, also in consideration of the confinement induced on mortar layers by the bricks in masonry assemblages.

As regards the crack pattern evolution, cubic specimens (Figure 2.14) show vertical cracks originating in the initial ascending branch when the load

is approximately 40÷50% of the maximum one, followed by the detachment of fragments from the external surfaces occurring in the softening phase; at the end of the test several cracks involve the whole specimen including the loaded surfaces.

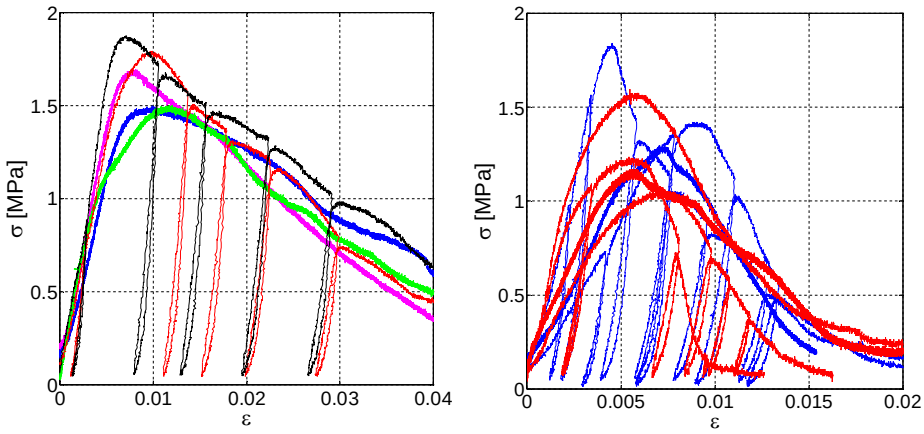

Figure 2.13. Experimental stress-strain curves of compression tests on cubic (left) and prismatic (right) mortar specimens (blue curves: slenderness ratio H/L=2; red curves: H/L=4).

Figure 2.14. Crack pattern in a compression test on a cubic sample.

The behaviour of prismatic specimens (Figures 2.15 and 2.16) is characterized by the appearance of a first narrow vertical crack when the load is about 70÷80% of the peak value, becoming evident only in an advanced phase of the softening branch; generally, only one crack characterizes the failure, and smaller cracks are detected on the loaded surfaces.

Figure 2.15. Crack pattern in a compression test on prismatic sample (slenderness ratio H/L=2).

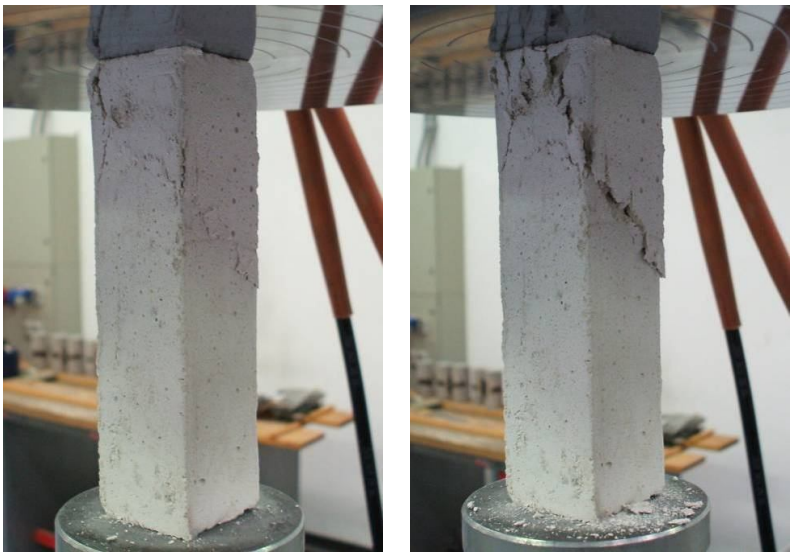

Figure 2.16. Crack pattern in a compression tests on a prismatic sample (slenderness ratio H/L=4).

	Compression strength f_m^c [MPa]	Deformation at peak stress $\varepsilon(f_m)$	Tangent stiffness E_m [MPa]
	Cubic specimens 5 samples		
Mean value	1.62	$10.6 \cdot 10^{-3}$	228.7
Standard deviation	0.21	$3.8 \cdot 10^{-3}$	61.8
	Prismatic specimens (slenderness ratio L/H = 2) – 4 samples		
Mean value	1.46	$7.8 \cdot 10^{-3}$	267.2
Standard deviation	0.23	$4.3 \cdot 10^{-3}$	138.2
	Prismatic specimens (slenderness ratio L/H = 4) – 4 samples		
Mean value	1.27	$5.8 \cdot 10^{-3}$	329.2
Standard deviation	0.23	$0.7 \cdot 10^{-3}$	156.6

Table 2.2. Experimental results of mortar samples under compression tests.

The mortar tensile strength is estimated through three point bending tests, carried out on 5 prismatic specimens, having dimensions $40 \times 40 \times 160 mm^3$, and an average value of 0.44MPa is found (Table 2.2); the load-displacement curves, showing the brittle failure observed in the tests, are plotted in Figure 2.17. The experiments are performed in conformity with the European Standard UNI EN 1015-11, and making use of the same set-up (Figure 2.17) adopted for three point bending tests on bricks.

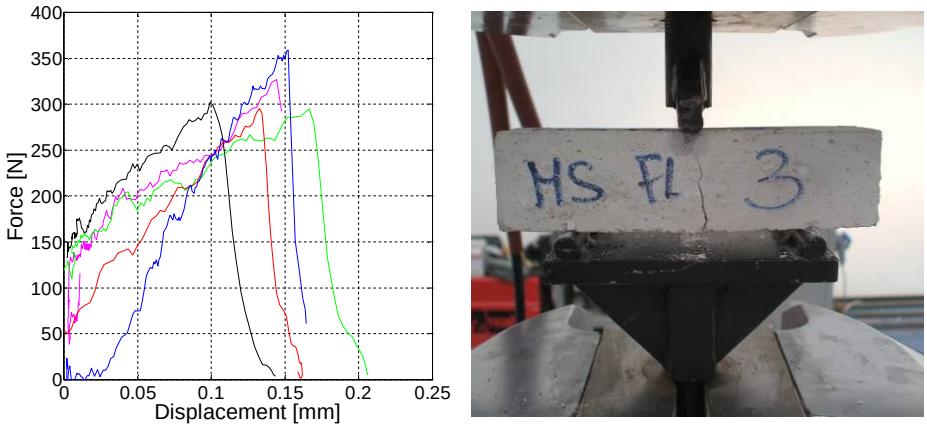

Figure 2.17. Three-point bending test on mortar specimens: force-displacement response curves (left) and a sample immediatelty before the collapse (right).

2.4. Experimental plan for brickwork

Aiming at investigating the mechanical response of historic brickwork under centered and eccentric compression, which is the stress condition experimented by the cross-section of vaults and piers, 19 specimens of various sizes and geometries (Figure 2.18) are built using the bricks and the mortar previously described. The arrangement of the bricks and the thickness of the mortar joints, as well as the bending axis, aim at reproducing a portion of a brick masonry arch.

After being aged for two years, the specimens are subjected to displacement controlled cyclic compression tests, with different values of loading eccentricity ranging from 0 to 110mm (Table 2.3); the load is applied by means of an *ad hoc* arranged equipment (Figure 2.18).

All the experiments are performed on the basis of the European Standard UNI EN 772-1 using the MTS hydraulic load frame and the acquisition devices described in paragraph 2.2.

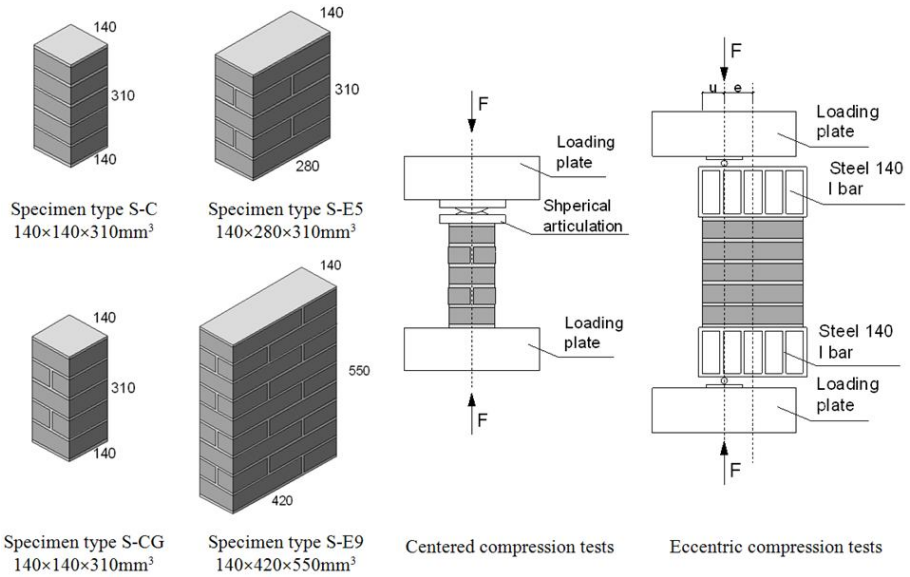

Figure 2.18. Schematic illustration of masonry specimen types and experimental set-up for centered and eccentric compression tests.

Test	Specimen type	Eccentricity e′ [mm]	Number of specimens
Centered cyclic compression	S-C	0	2
	S-CG	0	2
Eccentric cyclic compression	S-C	30	2
	S-CG	30	2
	S-E5	40	2
		60	2
		80	1
		100	2
	S-E9	70	2
		110	2

Table 2.3. Experimental plan for tests on brickwork prisms.

2.5. Brickwork under uniform compression

Four masonry specimens are tested under cyclic centered axial load; the prisms measure 140×140×310mm^3 and consist of five brick layers; two specimens (S-CG type) have a head mortar joint in the middle of the second and fourth layers, while the other two ones (S-C type) do not (Figure 2.18); both horizontal and head joints are 10÷12mm thick.

A spherical articulation is used to ensure a uniform stress distribution between specimen and loading plates. The global displacements are acquired by means of four linear potentiometers (stroke ±50mm, resistance 4.0 kΩ, and independent linearity ±0.15%), while local brick vertical and horizontal strains are acquired by means of two resistive strain-gauges (initial length 30mm), which are connected to the bricks by means of an acrylic glue, applied on an epoxy-based resin film ensuring the regularity of the contact surface (Figures 2.19 and 2.20).

The response curves are plotted in Figure 2.21 in the average stress-average strain plane. An initial elastic phase is found, in which a linear behaviour is recognizable, until the load reaches 70÷80% of the maximum value; the latter is preceded by a non-linear pre-peak phase and followed by a substantially linear softening phase. In the very first part of the ascending branch, a bedding effect is made evident by an apparent stiffness increase, similar to the one found in compression tests on brick and mortar specimens.

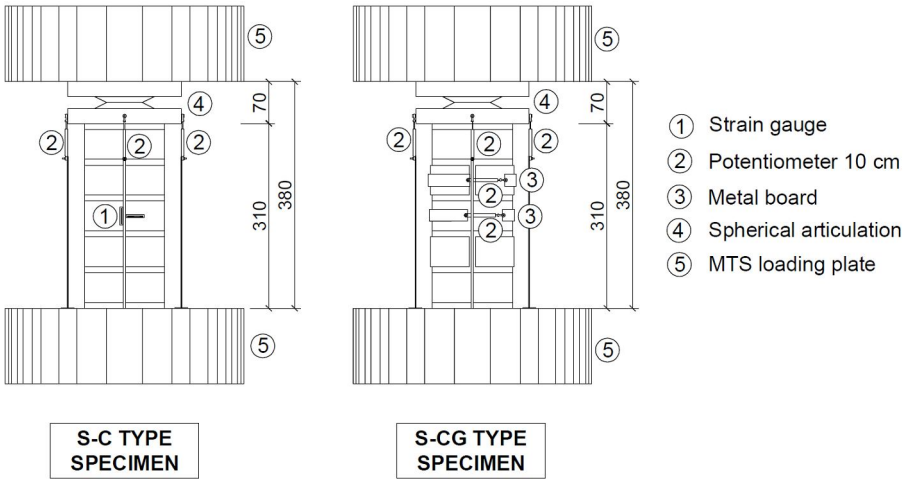

Figure 2.19. Schematic illustration of the equipment for centered compression tests on brickwork.

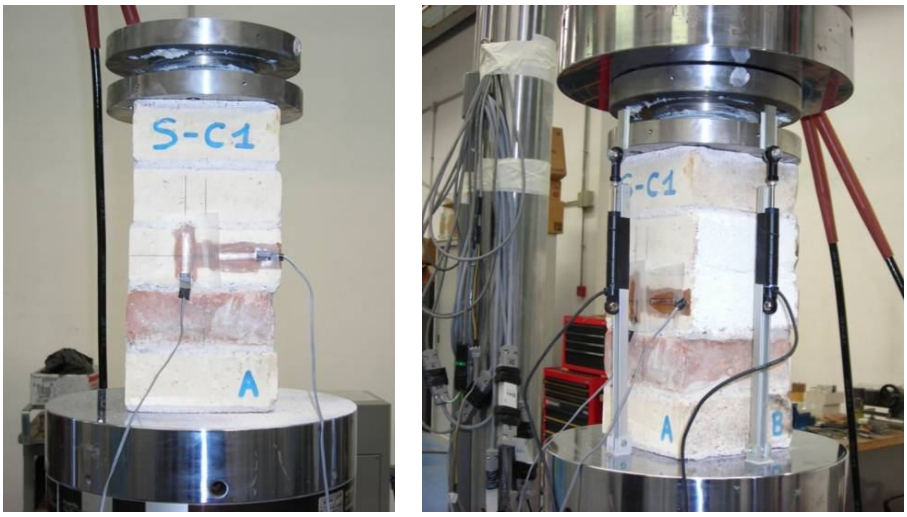

Figure 2.20. Equipment for centered compression tests on brickwork: strain-gauges and spherical articulation (left) and position transducers (right).

Table 2.4 lists the main properties resulting from the experiments: compression strength f_M and corresponding strain $\varepsilon(f_M)$, initial tangent stiffness E_{M0}, average of the stiffness values of unloading-reloading branches $E_{M,u\text{-}r}$, and, finally, slope of the softening branch $E_{M,s}$.

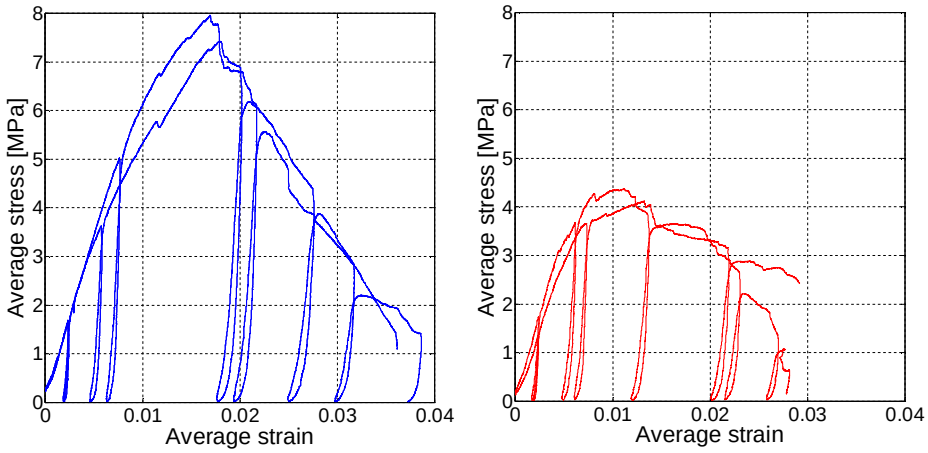

Figure 2.21. Experimental response curves of cyclic axial compression tests on S-C (left) and SC-G (right) type specimens.

Specimen	f_M [MPa]	$\varepsilon(f_M)$	E_{M0} [MPa]	$E_{M,u\text{-}r}$ [MPa]	$E_{M,s}$ [MPa]
S-C1	7.43	$18.1 \cdot 10^{-3}$	662.1	3191.3	-335.5
S-C3	7.96	$17.1 \cdot 10^{-3}$	668.3	2978.5	-351.6
S-CG1	4.37	$11.2 \cdot 10^{-3}$	726.5	2497.0	-127.1
S-CG3	4.12	$13.1 \cdot 10^{-3}$	585.0	2231.8	-162.8

Table 2.4. Experimental results of masonry prisms under cyclic axial load.

The stiffness in the reloading phases is higher than the slope of the first loading branch, as a result of the compaction process developing in horizontal mortar joints, where the inelastic strain is accumulated. The latter is associated to the maximum stress sustained during the loading history, as also pointed out in (Rosson et al., 1998). As a consequence, no variation in stiffness is detected in subsequent unloading-reloading cycles, while, once the load goes beyond the unloading value, the behaviour reverts to the skeleton curve of the monotonic test. The phenomenon of plastic strain accumulation in mortar layers can be also deduced by looking at the brick stress-strain curve, obtained from strain-gauge data during tests on S-C specimens: it is seen from the graph in Figure 2.22 (S-C1 sample) that the local strains in the brick reach a maximum value of $0.45 \cdot 10^{-3}$, and are much lower if compared with global values, reaching almost $40 \cdot 10^{-3}$; the energy dissipation in bricks appears negligible, so the low overall damping appears to be mainly associated to mortar response.

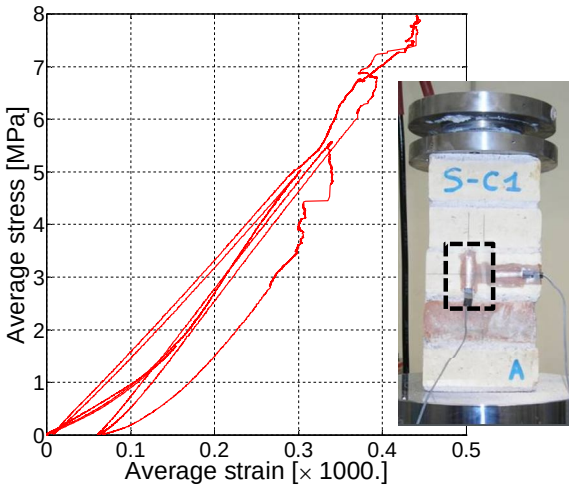

Figure 2.22. Brick stress-strain curve obtained from data acquired by the vertical strain-gauge during centered axial load test on S-C1 specimen.

The damage evolution is monitored during tests on S-C specimens (no head joints) and is shown in the photographs in Figure 2.23: some vertical cracks appear at about 80% of maximum load in a brick (often in the first or the last one, which are in contact with the loading plates) and then rapidly propagate into the other tiers. After the peak load is reached, the cracks increase in size and involve the entire sample. The rupture appears quite spread in transversal direction, while, looking at the specimens after the end of the tests, an evident transversal expansion of the central portion of the prism is clearly induced by some confining effect; finally, in the very last part of the experiment, some fragments are ejected and only the central core of the cross-section is still reactive.

Otherwise, looking at the damage evolution in SC-G specimens (provided with head joints) a preferential weakness plane is evident (Figure 2.24): vertical cracks propagate starting from the vertical mortar joints and then involve the whole sample, which is substantially divided into two portions (see the last photograph), leading to a lower failure load.

The reduction in strength found in the specimens with mortar head joints, passing from about 7.6MPa to about 4.2MPa (-45%), is accompanied by a slight reduction of the softening branch slope, while almost no variation in stiffness is recorded for the elastic branch (Table 2.4).

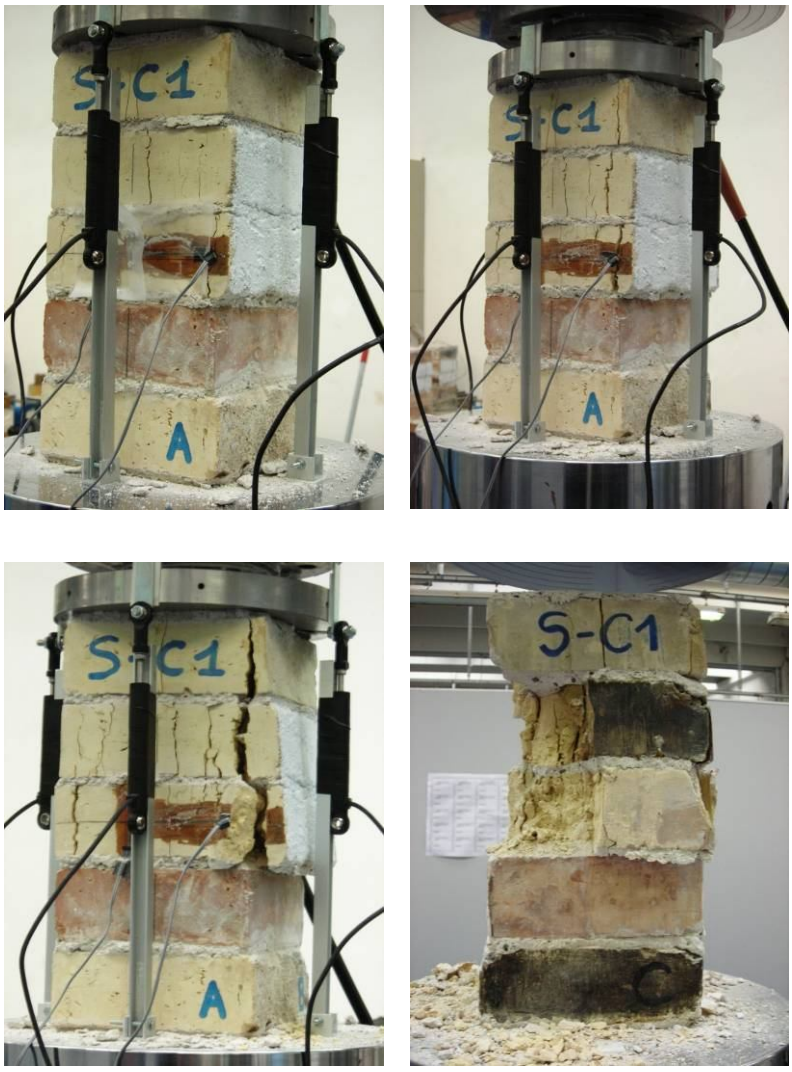

Figure 2.23. Failure pattern of historic brick masonry under centered compression: S-C specimens.

Figure 2.24. Failure pattern of historic brick masonry under centered compression: S-CG specimens.

2.5.1. Head-joint effect

As it is known (Hilsdorf, 1969), the failure of brick masonry under compression is driven by tensile horizontal stress developing in the bricks as a consequence of the mismatch of transverse dilatation between brick and mortar layers. In the present case, this phenomenon is amplified by the low mortar strength and stiffness if compared to those of the brick and, as a result of the confinement of the bed joints, the brickwork strength is much higher than that of mortar.

When head joints are present (S-CG specimens), the average tensile stress in the brick remains almost unchanged if compared to S-C type, but a stress concentration occurs and the maximum tensile stress significantly increases along the vertical plane of the head joints. Since the failure of the brick is brittle in traction, the strength is controlled by the maximum, rather than the average, stress; this explains the great reduction in strength observed in experiments. Conversely, the overall stiffness is mainly controlled by the average stress and therefore no significant variation occurs between the two specimen types, as observed in the tests.

A finite element analysis with a 3-D elastic model, reproducing the two brickwork patterns, provides a first explanation of the observed behaviour: the stress concentration resulting from the presence of head joints is such that the same value of maximum tensile stress is reached in S-CG specimen for a vertical load about 45% lower than in S-C specimen. The ratio between compressive strength of stack bond (S-C) and running bond (S-CG) is 1.94, and is higher than the ones found in (Mann and Betzler, 1994) and in (Vermeltfoort, 1994) where, anyway, much lower difference in stiffness is found between the units and the mortar adopted for building the testing samples. In these works, a ratio between the elastic moduli of brick and mortar E_b/E_m of about 3 results in a ratio between stack bond and running bond strength values ranging from 1.3 to 1.4. On the contrary, in the present case, the ratio between elastic moduli is about 13 and the ratio between compressive strength values is 1.85.

The horizontal stress field in the two specimens under the maximum experimental load (142kN for S-C and 76kN for S-CG samples) is shown in Figure 2.25: both analyses give rise to almost the same value of the maximum horizontal tensile stress in the bricks ($\cong$1MPa).

Numerical simulations are performed considering the average experimental elastic modulus E_b=3900MPa for the bricks and an equivalent modulus E_m=60MPa for the mortar, much lower than the experimental value, to account for the inelastic deformation occurring in the tests; in particular, E_m is defined by requiring the vertical displacement of the model to be the same as the one measured in the test at the peak load. As regards the Poisson ratios, the values ν_b=0.15 and ν_m=0.35 are assumed for brick and mortar, respectively. It has to be noted that the latter is much higher than the elastic

Poisson ratio, so as to take into account that mortar behaves as an almost uncompressible medium when plastic strains develop.

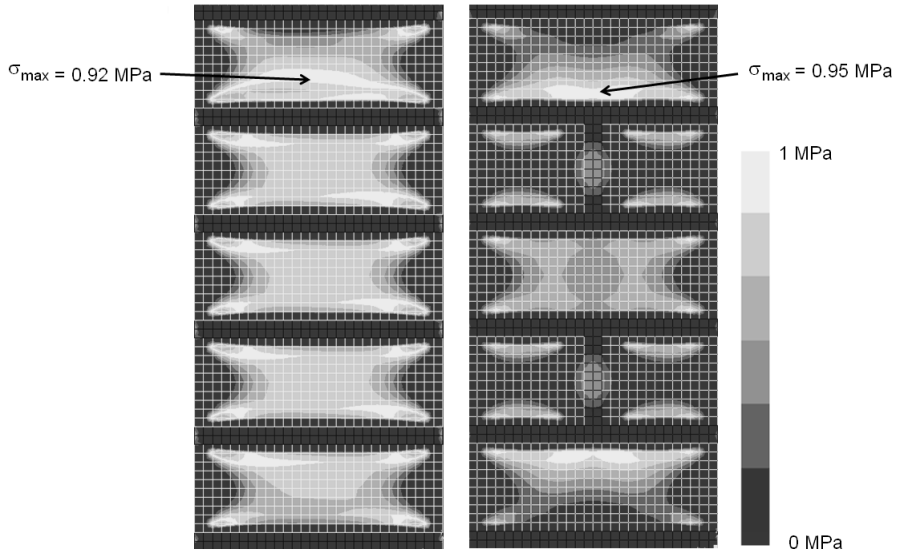

Figure 2.25. FE analysis results: contour plot of horizontal tensile stresses at failure in S-C (left, resultant load 142 kN) and S-CG (right, resultant load 76kN) specimens.

For a full explanation of the experimental behaviour, a refined non-linear model would be required to take into account the inelastic deformation occurring in mortar bed joints and the cracks forming in head joints before collapse, since both these effects strongly increase the tensile stress in the bricks. Anyway, the recourse to such a refined model would be suitable for small specimens but not for large structures like, for example, bridges. In the latter case, a simpler model has instead to be defined, in which masonry is considered as an equivalent homogeneous medium (Lourenço, 1998) and the effect of the head joint is included in the macroscopic properties of the material.

2.5.2. Strength and stiffness estimate through simple analytical models

According to an elastic approach in which brick masonry is regarded as a multi-layered medium and strain compatibility is imposed at the interfaces between brick and mortar (Hilsdorf, 1969), the compressive strength of brickwork f_M can be estimated according to the following analytical relation:

$$f_M = f_b^c \left(1 + \frac{\frac{f_b^c}{f_b^t}\left(\rho_2 \nu_m - \nu_b\right)}{\left(1-\nu_b\right) + \rho_1\rho_2\left(1-\nu_m\right)} \right)^{-1} \tag{2.2}$$

in which ρ_1 is defined as the ratio between brick and mortar layer thicknesses (t_m and t_b), while ρ_2 is the ratio between the elastic moduli (E_b and E_m):

$$\rho_2 = \frac{t_b}{t_m};\ \rho_1 = \frac{E_b}{E_m} \tag{2.3}$$

For S-CG type specimens, an equivalent mortar joint height is considered and an average value ν_{eq} of the Poisson coefficient is defined, as reported in (2.4), where the layer is not made of an entire block (Figure 2.26).

$$\nu_{eq} = \frac{\nu_b t_b + 2\nu_m t_m}{t_b + 2t_m} \tag{2.4}$$

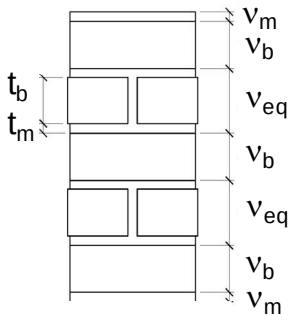

Figure 2.26. Identification of the equivalent mortar joint height in S-CG specimen for the analytical estimate of the ultimate load.

The estimated resistance values are 8.15MPa for S-C type specimens and 3.98MPa for S-CG ones, and are not very far from the average experimental results (7.7MPa and 4.25MPa for S-C and S-CG type specimens respectively).

As regards the elastic modulus, several expression are available in literature depending on the stiffness of the components (units and mortar), on the compressive strength of the assemblage, on the geometry, and on the water absorption of the unit (Brooks and Abu Baker, 1998). In the present case, an estimated value of 658MPa, not very different from the average vertical stiffness found in experimental tests (660MPa), can be obtained by

means of expression (2.5), proposed in (de Felice, 2001); such a relation results from an homogenization procedure and is independent from the bond characteristics.

$$E_M = \left(\frac{1}{E_b} + \frac{t_m}{t_b} \frac{(1-\nu_m{}^2)}{E_m} \right)^{-1} \tag{2.5}$$

2.6. Brickwork under compression and bending

Three different specimen types are tested under cyclic eccentric axial load (Figure 2.18 and Table 2.3); experiments are carried out under displacement control to determine the whole response curve in terms of both Force-Displacement and Moment-Curvature relations.

The first specimen type (made in 4 samples denoted as S-C and S-CG) is the same as for centered compression tests. It measures 140×140×310mm^3 and is made of five tiers, each consisting of half-brick units. S-CG specimens are provided with head joints in the second and in the fourth layers. The second type, denoted as S-E5 (7 samples), measures 280×140×310mm^3 and is made of five tiers consisting of a brick unit alternating with two half-brick units; there is a head mortar joint in the second and in the fourth layers, parallel to the major side of the cross-section, which is also the direction of the axial load eccentricity. Finally, the third type is denoted as S-E9 (4 samples) and measures 420×140×550 mm^3; it is made of nine tiers of bricks as shown in Figure 2.18. It presents a head joint parallel to the major side of the cross-section (as in S-E5 type specimen) in the second, forth, sixth and eighth tiers, observable on the minor lateral sides of the prism (named B and D); moreover, there are staggered head joints in the other direction.

All the specimens are built so as to reproduce the typical arch brick arrangement (Figure 2.27) and the way of applying the external load intends to replicate the stress condition effectively experimented by the cross-section (or by a segment) of a bridge vault.

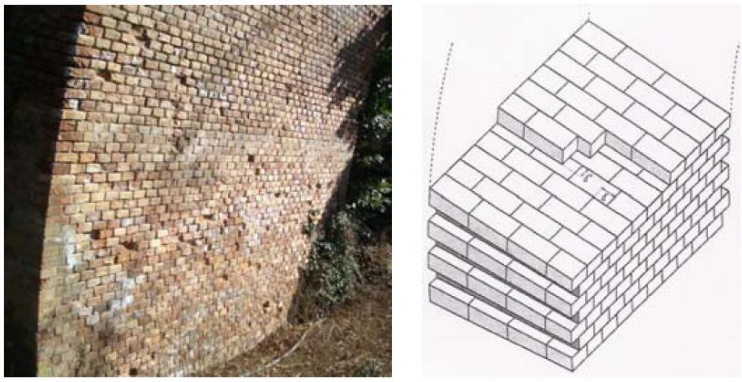

Figure 2.27. Brick arrangement of the vault of a masonry arch bridge (left) and schematic illustration of the texture (right).

2.6.1. Testing set-up for eccentric axial load tests

The eccentric axial load is applied by means of two steel bars with diameter ∅=20mm and two steel HEA140 I-beams, stiffened with vertical flanges, in contact with the bases of the masonry prism in order to apply compression with the desired eccentricity, avoiding local stress concentrations. The initial load eccentricity is known, since the stress resultant is forced to pass for the ∅20 steel bars, which are welded to 20mm thick squared steel plates to avoid stress concentrations on the loading plates of the MTS testing machine.

Displacement and strain data are measured using linear potentiometers (electrical stroke ±5mm, ±12.5mm, ±25mm, ±50mm; resistance 0.4÷4kΩ, independent linearity ±0.25%) and resistive strain-gauges (initial length 30mm), arranged as shown in Figures 2.28−2.30. In particular, four potentiometers are fixed to the HEA steel I-beam corners by means of threaded steel bars with diameter ∅=5mm welded to the I-beam edges, to get global displacements and derive the macroscopic response; local deformations are read by smaller transducers (positioned vertically and horizontally) and strain-gauges applied on the central bricks.

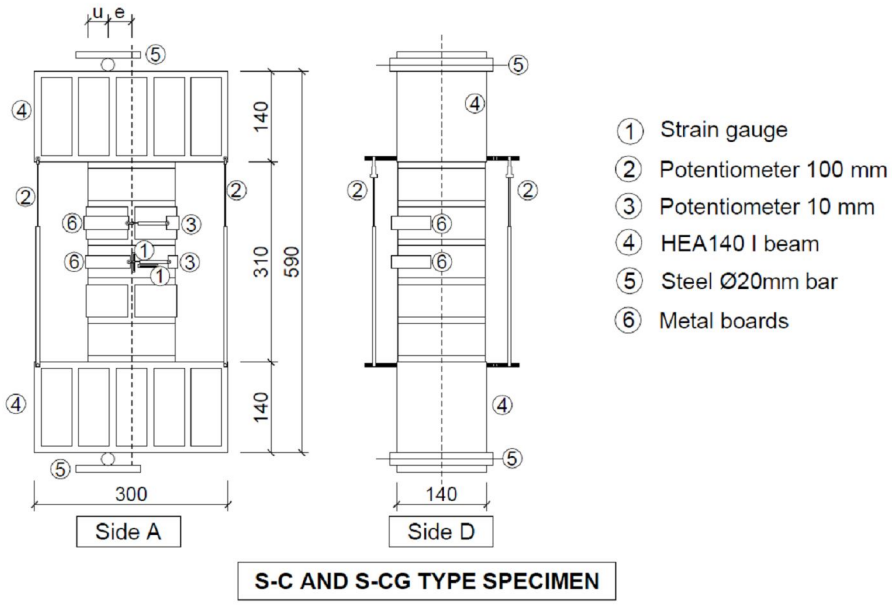

Figure 2.28. Schematic illustration of the equipment for eccentric axial load tests on S-C and S-CG brickwork specimens.

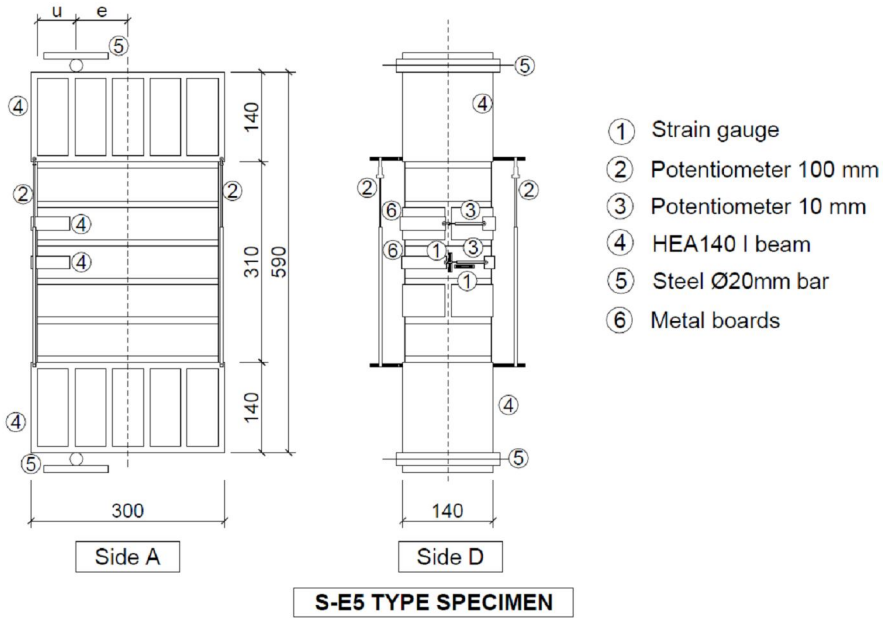

Figure 2.29. Schematic illustration of the equipment for eccentric axial load tests on S-E5 brickwork specimens.

The biggest specimen type (S-E9) is instrumented with 15 linear potentiometers in addition to the devices already adopted for the other types. Additional transducers are applied on the major lateral sides of the prism (named A and C), along five vertical alignments and divided into three sets (Figures 2.30−2.33) with the purpose of monitoring the cross-section rotation and the local deformations during the tests. The transducers are fixed to the bricks by means of threaded steel bars with diameter ∅=4mm, placed in 5mm deep drill holes and fixed by using a bi-component resin.

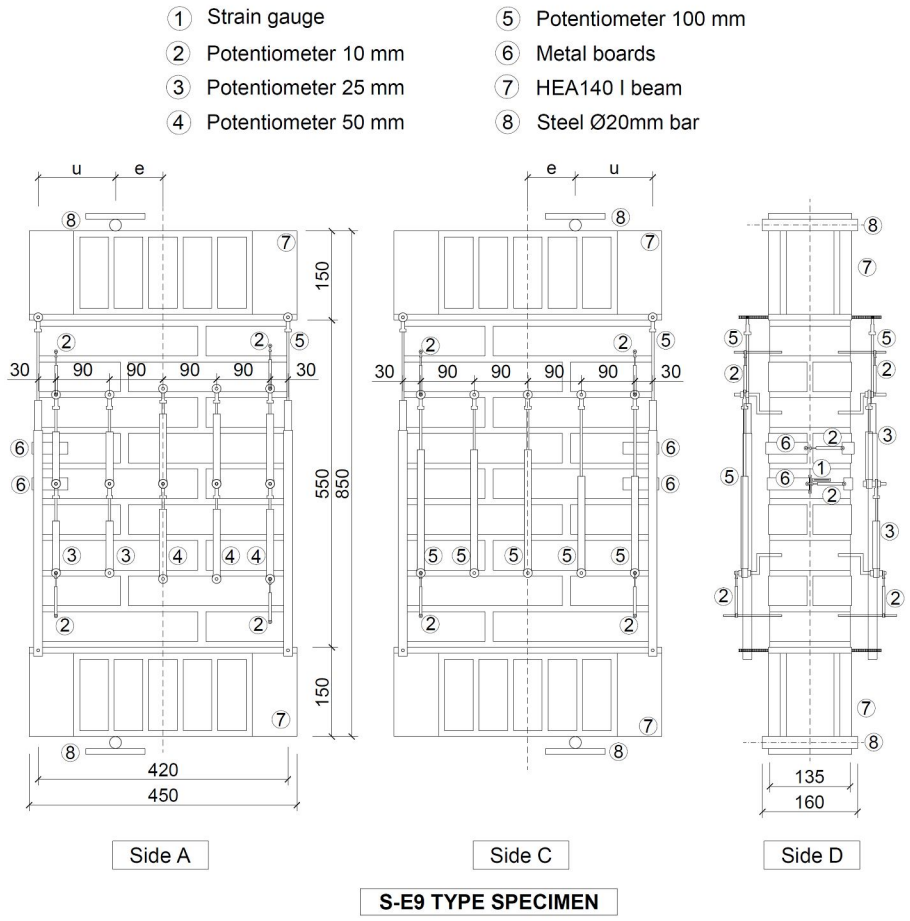

Figure 2.30. Schematic illustration of the equipment for eccentric axial load tests on S-E9 brickwork specimens.

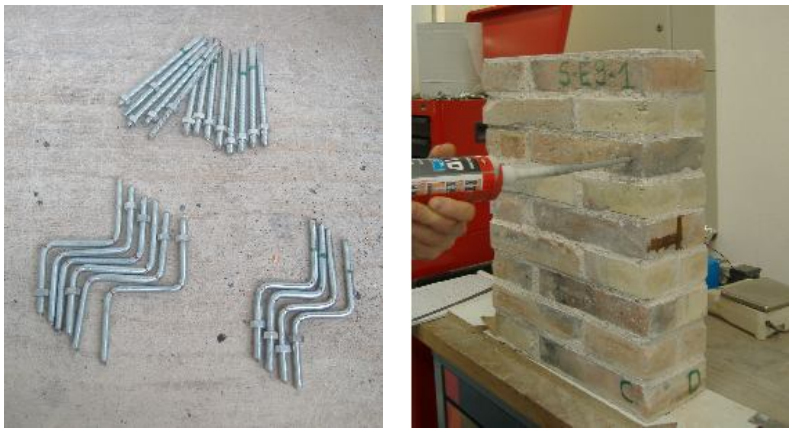

Figure 2.31. Specimen preparation: detail of the ∅=4mm threaded steel bars (left) and positioning in the drill holes through bi-component resin.

Figure 2.32. HEA-140 I-beam steel bar (left) and ∅20 steel bar (right) used for eccentric axial load tests on SE-9 brickwork specimens.

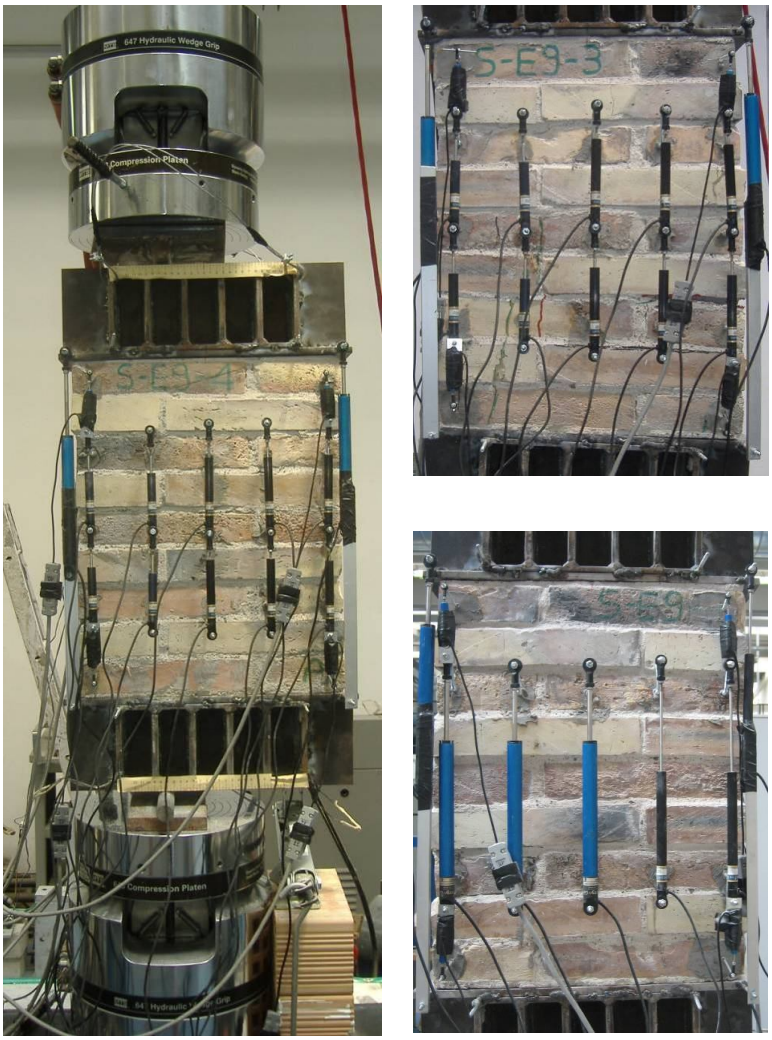

Figure 2.33. Test set-up for monitoring the cross-section deformation during eccentric axial load tests on S-E9 specimens.

2.6.2. Experimental results

Eccentric axial load tests lead to the determination of the response of a masonry element subjected to compression and bending in terms of Load-Displacement and Moment-Curvature relations.

The global curvature χ (which is the average value along the element height) and the global displacement δ (which is referred to the load

application point) are computed from the displacement data acquired by the transducers applied to the corners of the steel I-beams, according to the following expressions:

$$\Theta = \frac{\Delta H_2 - \Delta H_1}{2 \cdot B} \tag{2.6}$$

$$\chi = \frac{\Theta}{H} = \frac{\Delta H_2 - \Delta H_1}{2 \cdot B \cdot H} \tag{2.7}$$

$$\delta = \Delta H_1 + \frac{\Delta H_2 - \Delta H_1}{B}\left(\frac{B}{2} - e''\right) \tag{2.8}$$

$$e'' = \Theta \cdot h_p = \frac{\Delta H_2 - \Delta H_1}{2 \cdot B} \cdot h_p \tag{2.9}$$

In expressions (2.6−2.9) Θ is the average rotation of each I-beam steel bar, e'' is the second-order eccentricity (an increase of the effective eccentricity of the external load, up till about 10%, is induced by the rotation of the plates), and, finally, h_p is the height of the I-beams, equal to 140mm for S-C, S-CG and S-E5 type specimens and to 150mm for S-E9 type specimens. In fact, for the latter samples, the bars previously used for the other experiments are modified with the addition of 10mm thick plates and stiffening lateral flanges (Figure 2.32). The computation of Θ, and of all the quantities depending on it, is derived directly from the data read by the potentiometers at plate edges ΔH_1 and ΔH_2, being ΔH_i (i=1, 2) the average value of the relative displacements measured by the transducers on side i, and B the specimen width (i.e. the distance between the transducers), as shown in Figure 2.34.

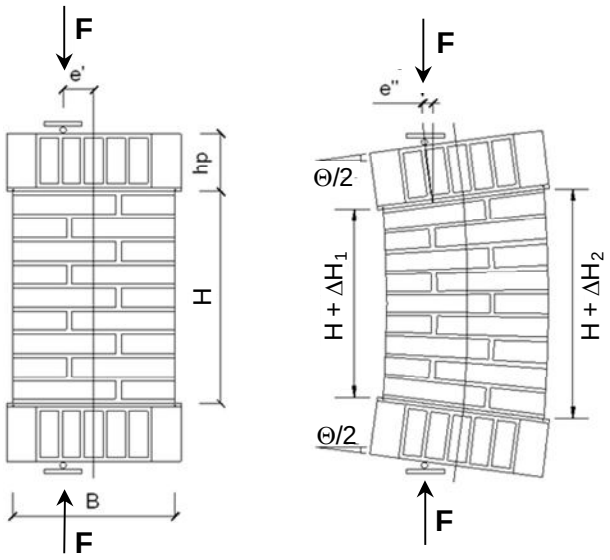

Figure 2.34. Schematic illustration of brickwork specimen in its initial and deformed configurations.

The value of the applied load F is directly acquired by the load cell integrated in the MTS machine, while the bending moment is computed by taking into account the second order effects deriving from the rotation of the steel plates (Figure 2.34) according to the following expression:

$$M = F \cdot e = F \cdot (e' + e'') \tag{2.10}$$

The results are shown in Figures 2.35−2.38 for the various specimens and eccentricities; for each test, the Load-Displacement (F-δ) and Moment-Curvature (M-χ) diagrams are plotted.

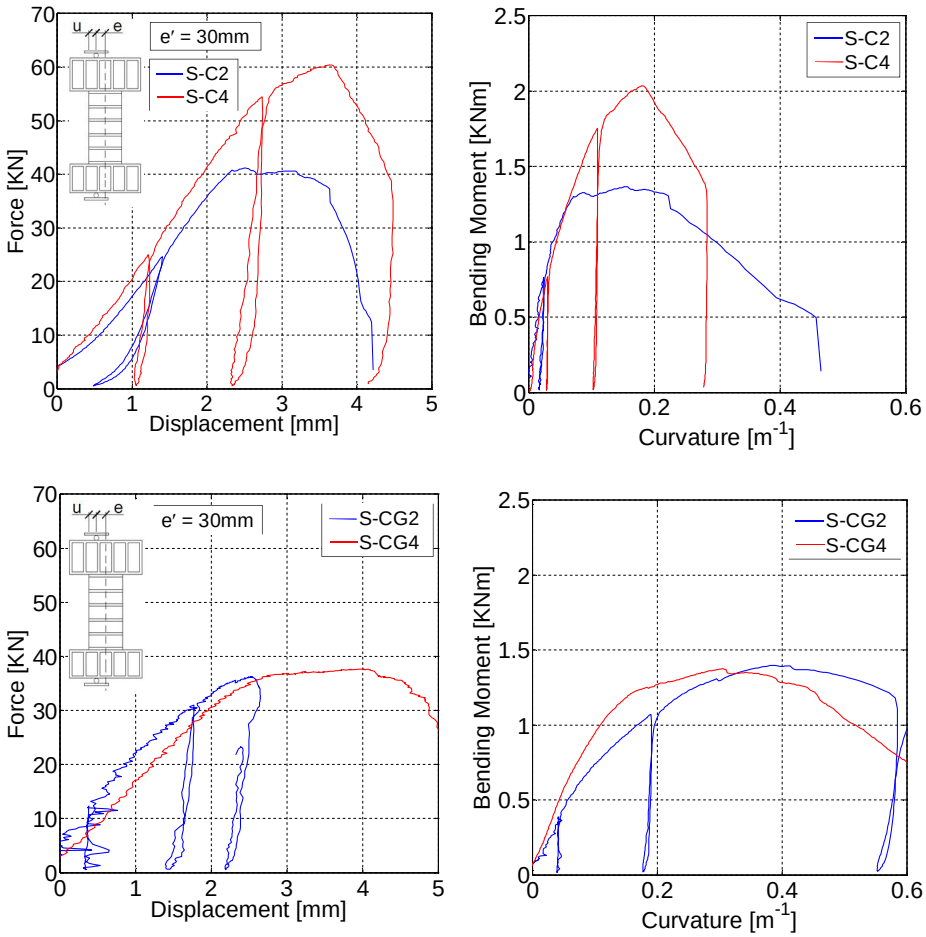

Figure 2.35. Experimental results of eccentric (e′=30mm) axial load tests on S-C (up) and S-CG (down) masonry specimens.

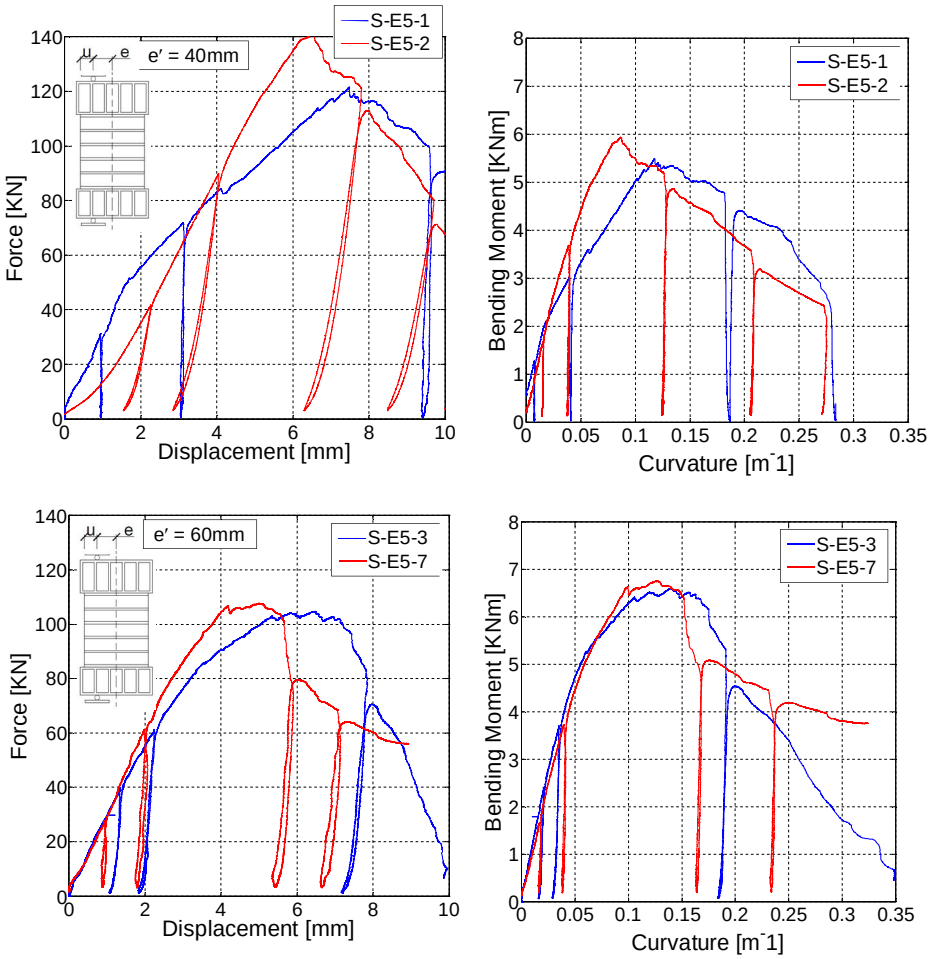

Figure 2.36. Experimental results of eccentric axial load tests on S-E5 masonry specimens for different eccentricities (e′=40, 60mm).

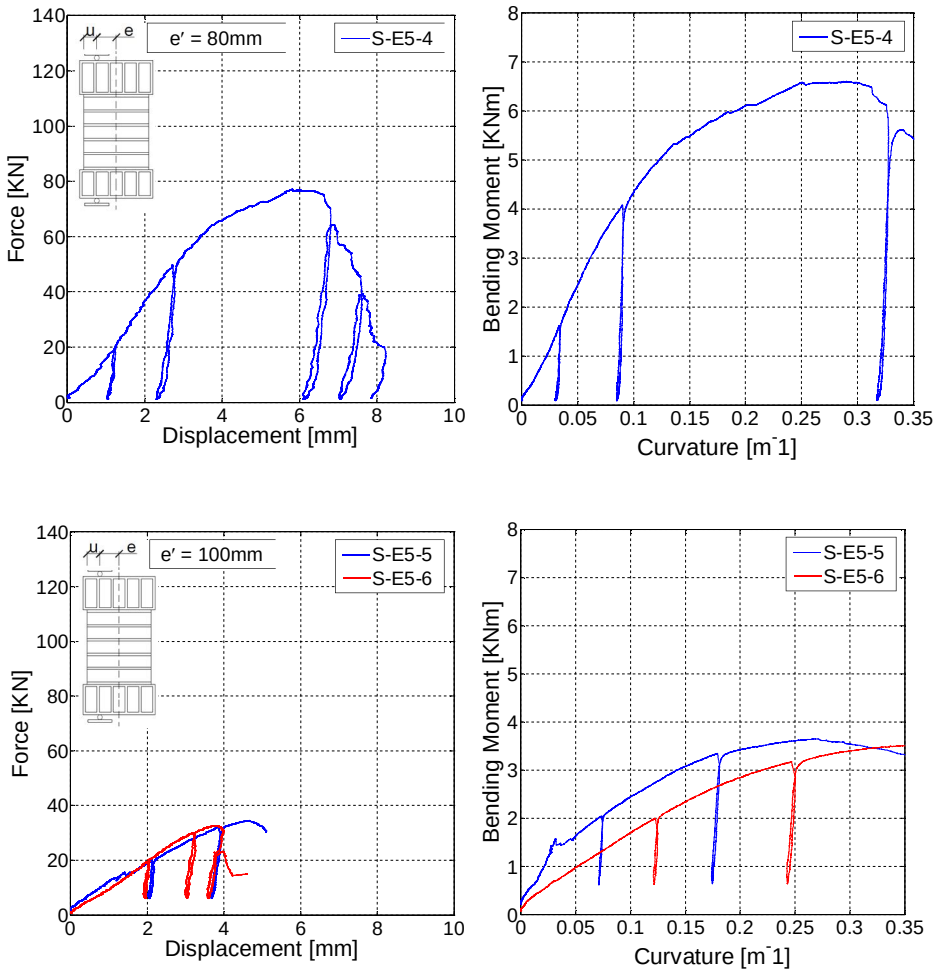

Figure 2.37. Experimental results of eccentric axial load tests on S-E5 masonry specimens for different eccentricities (e′=80, 100mm).

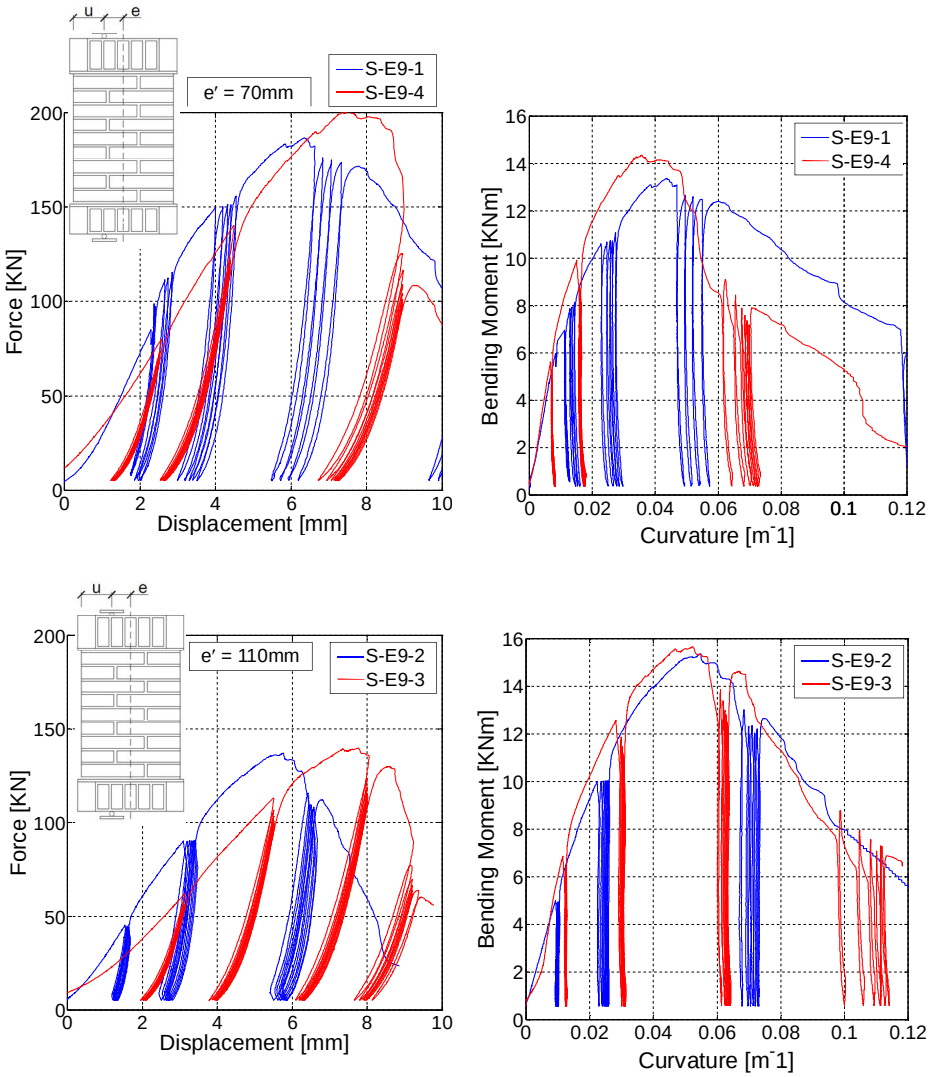

Figure 2.38. Experimental results of eccentric axial load tests on S-E9 masonry specimens for different eccentricities (e′=70mm, 110mm).

The response curves of eccentrically loaded masonry specimens show some similar properties if compared to the ones found in centered compression tests: an initial elastic branch followed by a non-linear pre-peak phase is found; then, after the displacement corresponding to the maximum force $\delta(F_0)$ and the curvature corresponding to the maximum bending

moment $\chi(M_0)$ are exceeded, the behaviour is characterized by a linear softening phase.

The synthetic results of the experimental campaign on eccentrically loaded historic brickwork are summarized in Table 2.5 in which, for each test, the peak values are collected together with the type and the name of the specimen, the initial eccentricity e′ and the correspondent distance u=e′−B/2.

As in the case of centered compression, the cyclic tests show the capability of brickwork to sustain unloading-reloading cycles, also when performed in the softening branch. Cyclic loading induces a weak strength degradation, even if the skeleton curve can still be seen as the envelope of the cyclic one, and no heavy stiffness reduction is found. The compaction of mortar bed joints results in an increase of the overall stiffness; thus, the slope of the reloading branches is higher than the initial elastic one.

Specimen type	Name	e′ [mm]	u [mm]	F_0 [kN]	$\delta(F_0)$ [mm]	M_0 [kNm]	$\chi(M_0)$ [m^{-1}]
S-C	S-C2	30	40	41.2	2.41	1.51	0.18
	S-C4	30	40	60.4	3.67	2.26	0.18
S-CG	S-CG2	30	40	36.2	3.25	1.72	0.43
	S-CG4	30	40	37.7	4.07	1.62	0.33
S-E5	S-E5-1	40	100	121.1	8.61	5.48	0.12
	S-E5-2	40	100	141.1	5.22	6.21	0.09
	S-E5-3	60	80	104.6	6.41	6.92	0.14
	S-E5-7	60	80	107.3	5.04	7.04	0.12
	S-E5-4	80	60	76.7	5.89	7.07	0.30
	S-E5-5	100	40	34.5	4.62	3.85	0.27
	S-E5-6	100	40	32.6	3.80	3.79	0.38
S-E9	S-E9-1	70	140	186.2	6.22	13.13	0.025
	S-E9-4	70	140	201.2	8.07	14.36	0.035
	S-E9-2	110	100	137.1	7.89	15.37	0.054
	S-E9-3	110	100	139.9	8.26	15.67	0.052

Table 2.5. Experimental results of masonry specimens under axial load and bending moment.

2.6.3. Crack pattern evolution

The damage pattern observed in eccentric axial load tests is documented by the photographs in Figures 2.39−2.41, and, in general, develops as follows: the first crack appears in the compressed edge at about 70÷80% of the peak load; then, cracks spread vertically crossing the mortar joints until they affect the whole specimen height, while small cracks also form in the lateral faces.

At the same time, one or more horizontal mortar joints start to open in the opposite side. When deformation increases, a localization of cracks develops, characterized by the crushing of one or two bricks on the compressed edge,

and the opening of the corresponding horizontal bed joint on the opposite one (Figures 2.40−2.41).

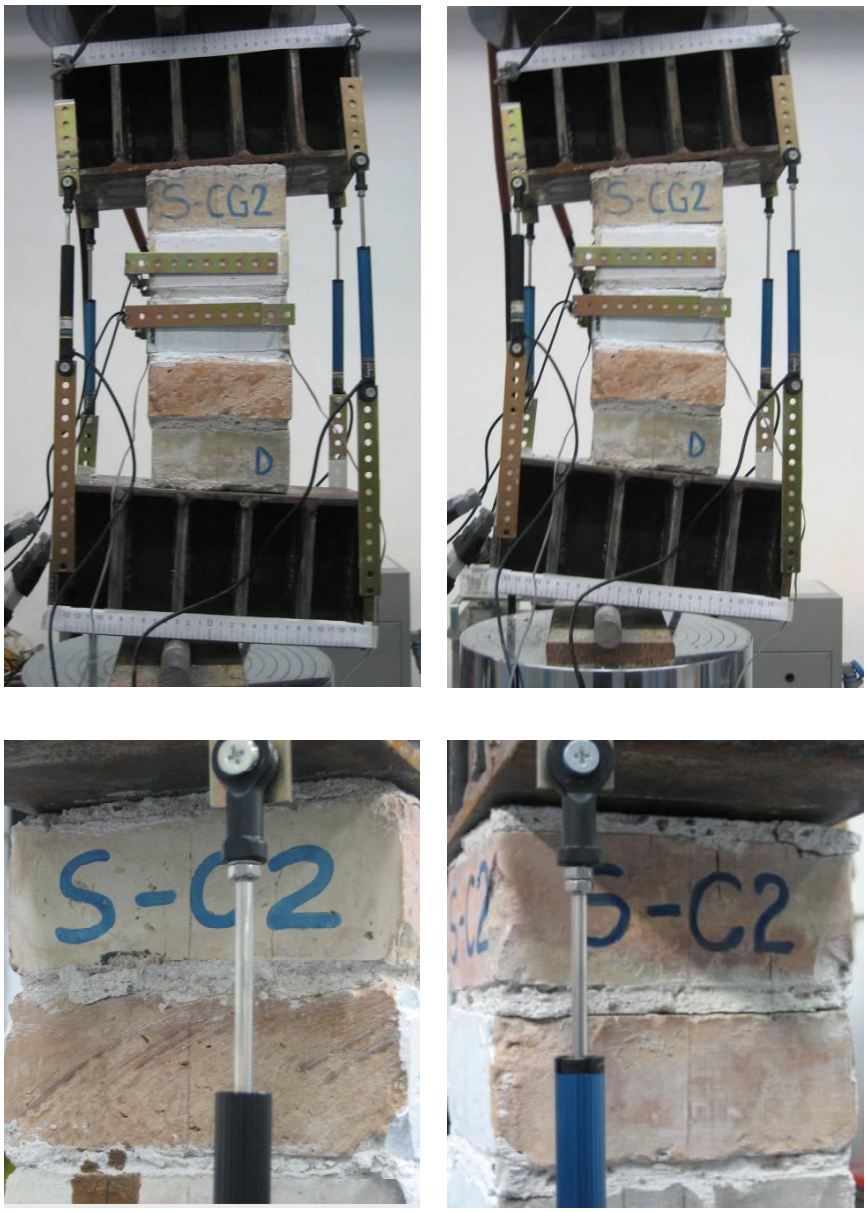

Figure 2.39. Crack pattern evolution of eccentric axial load test on S-C2 brickwork specimen: deformed configuration (up) and detail of the cracks in the compressed edge (down, left side) and of the opening of the bed joint (down, right side).

Figure 2.40. Crack pattern evolution of eccentric axial load test on S-E5-4 brickwork specimen.

Figure 2.41. Crack pattern evolution of eccentric axial load test on S-E9-4 brickwork specimen.

2.6.4. Maximum load estimate

Experimental tests show that for high eccentricities (load-resultant out of the third medium) the maximum load no longer depends on the specimen width B but only on the distance between load resultant and compressed edge u=B/2−e. In fact, by comparing the results of SC-G and S-E5 specimens for u'=40mm, and those of S-E5 and S-E9 specimens for u′=100mm (Table 2.5), comparable values of the maximum load F_0 are obtained. The experimental results for all specimens provided with head joints are plotted in the F_0–u plane in Figure 2.42, showing an almost linear dependence of the maximum load on the distance from the compressed edge; S-C type specimens are not included in this comparison because of the different arrangement of bricks.

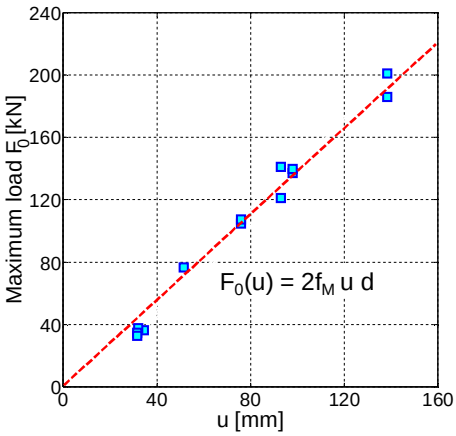

Figure 2.42. Maximum load (F_0) vs. distance to the compressive edge (u).

Therefore, for high eccentricities, a rough estimate of the load capacity can be obtained simply by expression (2.11) considering a uniform stress distribution equal to the masonry compressive strength f_M over a section area equal to 2·u·d (where d is the specimen depth), as it happens for perfectly plastic materials.

$$F_0 \cong 2\, f_M u\, d \tag{2.11}$$

The depth of an equivalent stress-block y*=2u is plotted in Figure 2.43 against the neutral axis depth y_c (i.e. the distance between neutral axis and compressed edge). Experimental results provide an average value of 0.73 for the ratio y^*/y_c, which is slightly lower than the value 0.80 currently used for reinforced concrete sections.

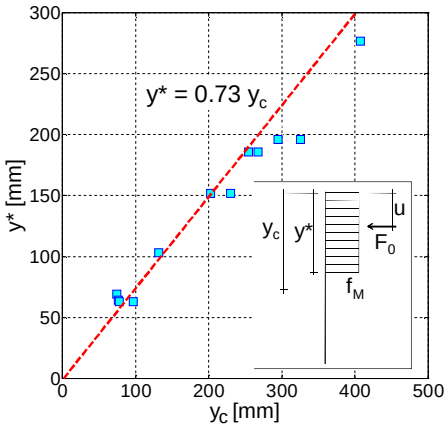

Figure 2.43. Stress block depth (y*) vs. neutral axis depth (y_c).

2.6.5. Behaviour after several load cycles

In eccentric compression tests on S-E9 specimens, several unloading-reloading ramps are repeated at different levels of displacement or force, aiming at investigating the development of the phenomenon of plastic strain accumulation. This issue has been widely investigated for concrete and r.c. structural elements (see for instance Sakai and Kawashima, 2000), but has remained almost unexplored for masonry. Figure 2.44 shows the detail of the Force-Displacement response curve at one of the unloading displacement levels, for two specimens having different eccentricity values (e′=70mm and e′=110mm) imposed at the beginning of the tests.

An asymptotic load decrease is clearly observable, probably due to the progressive exhaustion of the mortar compaction in the bed joints. A limit condition defined by a stability point, as it is named in (AlShebani and Sinha, 1999), can be identified in each step. Herein the stability point is found for each displacement value where unloading-reloading cycles are performed as follows: force values at the beginning of each unloading branch are collected, then the experimental data are interpolated by using a hyperbolic function (2.12). The latter is similar to the expressions typically adopted to represent age and long term effects on masonry elements (Brooks and Abu Baker, 1994; Brooks et al., 1997), and was initially proposed to describe creep phenomena on concrete (Ross, 1937).

The force value $F^{(n)}$ after *n* cycles is given by (2.12), depending on the first value $F^{(0)}$ (point on the skeleton curve), on the number of cycles *n*, and on two scalar coefficients b_1 and b_2; this kind of expression is found to be suitable to represent the strength reduction induced by damage evolution, as proved by the values of R^2, all very close to 1.0 (Figures 2.45 and 2.46).

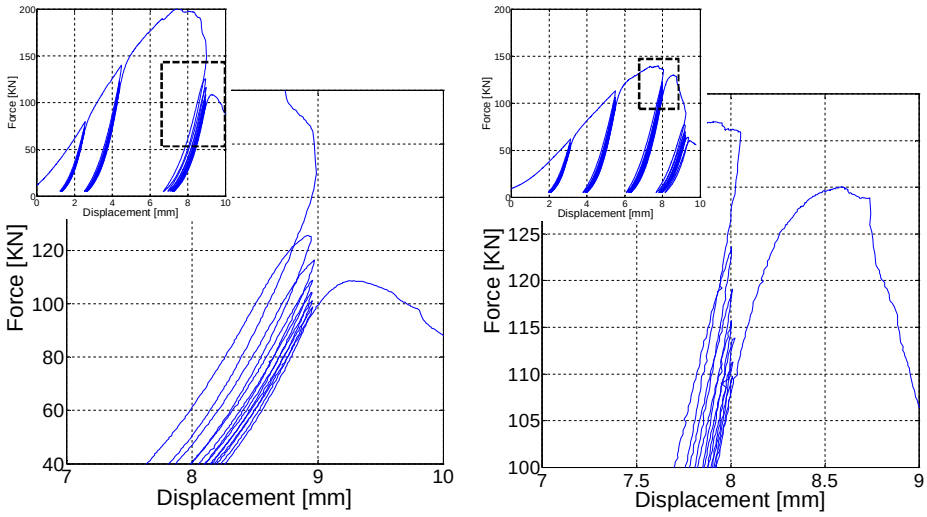

Figure 2.44. Detail of the experimental F-δ response curve of S-E9 type specimens for the eccentricity values e′=70mm (specimen S-E9-4, left) and e′=110mm (specimen S-E9-3, right).

$$F^{(n)} = F^{(0)}\left(1 - \frac{b_1 \cdot n}{b_2 + n}\right) \tag{2.12}$$

When $n \to \infty$ the force tends to $F^{(0)} \cdot (1 - b_1)$; in this condition the plastic strain is considered completely stabilized. The parameter b_1 expresses the part of $F^{(0)}$ that is lost because of a completely developed strength degradation, while b_2 determines the degradation rate.

The coefficients b_1 and b_2 are easily determined by performing a variable transformation k=1/n leading to the linear relation (2.13), whose terms are explicated in (2.14). In the k–G(k) plane a linear regression is performed to determine the coefficients C_1 and C_2; then, the parameters of the damage function are in turn found according to (2.14).

$$G(k) = C_1 k + C_2 \tag{2.13}$$

$$G = \frac{1}{F^{(0)} - F^{(n)}};\ C_1 = \frac{b_2}{F^{(0)} \cdot b_1};\ C_2 = \frac{1}{F^{(0)} \cdot b_1} \tag{2.14}$$

Starting from the so determined stability points, a stability curve is estimated, intending to represent the masonry response after several (to the limit, infinite) wide cycles, or, more generally, after whatever complex loading history. Such a relation could be used to represent the material

properties within a numerical simulation directed to achieve a lower-bound estimate of the long-term resistance of a masonry construction.

The stability curves are plotted in Figure 2.47 for the two considered S-E9 specimens.

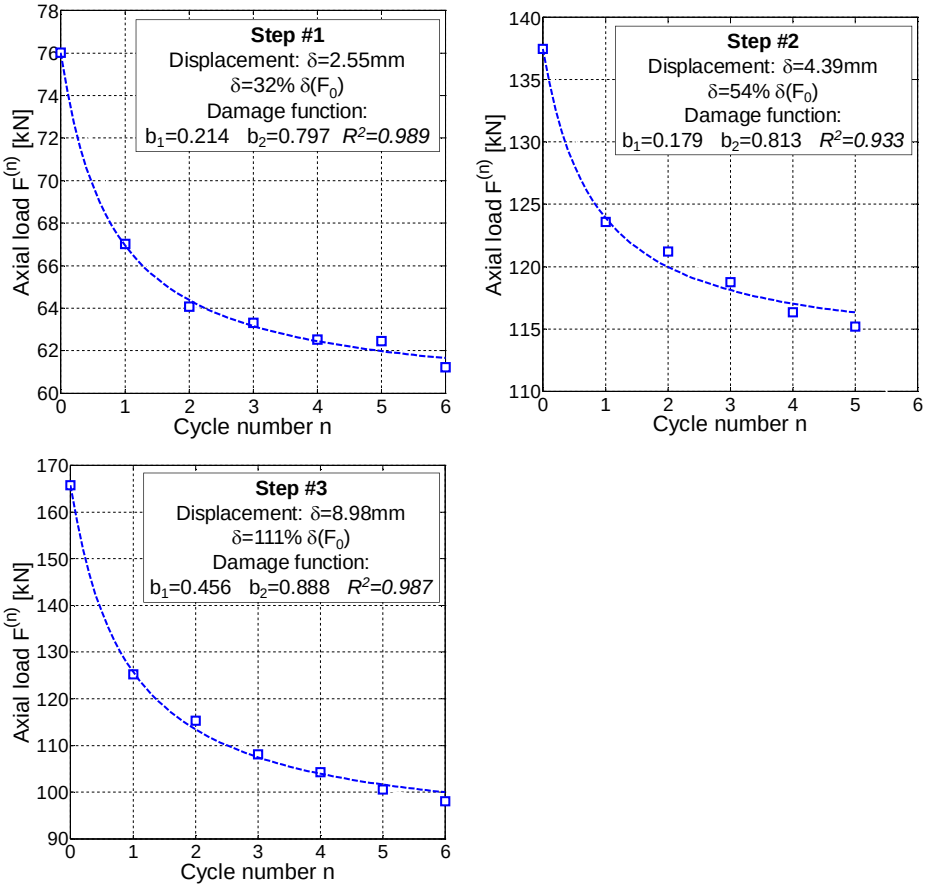

Figure 2.45. Interpolation through damage function of experimental force values at the beginning of unloading phases for specimen S-E9-4 (e′=70mm).

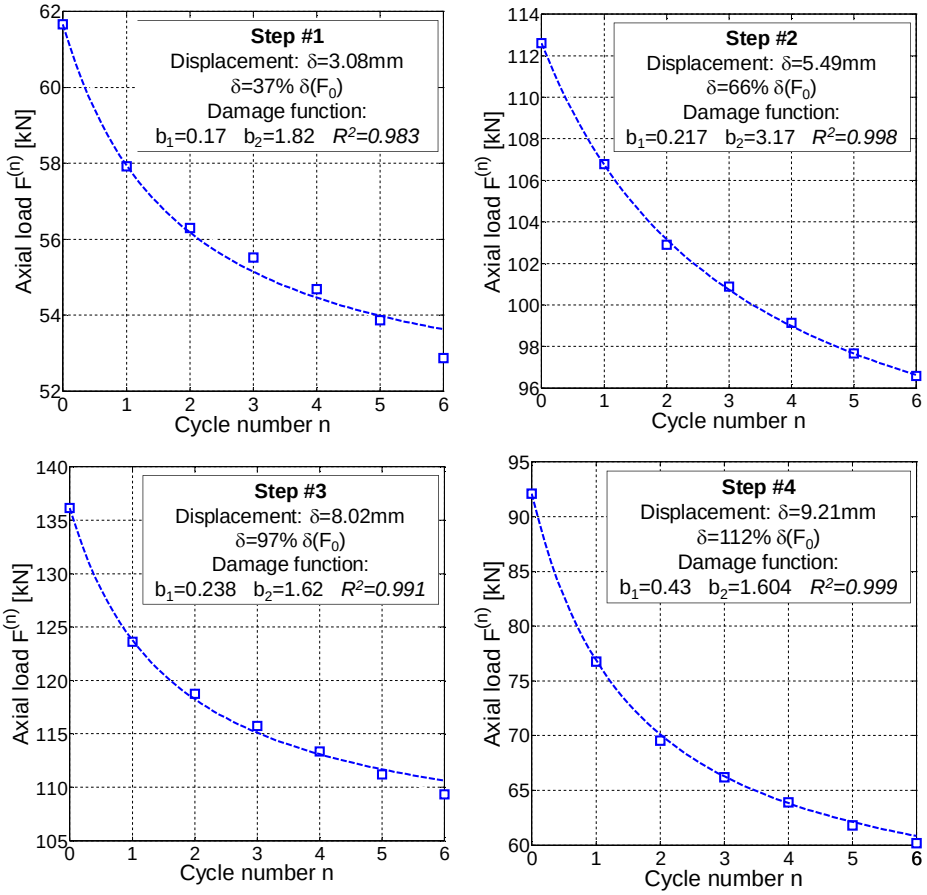

Figure 2.46. Interpolation through damage function of experimental force values at the beginning of unloading phases for specimen S-E9-3 (e′=110mm).

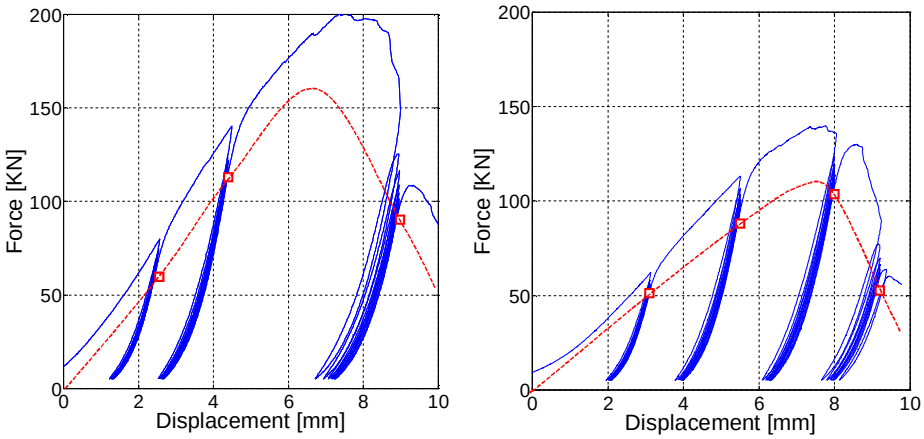

Figure 2.47. Stability curves for S-E9 specimens, for different eccentricity values: e′=70mm (Specimen S-E9-4, left) and e′=110mm (S-E3-4, right).

Finally, it has to be pointed out that the study of this particular aspect of the mechanical response of masonry does not intend to investigate its fatigue strength; in such a case several thousands of unloading-reloading cycles should be carried out (Tomor and Wang, 2010), with a narrow load variation (the one that could be induced by typical exercise conditions, like the traffic loads) starting from lower stress levels in the first loading branch (the stress induced by the self weight of the structure).

2.6.6. Cross-section behaviour

The experimental campaign on historic brickwork allows the global cross-section behaviour of masonry prisms subjected to compression and bending to be investigated; moreover, it provides information on whether the plane section assumption can be considered adequate for representing brickwork elements under eccentric loading.

The set-up of the tests, equipped with the steel plates through which the force is applied, ensures that the section is enforced to be plane at the boundary of the specimen; the strain distribution at the local level is monitored by means of three sets of vertical potentiometers arranged on the front and on the back sides of the prism (Figures 2.30−2.33). The cross-section deformation during the test is therefore deduced starting from the relative displacements between the couples of points where instruments are fixed, divided by the distance between them. The latter is approximately equal to 120mm for the two sets of transducers on side A, and to 240mm for the transducers on side C.

On side A, the average of the strains read by each couple of instruments (stroke ±25mm and ±50mm) at every vertical alignment is named *local strain*; the strain measured by the transducers on side C (stroke ±100mm) is named *intermediate strain.*

The results are plotted in Figures 2.48 and 2.49 for two samples having different eccentricities (e′=70mm and e′=110mm). Local and intermediate strains are compared with the average strain of the whole prism, as detected by the global potentiometers at its edges. The steps of the tests in which the results are represented are identified by a rate of the displacement corresponding to the maximum load $\delta(F_0)$, ranging from 25% to 125%.

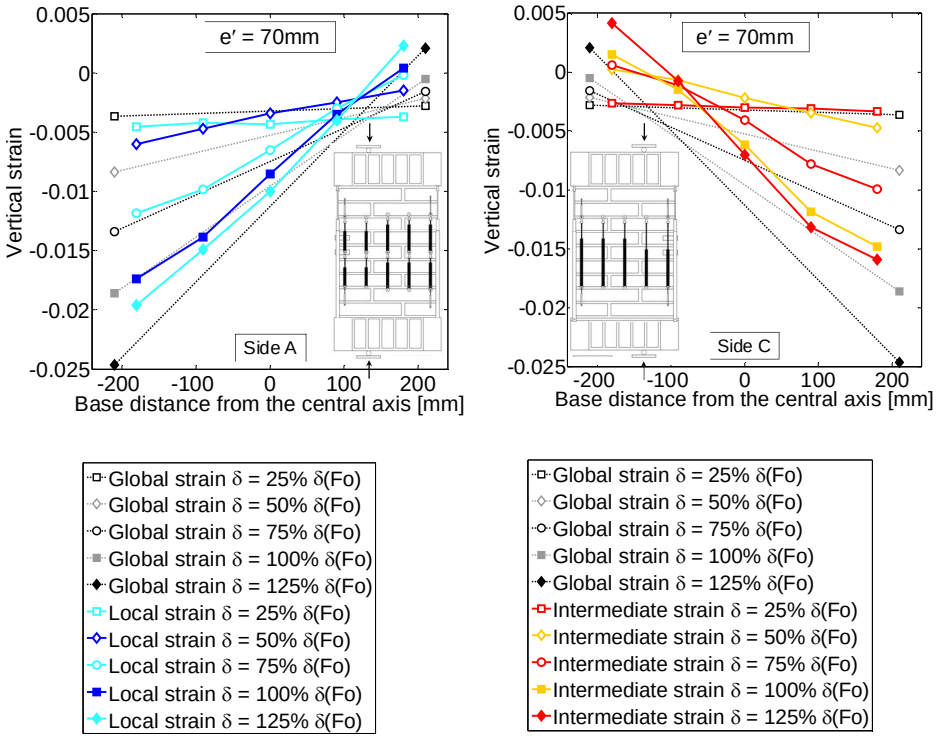

Figure 2.48. Cross-section local (left) and intermediate (right) deformation of a brickwork specimen under eccentric loading at different displacement steps: δ=0.25÷125 $\delta(F_0)$; e′=70mm.

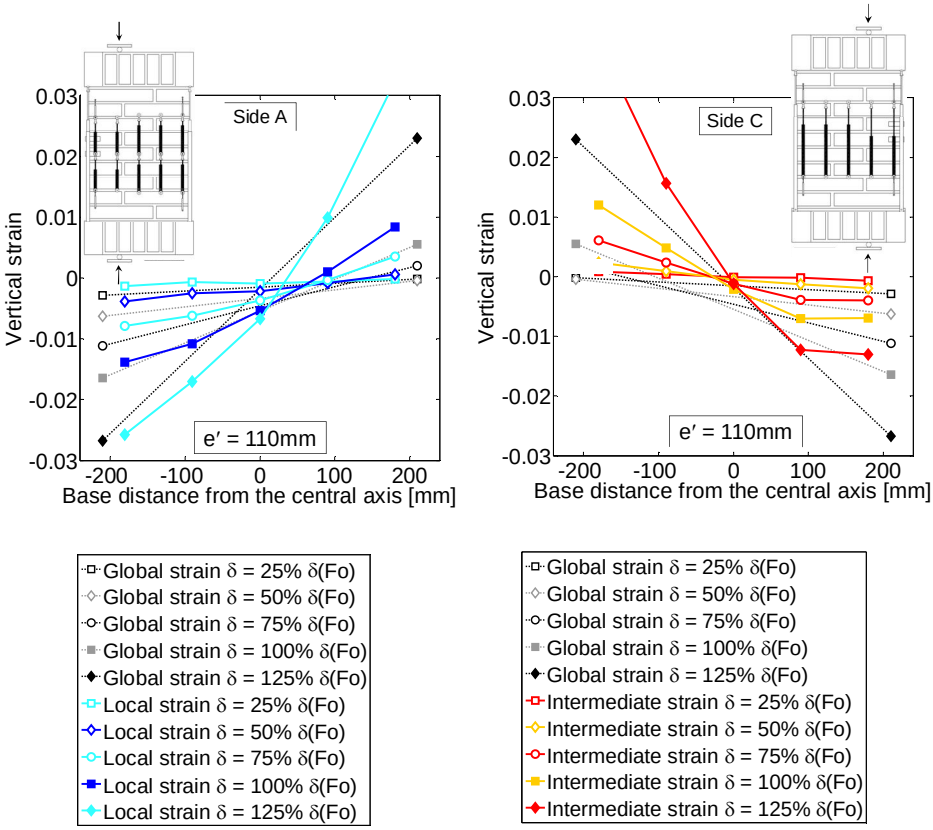

Figure 2.49. Cross-section local (left) and intermediate (right) deformation of a brickwork specimen under eccentric loading at different displacement steps: δ=0.25÷125 $\delta(F_0)$; e′=110mm.

It is seen that the cross-section remains almost plane, and rotates around a fixed neutral axis as the displacement increases up to $\delta(F_0)$. Then, a slight deviation from the plane behaviour is displayed and the neutral axis moves towards the compressed side. Clearly, at this stage, mortar joints start to open and several cracks develop within the specimen, leading to stress and strain concentrations; a deviation from a linear distribution results from these phenomena, as it is pointed out also in (Brencich et al., 2002) and in (Brencich and Gambarotta, 2005), where, anyway, the specimens are made of four entire bricks (so there are no head joints) and the cross-section behaviour is estimated starting from the relative displacements between couples of points separated by one only bed joint.

The comparison between average and local strains shows that the former ones are higher up to the attainment of the maximum load, probably because

they are influenced by the crushing occurring in the mortar joints in contact with the steel plates and by the detachment of the plates from the specimen at the tensile edge. At higher displacements, local strains increase until they exceed global ones.

The same remarks can be made for the intermediate deformation: the cross-section rotation appears smaller than the global average rotation, especially in the compressed edge of the specimen.

Finally, it has to be pointed that the wide cracks developing at the end of the test disturb the instrumental readings which become unreliable.

In conclusion, according to the experimental results, it seems that, from an engineering point of view, brick masonry under axial load and bending moment behaves according to the plane section assumption, also in the non-linear range and at least until a state of heavy damage is reached. This consideration makes it possible to adopt a beam element to represent the response of masonry elements under eccentric compression.

3. Modelling brickwork elements through fiber beams

3.1. The fiber beam element

3.1.1. Beam element formulation

The modelling strategy developed within the present work for the analysis of multi-span masonry bridges makes use of a beam mixed finite element with fiber cross-section, that has been originally developed for the simulation of reinforced concrete members under seismic actions (Spacone et al., 1996). It is a non-linear element with distributed plasticity providing an accurate description of the structural response when distributed inelastic phenomena occur, thanks to an adequate representation of the interaction between axial force and bending moment on the cross-section under biaxial loading conditions. Moreover, it takes into account the highly non-linear hysteretic behaviour of the material, offering the possibility of performing structural analyses under complex loading histories. Finally, the simplicity intrinsic in a frame element assures relatively low computational and modelling costs.

The cross-section is discretized into n×m fibers, characterized by uniaxial constitutive relations. The section force-deformation law is derived by numerical integration of normal stress and stiffness of the fibers at the integration points and is based on the assumption that deformations are small and that plane sections remain plane during the loading history; thus, no sliding between fibers is allowed.

The formulation is based on the mixed method, and is extensively illustrated in (Taucer et al., 1991). The starting point is the description of the force distribution within the element by interpolation functions that satisfy equilibrium. The selection of flexibility dependent shape functions for the deformation field considerably simplifies the final equations; thus, the mixed method can be seen as a particular case of the flexibility method, in which the choice of adequate shape functions is made.

The solving procedure is based on a flexibility based state determination iterative algorithm and is such that the equilibrium and the compatibility of

the element are always satisfied by the assumed force and deformation interpolation functions, as well as by the section constitutive relation, within a specified tolerance.

The formulation starts from the definition of the deformation **d**(x) and force **D**(x) fields along the element. Their expressions (3.1−3.3) depend on the deformation **a**(x) and force **b**(x) interpolation matrices, chosen a priori. In (3.1−3.3) Δ denotes the increments of the corresponding quantities, **Q** the element force vector, **q** the element deformation vector and, finally, i the step of the iterative solution algorithm loop. The latter is performed at the structure degrees of freedom until equilibrium between applied loads and internal resisting forces is satisfied.

$$\mathbf{D}^{i}(x) = \mathbf{b}(x)\mathbf{Q}^{i} \tag{3.1}$$

$$\Delta\mathbf{D}^{i}(x) = \mathbf{b}(x)\Delta\mathbf{Q}^{i} \tag{3.2}$$

$$\Delta\mathbf{d}^{i}(x) = \mathbf{a}(x)\Delta\mathbf{q}^{i} \tag{3.3}$$

The integral forms of the linearized section force-deformation relation and of equilibrium are combined to obtain the relation between element force and deformation increments.

The former is derived from a weighted integral along the element, whose length is denoted as L, as it is stated by expression (3.4), in which $\mathbf{f}^{i-1}(x)$ is the section flexibility matrix computed at the step i-1 and relating force and deformation fields within the section, while $\delta\mathbf{D}^{T}$ denotes a virtual section force field. Equation (3.5) is then obtained by substituting (3.1−3.3) in (3.4), and, as the it must hold for any virtual element force vector $\delta\mathbf{Q}^{T}$, equation (3.6) is derived:

$$\int_{0}^{L} \delta\mathbf{D}^{T}(x)\left[\Delta\mathbf{d}^{i}(x) - \mathbf{f}^{i-1}(x)\Delta\mathbf{D}^{i}(x)\right]dx = 0 \tag{3.4}$$

$$\delta\mathbf{Q}^{T}\int_{0}^{L} \mathbf{b}^{T}(x)\left[\mathbf{a}(x)\Delta\mathbf{q}^{i}(x) - \mathbf{f}^{i-1}(x)\mathbf{b}(x)\Delta\mathbf{Q}^{i}(x)\right]dx = 0 \tag{3.5}$$

$$\mathbf{T}\,\Delta\mathbf{q}^{i}(x) - \mathbf{F}^{i-1}\,\Delta\mathbf{Q}^{i}(x) = 0 \;\Rightarrow\; \mathbf{T}\,\Delta\mathbf{q}^{i}(x) = \mathbf{F}^{i-1}\,\Delta\mathbf{Q}^{i}(x) \tag{3.6}$$

In the linearized section force-deformation law (3.6), $\mathbf{F}^{i-1}$ is the element flexibility matrix (3.7) and **T** a matrix that only depends on the interpolation function matrices (3.8).

$$\mathbf{F}^{i-1} = \int_0^L \mathbf{b}^T(x)\mathbf{f}^{i-1}(x)\mathbf{b}(x)\,dx \tag{3.7}$$

$$\mathbf{T} = \int_0^L \mathbf{b}^T(x)\mathbf{a}(x)\,dx \tag{3.8}$$

The equilibrium equation (3.9) is derived from the virtual displacement principle and contains the external forces vector $\mathbf{P}^i$ and the virtual element deformation vector $\delta\mathbf{q}^T$. As it must hold for any arbitrary $\delta\mathbf{q}^T$, equation (3.10) follows, which is the matrix expression of the integral form of the element equilibrium equations:

$$\delta\mathbf{q}^T \int_0^L \mathbf{a}^T(x)\left[\mathbf{b}(x)\mathbf{Q}^{i-1}(x) + \mathbf{b}(x)\Delta\mathbf{Q}^i(x)\right]dx = \delta\mathbf{q}^T\,\mathbf{P}^i \tag{3.9}$$

$$\mathbf{T}^T\,\mathbf{Q}^{i-1} + \mathbf{T}^T\Delta\mathbf{Q}^i = \mathbf{P}^i \tag{3.10}$$

Combining equations (3.6) and (3.10) results to the system (3.11), in which the first equation is solved in $\Delta\mathbf{Q}^i$ and substituted in the second one to get equation (3.12):

$$\begin{bmatrix} -\mathbf{F}^{i-1} & \mathbf{T} \\ \mathbf{T} & \mathbf{0} \end{bmatrix}\begin{bmatrix} \Delta\mathbf{Q}^i \\ \Delta\mathbf{q}^i \end{bmatrix} = \begin{bmatrix} \mathbf{0} \\ \mathbf{P}^i - \mathbf{T}^T\,\mathbf{Q}^{i-1} \end{bmatrix} \tag{3.11}$$

$$\mathbf{T}^T\left[\mathbf{F}^{i-1}\right]^{-1}\mathbf{T}\,\Delta\mathbf{q}^i = \mathbf{P}^i - \mathbf{T}^T\,\mathbf{Q}^{i-1} \tag{3.12}$$

A special choice of the deformation shape functions $\mathbf{a}(x)$ results in considerable simplification; in fact, if the shape functions assume the expression stated in (3.13), matrix $\mathbf{T}$ reduces to the identity matrix $\mathbf{I}$ (it has to be noted that $\mathbf{a}(x)$ changes during the iterative solving procedure), as it is demonstrated in (3.14) and (3.15). With this choice of the deformation shape functions, equation (3.12) is simplified, assuming the form stated by (3.16).

$$\mathbf{a}(x) = \mathbf{f}^{i-1}(x)\mathbf{b}(x)\left[\mathbf{F}^{i-1}\right]^{-1} \tag{3.13}$$

$$\Delta\mathbf{d}^i(x) = \mathbf{f}^{i-1}(x)\mathbf{b}(x)\left[\mathbf{F}^{i-1}\right]^{-1}\Delta\mathbf{q}^i \tag{3.14}$$

$$\mathbf{T} = \int_0^L \mathbf{b}^T(x)\mathbf{f}^{i-1}(x)\mathbf{b}(x)\left[\mathbf{F}^{i-1}\right]^{-1} dx = \left[\int_0^L \mathbf{b}^T(x)\mathbf{f}^{i-1}(x)\mathbf{b}(x)\, dx\right]\left[\mathbf{F}^{i-1}\right]^{-1} = \mathbf{I} \tag{3.15}$$

$$\left[\mathbf{F}^{i-1}\right]^{-1}\Delta\mathbf{q}^i = \mathbf{P}^i - \mathbf{Q}^{i-1} \tag{3.16}$$

The latter equation expresses the linearized relation between the applied unbalanced forces $\mathbf{P}\text{-}\mathbf{Q}^{i-1}$ and the corresponding deformation increment $\Delta\mathbf{q}^i$ at the element level. The element stiffness matrix $\mathbf{K}=[\mathbf{F}]^{-1}$ is written in the form of inverted flexibility matrix to indicate that the latter is firstly determined and then inverted.

In the present case, the force interpolation functions assume the following form, leading to linear bending moments and constant axial force along the element:

$$\mathbf{b}(x) = \begin{bmatrix} \left(\frac{x}{L}-1\right) & \left(\frac{x}{L}\right) & 0 & 0 & 0 \\ 0 & 0 & \left(\frac{x}{L}-1\right) & \left(\frac{x}{L}\right) & 0 \\ 0 & 0 & 0 & 0 & 1 \end{bmatrix} \tag{3.17.}$$

3.1.2. State determination process

The state determination process calculates the resisting forces starting from the given deformations, and is organized into three nested phases corresponding to the structure level, the element level and, finally, the cross-section level.

The nested iterative procedures are identified by different superscripts:

- *k* denotes the applied load; the external load **P** is imposed in a sequence of load increments $\Delta\mathbf{P}^k$, so that at generic step *k* the total external load is $\mathbf{P}^k = \mathbf{P}^{k-1} + \Delta\mathbf{P}^k$;

- *i* denotes the Newton-Raphson iteration at the structure level, i.e. the structure state determination process iteration, yielding the structural displacements $\mathbf{p}^k$ corresponding to the applied loads $\mathbf{P}^k$;

j denotes the iteration in the element state determination process, yielding the element resisting forces $\mathbf{Q}^i$ corresponding to the element deformations $\mathbf{q}^i$, during the i-th Newton-Raphson iteration.

If the element cross-section is subdivided into fibers a fourth internal loop is added to the process, yielding the resisting stresses and the stiffness of the cross-section at the integration point, given the strains, within the j-th iteration of the element state determination process.

Input and output of the nested state determination processes are summarized in Table (3.1), while the detailed steps of the process are shown in the flow charts in Figures 3.2−3.4.

Module	Input	Output
Structure (*k*)	Applied force increment $\Delta\mathbf{P} = \Sigma_k\mathbf{P}^k$	Total displacements **p** Displacement increments $\Delta\mathbf{p}$ Resisting forces $\mathbf{P}_R$ Stiffness $\mathbf{K}_S$
Element (*i*)	Total deformations **q** Deformation increments $\Delta\mathbf{q}$	Resisting forces **Q** Stiffness **K**
Section (*j*)	Force increments $\Delta\mathbf{D}(x)$	Residual deformation $\mathbf{r}(x)$ Flexibility $\mathbf{f}(x)$
Fiber	Total strains $\mathbf{e}(x)$ Strain increments $\Delta\mathbf{e}(x)$	Resisting stresses $\mathbf{E}(x)$ Stiffness E_{tan}

Table 3.1. Input and output data for each module of the state determination process.

The whole process is organized as follows:

1. The external load **P** to assign to the structure is divided into a certain number of load increments $\Delta\mathbf{P}^k$. At each step k of the incremental analysis, the corresponding structure displacements $\Delta\mathbf{q}^k$ are determined by the Newton-Raphson iterative algorithm. At the i-th iteration of the solving procedure, the structure tangent stiffness matrix $\mathbf{K}_S^{i-1}$, computed at the previous step, is adopted for solving the equilibrium equation:

$$\mathbf{K}_S^{i-1}\,\Delta\mathbf{p}^i = \Delta\mathbf{P}^i \tag{3.18}$$

2. The element deformations are determined from the structure displacement by means of a matrix **L**, which is the combination of two transformations: in the first transformation the element displacements in the global reference system **p** are transformed to the displacements in the element local one **q***; in the second transformation the element displacements are transformed in the element deformation **q** by elimination of the rigid-body modes.

The incremental form of the transformation from structure displacements to element deformations is expressed by relation (3.19).

$$\Delta\mathbf{q}^{i} = \mathbf{L}_{\text{Elem}}\ \Delta\mathbf{p}^{i} \tag{3.19}$$

The element deformations $\Delta\mathbf{q}^{i}$ do not change during the i-th step of the solution algorithm; this ensures displacement compatibility at the element ends, as it is illustrated in Figure 3.2, where points B, D and F (representing the state of the element at the end of subsequent iterations in loop j) lie on the same vertical line. From now on, the resisting forces for the given element deformations $\Delta\mathbf{q}^{i}$ are established in the element state determination process.

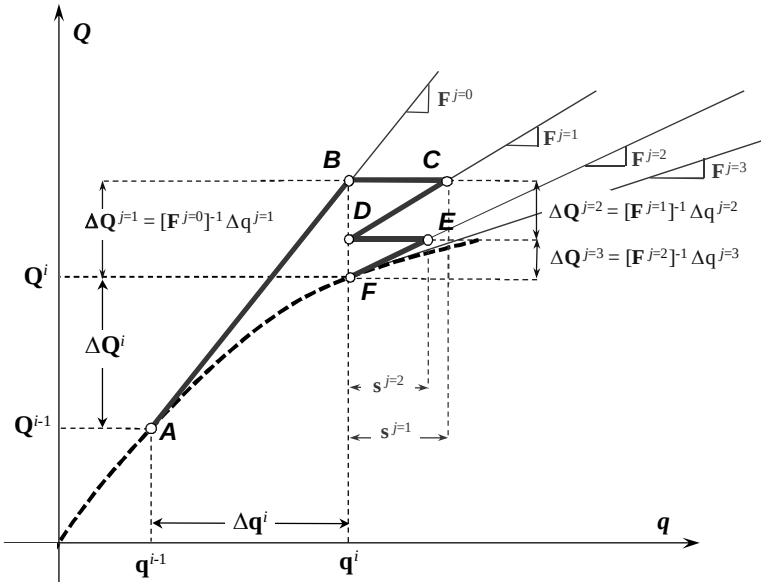

Figure 3.1. Graph of the element state determination.

3. The element state determination is performed for each element in loop j. The element force increments are determined with the element stiffness matrix, evaluated at the end of the previous iteration j-1 (3.20), and the element forces are updated (3.21):

$$\Delta\mathbf{Q}^{j} = \mathbf{K}^{j-1}\Delta\mathbf{q}^{j} \tag{3.20}$$

$$\mathbf{Q}^{j} = \mathbf{Q}^{j-1} + \Delta\mathbf{Q}^{j} \tag{3.21}$$

In the initial step (j=1) the following values are taken for element stiffness matrix, element deformations and element forces:

$$\mathbf{K}^0 = \mathbf{K}^{i-1} \tag{3.22}$$

$$\Delta\mathbf{q}^1 = \Delta\mathbf{q}^i \tag{3.23}$$

$$\mathbf{Q}^0 = \mathbf{Q}^{i-1} \tag{3.24}$$

where i-1 corresponds to the state at the end of the last Newton-Raphson iteration.

4. The section state determination is performed for each control section (integration point) of the element. The section force increments $\Delta\mathbf{D}^j(x)$ are determined from the force interpolation functions $\mathbf{b}(x)$ (3.25), and then the section forces are updated (3.26).

$$\Delta\mathbf{D}^j(x) = \mathbf{b}(x)\Delta\mathbf{Q}^j \tag{3.25}$$

$$\mathbf{D}^j(x) = \mathbf{D}^{j-1}(x) + \Delta\mathbf{D}^j(x) \tag{3.26}$$

5. The section deformation increments $\Delta\mathbf{d}^j(x)$ are determined by adding the residual section deformations from the previous iteration $\mathbf{r}^{j-1}(x)$ to the deformation increments produced by the section force increments $\Delta\mathbf{D}^j(x)$ (3.37). The latter are determined with the section flexibility matrix $\mathbf{f}^{j-1}(x)$ at the end of the previous iteration loop j (3.28):

$$\Delta\mathbf{d}^j(x) = \mathbf{r}^{j-1}(x) + \mathbf{f}^{j-1}(x)\Delta\mathbf{D}^j(x) \tag{3.27}$$

$$\mathbf{d}^j(x) = \mathbf{d}^{j-1}(x) + \Delta\mathbf{d}^j(x) \tag{3.28}$$

In the initial step (j=1) $\mathbf{r}^0(x) = \mathbf{0}$.

6. The tangent stiffness $\mathbf{k}^j(x)$ and flexibility $\mathbf{f}^j(x)$ matrices, and the section resisting forces $\mathbf{D}_R(x)$ are determined by means of the section constitutive law. The latter can be explicitly known or, if the section in discretized into fibers, assembled starting from the geometric and mechanical properties of the fibers.

7. The unbalanced forces and the residual section deformations are determined:

$$\mathbf{D}_U^j(x) = \mathbf{D}^j(x) - \mathbf{D}_R^j(x) \tag{3.29}$$

$$\mathbf{r}^j(x) = \mathbf{f}^j(x)\mathbf{D}_R^j(x) \tag{3.30}$$

8. The element flexibility and stiffness matrices are determined:

$$\mathbf{F}^j = \int_0^L \mathbf{b}^T(x)\mathbf{f}^j(x)\mathbf{b}(x)\,dx \tag{3.31}$$

$$\mathbf{K}^j = \left[\mathbf{F}^j\right]^{-1} \tag{3.32}$$

9. Convergence test is performed:
   - if the unbalanced forces at all element sections are sufficiently small (i.e. lower than a specified tolerance) the element is considered to have converged; the element force vector and stiffness matrix are set for the new step i+1:

$$\mathbf{Q}^i = \mathbf{Q}^j \tag{3.33}$$

$$\mathbf{K}^i = \mathbf{K}^j \tag{3.34}$$

   - if some sections have not converged the residual element deformation $\mathbf{s}^j$ are determined by integration of the residual section deformations $\mathbf{r}^j(x)$ (3.35), j is incremented to j+1, and the new iteration begins with a new deformation increment $\Delta\mathbf{q}^{j+1}$; the latter is set equal to $-\mathbf{s}^j$ (3.36).

$$\mathbf{s}^j = \int_0^L \mathbf{b}^T(x)\mathbf{r}^j(x)\,dx \tag{3.35}$$

$$\Delta\mathbf{q}^{j+1} = -\mathbf{s}^j \tag{3.36}$$

The convergence criterion widely used in the analyses presented in the present work is based on the energy increment the system experiences at each iteration (3.37) (Spacone et al., 1996).

$$\frac{\mathbf{s}^{jT}\mathbf{K}^j\mathbf{s}^j}{\Delta\mathbf{q}^{1T}\mathbf{K}^0\mathbf{q}^{1T}} \le \text{tol} \tag{3.37}$$

When all the elements have converged the step i is complete and a new iteration i+1 can begin.

10. The updated structure resisting forces are determined by assembling the element force vectors (3.38); the current element stiffness matrices are assembled to form a new structure stiffness matrix (3.39).

$$\mathbf{P}_R{}^i = \sum_{Elem=1}^{n} \mathbf{L}_{Elem}^T \left(\mathbf{Q}^i\right)_{Elem} \tag{3.38}$$

$$\mathbf{K}_S{}^i = \sum_{Elem=1}^{n} \mathbf{L}_{Elem}^T \left(\mathbf{K}^i\right)_{Elem} \mathbf{L}_{Elem} \tag{3.39}$$

11. At this point the structure resisting forces are compared with the total applied loads; if the difference (named structure unbalanced force vector $\Delta\mathbf{P}_U{}^i$) is within the specified tolerance, i is incremented to i+1, and the new Newton-Raphson iteration begins. Steps 1−11 are repeated after replacing $\Delta\mathbf{P}^i$ with $\Delta\mathbf{P}^{i+1} = \Delta\mathbf{P}_U{}^i$ until convergence takes place at structure degrees of freedom.

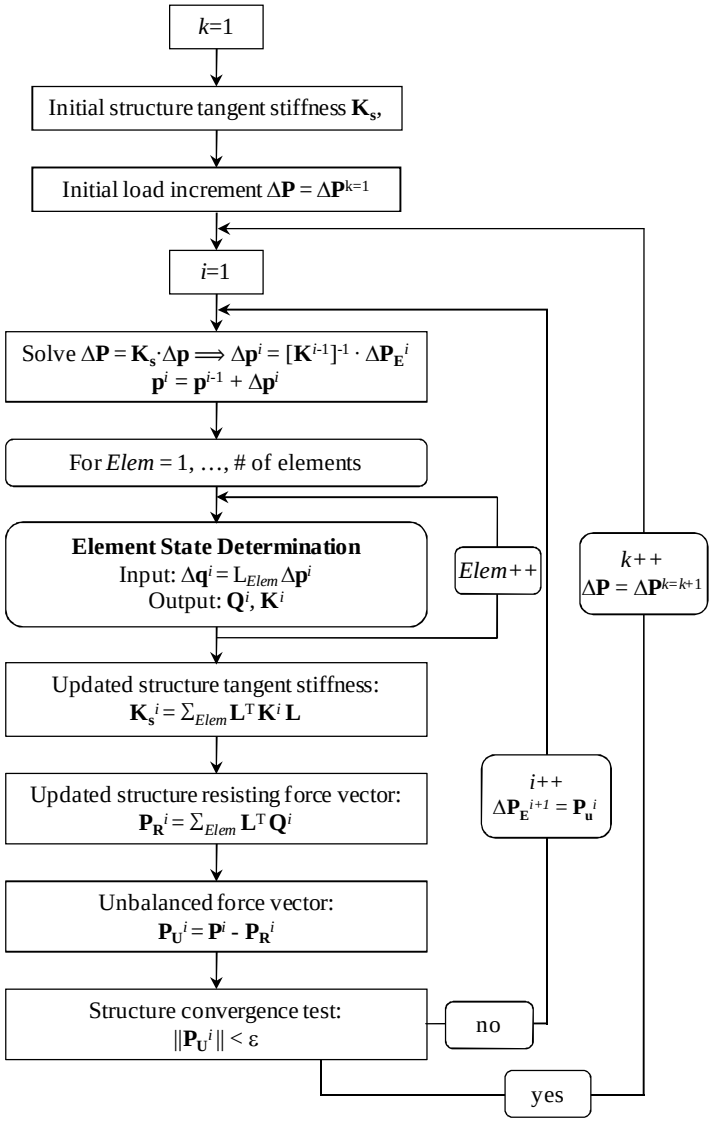

Figure 3.2. Flow chart of the structure state determination.

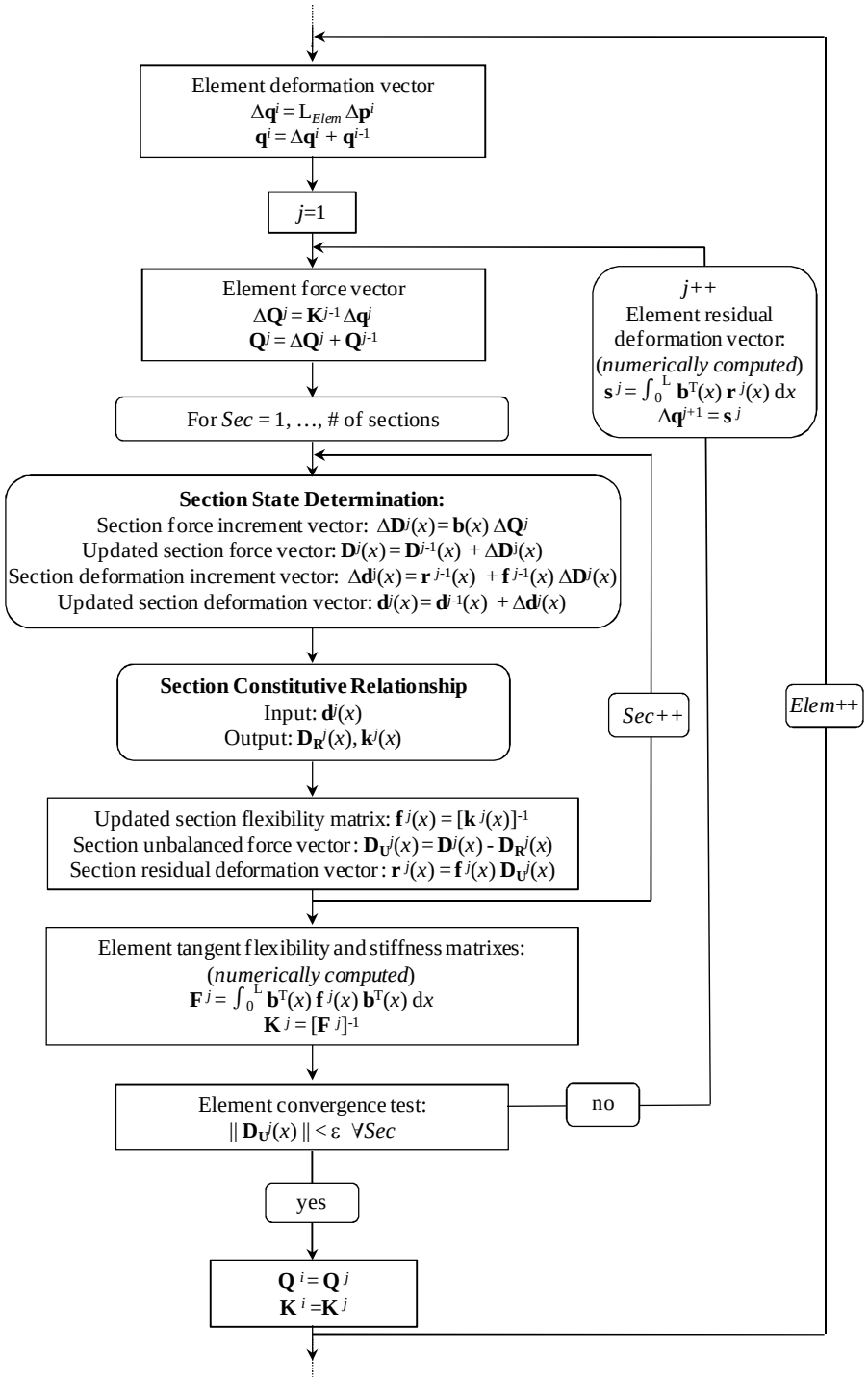

Figure 3.3. Flow chart of the element state determination.

If the cross-section is discretized into fibers, its force-deformation law is not explicit, but is derived from the constitutive relations of the fibers by means of a section state determination process, which is summarized in the flow chart in Figure 3.4 and in the graph in Figure 3.5.

The section deformation vector $\mathbf{d}(x)$ is related to the fiber strain vector $\mathbf{e}(x)$ according to (3.40), where $\mathbf{l}(x)$ is a linear geometric matrix containing the position of the fibers (3.41):

$$\mathbf{e}(x) = \mathbf{l}(x)\,\mathbf{d}(x) \tag{3.40}$$

$$\begin{bmatrix} \varepsilon_1(x, y_1, z_1) \\ \vdots \\ \varepsilon_{ifib}(x, y_{ifib}, z_{ifib}) \\ \vdots \\ \varepsilon_n(x, y_n, z_n) \end{bmatrix} = \begin{bmatrix} -y_1 & z_1 & 1 \\ \vdots & \vdots & \vdots \\ -y_{ifib} & z_{ifib} & 1 \\ \vdots & \vdots & \vdots \\ -y_n & z_n & 1 \end{bmatrix} \begin{bmatrix} \chi_z(x) \\ \chi_y(x) \\ \varepsilon(x) \end{bmatrix} \tag{3.41}$$

Analogously, the fiber deformation increment at step j of the element state determination process is obtained from the element deformation increment (3.42); once this is known, the fiber deformation can be updated (3.43):

$$\Delta\mathbf{e}^j(x) = \mathbf{l}(x)\,\Delta\mathbf{d}^j(x) \tag{3.42}$$

$$\mathbf{e}^j(x) = \mathbf{e}^{j-1}(x) + \Delta\mathbf{e}^j(x) \tag{3.43}$$

The stress and the tangent modulus of each fiber is determined from the appropriate stress-strain law; the fiber stresses $\sigma_{ifib}^{\,j}$ are then grouped in vector $\mathbf{E}^j$ and the elastic moduli in a diagonal matrix $\mathbf{E}^j_{tan}$. Calling $\mathbf{A}$ a diagonal matrix containing the areas of the fibers, the section tangent stiffness matrix is written as follows:

$$\mathbf{k}^j(x) = \mathbf{l}^T(x)\left(\mathbf{E}^j_{tan}\mathbf{A}\right)\mathbf{l}(x) = \begin{bmatrix} \sum_{ifib=1}^{n(x)} E^j_{ifib} A_{ifib} y^2_{ifib} & \sum_{ifib=1}^{n(x)} E^j_{ifib} A_{ifib} y_{ifib} z_{ifib} & -\sum_{ifib=1}^{n(x)} E^j_{ifib} A_{ifib} y_{ifib} \\ \sum_{ifib=1}^{n(x)} E^j_{ifib} A_{ifib} y_{ifib} z_{ifib} & \sum_{ifib=1}^{n(x)} E^j_{ifib} A_{ifib} z^2_{ifib} & \sum_{ifib=1}^{n(x)} E^j_{ifib} A_{ifib} z_{ifib} \\ -\sum_{ifib=1}^{n(x)} E^j_{ifib} A_{ifib} y_{ifib} & \sum_{ifib=1}^{n(x)} E^j_{ifib} A_{ifib} z_{ifib} & \sum_{ifib=1}^{n(x)} E^j_{ifib} A_{ifib} \end{bmatrix} \tag{3.44}$$

The section stiffness matrix $\mathbf{k}^j(x)$ is inverted to get the flexibility stiffness matrix $\mathbf{f}^j(x)$, and the section resisting forces $\mathbf{D}_R{}^j(x)$ are derived from the contribution of all fibers (3.45).

$$\mathbf{D}_R{}^j(x) = \begin{bmatrix} M_z(x) \\ M_y(x) \\ N(x) \end{bmatrix} = \mathbf{l}^T(x)\,\mathbf{A}\,\mathbf{E}^j = \begin{bmatrix} -\sum_{ifib=1}^{n} \sigma_{ifib}^j \cdot A_{fib} \cdot y_{fib} \\ \sum_{ifib=1}^{n} \sigma_{ifib}^j \cdot A_{fib} \cdot z_{fib} \\ \sum_{ifib=1}^{n} \sigma_{ifib}^j \cdot A_{fib} \end{bmatrix} \tag{3.45}$$

Since the beam element is based on the plane section assumption no shear deformation can be simulated, unless more complex form of the compatibility matrix $\mathbf{l}(x)$ is adopted. In this case, even if sliding between fibers remains not allowed, a supplementary deformation is added to the one due to flexure.

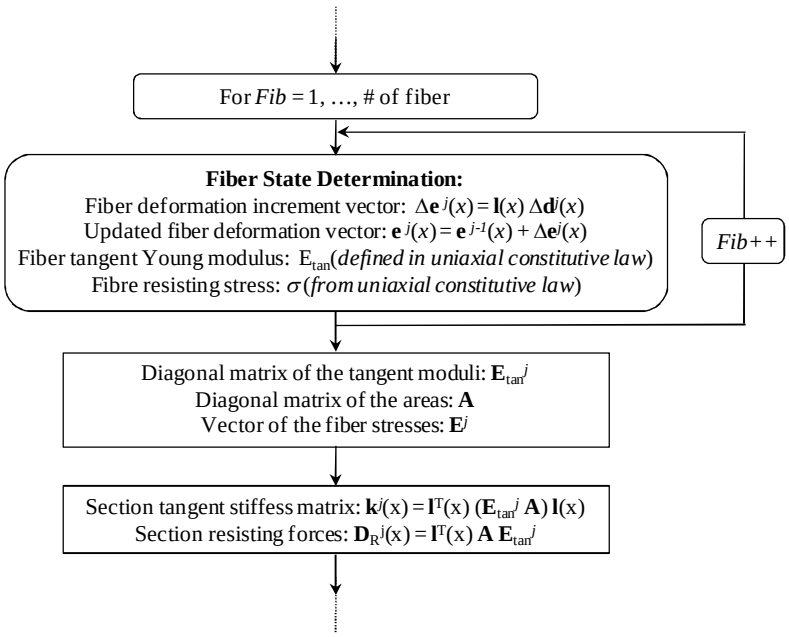

Figure 3.4. Flow chart of the section state determination.

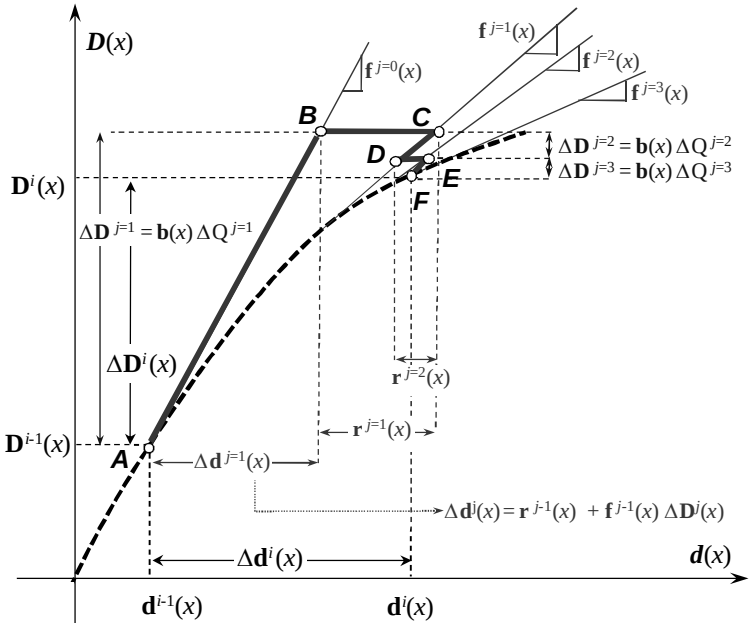

Figure 3.5. Graph of the section state determination.

The element state determination process is performed in the local element reference system, while the structure equilibrium is solved in the global one. The transformation between the two reference systems is governed by matrix **B**. It is applied to the vector of the element basic forces **W** (axial load, shear and bending moment in the deformed configuration) and yields the vector of element forces **Q** (nodal forces in the undeformed configuration). The element force vectors of all the elements are assembled to build the solving system of the structure equilibrium problem (Figure 3.6).

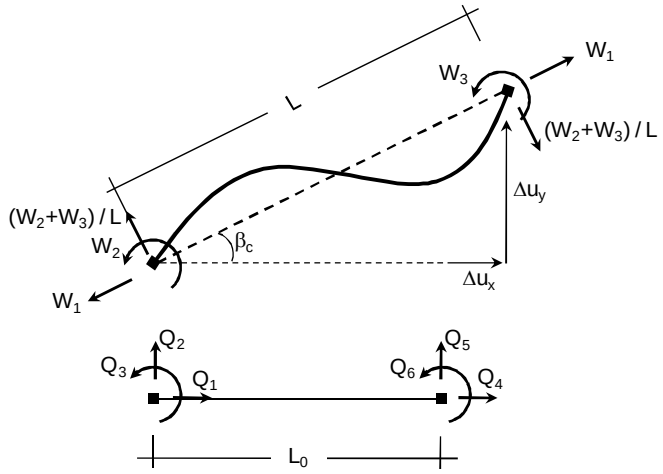

Figure 3.6. Equilibrium of frame element in the deformed configuration and its projection on the undeformed configuration (plane case).

If geometric non-linearities are negligible, a linear geometric transformation between local and global reference system can be used; it consists in writing the equilibrium of the element, at each step, by evaluating the stiffness matrix **K** in the initial undeformed configuration; in this case **B** is constant. On the contrary, when large rotations and P-Δ (buckling) effects have to be taken into account, a corotational approach is adopted; it consists in introducing a third reference system, in addition to the local element and the global ones, evolving during the load application; in this case, **B** depends on the element deformation vector **q** (3.46−3.47):

$$\mathbf{Q} = \mathbf{B}(\mathbf{q})\,\mathbf{W} \tag{3.46}$$

$$\begin{bmatrix} Q_1 \\ Q_2 \\ Q_3 \\ Q_4 \\ Q_5 \\ Q_6 \end{bmatrix} = \mathbf{B}(\mathbf{q}) \begin{bmatrix} W_1 \\ W_2 \\ W_3 \end{bmatrix} \tag{3.47}$$

The transformation matrix in the corotational approach has the form stated by (3.48), where L_0 is the element initial length and β_c is the element chord rotation in the updated configuration, as shown in Figure 3.6.

$$\mathbf{B}^{\mathrm{COR}}(\mathbf{q}) = \begin{bmatrix} -\cos(\beta_c) & \sin(\beta_c)/L_0 & \sin(\beta_c)/L_0 \\ -\sin(\beta_c) & \cos(\beta_c)/L_0 & \cos(\beta_c)/L_0 \\ 0 & 1 & 0 \\ \cos(\beta_c) & \sin(\beta_c)/L_0 & \sin(\beta_c)/L_0 \\ \sin(\beta_c) & -\cos(\beta_c)/L_0 & -\cos(\beta_c)/L_0 \\ 0 & 0 & 1 \end{bmatrix} \tag{3.48}$$

The chord rotation can be expressed by its truncated series expansion:

$$\beta_c = \arctan\left(\frac{\Delta u_y}{L_0 + \Delta u_x}\right) \cong \frac{\Delta u_y}{L_0} + \frac{\Delta u_x \cdot \Delta u_y}{{L_0}^2} \tag{3.49}$$

If the effect of the element rotation is neglected, $\sin(\beta_c)$ is assumed to be null when divided for L_0 and $\cos(\beta_c)$ is confused with 1; the resulting transformation matrix considers only P-Δ effects, and has the following form:

$$\mathbf{B}^{\mathrm{P-\Delta}}(\mathbf{q}) = \begin{bmatrix} -1 & 0 & 0 \\ -\sin(\beta_c) & 1/L_0 & 1/L_0 \\ 0 & 1 & 0 \\ 1 & 0 & 0 \\ \sin(\beta_c) & -1/L_0 & -1/L_0 \\ 0 & 0 & 1 \end{bmatrix} \tag{3.50}$$

Finally, the linear form of **B** is derived by assuming that β_c is negligible:

$$\mathbf{B}^{\mathrm{LIN}} = \begin{bmatrix} -1 & 0 & 0 \\ 0 & 1/L_0 & 1/L_0 \\ 0 & 1 & 0 \\ 1 & 0 & 0 \\ 0 & -1/L_0 & -1/L_0 \\ 0 & 0 & 1 \end{bmatrix} \tag{3.51}$$

3.2. Macroscopic constitutive relations

3.2.1. Monotonic behaviour

The constitutive relation chosen to describe the global response of historic brickwork under monotonic compression is the modified Kent and Park model, which is the stress-strain relation proposed for concrete by Kent and Park (1971) as extended in (Scott et al., 1982). Since it offers a good balance between simplicity and accuracy it is widely adopted for r.c. structures, while it has been less used for masonry. Nonetheless, it is suitable to represent the main properties shown by historic brickwork in experimental tests: initial elastic branch followed by a non-linear phase before the peak stress; post-peak behaviour characterized by a linear softening branch, with a residual stress that, on the base of experimental data, is negligible for the brickwork that is of interest within this work.

In the modified Kent and Park model the monotonic stress-strain relation in compression is described by three regions (Figure 3.7), in which it assumes the expressions stated in (3.52−3.54), in which f_{cp} is the compressive strength, ε_{c0} the corresponding strain, f_{cu} the residual resistance and ε_{cu} the strain value at the end of the softening branch; the convention that compression is positive is assumed.

Region O-A: $\varepsilon < \varepsilon_{c0}$ $$\sigma = f_{cp} \cdot \frac{\varepsilon}{\varepsilon_{c0}} \cdot \left(2 - \frac{\varepsilon}{\varepsilon_{c0}} \right) \tag{3.52}$$

Region A-B: $\varepsilon_{cu} < \varepsilon < \varepsilon_{cu}$ $$\sigma = \left(f_{cu} - f_{cp} \right) \cdot \left(\frac{\varepsilon - \varepsilon_{c0}}{\varepsilon_{cu} - \varepsilon_{c0}} \right) + f_{cp} \tag{3.53}$$

Region B-C: $\varepsilon > \varepsilon_{cu}$ $$\sigma = f_{cu} \tag{3.54}$$

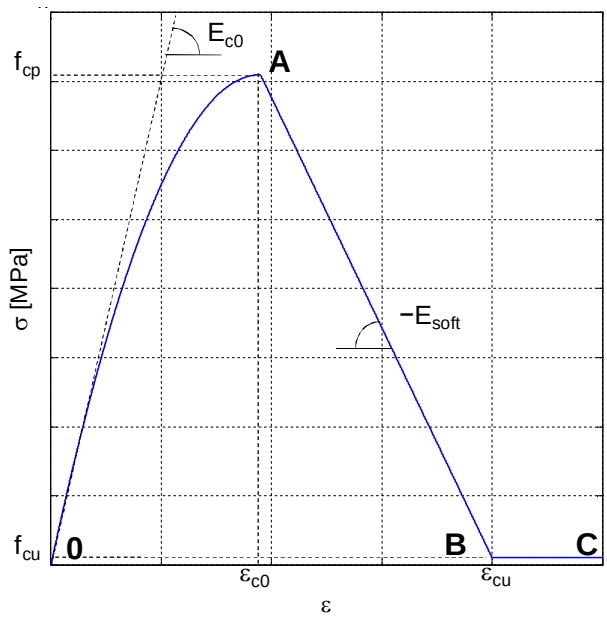

Figure 3.7. Modified Kent and Park model (1982) for monotonic compression.

For each strain value, the corresponding stress has to be defined, together with the tangent modulus, in order to assemble the stiffness vector of the cross-section. The tangent moduli of the three regions are stated by expressions (3.55−3.57).

Region O-A:
$$E(\varepsilon) = E_{c0}\left(1-\frac{\varepsilon}{\varepsilon_{c0}}\right) \tag{3.55}$$

Region A-B:
$$E_{soft} = \frac{f_{cu}-f_{cp}}{\varepsilon_{cu}-\varepsilon_{c0}} < 0 \tag{3.56}$$

Region B-C:
$$E = 0 \tag{3.57}$$

The Kent and Park relation adequately represent the response of historic brickwork under compression, as it is shown by the graphs in Figure 3.8, where it is plotted together with the experimental curves for the two different typologies of specimen tested under pure compression (S-C and S-CG); the parameters assigned to the constitutive law (coordinates of the peak and of the first point of the horizontal final branch) are reported in Table 3.2.

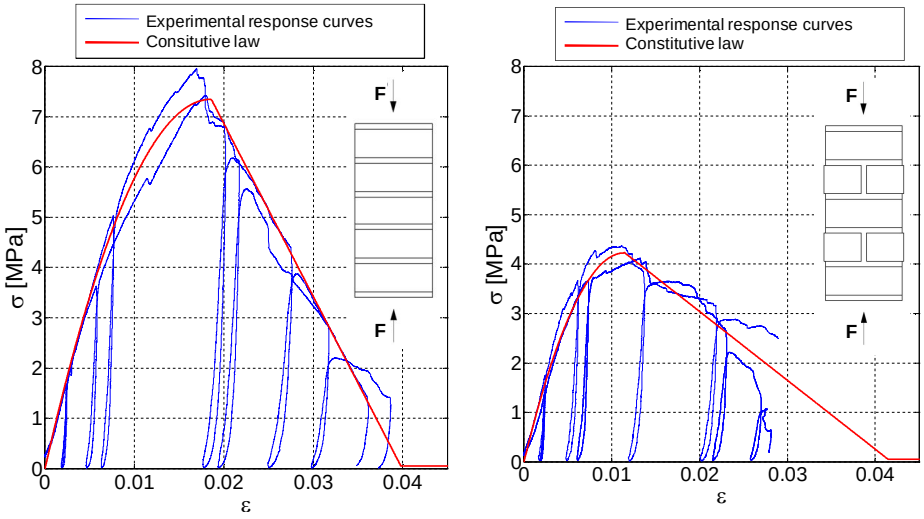

Figure 3.8. Experimental stress-strain curves for S-C (left) and S-CG (right) type specimens under centered compression and Kent and Park relations.

Description	Symbol	S-C Specimen	S-CG Specimen
Compressive strength	f_{cp}	-7.1 MPa	-4.23 MPa
Strain at compressive strength	ε_{c0}	-0.0186	-0.0115
Crushing strength (residual resistance)	f_{cu}	-0.05 MPa	-0.05 MPa
Strain at crushing strength	ε_{cu}	-0.0405	-0.0415

Table 3.2. Parameters of the constitutive relation for the two specimen types.

The modified Kent and Park model is already implemented in OpenSees, which is the software used to perform numerical simulations within the present work, and is named Concrete01.

3.2.2. Proposed cyclic constitutive relation without strength degradation

The cyclic behaviour of the modified Kent and Park constitutive relation implemented in OpenSees in material Concrete02 is described by the hysteretic unloading and reloading rules proposed in (Yassin, 1994), which are a set of linear stress-strain relations. Anyway, it is not able to accurately reproduce the unloading-reloading behaviour of historic brickwork, as it is found in experimental tests, and presents the restriction that the stiffness of the reloading phase and the amplitude of hysteretic cycles are defined by means of a unique parameter, so that once one of them is chosen the other one is automatically determined. Thus, a modified constitutive law named

Masonry01, is defined and implemented in OpenSees source code within the present research work. The stiffness of the unloading and reloading branches can be separately defined (Figure 3.9) allowing the user to choose the amplitude of hysteretic cycles; thus the effective cyclic response is better represented. The skeleton curve is the same of Concrete01 and Concrete02 materials implemented in OpenSees.

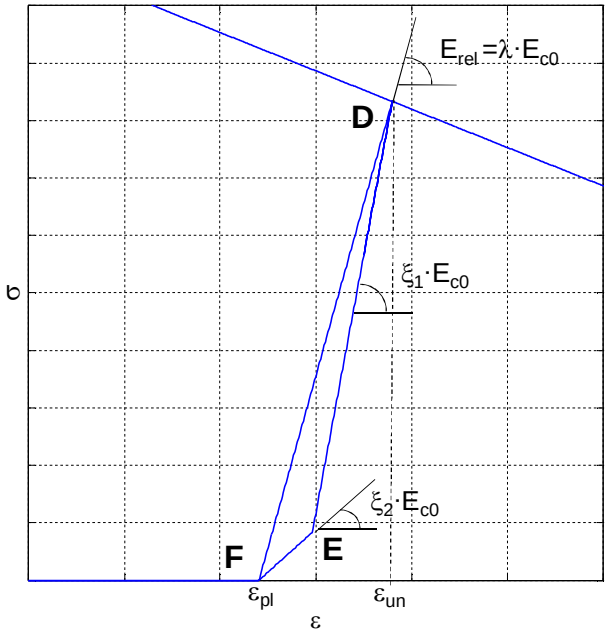

Figure 3.9. Unloading-reloading branches in Masonry01 constitutive model.

In Masonry01 constitutive relation the unloading branch D-E-F is described by a bi-linear function, while the reloading phase is represented by a linear one F-D (Figure 3.9); the resulting hysteretic cycle is closed, so damping properties can be modelled, but neither an eventual strength nor stiffness degradation are taken into account. The slopes of the three branches are defined by means of the positive scalar coefficients ξ_1, ξ_2 and λ, as a rate of the initial tangent stiffness E_{c0}.

Table 3.3 collects the parameters of Masonry01 constitutive relation; note that the compressive stresses and strains have to be defined as negative values in the implementation, even if the assumption that compression is positive is made in the graphs.

Symbol	Description	Range	Assigned value
f_{cp}	Compressive strength	< 0	-7.1 MPa
ε_{c0}	Strain at compressive strength	< 0	-0.019
f_{cu}	Crushing strength (residual resistance)	≤ 0	-0.05 MPa
ε_{cu}	Strain at crushing strength	≤ 0	-0.0405
λ	Parameter defining the slope of the reloading branch*	> 0	4.0
ξ_1	Parameter defining the initial slope of the unloading branch*	≥ λ	6.0
ξ_2	Parameter defining the final slope of the unloading branch**	(0,1)	0.25

**: with respect to the initial tangent stiffness E_{c0}*
***: with respect to the initial slope of the unloading branch $\xi_1 E_{c0}$*

Table 3.3. Parameters of Masonry01 constitutive relationship and values assigned on the base of experimental results on S-C specimens.

Masonry01 curve is represented in Figure 3.10 together with the experimental response of a S-C specimen and Concrete02 law, to show the improvement in describing the cyclic response; the parameters assigned to both the constitutive models are the best choice that can be made to match the experimental data.

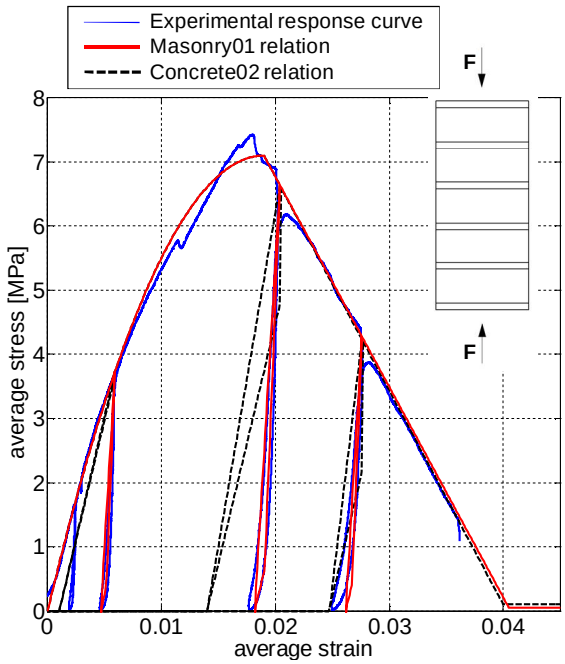

Figure 3.10. Experimental stress-strain curve of S-C specimen under cyclic centered compression, Masonry01 and Concrete02 constitutive models.

3.2.3. Proposed cyclic constitutive relation with strength degradation

Aiming at simulating the strength degradation observed in experimental tests on masonry specimens, a second constitutive relation named Masonry02 is defined and implemented in OpenSees source code within the present research work. The skeleton curve is the same of Masonry01 law, while the unloading-reloading phase is defined on the base of experimental data to capture damage accumulation and energy dissipation in the material due to cyclic loading. The shape of unloading and reloading curves depends on the amount of non recoverable damage, and on micromechanical phenomena occurring in mortar layers and in bricks, as well as in their interface, that herein are treated at macroscopic level to reproduce the masonry element global response.

Many researchers have introduced constitutive relations for describing this kind of effects on concrete as it is illustrated, among others, in (Chang and Mander, 1994; Orakcal et al., 2006; Sima et al., 2008), but only a few papers have been published regarding the strength degradation due to cyclic loading on masonry. In (AlShebani and Sinha, 1999) the response after several loading cycles is considered, but no hysteretic dissipation is included and the analytical constitutive model, which is experimentally derived, has not been implemented in a structural model code.

Herein, the unloading curve is defined by an exponential function, which is concave from the unloading point and characterized by a high stiffness at the beginning and a lower slope at low stresses. The reloading curve is a linear function, and the reloading stiffness depends on strain level and strength degradation. Differently from Concrete02 and Masonry01 relations, the hysteretic cycle is not closed and its final point has a lower stress value than the initial point (Figure 3.11). The expressions of unloading and reloading branches are stated by (3.58−3.61), while Table 3.4 collects the parameters of Masonry02 constitutive relation; note that compressive stresses and strains have to be defined as negative values in the implementation.

Unloading branch (G-H):

$$\sigma = \exp\left[D \cdot \left(1 - \frac{\varepsilon - \varepsilon_{pl}}{\varepsilon_{un} - \varepsilon_{pl}} \right) \right] \cdot E_{c0} \cdot \left(\varepsilon - \varepsilon_{pl} \right) \tag{3.58}$$

$$D = \ln\left[R \cdot d_h \cdot \frac{r-1}{r} \right];\ R = \frac{\lambda}{\zeta};\ r = \frac{\varepsilon_{un}}{\varepsilon_{pl}} \tag{3.59}$$

Reloading branch (H-I):

$$\sigma = \left(\varepsilon - \varepsilon_{pl}\right) \cdot E_{rel} \tag{3.60}$$

$$E_{rel} = \frac{\sigma^{(1)}}{\varepsilon_{un} - \varepsilon_{pl}};\ \sigma^{(1)} = \sigma^{(0)} \cdot \left(1 - \frac{b_1}{b_2}\right) \tag{3.61}$$

Symbol	Description	Range	Assigned value
f_{cp}	Compressive strength	< 0	-7.1 MPa
ε_{c0}	Strain at compressive strength	< 0	-0.019
f_{cu}	Crushing strength (residual resistance)	≤ 0	-0.05 MPa
ε_{cu}	Strain at crushing strength	≤ 0	-0.0405
λ	Parameter defining the slope of the reloading branch*	> 0	4.0
d_h	Parameter defining the amplitude of hysteretic cycles	[0,1]	0.3
ζ	Parameter defining the final slope of the unloading branch*	> 0	1.0
b_1	Parameter defining the strength loss after infinite cycles**	[0,1]	0.27
b_2	Parameter defining the strength degradation rate	> 0	1.44

**: with respect to the initial tangent stiffness*
***: with respect to the initial force value $F^{(0)}$*

Table 3.4. Parameters of Masonry02 constitutive relation and values assigned on the base of experimental results on S-C specimens.

After n unloading-reloading cycles the compressive strength $\sigma^{(n)}$ is defined by an expression depending on the initial value $\sigma^{(0)}$, on the scalar parameters b_1 and b_2 (to be determined experimentally), and on n itself (3.62). Note that this is the same expression adopted to identify the stability point in eccentric compression tests on S-E9 specimens (2.12).

$$\sigma^{(n)} = \sigma^{(0)} \cdot \left(1 - \frac{b_1 \cdot n}{b_2 + n}\right) \tag{3.62}$$

If n=0 the point describing the actual state of the fiber is on the skeleton curve and its coordinates are (ε^{un}, $\sigma^{(0)}$). When n>0, $\sigma^{(n)}$ decreases, and when $n \to \infty$, the stress tends to the asymptotic value $\sigma^{(\infty)}$ (3.63). The stability point (AlShebani and Sinha, 1999) has coordinates (ε^{un}, $\sigma^{(\infty)}$).

$$\sigma^{(\infty)} = \sigma^{(0)} \cdot \left(1 - b_1\right) \tag{3.63}$$

The parameter b_1 defines the rate of the initial stress that is lost after a very high (to the limit infinite) number of cycles; its complementary $(1-b_1)$ quantifies the stress at the stability point, value below which it is not possible to go, despite the degradation induced by the loading history. The parameter b_2 defines the degradation rate; with high values of b_2 the strength reduction

is slow, while if b_2 is small the stability point is rapidly reached. Finally, the parameter d_h governs the amplitude of the hysteretic cycles, which can be assumed as a reliable measure of energy dissipation: when d_h is small the cycles are narrow (if it becomes 0 their area is null), while high values of d_h (close to 1.0) result in large cycles and, consequently, strong dissipation (Figure 3.12).

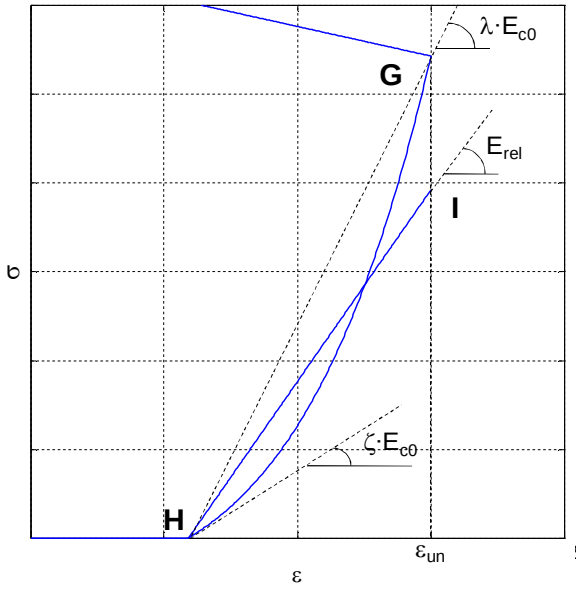

Figure 3.11. Unloading-reloading branches in Masonry02 constitutive model.

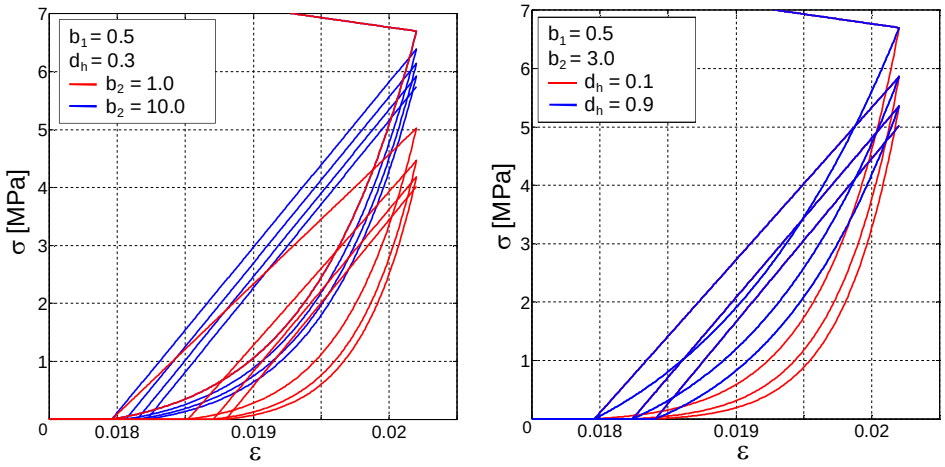

Figure 3.12. Masonry02 constitutive relation: unloading-reloading branches for different values of b_2 (left) and d_h (right).

Masonry02 curve is plotted in Figure 3.13 together with the experimental curve of a S-C specimen, showing that it yields a satisfactory representation of the effective cyclic response of historic brickwork under compression, taking into account the strength degradation induced by cyclic loading. The parameters assigned to the constitutive relation are collected in Table 3.4, and are determined as follows: λ, d_h and ζ are chosen so as to match the experimental response curve, while b_1 and b_2 are got from the results of the tests on S-E9 specimens and are equal to the average values of the parameters of the interpolating functions (Figures 2.45 and 2.46).

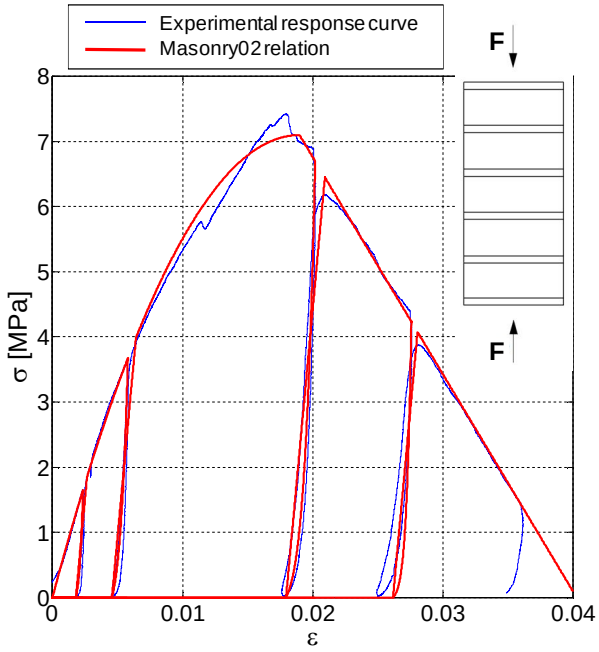

Figure 3.13. Experimental stress-strain curve of S-C specimen under cyclic centered compression and Masonry02 constitutive model.

3.3. Simulation of eccentric compression tests

Eccentric axial load tests on historic brickwork are simulated by using the fiber beam model described in the first section of this chapter. The choice of recurring to a beam element to model eccentrically loaded masonry prisms is

supported by the consideration that the cross-section remains substantially plane, as it is found in experimental tests (Figures 2.48 and 2.49).

The constitutive law assigned to the fibers is Masonry01, which accurately describes the effective response of the material needing a the same time a lower computational effort than Masonry02; its parameters are those collected in Table 3.3 and their values are determined on the base of centered compression experiments. The capability of the model to predict both failure conditions and whole response curve of masonry prisms under compression and bending is investigated.

The model is drawn in Figure 3.14: the central beam represents the specimen and the rigid links on both ends represent the steel I-beam plates by means of which the load is applied, so as to take into account the second order effects developing during the tests. Moreover, in order to reproduce the effective experimental conditions, two elasto-plastic no-tensile resisting elements are also included between the links and the beam, to simulate the detachment of the plate at the tensile edge of the specimen and the crushing of mortar at the compressed one. The calibration of these elasto-plastic elements is carried out on the base of displacement data acquired by 10mm transducers set up for the purpose on S-E9 tests (Figures 2.30 and 2.33). Analyses are carried out through software OpenSees under displacement control; a corotational reference transformation rule and an energy increment-based convergence criterion are assumed.

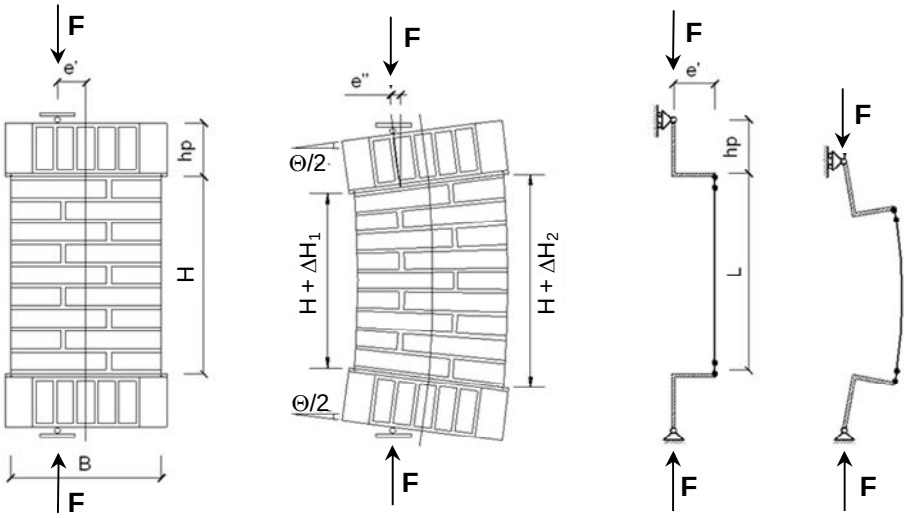

Figure 3.14. Schematic illustration of brickwork specimen and of the fiber beam model in the initial and deformed configurations.

3.3.1. Failure criterion

For the purpose of defining the strength domain of brickwork, the normalized plane M/M_0 - F/F_0 is used, where $F_0 = f_M$ B d, and $M_0 = F_0$ B/4, being B and d the specimen width and depth, respectively, and f_M the average experimental compressive strength. The normalization permits a comparison of the results of different specimen types in the same graph, as shown in Figure 3.15 where the experimental data are plotted together with those presented in (Brencich and de Felice, 2009). Numerical predictions are obtained for compressive strength (f_{cp}) equal to 0.9 ÷ 1.1 f_M, thus taking into account the intrinsic uncertainty in its estimate (Brencich et al., 2007). It is seen from the graph that the axial force-bending moment interaction can be predicted with a good approximation; anyway, some experimental points lie out of the region delimited by the numerical curves, which could be ascribed to some discrepancies between effective and expected eccentricities.

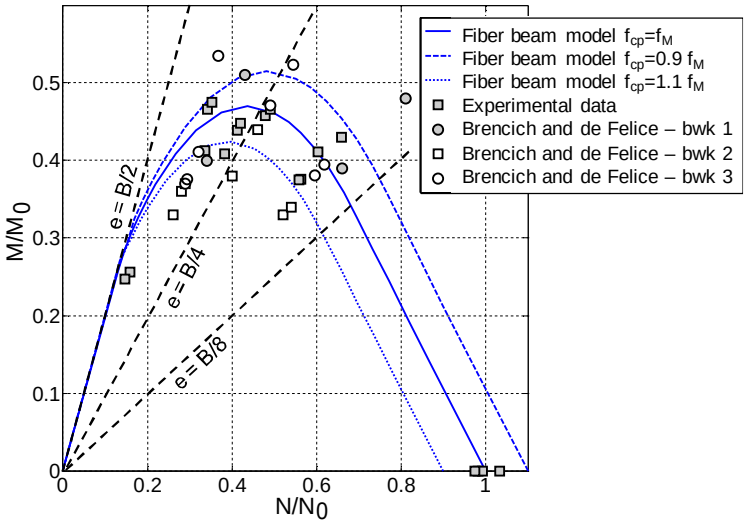

Figure 3.15. Strength domains of brickwork under eccentric loading according to the numerical model and corresponding experimental data.

The peak values of the experimental bending moment are collected in Table 3.5 together with the ones estimated by the numerical model (M_0^{num}) and the error in the prediction, expressed as the ratio between laboratory data and finite element results. The mismatch is always lower than 8% except for S-C specimen type.

Specimen	e' [mm]	u' [mm]	Experimental Maximum Bending Moment M_0 [kNm]		Numerical Maximum Bending Moment M_0^{num} [kNm]	Numerical/ Experimental Ratio M_0^{num} / M_0 (average)
			Specimen 1	Specimen 2		
S-C	30	40	1.51	2.26	2.13	+13.0%
S-CG	30	40	1.72	1.62	1.71	+2.4%
S-E5	40	100	5.48	5.85	5.53	-2.3%
	60	80	6.92	7.04	6.79	-2.7%
	80	60	7.07	-	6.82	-3.5%
	100	40	3.85	3.79	3.54	-7.3%
S-E9	70	140	13.13	14.36	14.12	+2.3%
	110	100	15.37	15.67	14.31	-7.8%

Table 3.5. Comparison between experimental and numerical results.

3.3.2. Overall monotonic response curve

Displacement controlled analyses allow the whole force-displacement and bending moment-curvature behaviour of brickwork under eccentric loading to be simulated. Figures 3.16−3.20 show the numerical estimate compared to the experimental results: Force-Displacement and Bending Moment-Curvature diagrams are plotted together with Eccentricity-Displacement graph; the latter represents the progressive increase of eccentricity (e) from the initial value (e′), due to second order effects induced by the rotation of end plates. Second order effects are considered in the model by means of a corotational geometric transformation. The comparison reveals a good agreement between numerical simulations and experiments for specimen types S-C, S-CG, S-E5, both in ascending and softening branches, with a slight overestimate of the post-peak strength. A higher discrepancy appears for S-E9 specimen type, with eccentricity e'=110mm (Figure 3.22), where the finite element predictions overestimate force and bending moment capacity and are not able to follow the rapidly descending softening branch. Probably, one of the reasons for this mismatch lies in the lack of fit between model estimate of the second order eccentricity e'' and of the corresponding experimental value; such a discrepancy is due to the difficulty in modelling the mortar layers in contact with the loading plates, where severe crushing takes place during the tests. As shown in Figure 3.22, a slight underestimate of e'' in the softening phase may induce a strong overestimate of the corresponding force and moment predictions. It should be considered also that, in the softening phase, the plane section assumption is no longer ensured (Figure 2.49) and therefore a beam model is less reliable.

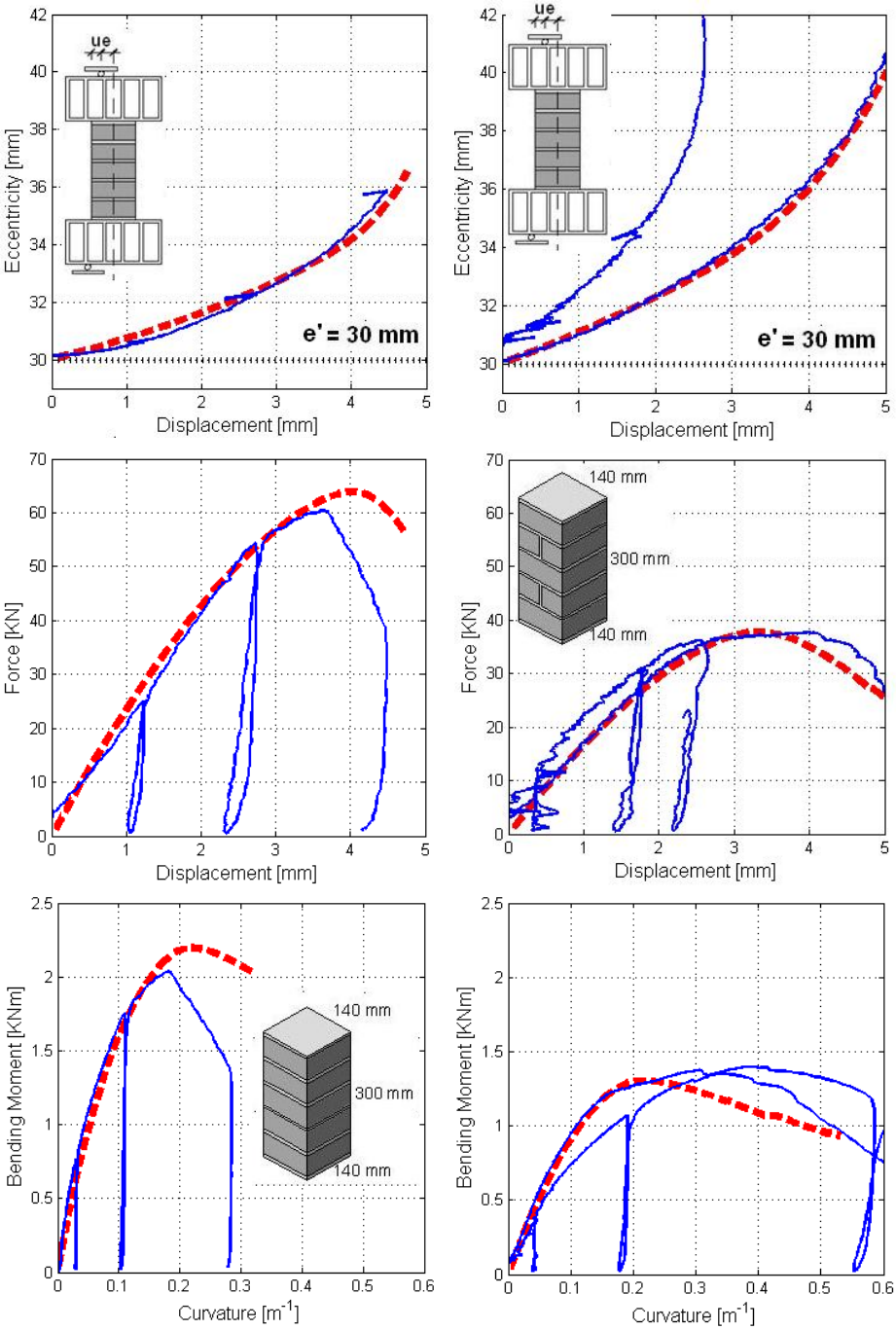

Figure 3.16. Experimental results (solid blue lines) and fiber beam model simulation (dotted red line) of eccentric (e'=30mm) axial load tests on S-C (left) and S-CG (right) masonry specimens.

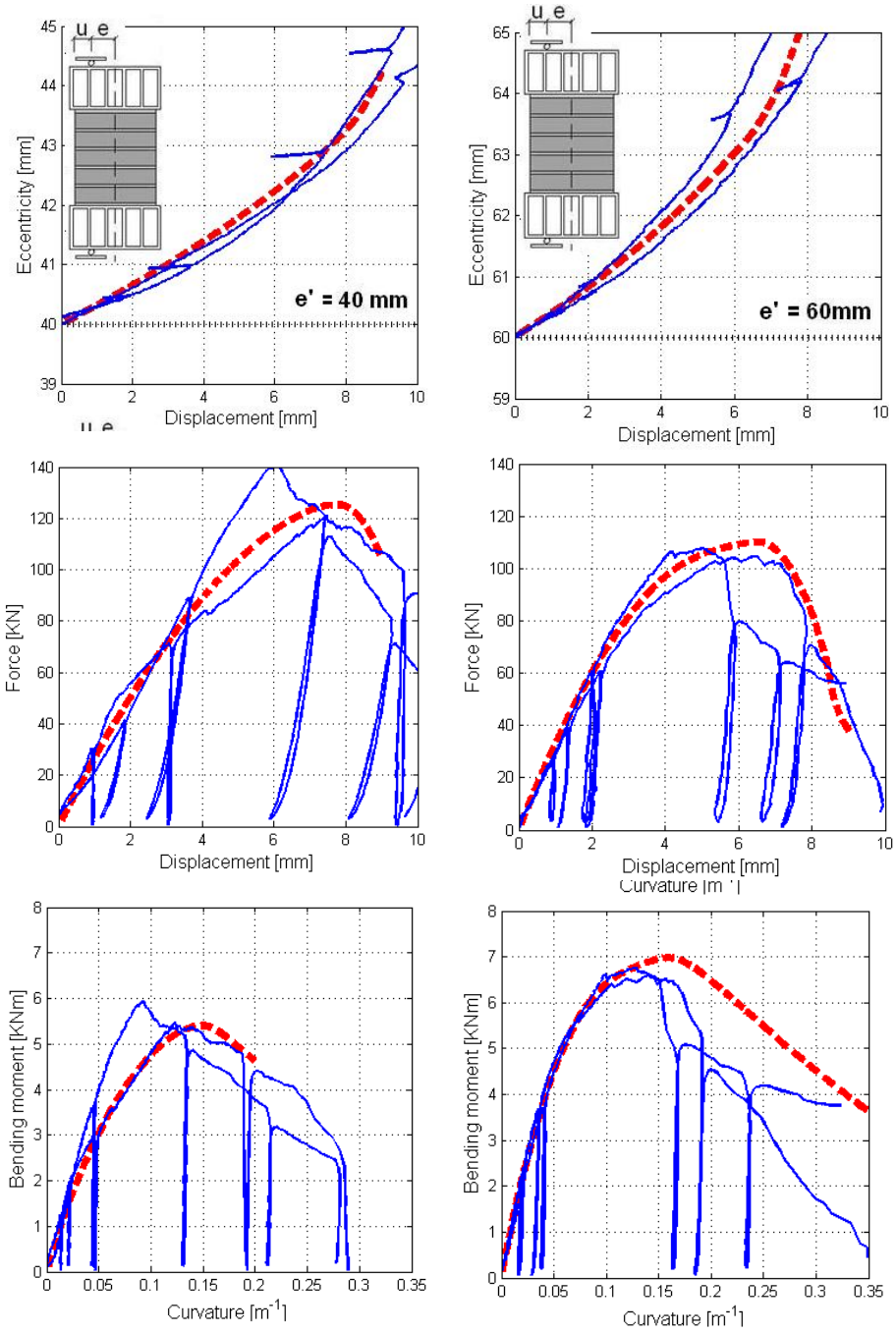

Figure 3.17. Experimental results (solid blue lines) and fiber beam model simulation (dotted red line) of eccentric axial load tests on S-E5 masonry specimens: e'=40mm (left) and e'=60mm (right).

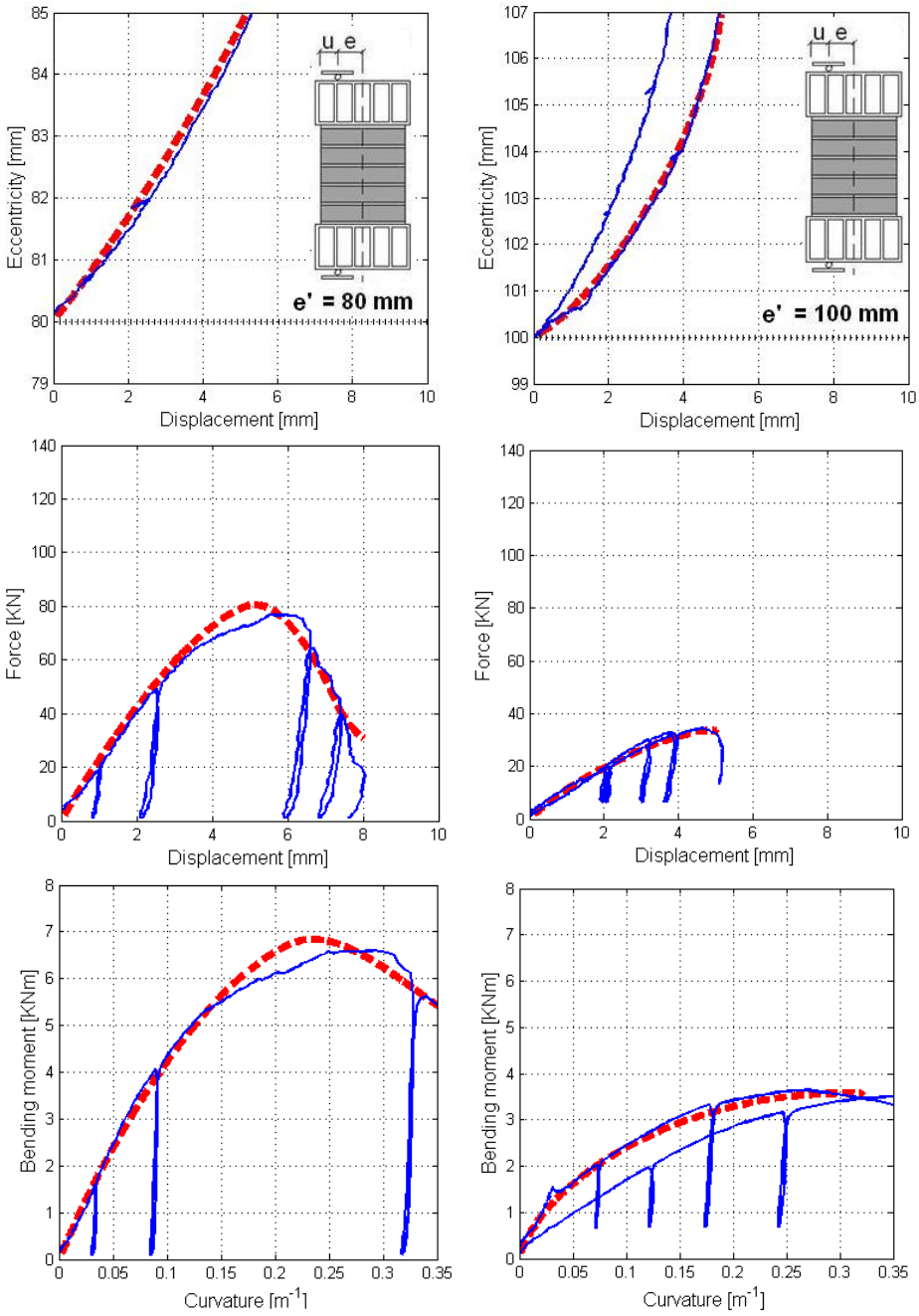

Figure 3.18. Experimental results (solid blue lines) and fiber beam model simulation (dotted red line) of eccentric axial load tests on S-E5 masonry specimens: e'=80mm (left) and e'=100mm (right).

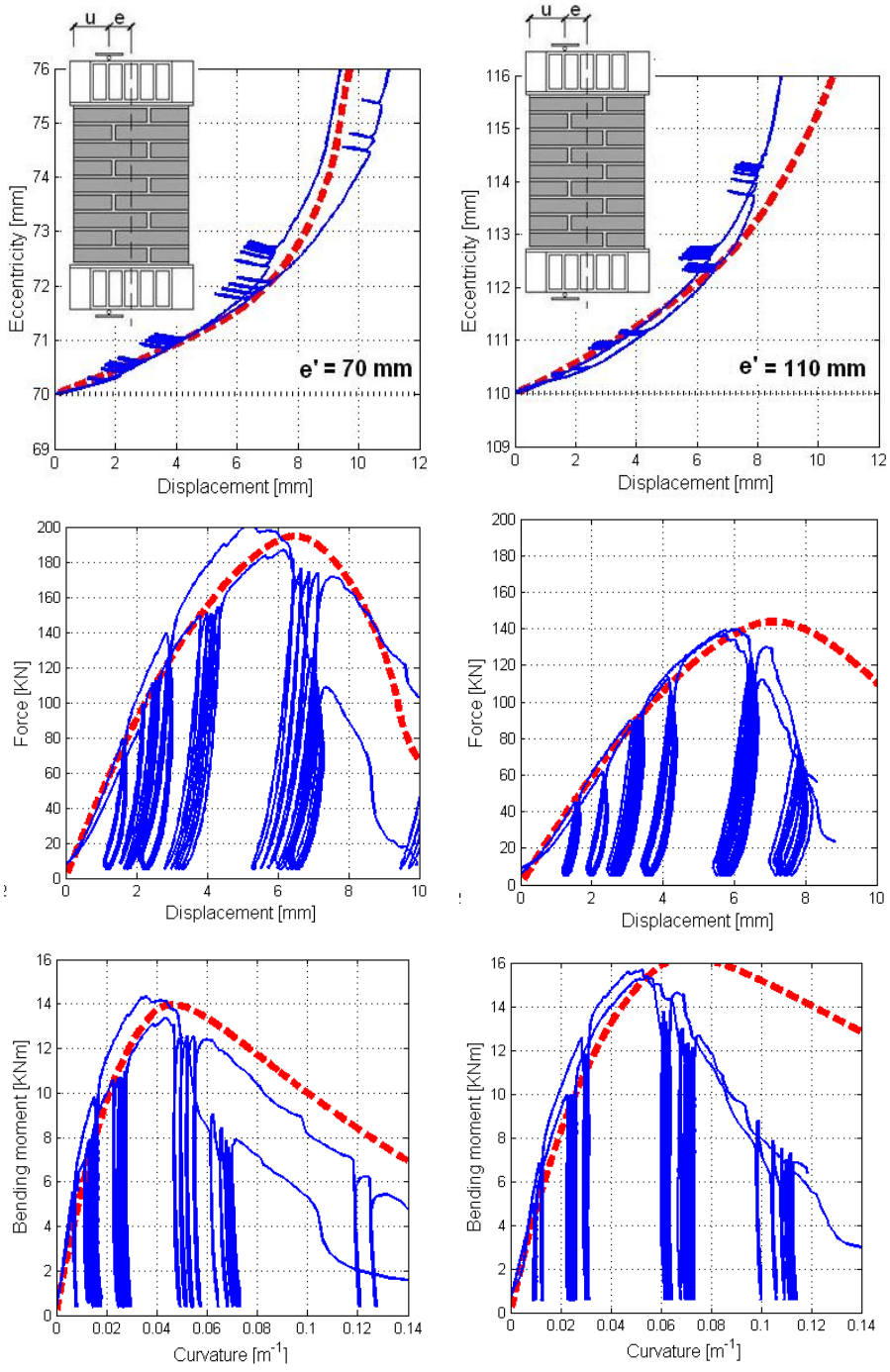

Figure 3.19. Experimental results (solid blue lines) and fiber beam model simulation (dotted red line) of eccentric axial load tests on S-E9 masonry specimens: e'=70mm (left) and e'=110mm (right).

3.3.3. Cyclic behaviour

The comparison between experimental and numerical curves proves the capability of the fiber beam model and of Masonry01 relation to simulate the cyclic response of brickwork. The M-χ response of an S-E5 sample with e′=40mm is represented, by way of example, in Figure 3.20, together with the finite element prediction. A satisfactory agreement for what concerns the unloading-reloading phases is found, even if a certain underestimate of the unloading and reloading stiffness values is observed, especially in the ascending branch.

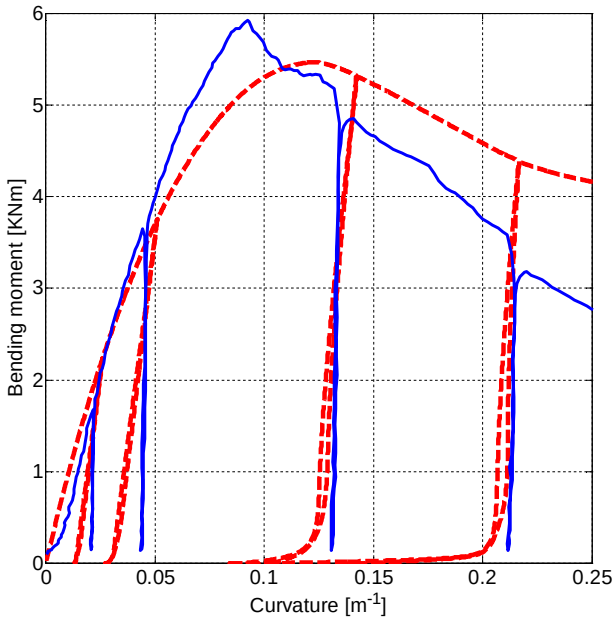

Figure 3.20. Experimental result (solid blue line) and fiber beam model simulation (dotted red line) of a cyclic eccentric axial load tests on a masonry specimen (e'=60mm; specimen type: S-E5).

Concluding, the proposed modelling approach provides an adequate prediction of the effective non-linear response of a brickwork element under compression and bending, also when unloading-reloading cycles occur, offering, at the same time, a good compromise between accuracy and simplicity.

It proves to yield a good description of the failure condition, especially when hinge mechanism and material crushing occur at the same time, unlike the classical elasto-plastic or elasto-brittle models, traditionally adopted for the structural analysis of masonry pillars and arches.

4. Load-carrying capability of masonry bridges

4.1. State-of-the-art

In the past, the design of masonry bridges was based on simplified methods, adopted for the dimensioning of the main structural elements like vaults and pillars. Traditional building rules are illustrated in several theoretical-practical treatises and manuals of XVIII, XIX and XX Centuries (Gautier, 1716; Belidor, 1729; Perronet, 1788; Rondelet, 1802; Gauthey, 1809; Mery, 1840; Curioni, 1865; Dupuit, 1870; Auric, 1911; Séjourné, 1913; Jorini, 1918; Breymann, 1926; Campanella, 1928), dating from 80 to almost 300 years ago, as well as in old design instructions such as (Ferrovie dello Stato, 1907) that is the first Italian National Technical Code issued by the Italian Railway Institution. In some cases, empirical relations (Tables 4.1−4.2.) were used, based on experience or practical optimization of previous formula (Brencich and Morbiducci, 2007; Oliveira et al., 2010). Otherwise, graphic statics was employed for deriving the thrust line in the arch (Figures 4.1−4.2).

It is now necessary, and of great interest as well, to assess the safety level of existing masonry bridges towards actual traffic loads by means of the tools available at present time. Several alternative approaches have been proposed in the last decades for the evaluation of the load-carrying capability (Huges and Blackler, 1997), involving different degrees of complexity.

Two of the most widely used empirical methodologies are the MEXE and the SMART methods. The Modified Military Engineering Experimental Establishment (MEXE) Method (UK Department of Transport, 1997; Wang et al., 2010) was proposed in 1930s, used during the Second World War to quickly classify bridges according to their capability to carry military vehicles, and then modified several times up to the current version that is recommended by the Department of Transport of UK. The SMART (Sustainable Masonry Arch Resistance Technique) Method (Melbourne et al.,

2007) is anonther expeditious procedure that provides an estimate of long-term service life and permissible loading limits.

Limit analysis-based methods, deriving from Heyman's studies on the yield design of arches (Heyman, 1966; 1982), are widely adopted for the structural analysis of masonry bridges. Assuming that the material has infinite compressive strength and no tensile resistance, and that sliding between voussoirs cannot occur, the safety assessment becomes a pure geometrical matter requiring the load thrust line to be anywhere within the arch profile; the collapse multiplier, defined as the live load resultant divided by the dead load, that turns the arch into a mechanism is generally found through an iterative minimization procedure. Simplicity and speed have made limit analysis-based approaches suitable for a preliminary estimate of the load-carrying capability of masonry arches and multi-span bridges; some examples are presented, among others, in (Harvey, 1988; Gilbert and Melbourne, 1994; Clemente, et al., 1995. Boothby, 1997). In order to overpass the most important limit of the yield design, that is the assumption of infinite crushing strength of the material, an adequate reduction of the effective thickness of the arch cross-section can be assumed (Clemente et al., 2010).

Some applications to masonry arches of the discrete element method (DEM) have been proposed (Lemos, 2007); anyway, this approach is suitable for small bridges made of a limited number of stones, like, for example, ancient roman arches; in this case the faithful reproduction of the single units and joints is possible, while a continuum approach with finite elements could be considered conceptually wrong, or, at least, should take into account the representation of the heterogeneities at the micro-scale and the opening of cracks by means of mesh updating procedures. Anyway, the use of such micromodels has generally been restricted to the study of small portions or isolated parts of masonry structures and mainly aimed at the calibration of simpler models to be subsequently adopted for the whole construction, as in (Page, 1978; Ali and Page, 1988; Lourenço, 1994).

On the contrary, a homogenized approach is preferable when large structures have to be analyzed: the representation of the single units and joints is not necessary and it would rather entail a heavy modelling and computational effort.

Incremental finite element analysis with 1-D models has proved to be an efficient approach for the assessment of the load-carrying capability of masonry arches and, even more, of multi-span bridges. Applications have been presented in (Molins and Roca, 1998; Boothby, 2001; Brencich and De Francesco, 2004a; 2004b; Brencich et al., 2004; de Felice, 2009), in which different material constitutive laws, descriptions of the effect of spandrel walls and backing, stress distribution criteria within the fill soil, procedures for the identification of collapse mechanisms, crack pattern and compressive stresses in the vaults have been proposed, and several real cases analyzed.

Some of those case studies are existing bridges; in this case the uncertainties in the material properties have often to be faced, and one possibility is to treat them as probabilistic variables, as it is done in (Brencich et al., 2007), where the load-carrying capability of an existing bridge is assessed assuming a stochastic distribution for masonry compressive strength.

Finally, as an alternative to finite element and distinct element methods, discontinuous deformation analysis (DDA) can be used; it is based on an assumed deformation field within distinct domains and a rigorous imposition of contact constraints (Shi, 1988), and has been applied to stone arches in (Ma et al., 1995) to represent the possibility of sliding between blocks.

The wider and wider space devoted to experimental investigation activities also witnesses the great interest of the scientific community in a deeper knowledge of masonry bridges. Tests have been carried out on scale bridge specimens (Melbourne and Wagstaff, 1993; Prentice and Ponniah, 1994; Robinson et al., 1997; Fanning and Boothby, 2001; Fanning et al., 2005; Melbourne and Tomor, 2006; Gilbert et al., 2007b) as well as on real bridges under traffic loads (Huges and Pritchard, 1998) or up to collapse when destined to demolition (Page, 1987; Léon and Espejo, 2007). The contribution of spandrel walls and fill soil, or the response to exceptional loads such as impacts (Lourenço et al., 2010), are observed, and acquired data are mainly used to calibrate numerical models. In other cases, innovative techniques are developed to determine the bridge actual stress and damage conditions and predict the life expectancy, on the base of acoustic emissions (Tomor and Melbourne, 2007) or Moiré photography (Harvey et al., 2001).

Recently, refined modelling strategies have been proposed to simulate the interaction between vaults, spandrels and fill, in which the explicit detailed representation of all structural and non-structural elements is made by using 2-D or 3-D finite elements (Fanning and Boothby, 2001; Fanning et al., 2005; Harvey et al., 2005; Cavicchi and Gambarotta, 2005; 2007; Gilbert et al., 2007a; Domède and Sellier, 2010). These approaches present some difficulties associated to the determination of the mechanical parameters, towards which a strong sensitivity is often found; moreover, high computational efforts are needed, especially for multi-span bridges.

Within the field of structural analysis of masonry bridges, greater and greater attention has been devoted in the last years to historic constructions; several applications are strictly connected to the safety assessment of in service bridges under exercise loads, as well as to the strengthening, retrofitting and repairing (Melbourne and Tomor, 2004; Léon et al., 2004; Brookes, 2008; Oliveira et al., 2010; Zheng et al., 2010), including, among others, applications of externally bonded surface reinforcements (Valluzzi et al., 2001; Foraboschi, 2004; Drosopoulos et al., 2007; De Lorenzis et al., 2007b) and of non-invasive techniques (Brookes, 2008).

At the same time, wide space has been devoted to the knowledge and valorization of historic heritage, deepening or simply collecting and

rediscovering historic design rules (Brencich and Morbiducci, 2007) and construction technologies (Brencich and Colla, 2002), or surveying the most recurrent typologies and geometrical properties of ancient bridges in a particular geographic area (Oliveira et al., 2010).

Date	Author	Deep arch	Shallow arch
1716	Gautier	$s = 0.32 + S/15$	–
1788	Perronet	$s = 0.325 + 0.035S$	$s = 0.325 + 0.0694R$
1809	Gauthey	$s = 0.33 + S/48$ ($S < 16m$)	–
		$s = S/24$ ($16m \leq S < 32m$)	–
		$s = 0.67 + S/48$ ($S > 32m$)	–
1809	Sganzin	$s = 0.325 + 0.03472S$	–
1845	Déjardin	$s = 0.30 + 0.045S$	$s = 0.30 + 0.025S$
1854	L'Éveillé	$s = 0.333 + 0.033S$	$s = 0.33 + 0.033\sqrt{S}$
1855	Lesguillier	$s = 0.10 + 0.20\sqrt{S}$	$s = 0.10 + 0.20\sqrt{S}$
1862	Rankine	$s = 0.19\sqrt{R}$	–
1865	Curioni	$s = 0.24 + 0.05S$	$s = 0.24 + 0.07R$ ($\alpha < 45°$)
			$s = 0.24 + 0.05R$ ($\alpha < 60°$)
1870	Dupuit	$s = 0.20\sqrt{S}$	$s = 0.15\sqrt{S}$
1885	Croizette-Desnoyers	$s = 0.15 + 0.20\sqrt{R}$	–
XIX Cent.	Udine-Pontebba railway	$s = (1 + 0.10S)/3$	$(1 + 0.20R)/3$
1914	Séjourné	$s = 0.15 + 0.15\sqrt{S}$	
1926	Breymann	2 brick heads (24cm) ($S < 1.75m$)	1 brick head more than for deep arches
		3 brick heads (36cm) ($2m < S < 3m$)	
		4 brick heads (48cm) ($3.5m < S < 5.75m$)	
		5 brick heads (60cm) ($6m < S < 8.5m$)	
		$s = S/15 \div S/12$ ($S > 8.5m$)	

Table 4.1. Historical empirical rules for the crown arch thickness from different authors (brickwork arches only).
s: thickness of the arch crown; S: span; R: radius; a: Skewback angle.

Year	Author	Pier thickness
1684	Blondel	$S/4 \leq P \leq S/3$ (Shallow arches)
		$P = S/4$ (Deep arches)
1716	Gautier	$P = S/5$
1788	Perronet	$P = 2.25s$
XIX Cent.	German engineers	$P = 0.292 + 2s$
1881	Rofflaen	$P = 2.5s$ ($10m \leq S$)
		$P = 3.5s$ ($10m \leq S$)
1914	Séjourné	$S/10 \leq P \leq S/8$

Table 4.2. Historic empirical rules for the top thickness of the pier from different authors.
s: thickness of the arch crown; S: span; P: thickness of the pier top section.

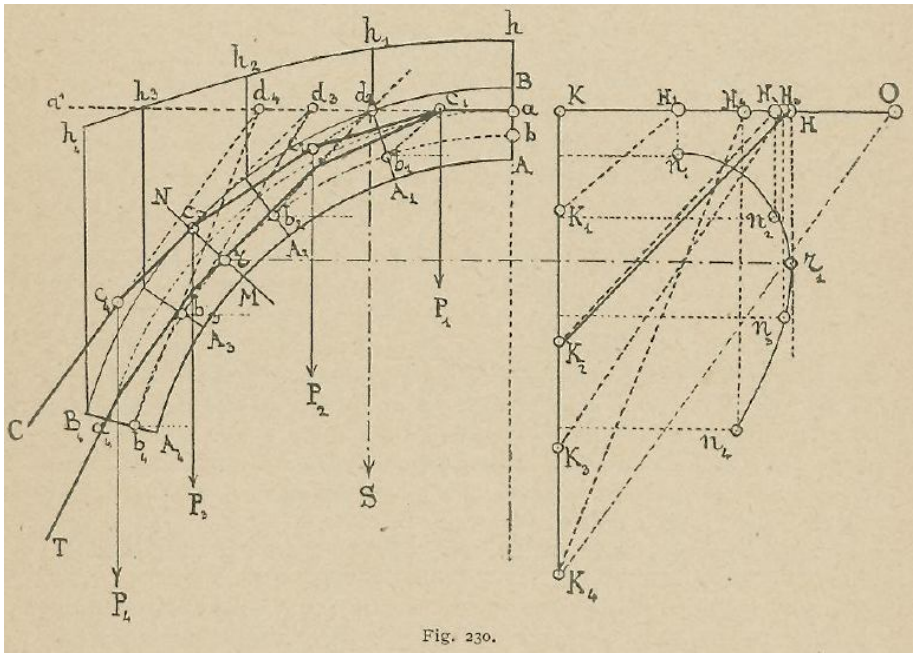

Figure 4.1. Mery's Method for the design of an arch (From Jorini, 1918).

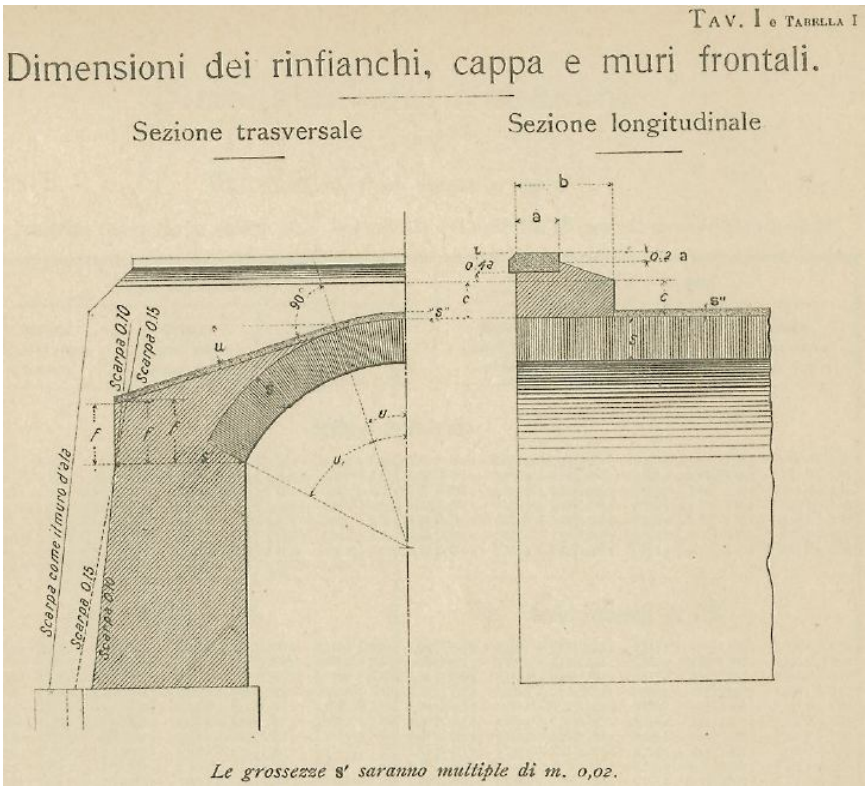

TABELLA I. **Valori di s'', c, u e b.**

Luce	s''	c (valore minimo)	u: Archi a tutto sesto	u: Archi ribassati ad: 1/3	u: 1/4	u: 1/5	u: 1/6, 1/8 ed 1/10	b: Archi a tutto sesto	b: Archi ribassati ad: 1/3, 1/4 ed 1/5	b: 1/6, 1/8 ed 1/10
m.	m.	m.						m.	m.	m.
1.00	0.05	0.10	18°	18°	18°	18°	17°	0.70	0.70	0.70
1.50	0.05	0.10	18°	16°.30′	15°	14°	14°	0.70	0.70	0.70
2.00	0.05	0.10	18°	15°	13°	12°	12°	0.70	0.70	0.70
2.50	0.05	0.10	18°	14°	12°	11°	11°	0.70	0.70	0.70
3.00	0.05	0.15	18°	13°	11°	10°	10°	0.70	0.70	0.70
3.50	0.06	0.15	18°	12°.30′	10°.30′	9°.30′	9°.30′	0.80	0.80	0.70
4.00	0.06	0.15	18°	12°	10°	9°	9°	0.80	0.80	0.80
5.00	0.06	0.20	18°	11°.30′	9°.30′	8°.30′	8°.30′	0.90	0.80	0.80
6.00	0.07	0.20	18°	11°	9°	8°	8°	0.90	0.80	0.80
7.00	0.07	0.20	18°	11°	8°.30′	8°	7°.30′	1.00	0.90	0.80
8.00	0.08	0.25	18°	10°.30′	8°.30′	7°.30′	7°.30′	1.00	0.90	0.80
9.00	0.08	0.25	18°	10°.30′	8°.30′	7°.30′	7°.30′	1.00	0.90	0.80
10.00	0.10	0.25	18°	10°.30′	8°	7°.30′	7°	1.00	1.00	0.90
12.00	0.10	0.25	18°	10°.30′	8°	7°	7°	1.10	1.00	0.90
15.00	0.10	0.25	18°	10°.30′	8°	7°	7°	1.20	1.00	0.90

Le presenti modalità si adotteranno anche per i manufatti obbliqui e per i viadotti.

Per i valori di s, s', f, u_1 e dei raggi d'intradosso ved. Tabelle a pag. 7-8-9-10.

Figure 4.2. Empirical relations for the dimensioning of the structural elements of a bridge (From Ferrovie dello Stato, 1907).

In this chapter, an approach for the evaluation of the load-carrying capability of masonry bridges is proposed, which makes use of the fiber beam element presented in the previous chapter to obtain a simple but reliable representation of the overall structural response. Most of the main features related to the mechanical behaviour of a multi-span masonry bridge are taken into account, like the effective material properties (including pre-peak non-linearities and post-peak softening response), the complex interagency of axial force, bending moment and curvature in the cross-section of vaults and piers and, finally, the interaction between arches and piers as well as between adjacent spans. On the other hand, the use of 1-D finite elements ensures a limited computational effort, making the proposed strategy suitable for practical applications.

Aiming at validating the fiber beam approach, the comparison with an experimental test on a large-scale bridge model performed in Bolton Institute (Melbourne et al., 1997) is made and the correspondence between limit analysis and fiber beam modelling, under the same constitutive assumptions, is also verified. The load-carrying capability of two existing Italian rail viaducts is assessed investigating the effect of material properties on overall safety level to underline to what extent a yield design-based method can be considered reliable. The collapse mechanism and expected damages are also identified. Finally, some considerations on the safety under rail traffic loads are illustrated with reference to a sample of twelve Italian large-span masonry bridges of different typologies.

4.2. Modelling masonry bridges by means of fiber beam elements

The proposed modelling strategy for the structural analysis of multi-span masonry bridges makes use of beam elements with fiber cross-section, as it is represented in Figure 4.3; the whole model can be defined in a 2-D or in a 3-D domain to simulate both in-plane and out-of-plane behaviours.

The vaults are described as segmental arches made of rectilinear beam elements, the piers simply as 1-D columns; the tapering of vaults and pillars, when present, is represented in a discrete way. The connection between two adjacent arches and the pier on which they are built on is modelled by rigid links to take into account the effective relative positions of their central axes. Generally, no shear deformation is considered for the vault, while it is included in the pier properties to avoid an overestimate of the effective

stiffness, especially for squat piers. The discretization of the cross-section into fibers, beyond the advantages in deriving the global section force-deformation law by means of the uniaxial material behaviour, already discussed in the previous chapter, also allows the presence of different materials to be reproduced, as it may happen for the piers. In fact they were often built with regular squared stones in the external leaf, while the internal core is made of rubble masonry with poor mechanical properties.

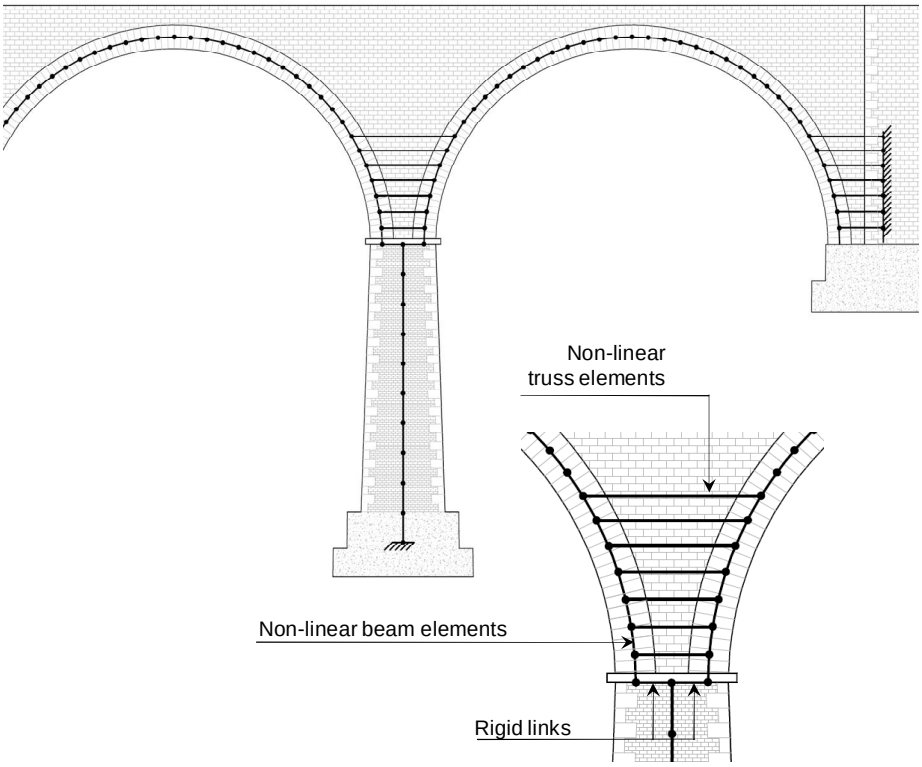

Figure 4.3. Structural elements of a masonry bridge modelled through 1-D finite elements.

The number of beam elements and of fibers in the cross-section is determined through a preliminary mesh validation. A good compromise is pursued between robustness and accuracy on the one hand, and computational sustainability and modelling simplicity on the other hand.

First of all, sensitivity analyses are performed on two extremely simple cases: a beam subjected to uniform bending moment and a single arch under vertical load concentrated in the key node. Two different materials are considered: the first one has infinite strength and linear elastic behaviour in compression, and no tensile resistance (ENT constitutive model), while the

second one is Masonry01 relation, defined and calibrated in the previous chapter to represent the effective mechanical response of brickwork under compression. Analyses are carried out under displacement control until convergence is achieved, with a corotational transformation criterion to account for second order effects. The resulting curves are the moment-curvature response for the beam, and the load-displacement response referred to the crown section for the arch; they are reported in Figure 4.4. It is seen that, apart from the cases in which a very few number of beams or fibers is chosen, no significant variation in the shape of the response curves is found. Nevertheless, a strong dependence is obtained in terms of numerical robustness; instabilities arise for very high curvature values (the last part of the softening branch) in the beam, but not in the arch, where the loss of convergence may also occur in the ascending branch of the load-displacement curve. Finally, it has to be noted that an increase in the number of elements in the arch is associated to a worse numerical stability. The best choice, in this case, appears to be 20 beam elements and 100 fibers; anyway, analogous specific sensitivity analyses are carried out to validate the mesh of all finite element models used for the numerical simulations illustrated later on.

It is well-known that, when dealing with unreinforced masonry structures, the softening local behaviour of all the elements results in a softening overall structural response, which is very difficult to simulate even if a displacement control procedure is used (Taucer et al., 1991). In the cases considered in the present work, convergence is found to be not always satisfactory, which has to be attributed to the steep softening branch of assumed constitutive relations.

Passing to the other structural elements, the backing is modelled by using horizontal truss elements having the same depth of the vault and connecting corresponding nodes of adjacent arches up to the appropriate height. It has to be pointed out that the interaction between adjoining vaults strongly depends on the height of the backing, which allows the activation of a multiple arch mechanism. Great attention has to be paid to original drawings and documents to check the effective dimensions of building details. Similarly, the abutments are described through an adequate number of horizontal truss elements, connecting the nodes of the lateral vault to as many perfectly fixed nodes. This constraint condition is based on the assumption that the abutments are stiff and no foundation settlements occur.

Spandrel walls and fill soil are not explicitly included in the model, even if their self-weight is always considered. Moreover, the diffusion of the load from the trampling level to the arch extrados is taken into account by assuming an adequate value of the diffusion angle θ_d depending on the fill mechanical properties (Figure 4.5).

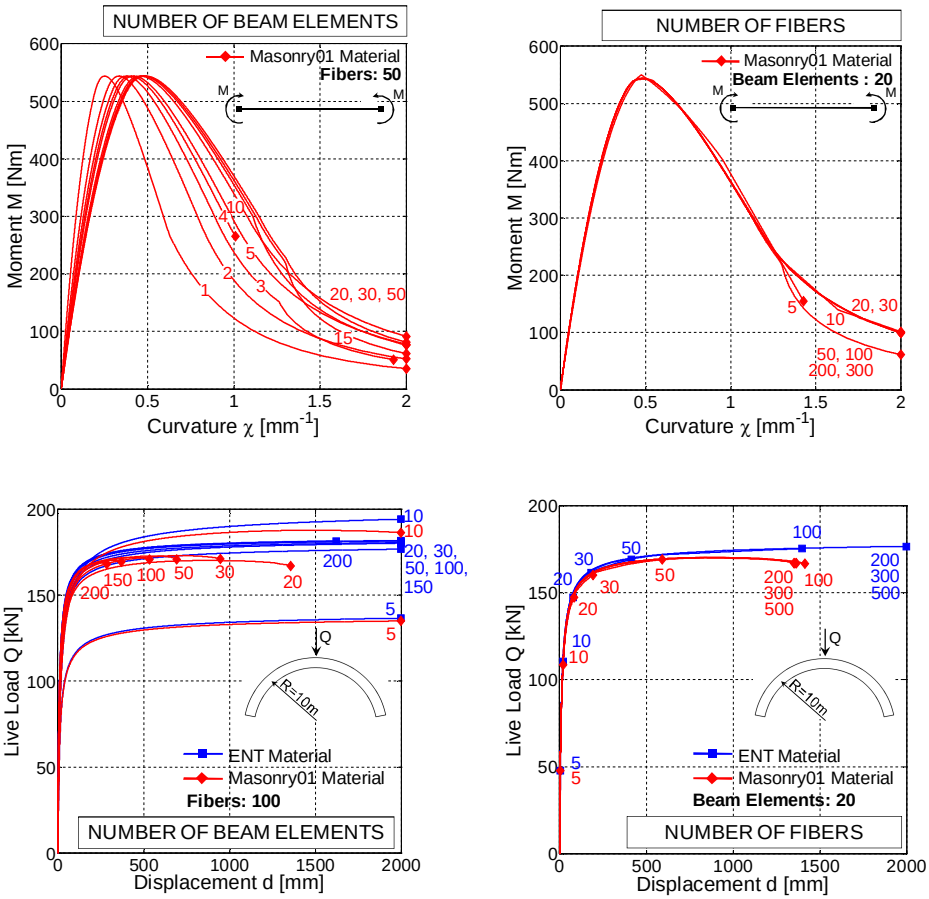

Figure 4.4. Sensitivity analyses on a beam under uniform bending moment (up) and on a single arch under vertical load concentrated in the crown section (down), for the identification of the adequate number of beam elements (left side graphs) and of fibers in the cross-section (right side graphs), considering an elastic-no tensile resistant material (ENT, blue curves) and Masonry01 constitutive law (red curves).

A linear or corotational coordinate transformation rule is adopted, depending on the specific requirements of the considered case. The former is chosen any time that second order effects are assumed to be substantially negligible; moreover, it ensures better performances of the numerical model in terms of both computational effort and convergence stability.

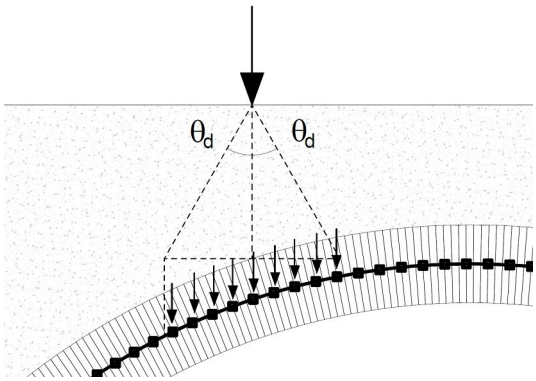

Figure 4.5. Diffusion of the load from the trampling level to the arch extrados and identification of the loaded nodes.

4.3. Comparison with experimental results

Aiming at validating the modelling strategy with fiber beams, an experimental test is simulated. The specimen is a large scale model (Figure 4.6) made of three shallow arches and two squat piers (namely North Pier and South Pier) tested up to collapse in Bolton Institute (Melbourne et al., 1997). The main geometric and mechanical properties of the bridge are collected in Table 4.3. The spandrel walls are detached from the arch barrels of the three vaults (Figure 4.7) but are built on the same piers and abutments supporting them, so that a limited (even if not completely negligible) interaction between arches and spandrels occurs.

Actually, the experimental campaign described in (Melbourne et al., 1997) totally includes three bridges, and the one considered within this Thesis is named Bridge #2 in the cited paper. The other two specimens present attached spandrel walls so that a more refined strategy should be used to model them, including their explicit representation by using, for example, 2-D elements.

During the test, the load is applied by means of a 420mm wide and 2.6m long concrete beam, positioned transversally at the quarter point of the central span (750mm from the crown). The force and the displacements of the loaded arch and of the two piers are recorded; the load values corresponding to the occurrence of cracks are also registered. The observed

failure mode is a hinged mechanism, as it is expected when the material is very strong and the span is relatively short.

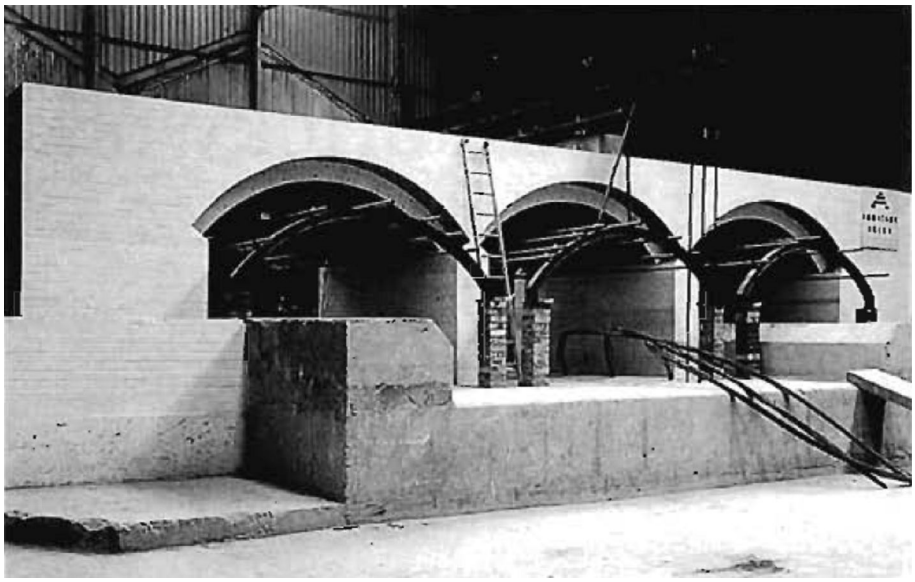

Figure 4.6. Bolton Institute experimental model.

Span	3.00 m
Rise	0.75 m
Span/rise ratio	4:1
Arch thickness	0.215 m
Arch depth	2.88 m
Pier height	1.50 m
Pier thickness	0.44 m
Brickwork unit weight	22.4 kN/m^3
Brickwork compressive strength	26.8 MPa
Brickwork initial tangent elastic modulus	16.2 GPa
Fill unit weight	22.2 kN/m^3

Table 4.3. Geometric and mechanical characteristics of Bolton Institute (Melbourne et al., 1997) experimental model.

To perform numerical simulations, the bridge is modelled using 50 fiber beam elements for each arch and 20 for each pier (Figure 4.8). The section of all the beams is subdivided into 75×1 fibers; Masonry01 constitutive relation is assigned to all of them and a ductility $\eta=\varepsilon_{c0}/\varepsilon_{cu}=3$ is assumed. Anyway, it should be noted that, because of the high material crushing strength, combined with the small dimensions of the bridge, the local resistance does not significantly affect the overall load-carrying capability and the failure

mechanism; therefore, the classical assumption of infinite compressive resistance would lead to comparable results.

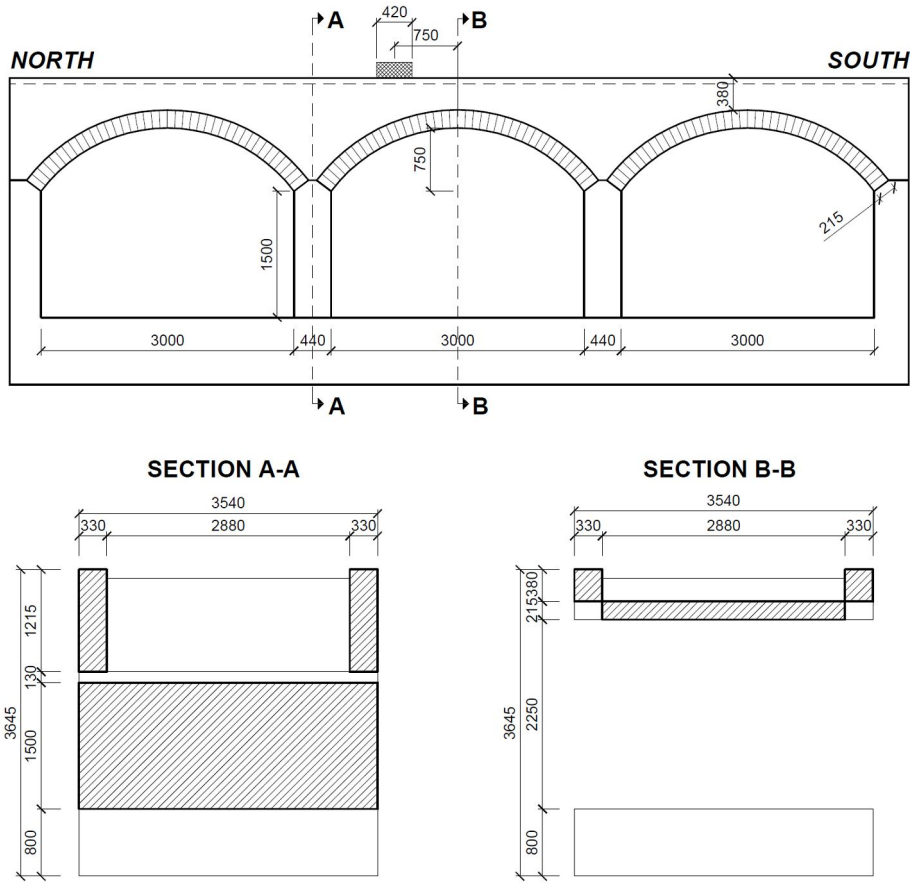

Figure 4.7. Geometry of the bridge (distances in millimeters).

The fill is not explicitly modelled but its weight and its effect in terms of load spreading are taken into account; the distribution of the load from the trampling level to the underlying arch is governed by a diffusion angle θ_d assumed to be equal to 35°+35°; the loaded nodes of the arch are hence identified as Figure 4.8 shows. Neither the spandrel walls are included in the model, while the backing is just not present in the experimental specimen.

The model is defined into a 2-D domain (this is the reason why the discretization of the cross-section into fibers is in one direction only) and a corotational reference transformation rule is adopted; the analysis is performed under displacement control to get the overall softening response of the bridge; the convergence test is based on the energy increment (3.37).

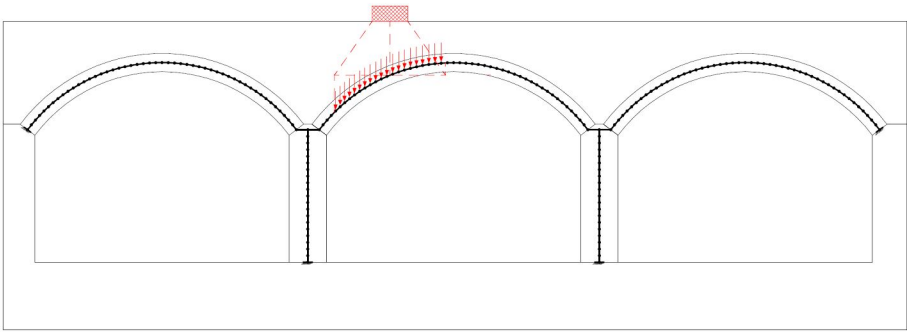

Figure 4.8. Numerical model with fiber beam elements: position of the external load and identification of the loaded nodes.

The simulation provides a load-carrying capability of 325kN, which is slightly higher than the failure load of 320kN given by the test. The entire load-displacement numerical response is compared to the experimental one in Figure 4.9: the vertical displacement of the node under the point of application of the external load is plotted in the left side graph, while the horizontal displacement of the top of the two piers is represented in the right side one. On the whole, a good agreement is found despite a slight mismatch in the phase of onset of strongly non-linear response (occurring at about 60% of the maximum load), in which the numerical model appears stiffer than the physical one. A marked difference is also found in the displacement of the North Pier which is the one near to the external load: in the experimental test a significant movement is measured while it is nearly not mobilized according to the simulation. This difference, that is responsible for the higher stiffness of the fiber beam model, is due to the fact that the spandrel wall is built on the pier, producing *de facto* an interaction between arches and piers that is not present in the simulation.

The collapse mechanism, the position of the plastic hinges, the order in which they develop and the corresponding load values are also well predicted (Figure 4.10). The average curvature along each beam element is derived starting from the coordinates (x_1, y_1 and x_2, y_2) and the rotations (κ_1, κ_2) of its end nodes, referred to the global reference system, in the deformed configuration, as it is stated in expression (4.1) in which κ^c_1 and κ^c_2 are the rotations with respect to the chord and are considered to remove the rigid rotation of the beam (Figure 4.11). By doing so, the most deformed sections of the bridge are identified (Figure 4.12); the position of the plastic hinges is evident even if the continuum nature of the finite element method results in a certain spreading of the deformation and in the formation of distributed plastic hinges. Within this procedure, a cross-section is considered to be turned into a plastic hinge when its partialization level becomes higher than 0.5, i.e. the neutral axis crosses its center of gravity.

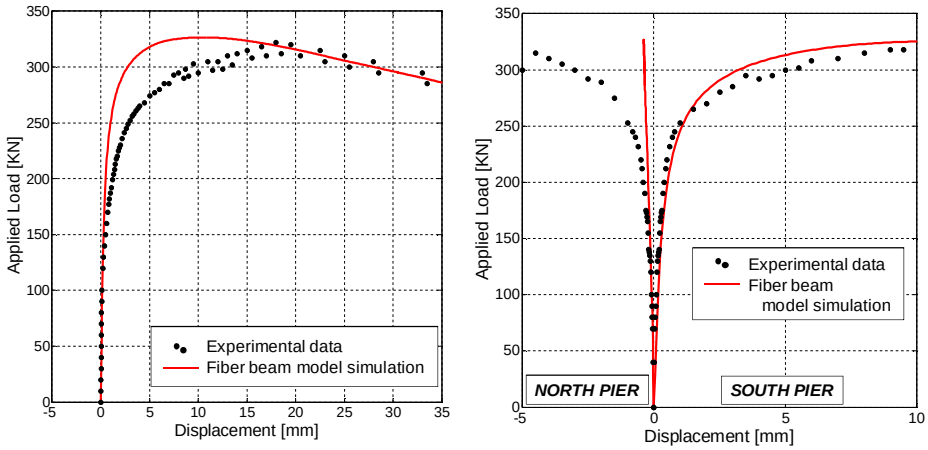

Figure 4.9. Comparison between numerical and experimental results: load vs. crown displacement curve (left) and load vs. pier displacement curves (right).

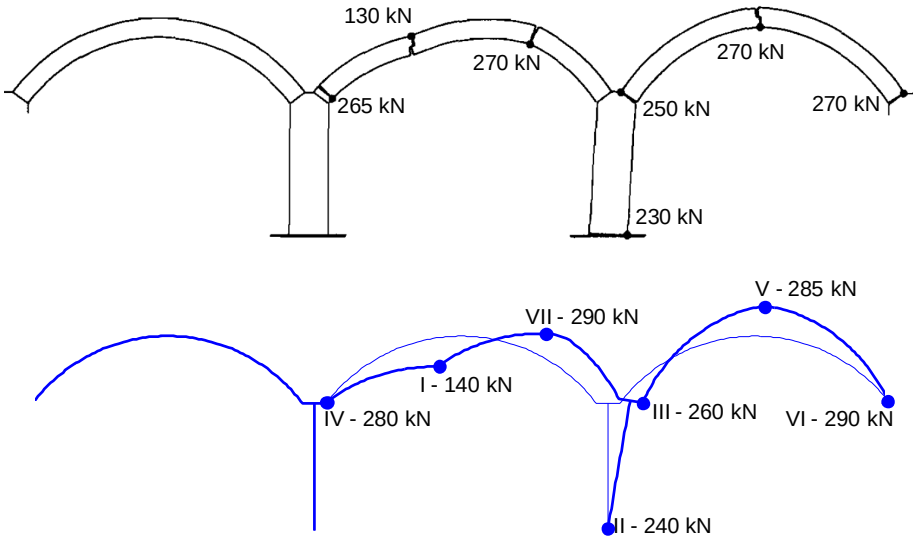

Figure 4.10. Failure mode: comparison between experimental (up) and numerical (down) models. Roman numbers represent the sequence of developing of plastic hinges; force values indicate the corresponding applied load.

$$\bar{\chi} = \frac{\kappa_2^c - \kappa_1^c}{L} = \frac{\kappa_2 - \kappa_1}{\sqrt{(x_2 - x_1)^2 + (y_2 - y_1)^2}} \tag{4.1}$$

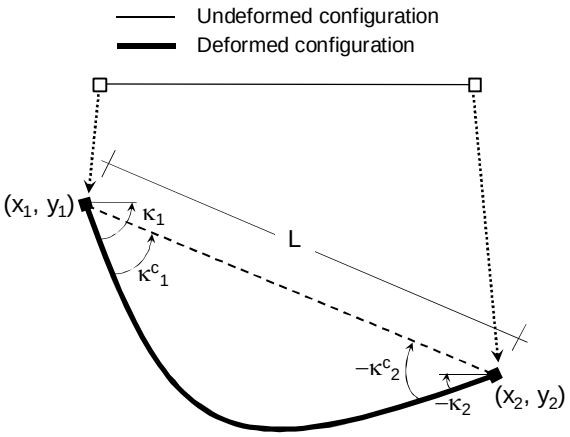

Figure 4.11. Undeformed and deformed beam element.

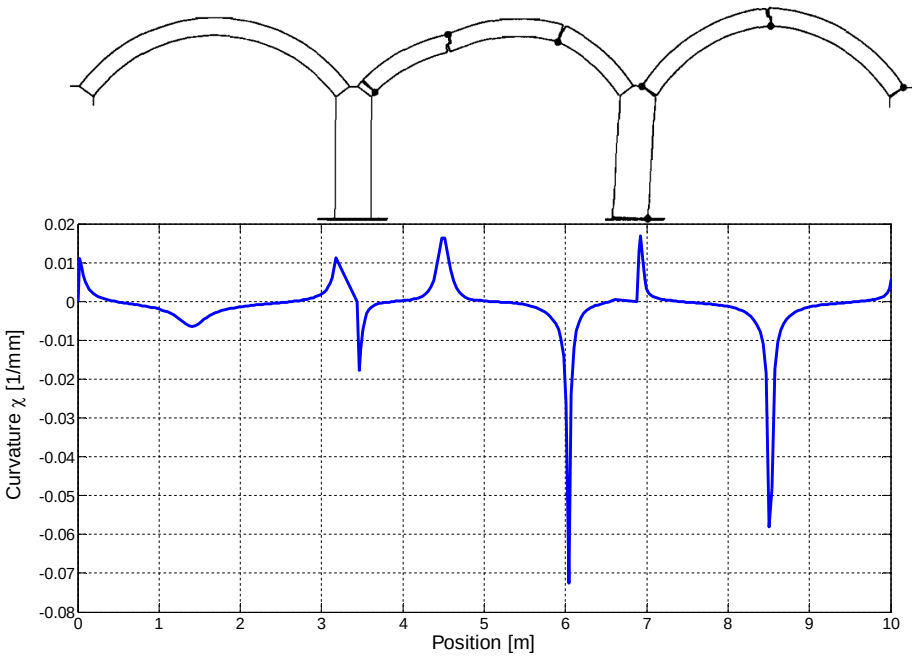

Figure 4.12. Curvature of the beam elements in the numerical model for the identification of the plastic hinges and comparison with the experimental failure mode.

The comparisons between numerical and experimental results give a confirmation of the good capability of a fiber beam approach in simulating the mechanical response of a multi-span masonry bridge, including not only

its ultimate resistance but also its entire response and the progressive development of damage.

4.4. Load-carrying capability of Ronciglione Viaduct

4.4.1. Description of the bridge

Roma-Viterbo rail line connects the stations of Roma Trastevere and Viterbo Porta Fiorentina and has a total length of 95.3km (Figure 4.13). It was designed in 1889 and built between 1890 and 1894. Because of the uneven ground, the line presents a large number of trenches, surveys, galleries, and viaducts with spans ranging from 10m to 25m.

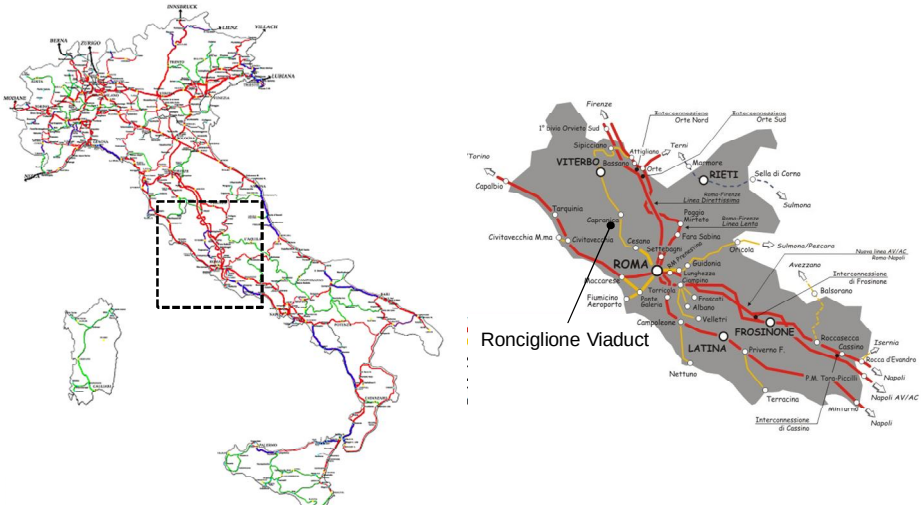

Figure 4.13. Position of Ronciglione Viaduct in the Italian Rail Network.

Ronciglione Viaduct is close to the final station of the branch going from Capranica to Ronciglione and is the most important work of the whole line; it is not in service any more but is still in good maintaining conditions. The bridge has a rectilinear layout and is made of seven circular barrel vaults and

six piers with a maximum height of about 35m, giving the construction a very slender aspect (Figures 4.14−4.15).

The barrel vaults are built with clay bricks realized in Nepi kiln (situated near Rome) and having dimensions 28×14×6cm^3; hydraulic mortar made with lime and pozzolana without cement was used; it is analogous to the mortar described in the second chapter of the Thesis. The arches have 18m span, 9m rise, 1.07m thickness and 4.60m depth (Figure 4.16; Table 4.4).

Figure 4.14. Ronciglione Viaduct.

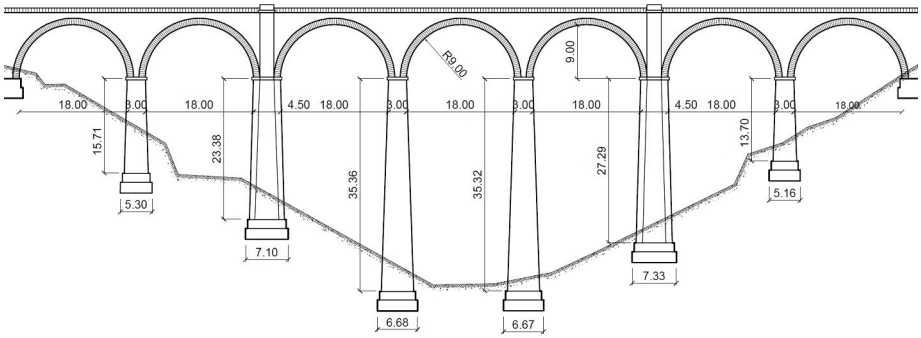

Figure 4.15. Ronciglione viaduct: longitudinal view (distances in meters).

The bridge is founded on flint and pozzolana concrete plinths based on volcanic tuff soil. The masonry of the piers is in rough tuff stone with squared units on the external face; there are corners and horizontal chains every 3m made of squared flint stones (Figure 4.16−4.17). All the piers have a vertical slope of 3.5% in longitudinal direction and varying from 5% and 6% in transversal one. The second and the fifth piers are provided with buttresses in transversal direction and are dimensioned 1.50m larger in longitudinal one to be able to carry asymmetric arch thrusts during the

buildings phases; this device allowed the vaults to be made in three subsequent steps making use of the same wood centrings (Table 4.5).

The spandrel walls are 75cm thick and 11m high from the springers and are made of regular courses of tuff squared stones; finally, the backing height is about 4.70m.

Barrel vaults span	18.00 m
Barrel vaults rise	9.00 m
Span/rise ratio	2:1
Barrel vaults thickness	1.07 m
Barrel vaults depth	4.60 m
Fill height in crown	0.93 m
Backing height	4.76 m
Spandrel walls height	11.00 m
Brickwork specific weight	16.5 kN/m^3
Tuff masonry specific weight	15 kN/m^3
Fill specific weight	15 kN/m^3

Table 4.4. Ronciglione Viaduct geometric and mechanical characteristics.

Pier	Height	Top thickness	Bottom thickness	Top depth	Bottom depth
#1	15.71 m	3.00 m	4.10 m	4.6 m	5.38 m
#2	23.40 m	4.50 m	5.90 m	5.8 m	6.97 m
#3	35.36 m	3.00 m	5.47 m	4.6 m	6.36 m
#4	35.31 m	3.00 m	5.47 m	4.6 m	6.36 m
#5	27.28 m	4.50 m	6.13 m	5.8 m	7.16 m
#6	13.70 m	3.00 m	3.96 m	4.6 m	5.28 m

Table 4.5. Ronciglione Viaduct geometric characteristics: piers.

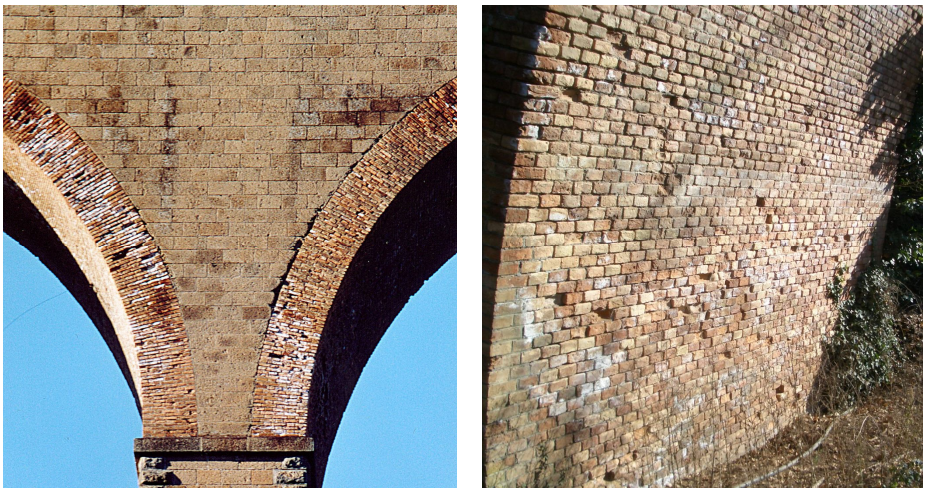

Figure 4.16. Vaults and spandrel walls (left) and detail of brick arrangement in the arches (right).

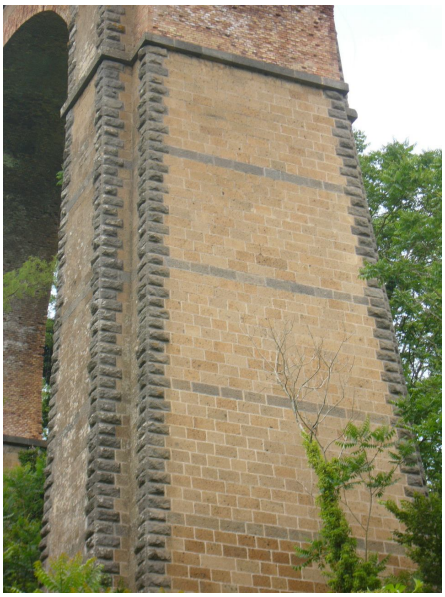

Figure 4.17. Ordinary piers and piers with buttresses.

The geometric dimensions of the structural elements and the main issues of the building phases and techniques are derived from available original drawings and documents (Figures 4.18−4.19) published by Società italiana per le strade ferrate del Mediterraneo (Italian society for Mediterranean railways).

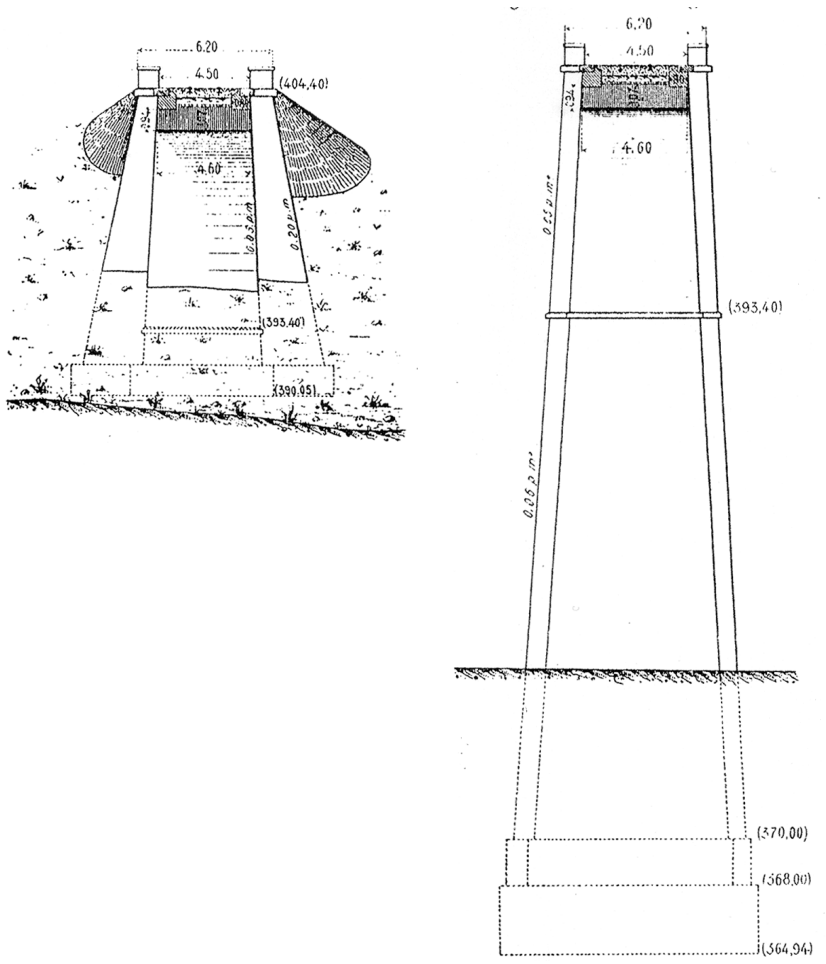

Figure 4.18. Original drawings from (Società italiana per le strade ferrate del Mediterraneo, 1894): transversal sections at the first (left) and at the central (right) span of Ronciglione Viaduct.

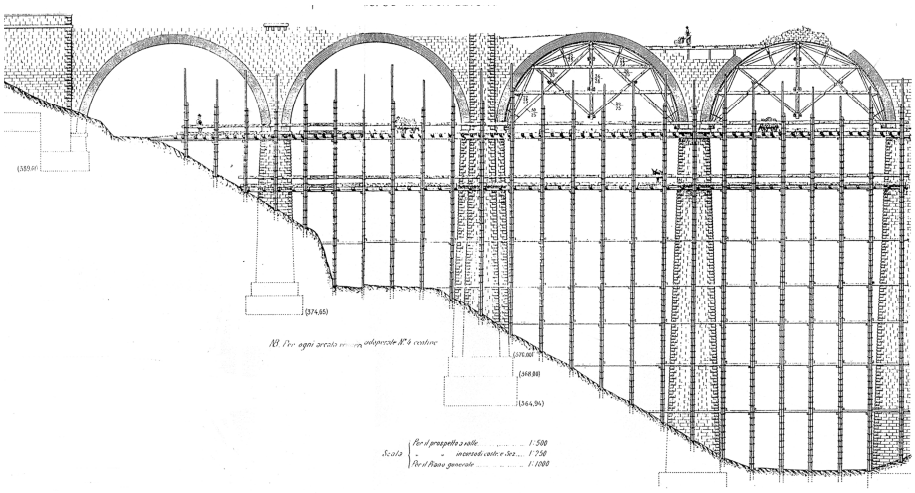

Figure 4.19. Original drawing from (Società italiana per le strade ferrate del Mediterraneo, 1894): bridge under construction.

4.4.2. Fiber beam-based modelling and comparison with limit analysis

Ronciglione viaduct is modelled by using 100 fiber beams for each arch and 50 for each pier, in both cases the cross-section is discretized into 100×1 fibers. The mesh is chosen after performing adequate sensitivity analyses, and ensures good numerical stability and result reliability. The backing and the abutments are described by using 17 truss elements. The tapering of the pillars in both longitudinal and transversal directions is included in the model, while no shear deformation is considered because, due to the pier height, it is assumed to play a negligible role. Either spandrel walls or fill soil are modelled in terms of stiffness and strength, but their self-weight is included and an angle θ_d=40°+40° is assumed to take into account the load distribution within the soil. The numerical model is defined in a 2-D domain and a linear geometric transformation is adopted, since it requires a lower computational effort and second order effects are assumed to play a negligible role; the incremental analyses are carried out under displacement control and the convergence test is based on the energy increment (3.37).

First of all, the load-carrying capability of the viaduct is evaluated under concentrated travelling load and the results are compared to the ones provided by a limit analysis approach performed by using software RING (Gilbert, 2005). The same constitutive laws are assumed for the material considering either infinite compressive strength (ENT constitutive model) or an elasto-plastic behaviour (EP constitutive model) with crushing resistance

f_{cp}=7.1MPa and unlimited ductility (Figure 4.20); an elastic modulus E=747MPa is assumed in both cases.

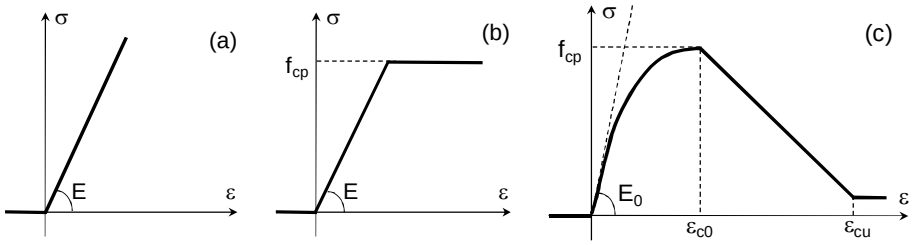

Figure 4.20. Constitutive relations adopted for load-carrying capability analyses on Ronciglione Viaduct: ENT (a), EP (b), Masonry01 (c).

The load-carrying capability curves are reported in Figure 4.21 showing, on the whole, a good agreement between the two approaches; the collapse mechanism is also well reproduced (Figure 4.22), even if a lower mobilization of the piers results from the mechanism method justifying the slight mismatch between the capacities. The plastic hinges can be identified by deriving the curvature of the beam elements employed to model the barrel vaults (Figure 4.23).

The weakest section belongs to the central span, built on the highest pillars. The asymmetric shape of the mechanism can be attributed to the interaction between arches and piers, making the critical position of the travelling load to be shifted from the crown of the central span towards its right side.

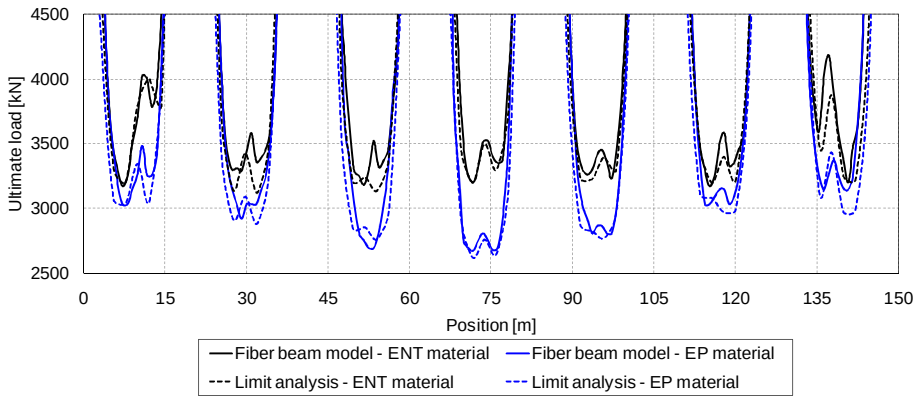

Figure 4.21. Load-carrying capability: comparison between fiber beam model and limit analysis.

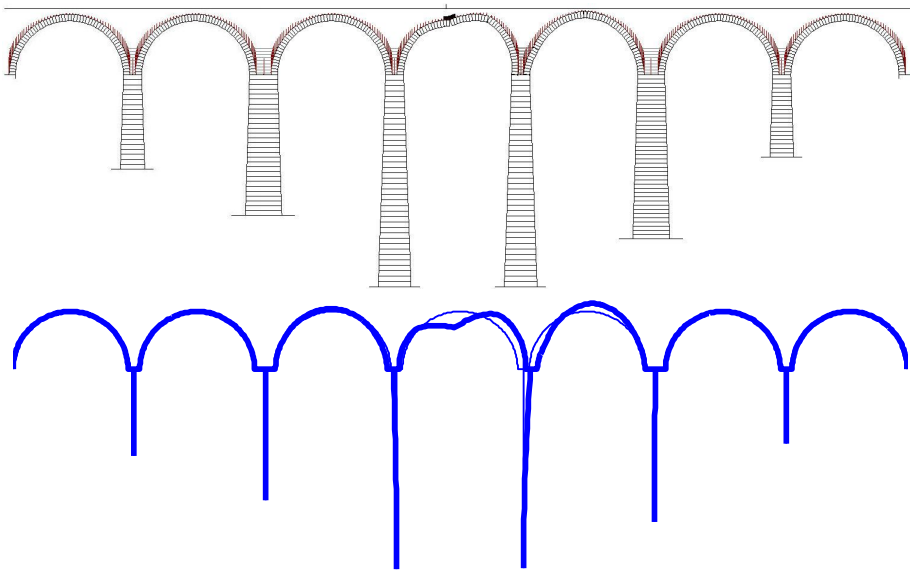

Figure 4.22. Collapse mechanism: comparison between fiber beam model and limit analysis.

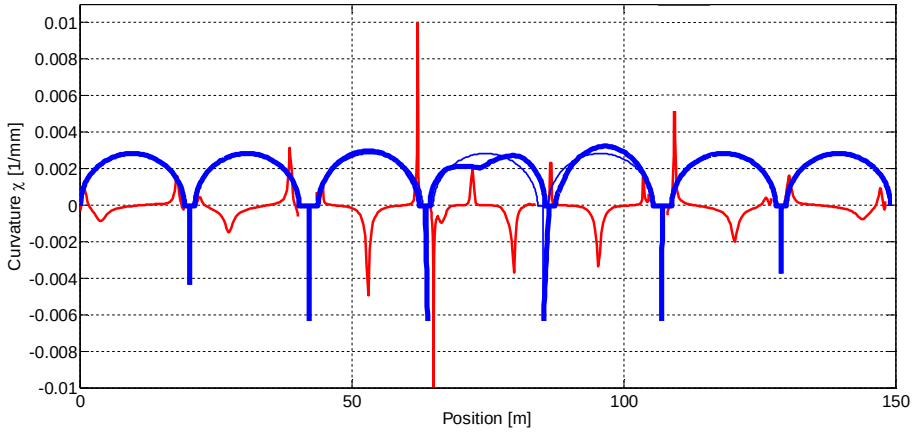

Figure 4.23. Collapse mechanism: curvature of the fiber beam elements and identification of the plastic hinges.

4.4.3. Load-carrying capability

After having checked the agreement between fiber beam model and limit analysis with ENT and EP constitutive relations, analyses under concentrated travelling load are repeated considering the effective material behaviour, described by Masonry01 constitutive law (Figure 4.20). The values assigned

to the parameters are those collected in Table 3.3 to fit experimental data, as it is discussed in chapters 2 and 3 of the Thesis. The resulting load-carrying capability curves are then compared to those provided by ENT and EP relations to evaluate the effect of the material properties on the overall structural response.

It is seen from Figure 4.24 that a significant decrease in load-carrying capability is found when assuming a constitutive relation with finite compressive resistance and limited ductility: the bridge strength when provided by the elasto-plastic (EP) and elastic no-tensile resistant (ENT) laws results to be overestimated in the order of about 70% and 100%, respectively.

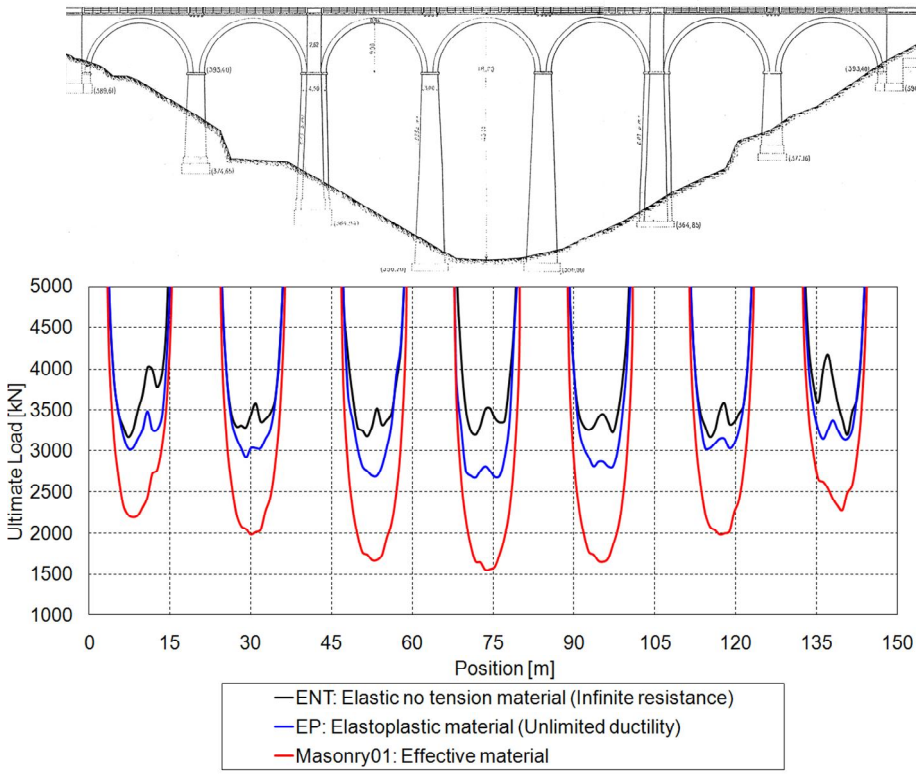

Figure 4.24. Load-carrying capability of Ronciglione Viaduct under concentrated travelling load for different material constitutive laws.

Load-carrying capability analyses are repeated assuming different values of the ductility η, ranging from 1 (brittle material) to ∞ (plastic material), to investigate the influence of the local post-peak behaviour on the overall capacity. The resulting curves referred to the central span are reported in the left side graph of Figure 4.25, showing evident variations in terms of both

ultimate load and weakest section. The increase of η is associated with an increase in load-carrying capability, which tends asymptotically to the perfectly plastic response (Figure 4.25, right side graph), as found in (de Felice, 2009) for the single arch.

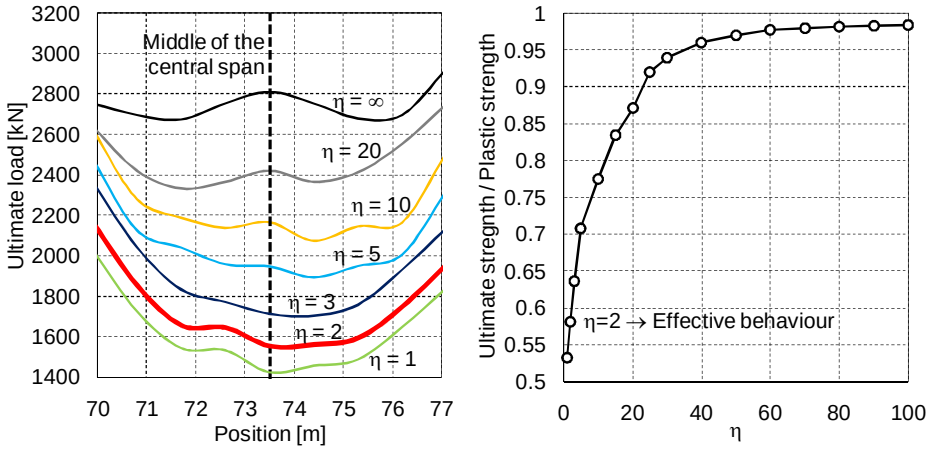

Figure 4.25. Effect of post peak behaviour; load-carrying capability curves of the central span (left) and ultimate resistance vs. $\eta=\varepsilon_{cu}/\varepsilon_{c0}$ (right).

When different materials are considered, not only the ultimate travelling load of the bridge, but also its position changes: when low ductility values are assumed, the crown of the central span turns out to be the critical position (73.50m), while with the increase of $\eta=\varepsilon_{cu}/\varepsilon_{c0}$ the minimum load-carrying capability is found for a distance of 74.60m from the left side of the first span, coinciding to the one previously provided by limit analysis. Thus, the variation in the material properties also results in the modification of the failure configuration: a hinge mechanism for ductile material, local crushing of the most stressed section for brittle material. When the effective properties are considered, these two phenomena are combined, showing that the response is intermediate between the limit cases they are related to.

Such a strong dependence of the constitutive model on the overall limit load of an arch is found also in (de Felice, 2009) and in (Brencich and Morbiducci, 2007); in the latter paper an elasto-plastic law is assumed with limited inelastic strain and a reduction of such a ductility results in lower ultimate load.

The displacement-controlled analysis allows the comparison of the post-peak behaviour of the bridge when different constitutive assumptions are made. The load-displacement curves corresponding to elasto-plastic and effective materials (EP and Masonry01 constitutive laws, respectively) are plotted in Figure 4.26, in which the crowns of the fourth and fifth spans are

considered. A concentrated load is applied in the middle of the former, being this loading condition the critical one. The negative displacement of the loaded arch corresponds to an upwards movement of the adjacent one because of their interaction, favored by the height of the piers allowing large displacements and by the presence of the backing.

The response of the elasto-plastic material appears superimposed to the effective one until the load reaches about 1200kN; then a significant overestimate of the response is found; besides, after the maximum load is reached, at a lowering of the crown of the loaded span of about 85mm, the elasto-plastic curve still grows and becomes substantially horizontal only for very large displacements.

In the overall softening branch, numerical instabilities do not allow simulations to be performed up to displacement values that are beyond the ones represented in the graph (about −135mm for span #4). Anyway, such a deformation should be considered to be well beyond the range of practical interest.

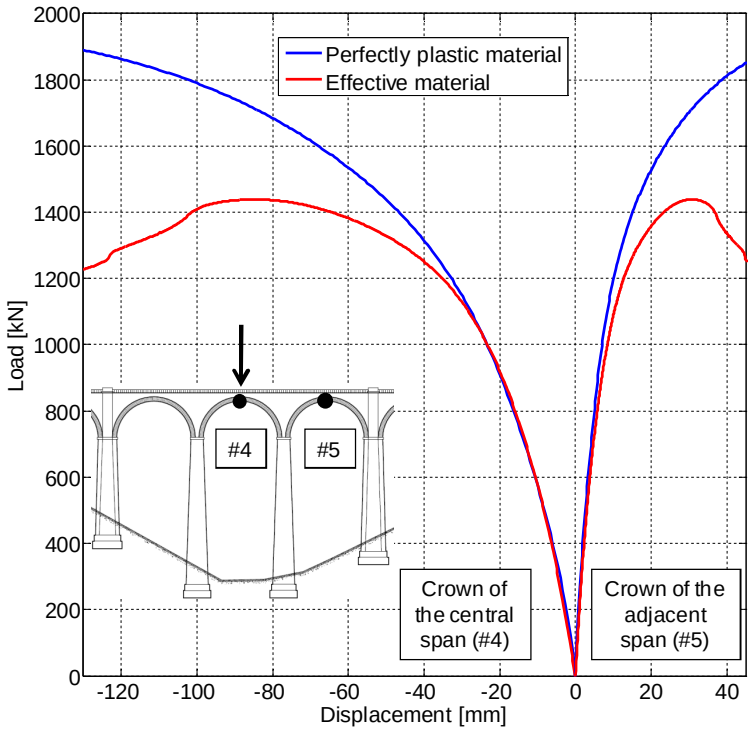

Figure 4.26. Load-displacement response for different material behaviour.

Once the load-carrying capability analyses are performed under concentrated travelling force, the rail traffic load defined by Eurocode 1 (CEN-EN 1991, 2005) and Italian code (Nuove norme tecniche per le

costruzioni, 2008) is considered. It consists of four concentrated forces of 250kN each, at a distance of 1.60m one from each other. A distributed load can also be applied, even if it is not included here and its effect will be discussed hereinafter in the present chapter. The comparison between the results provided by the different loading conditions (single force, four forces) is shown in Figure 4.27 underlining how a wider spreading results in a higher capacity; in fact, it is well-known that a distributed load allows the arch to behave more efficaciously. A measure of the bridge safety level is defined as the ratio between the ultimate load and the resultant of the design load (1000kN); in the present case a safety factor (SF) equal to 2.7 is found.

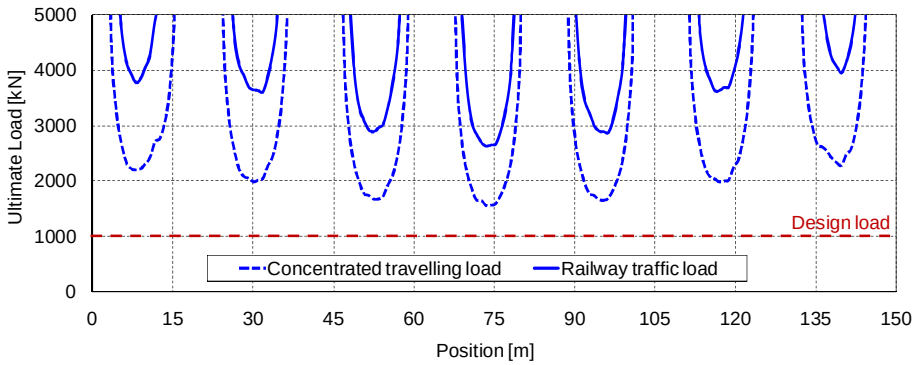

Figure 4.27. Load-carrying capability of Ronciglione Viaduct under concentrated travelling load and rail traffic load.

The collapse configuration under design traffic load is represented in Figure 4.28, where the cross-sections whose stress field is monitored during the analysis are also indicated: the crown and the most stressed sections in the haunches of the loaded span, the top and the base of the third and of the fourth piers (on which the loaded span in built on), and, finally, the most stressed sections in the haunches and close to the crown of the adjacent spans (the third and the fifth ones), which are symmetrically disposed.

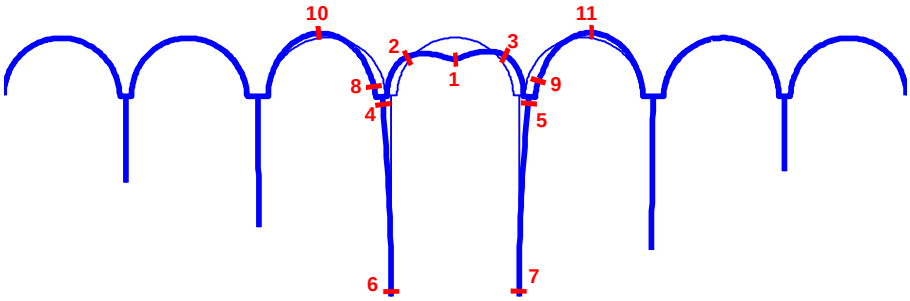

Figure 4.28. Collapse configuration under rail traffic load and monitored cross-sections.

Figures 4.29−4.31 reports their stress field under three different load conditions: the self-weight only, the resultant rail design load (1000kN) and the ultimate load. In the last two cases, the rail traffic load that should be adopted for design and verifications is applied in the middle of the central span.

It has to be said that the initial stress state does not intend to represent the exact stress field in the bridge, which depends on a wide number of variables that cannot be considered within this approach. It just means to indentify the order of magnitude of the internal forces and the reference stress state for the following application of exercise loads.

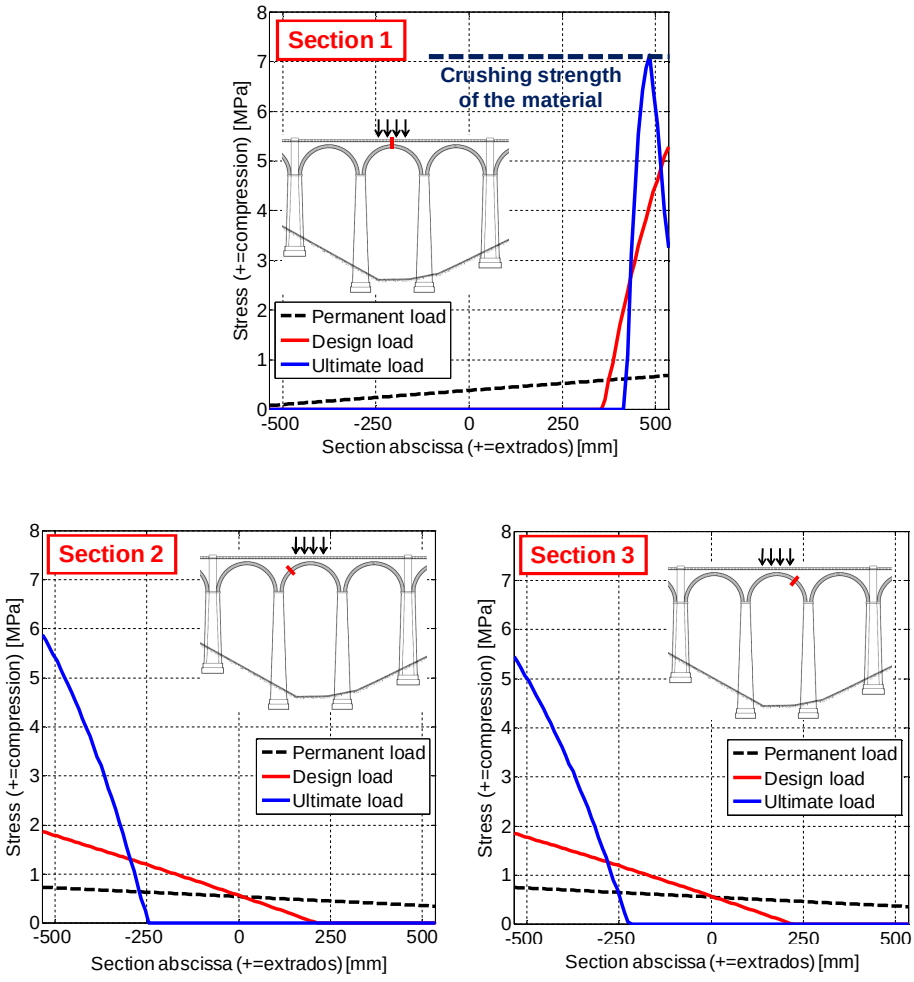

Figure 4.29. Stress field in the cross-section at the crown (up) and at the springers (down) of the central span, under self-weight only, rail load and ultimate load.

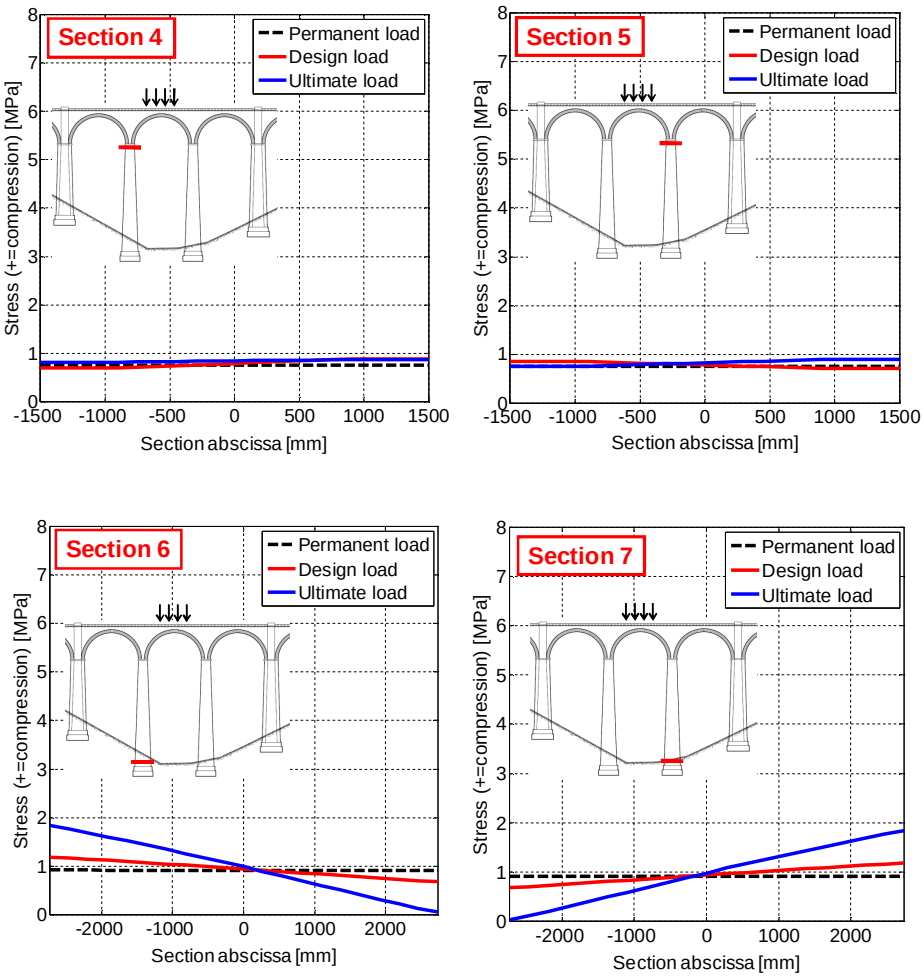

Figure 4.30. Stress field in the cross-section at the top (up) and base (down) of the third (left) and fourth (right) piers, under self-weight only, rail load and ultimate load.

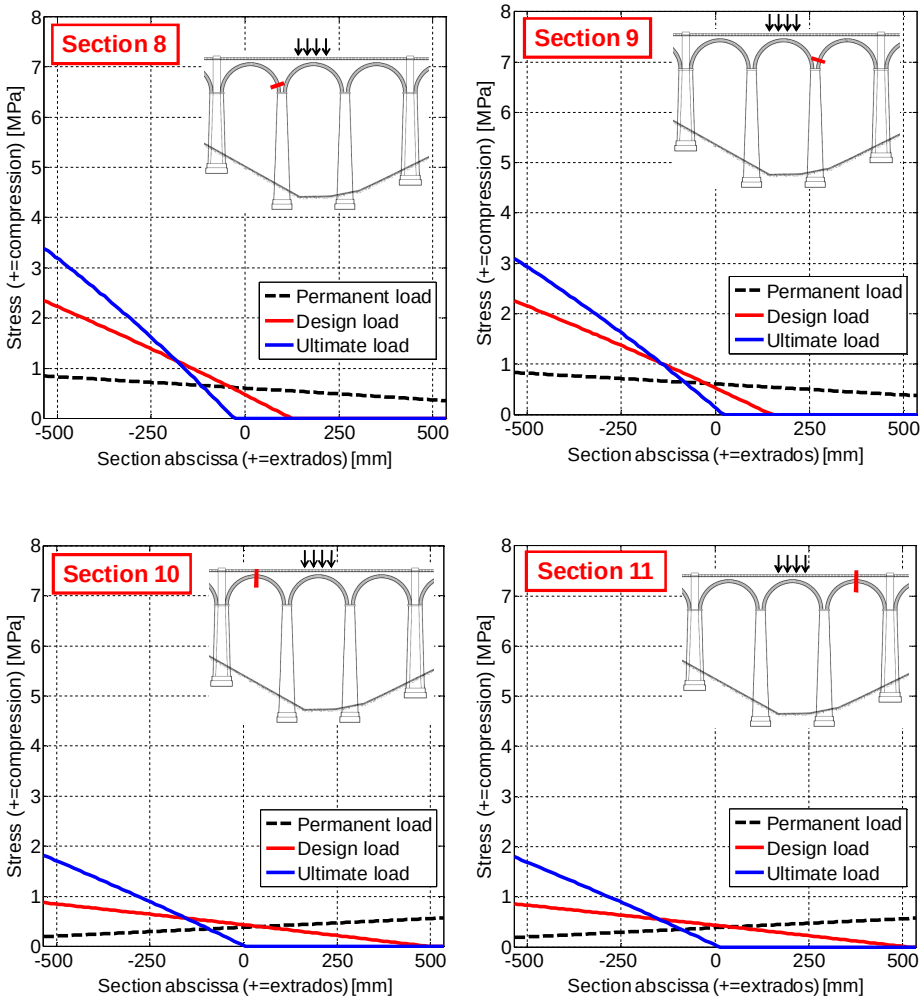

Figure 4.31. Stress field in the cross-section at the springer (up) and crown (down) of the third (left) and fifth (right) spans under self-weight only, rail load and ultimate load.

It is seen from the graphs that the vaults are still in a substantially elastic state under the permanent load; the application of the traffic load produces a partialization of some portions of the loaded arch, while under the ultimate load the most stressed cross-sections result strongly partialized; the crushing resistance (f_{cp}=7.1MPa) is reached in the extrados of the crown and the section edge has even exceeded the strain corresponding to such a peak value and is in the softening phase.

The detected stress field gives useful information on the damage state that is expected: a strong partialization reveals the opening of mortar joints, while high compressive stresses (reached by the crown in the extrados and the springers in the intrados) indicate the possibility of crushing failure and expulsion of material. In the present case, a certain damage, mainly consisting in the opening of mortar joints, is expected in the central arch already under design loads, as it is seen in the graphs relative to the crown and to the springer sections (Figure 4.29).

On the contrary, no partialization is observed in the piers, so no significant damage is expected, even if the neutral axis is next to the internal edge at the base in the failure condition (Figure 4.30).

Finally, the spans adjacent to the loaded one show a quite severe expected damage consisting in the opening of cracks in the extrados already under the design load in the springer sections, while a strong partialization of the crown of both the arches is attained under the collapse load; in these latter sections, moreover, an inversion of the bending moment is induced by the external load (Figure 4.31). Such a result indicates a marked interaction between the arches, which could be, as already discussed, attributed to the height of the piers allowing large displacements to occur, and to the backing.

Concluding, the structural response estimated on the base of the effective material behaviour results to be intermediate between the one provided by a yield-design based method (that implicitly assumes an elasto-plastic material) and the one obtained on the base of an elastic-based approach (considering an elasto-brittle material). Therefore, traditional assessment methodologies based on the assumption of limit analysis may lead to an overestimate of the load-carrying capability of a masonry bridge, since the material crushing can play a non-negligible role in the overall collapse. At the same time, an elasto-brittle approach may lead to an underestimate, since it assumes an instantaneous crushing failure of the critical section without any progressive damage and redistribution of internal stresses. An accurate representation of the effective material post-peak behaviour, and its effect on the overall response in terms of ultimate strength, failure mechanism, expected damage and displacement capacity may become particularly remarkable when a long span bridge made of weak masonry is under examination, like the case study considered in the present chapter.

On the other hand, it should be pointed out that the load bearing can strongly depend on the possibility of the arches to deform; in fact, a heavy dependence of the ultimate load on the pier stiffness is found, at least up to when the collapse mechanism involves them (Oliveira et al., 2010); moreover, the stiffening contribution of the spandrel walls, together with the passive reaction of the fill soil, would make the capacity of the viaduct in supporting vertical loads increase. Thus, the load-carrying capability provided by the present approach has to be considered as a conservative estimate.

4.5. Load-carrying capability of Cervo River Bridge

4.5.1. Description of the bridge

Santhià-Arona rail line was designed in the last years of the XIX Century and completed in 1906; it belongs to the international line connecting Briga (Switzerland) to Turin (Italy) through Sempione Pass.

Cervo River Bridge, crossing Cervo Stream, is situated close to Buronzo station (Figures 4.32−4.33) and is the most important work of the whole line. It has a rectilinear layout and consists of five shallow arches and four squat piers (Figure 4.34).

The barrel vaults are made with bricks and hydraulic mortar; the arches have 18m span (S) and 3.60m rise (r), 5:1 span to rise ratio (S/s), 0.95m thickness and 5.50m depth (Table 4.6). For their building, embossed frameworks were used (Figure 4.35).

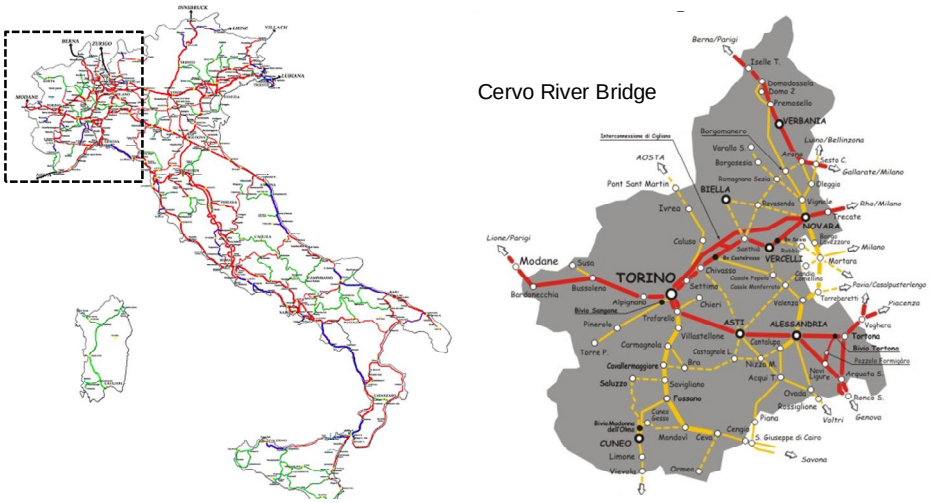

Figure 4.32. Position of Cervo River Bridge in the Italian Rail Network.

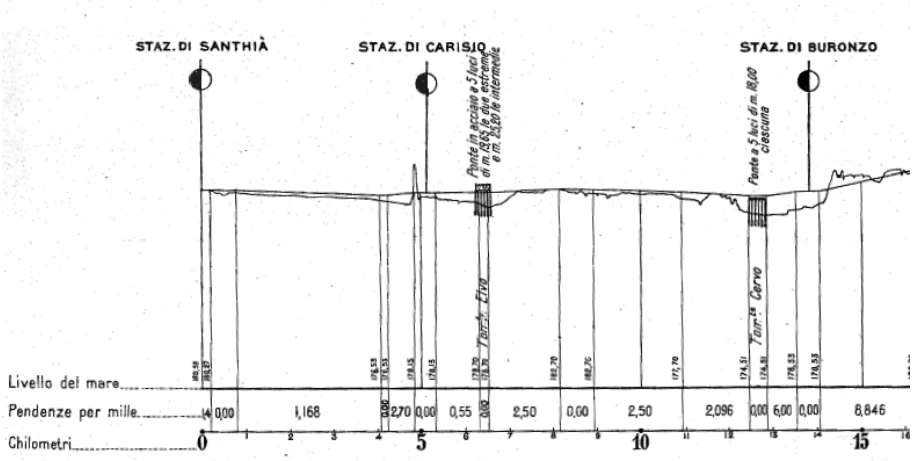

Figure 4.33. Altimetric outline of the first part of Santhià-Arona rail line, with the identification of Cervo River Bridge at km 12+500, from (Società italiana per le strade ferrate del Mediterraneo, 1906).

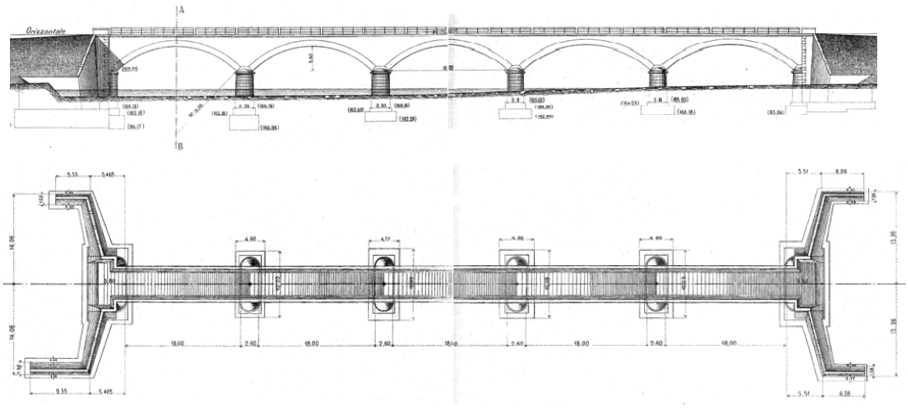

Figure 4.34. Original drawing from (Società italiana per le strade ferrate del Mediterraneo, 1906): longitudinal and upper view of Cervo River Bridge.

Vaults span	18.00 m
Vaults rise	3.60 m
Span/rise ratio	5:1
Vaults thickness	0.95 m
Vaults depth	5.50 m
Fill height in crown	0.76 m
Backing height	2.6 m
Spandrel walls height	5.00 m

Table 4.6. Cervo River Bridge geometric characteristics.

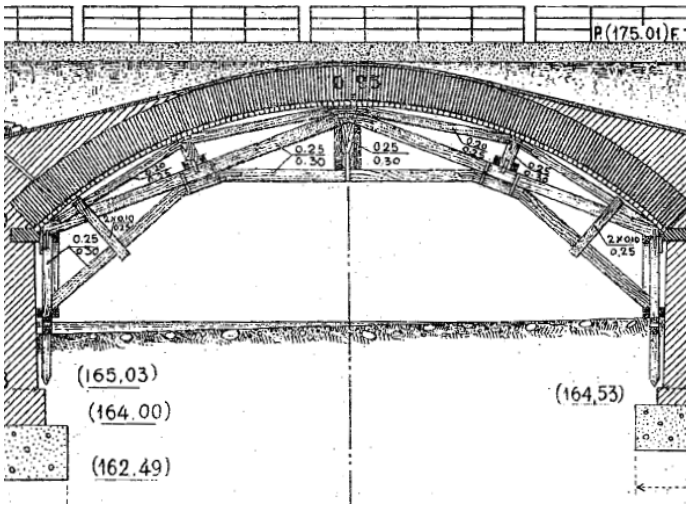

Figure 4.35. Original drawing from (Società italiana per le strade ferrate del Mediterraneo, 1906): Cervo River Bridge under construction.

The foundation plinths are made of concrete (realized with gravel and sand extracted from local pits) and reach a depth of about 4m under the water level; the soil on which they are based consists of gravel and sand. The placing of the foundations requested the realization of wood formworks to go deep under the river bed.

The piers are in syenite squared stone masonry, and their height (measured from the foundation top to the vault springer) ranges from 5.52m to 4.67m (Table 4.7; Figure 4.36). They all have rounded corners and a vertical slope of 3% in both longitudinal and transversal directions (Figures 4.37−4.38).

The spandrel walls are 1m thick and about 5m high from the springers and are made of regular courses of syenite squared stones; according to the original drawings (from which the dimensions of the structural elements are deduced), the backing height is about 2.60m from the springers.

Pier	Height	Top thickness	Bottom thickness	Top depth	Bottom depth
#1	5.52 m	2.60 m	2.93 m	8.43 m	8.60 m
#2	5.52 m	2.60 m	2.93 m	8.43 m	8.60 m
#3	4.67 m	2.60 m	2.88 m	8.43 m	8.57 m
#4	4.67 m	2.60 m	2.88 m	8.43 m	8.57 m

Table 4.7. Cervo River Bridge geometric characteristics: piers.

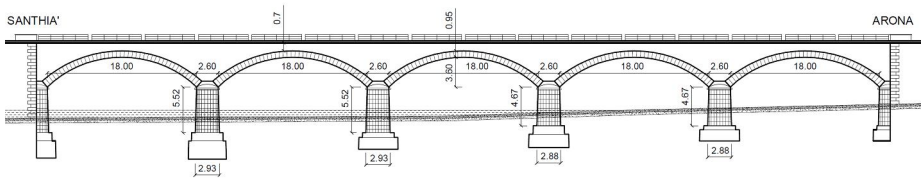

Figure 4.36. Longitudinal view of Cervo River Bridge (distances in meters).

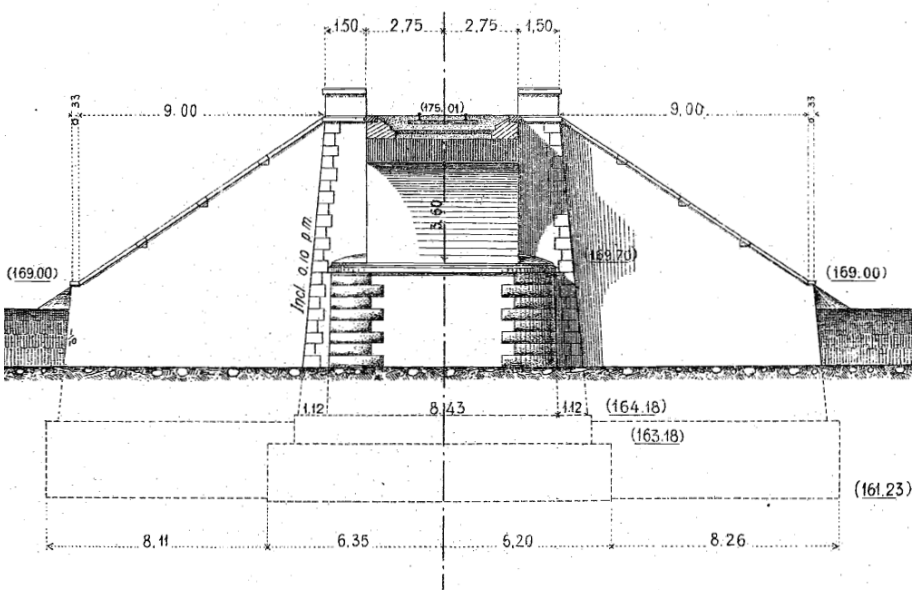

Figure 4.37. Original drawing from (Società italiana per le strade ferrate del Mediterraneo, 1906): transversal section in correspondence of the crown of the first span.

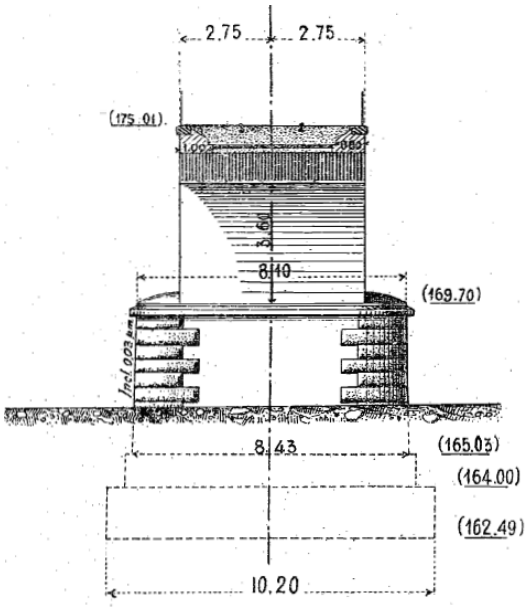

Figure 4.38. Original drawing from (Società italiana per le strade ferrate del Mediterraneo, 1906): transversal section in correspondence of the crown of the central span.

4.5.2. Load-carrying capability

Similarly to what is done for Ronciglione Viaduct, Cervo River Bridge is modelled by using 100 fiber beams for each arch and 30 for each pier, in both cases the cross-section is discretized into 100×1 fibers. The backing and the abutments are described by using 23 truss elements. The tapering of the pillars in longitudinal and transversal directions is reproduced in the model and, in this case, a shear flexibility is included in the cross-section by assuming a stiffness equal to the half of an elastic squat beam having the same pillar dimensions. As it is said in the previous chapter, the shear deformation is included in the model in the form of an additional bending flexibility; the plane section assumption remains satisfied since no sliding between fibers is allowed.

The load-carrying capability is assessed under concentrated travelling load and different material constitutive models are considered (Figure 4.20). The results of the analyses are similar to those found for Ronciglione Viaduct: a strong decrease of the ultimate load is observed when the simplifying assumptions of limit analysis (infinite crushing strength and unlimited ductility) are removed: an overestimate of about 70% results from the employment of a yield design-based analysis approach (EP law), while, if even no compressive strength is taken into account (ENT law), the failure

load is about 230% of the one corresponding to the effective material (Masonry01 law). The critical position of the travelling load (i.e. the one corresponding to its minimum value) belongs to the second span that is built on highest piers.

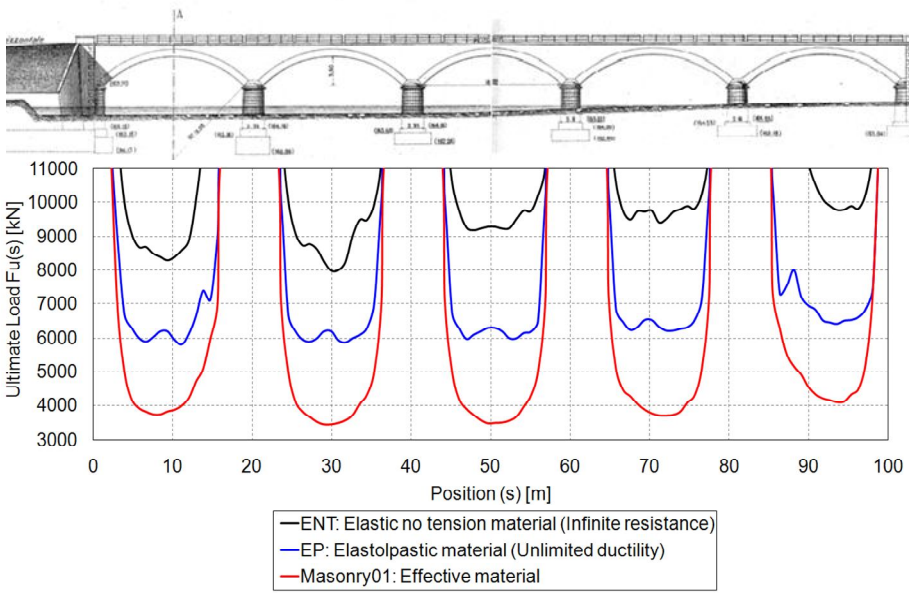

Figure 4.39. Load-carrying capability of Cervo River Bridge under concentrated travelling load for different material constitutive laws.

Load-carrying capability analyses under rail traffic load (four concentrated forces) are also performed, pointing out the increase in strength due to a wider load spread. Moreover, a higher safety factor (SF=6.0) for this bridge is found with respect to Ronciglione Viaduct (Figure 4.40), as it has to be expected in shallow arch bridges (Brencich and de Francesco, 2004; de Felice, 2009).

Some significant cross-sections are monitored during incremental analyses and their stress field is recorded to get information on the expected damage. The considered sections are shown in Figure 4.41 where the collapse configuration under rail traffic load is also represented (the load is applied in the critical position, that is the middle span of the second arch): the crown and the springers of the loaded span, the top and the base of the piers it is built on (piers #1 and #2) and, finally, the most stressed sections in the haunches and close to the crown of the adjacent spans (the first and the third ones). It is noteworthy that for the last four cross-sections an unsymmetrical choice is done because of the unsymmetrical failure mechanism which is, in turn, due to the unsymmetrical boundary conditions of the considered spans.

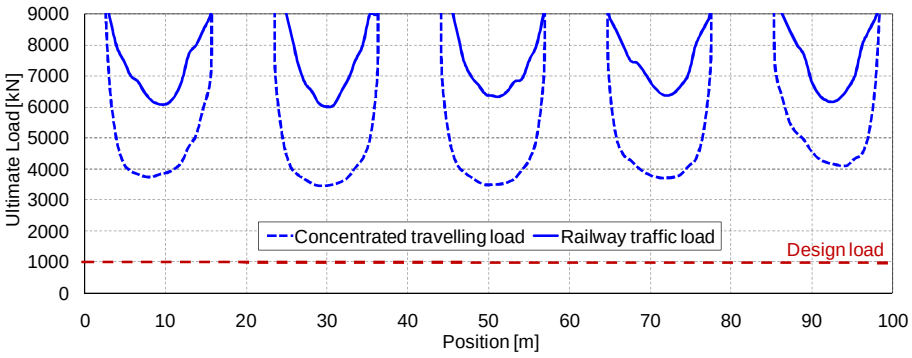

Figure 4.40. Load-carrying capability of Cervo River Bridge under concentrated travelling load (dotted line) and rail traffic load (solid line).

The comparison with Ronciglione Viaduct shows some differences in the mechanical response of deep and shallow arch bridges. Firstly, it is seen that the crown section of the loaded span results to be entirely compressed under the permanent load and partialized already under the design load (Figure 4.42); the crushing strength of the material is attained and the corresponding strain is exceeded before the collapse, when the extrados comes into the softening phase. Even if such a behaviour is similar to what is found for the previous case study, this time the partialization (and the associated expected damage) appears slightly less severe in both design and failure conditions.

Secondly, the springers result to be less damaged: they are entirely reactive under the design load and weakly partialized in the collapse condition in which, moreover, the maximum stress attained in the intrados is well below the crushing strength. In these sections an inversion of the bending moment is induced by the external loads.

Regarding the monitored piers (#1 and #2), the top of both of them is always entirely compressed, the stress results to be definitely low and neither the design load induces significant damages (Figure 4.43). On the contrary, and differently from the previous case study, a strong partialization of the base sections is detected under the collapse load as a consequence of the high bending moment resulting from the strong horizontal thrust, as it is typical of deep arches.

Finally, only the haunches of the adjacent spans result to be damaged under the collapse load (Figure 4.44); they are entirely compressed in the exercise conditions, as well as the crown sections, where, anyway, an inversion of the bending moment is evident after the exceeding of the traffic load. The comparison with the expected damage in Ronciglione Viaduct shows that a lower interaction between adjacent vaults is activated, probably because of the limited height of the piers. On the whole, a lower damage is associated to the design condition than the one induced by the collapse load, which is indeed approximately 6 times higher than the exercise one.

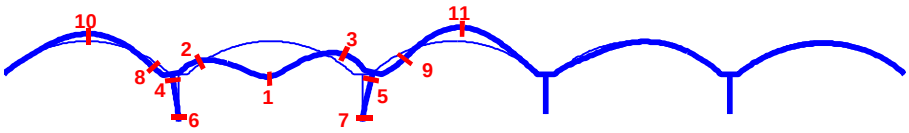

Figure 4.41. Figure 4.42. Collapse configuration under rail traffic load and monitored cross-sections.

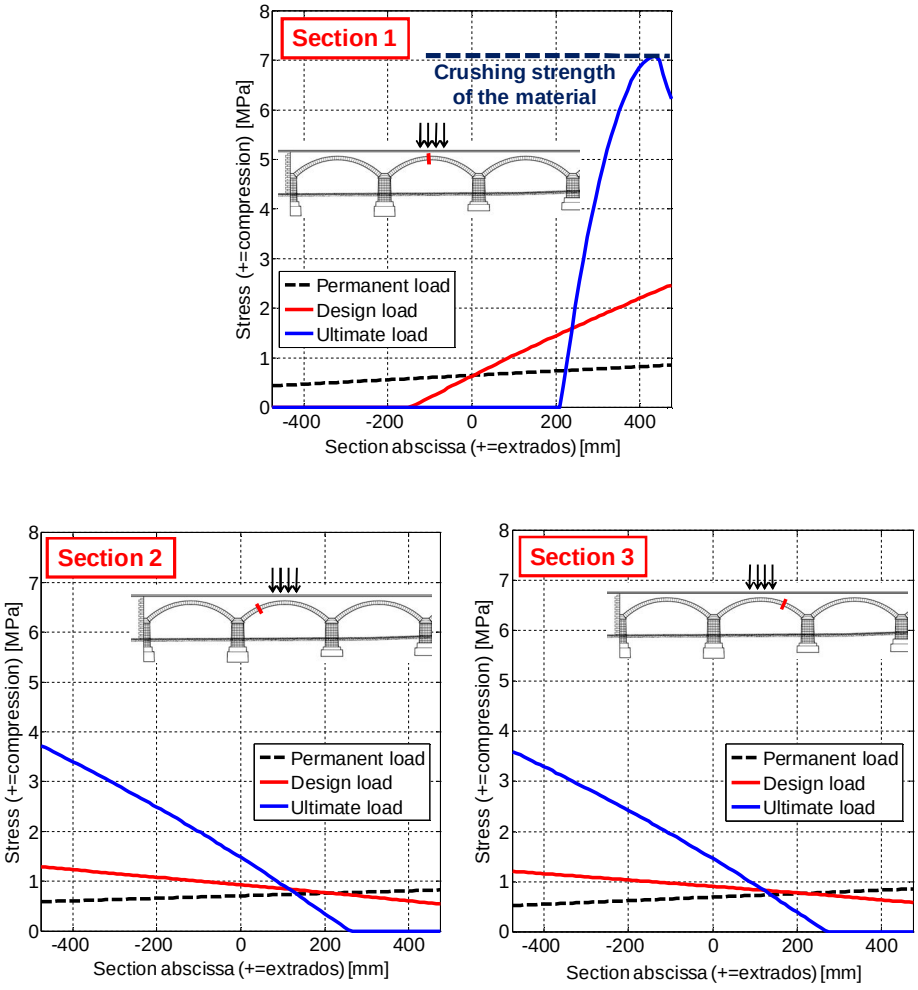

Figure 4.43. Stress field in the cross-section at the crown (up) and at the springers (down) of the central span, under self-weight only, rail load and ultimate load.

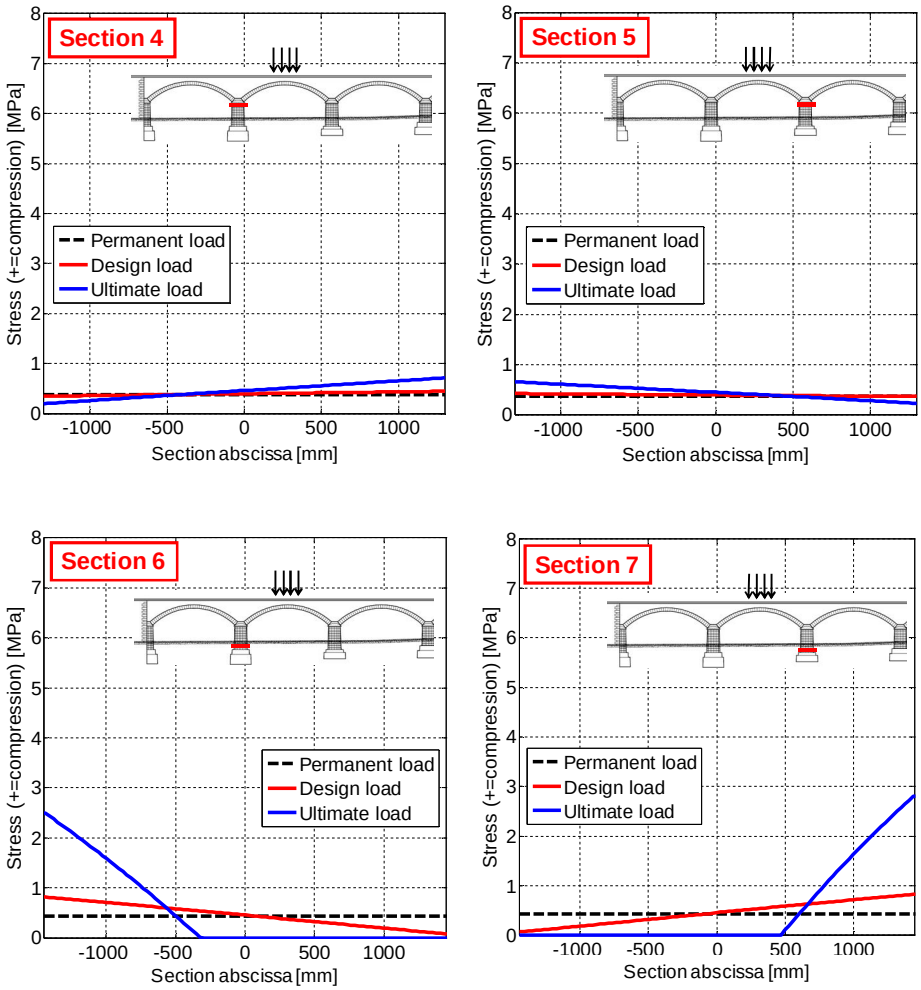

Figure 4.44. Stress field in the cross-section at the top (up) and base (down) of the first (left) and second (right) piers, under self-weight only, rail load and ultimate load.

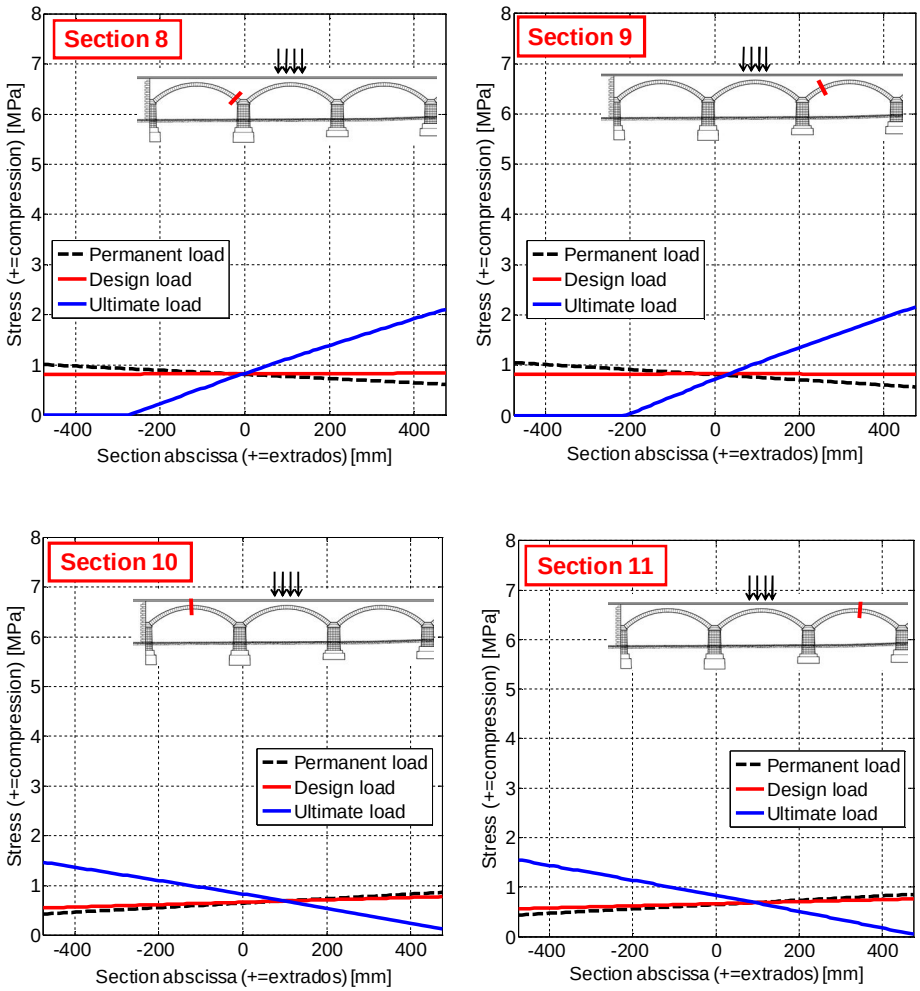

Figure 4.45. Stress field in the cross-section at the springing (up) and crown (down) of the first (left) and third (right) spans, under self-weight only, rail load and ultimate load.

4.5.3. Safety assessment under rail traffic loads

As stated previously, the Italian Code (Nuove norme tecniche per le costruzioni, 2008) defines a loading scheme to represent normal rail traffic on mainline railways, named Load Model (LM) 71. It acknowledges the rail traffic action defined by Eurocode 1 (CEN-EN 1991, 2005) and consists in four concentrated forces having value of 250kN each, and distance 1.60m from each other (intending to represent the axis of the engine), and in a

distributed load of 80kN/m, at a distance of 0.80m from the lateral forces, representing the wagons (Figure 4.45). The distributed load has to be applied for a length so as to produce the worst (less safe) condition. The effect of such a distributed load on the load-carrying capability of a multi-span bridge is investigated in this section.

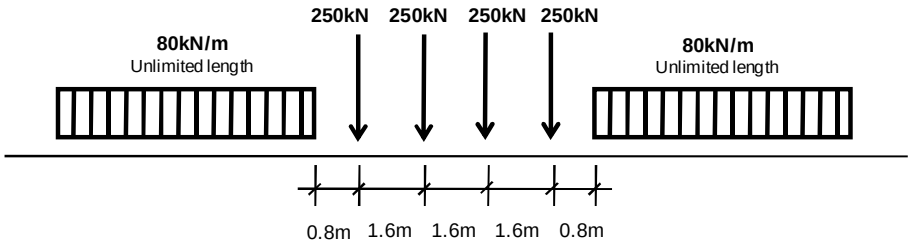

Figure 4.46. LM71 rail traffic load as it is defined by the Italian Code.

Displacement-based analyses are performed under three different loading conditions (Figure 4.46): the first one consists of the four concentrated forces only (loading condition #1, black) and is the same one assumed in the analyses already discussed in the previous paragraphs. In the other two loading cases, the distributed load is also included; it is applied on the first span only to investigate an unsymmetrical loading pattern (loading condition #2, red) and, finally, on both the first and the third spans (loading condition #3, blue).

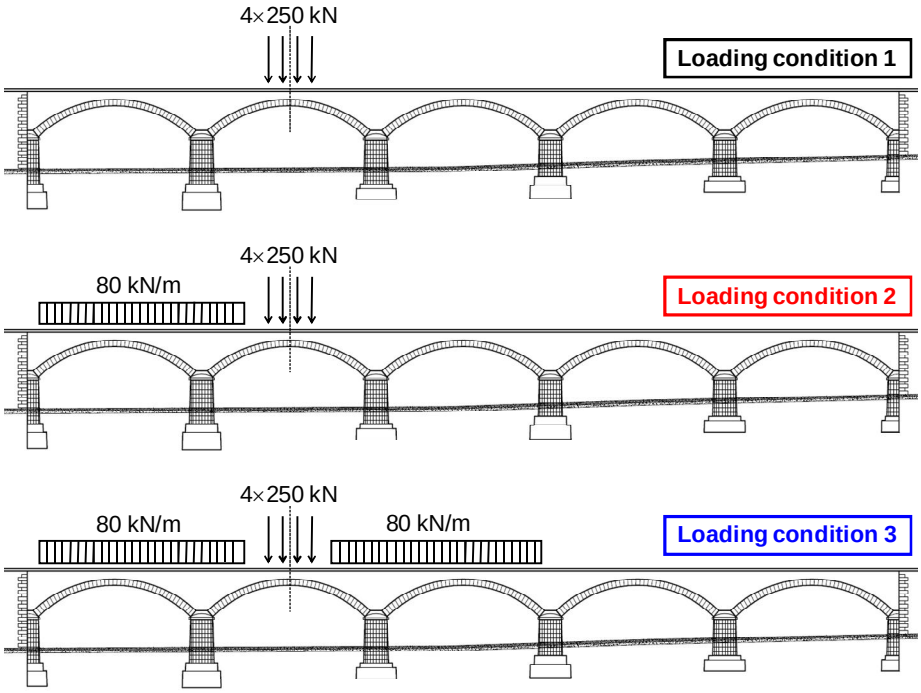

Figure 4.47. Rail traffic load: loading conditions.

The presence of the distributed load is found to lead to a higher ultimate load of the bridge, as it is shown in Figure 4.47, representing the load-displacement curves of the crown of the first three spans. Such an increase is due to a sort of a stiffening effect: the first and the third arches tend to move upwards when the second span is loaded, but the applied distributed load partially prevents or contains such a mechanism. It is seen in the graph that the displacement of the lateral spans corresponding to the attainment of the maximum load significantly changes; such a variation in the collapse mechanism is also represented in Figure 4.48.

Concluding, the analyses suggest that the only four concentrated forces should be considered to assess the load-carrying capability of a rail multi-span masonry bridge, while the distributed load should be neglected.

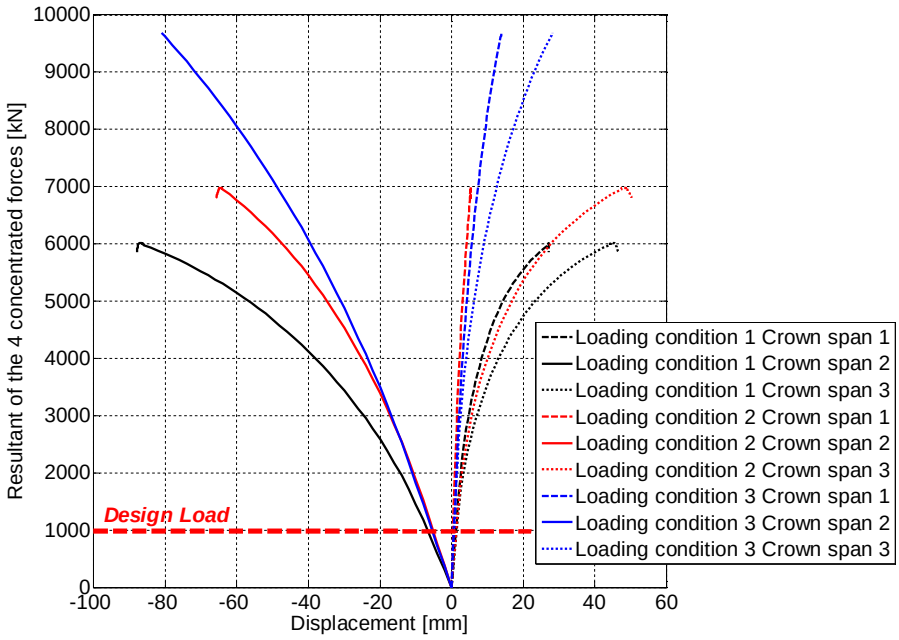

Figure 4.48. Load-displacement response curves for the different loading conditions (black lines: loading condition #1; red lines: loading condition #2: blue lines: loading condition #3).

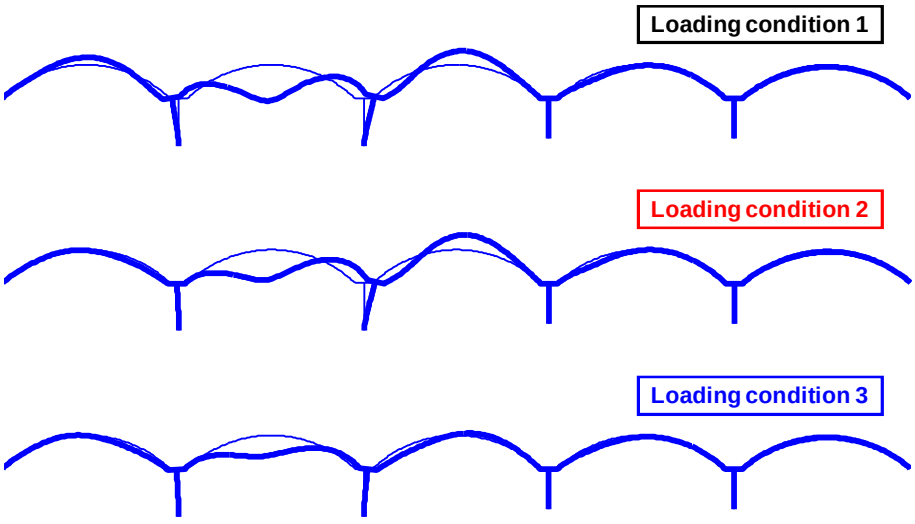

Figure 4.49. Collapse configurations corresponding to different loading conditions.

4.6. Safety assessment of different typologies of Italian large-span rail bridges

Ten masonry bridges are considered in addition to Ronciglione Viaduct and Cervo River Bridge; their safety level towards rail traffic load is assessed and their failure mode is detected. The surveyed sample is not so wide to be considered exhaustive, but however it is representative of the Italian large span-bridges built between about 100 and 160 years ago, also in consideration of the analogies they have in common. The bridges are collected in Table 4.8 together with the line they belong to and the year of construction, ranging from 1857 to 1906; they are also illustrated in Figures 4.49−4.58 (except for Ronciglione Viaduct and Cervo Rover Bridge, illustrated in detail in the previous paragraphs).

The considered artworks are different in terms of geographical position (Figure 4.59) and geometrical characteristics: span (S), rise (r), vault thickness (s), number of spans, maximum pier height (H_P), as it is reported in Table 4.10. The data regarding the arch thickness at the crown are plotted in Figure 4.60, superposed to the empirical rules adopted in the past for the dimensioning of the vaults (Table 4.1): all the bridges of the sample are within the envelope domain, with the only exception of bridge #10 that is just above the upper envelope limit. In Figure 4.61 the survey data and the values deriving from empirical design rules (Table 4.2) for the pier top thickness (P) are represented, showing that all the bridges in the sample are within the envelope.

	Bridge	Line	Year
#1	Agira River Bridge	Catania-Enna	1870
#2	Avella Bridge	Avellino-Rocchetta S. Venere	1895
#3	Cairasca Bridge	Domodossola-Isella	1905
#4	Calore River Viaduct	Avellino-Rocchetta S. Venere	1895
#5	Cervo River Bridge	Santhià-Arona	1906
#6	Chiaravagna Bridge	Genova-Asti	1894
#7	Diveria Bridge	Domodossola-Isella	1905
#8	Goriano Sicoli Viaduct	Roma-Pescara	1888
#9	Mergozzo Bridge	Arona-Domodossola	1905
#10	Rivisondoli Vaiduct	Roma-Sulmona	1888
#11	Ronciglione Viaduct	Roma-Viterbo	1894
#12	San Polo Bridge	Udine-Trieste	1857

Table 4.8. Surveyed sample of rail bridges: characteristics of the lines.

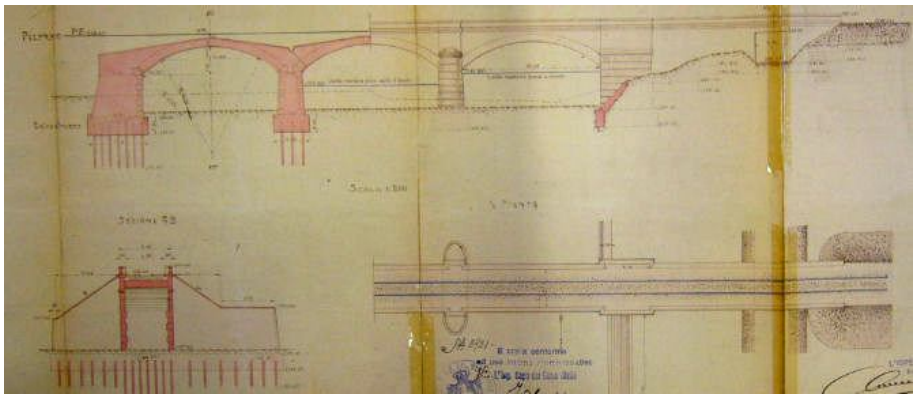

Figure 4.50. Longitudinal view, cross-section and upper view of Agira River Bridge.

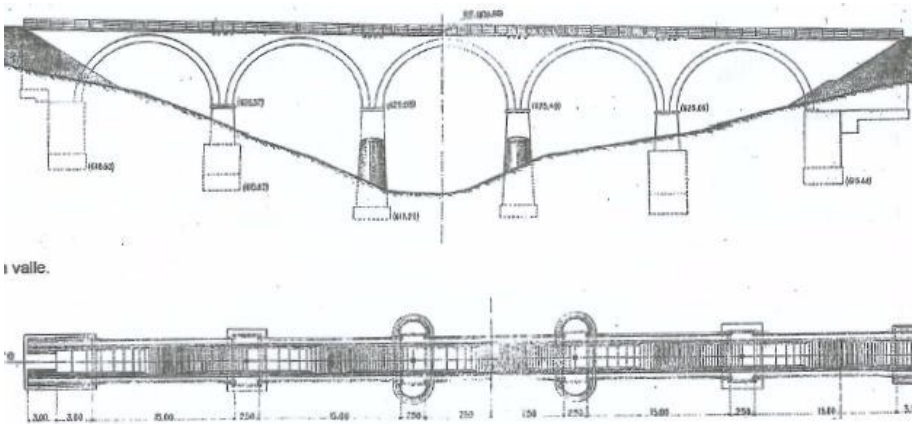

Figure 4.51. Longitudinal and upper views of Avella Bridge.

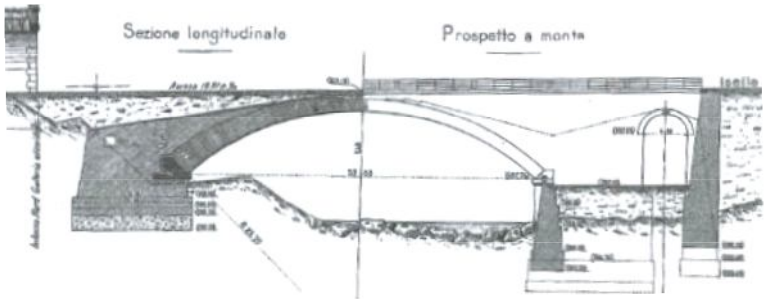

Figure 4.52. Longitudinal view of Cairasca Bridge.

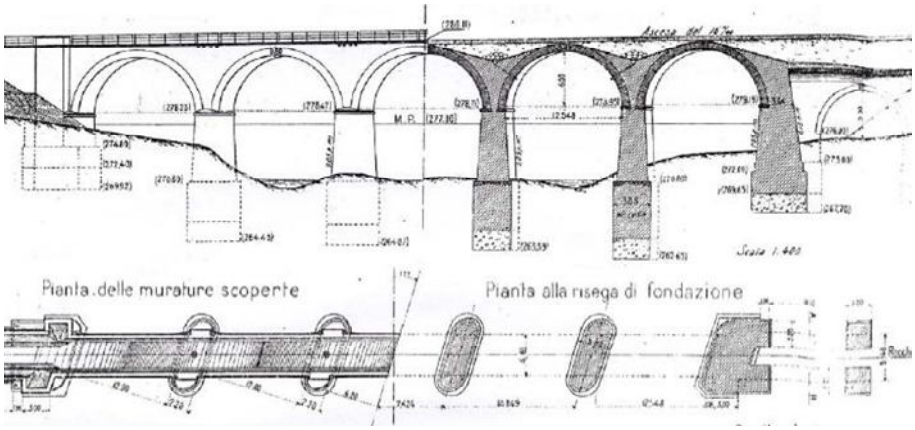

Figure 4.53. Longitudinal and upper views of Calore River Viaduct.

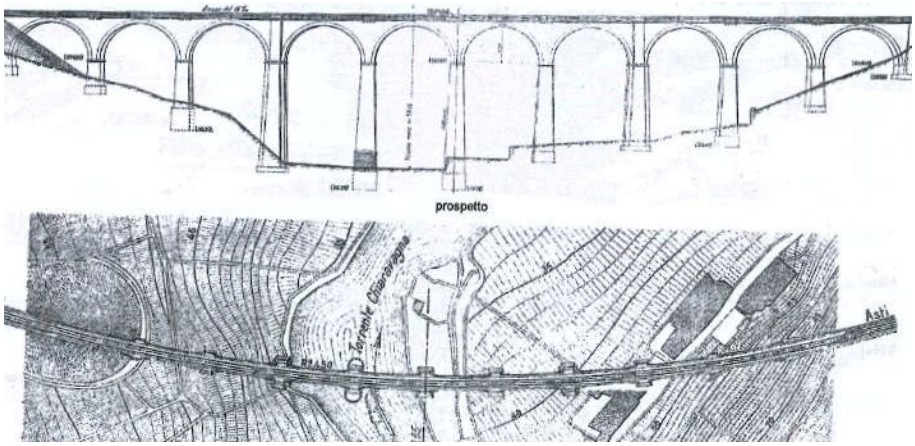

Figure 4.54. Longitudinal and upper views of Chiaravagna Bridge.

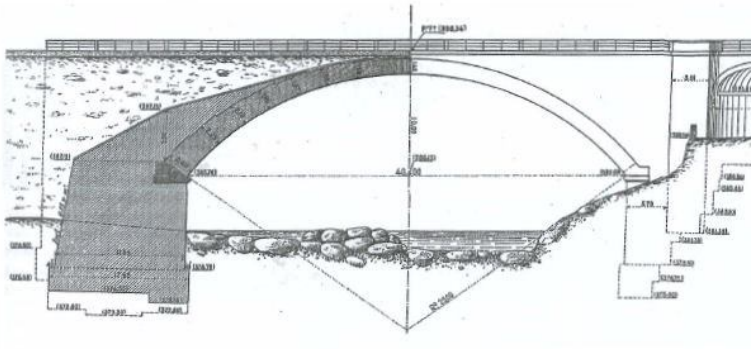

Figure 4.55. Longitudinal view of Diveria Bridge.

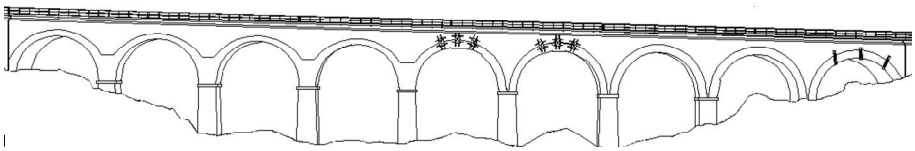

Figure 4.56. Longitudinal view of Goriano Sicoli Viaduct.

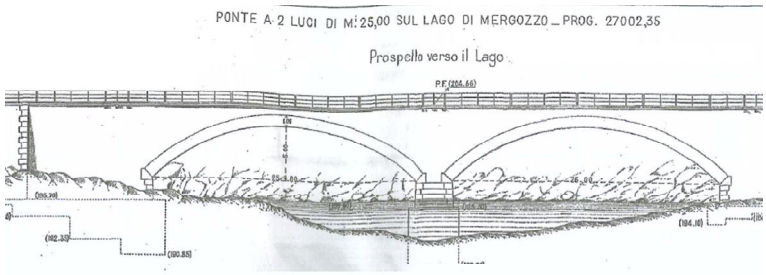

Figure 4.57. Longitudinal view of Mergozzo Bridge.

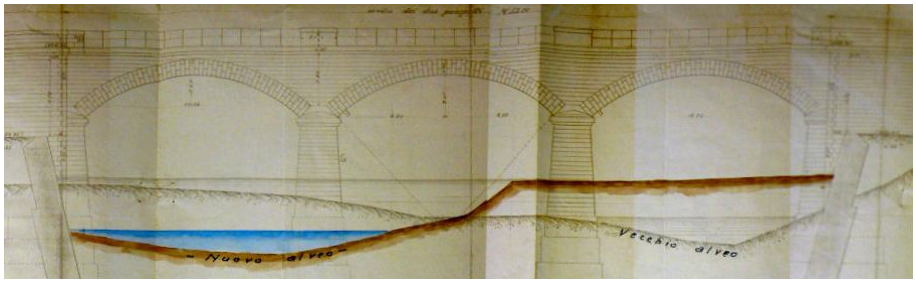

Figure 4.58. Longitudinal view of Rovisondoli Viaduct.

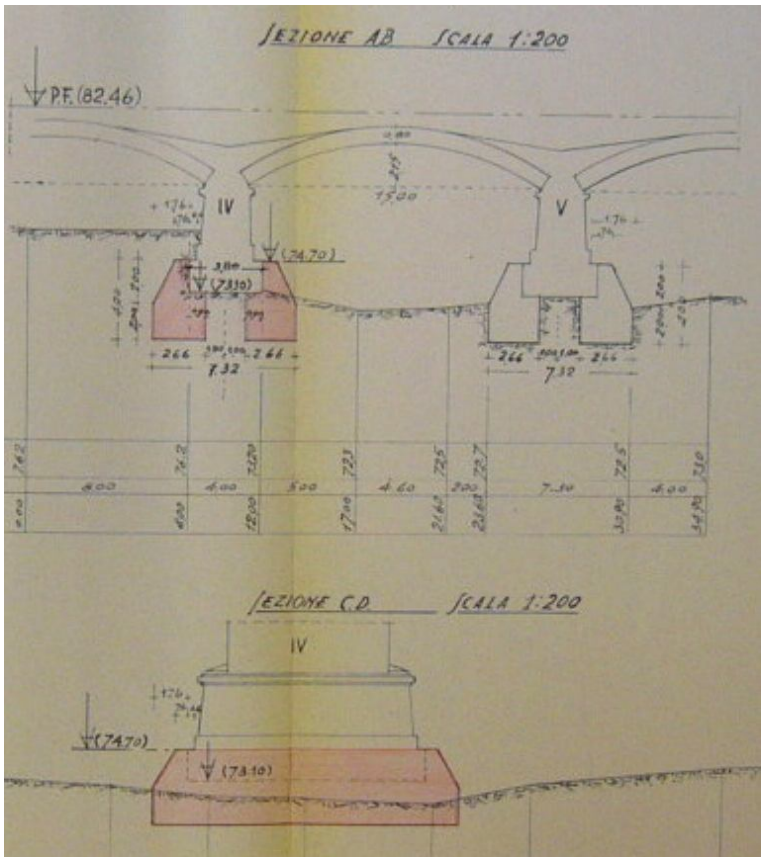

Figure 4.59. San Polo Bridge: details of the arch and of the foundations.

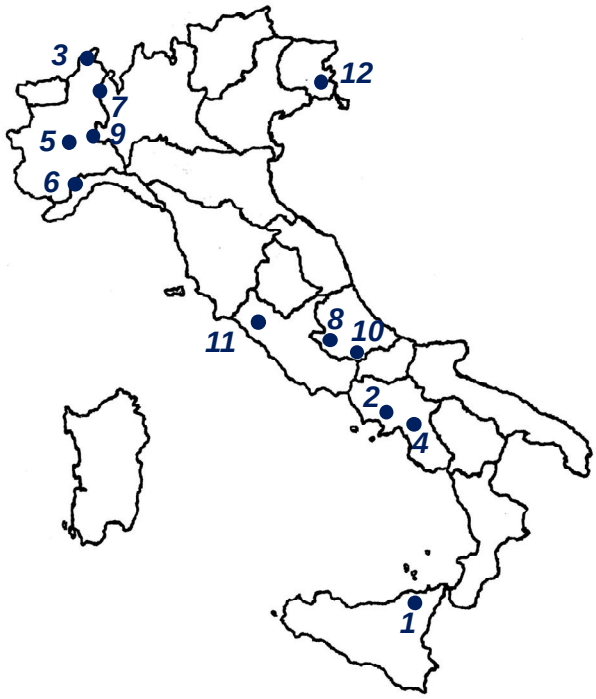

Figure 4.60. Position of the surveyed bridges on the Italian territory.

	Span (S) [m]	Rise (r) [m]	Vault thickness (s) [m]	Number of spans	Maximum pier height (H_P) [m]	Maximum pier width (P) [m]	r/S	s/S
#1	16.1	3.15	0.85	3	5.00	2.73	0.20	0.05
#2	15.0	7.50	0.81	5	12.72	2.60	0.50	0.05
#3	32.0	6.40	1.85	1	–	–	0.20	0.06
#4	12.6	6.00	0.80	5	8.15	2.20	0.48	0.06
#5	18.0	3.60	0.95	5	5.52	2.60	0.20	0.05
#6	18.5	9.25	1.07	10	28.70	3.00	0.50	0.06
#7	40.0	10.00	1.90	1	–	–	0.25	0.05
#8	10.0	5.00	0.70	9	2.48	2.08	0.50	0.07
#9	25.0	5.00	1.30	2	2.35	3.50	0.20	0.05
#10	12.0	2.40	0.95	3	5.80	2.20	0.20	0.08
#11	18.0	9.00	1.07	7	35.37	3.00	0.50	0.06
#12	15.0	2.15	0.85	14	3.10	2.30	0.14	0.06

Table 4.9. Bridge sample: geometric characteristics.
For bridges #6 (Chiaravagna Bridge) and #11 (Ronciglione Viaduct) the width of the piers without buttresses is considered.

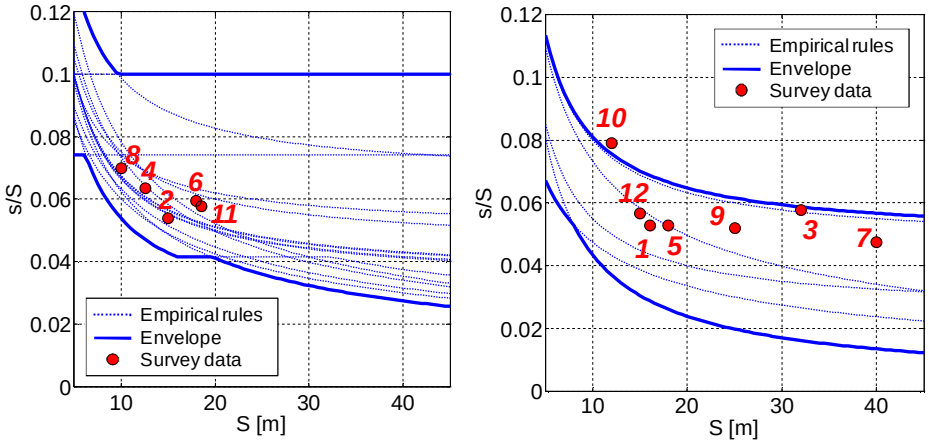

Figure 4.61. Comparison between empirical rules (single relations and envelope) and survey data in terms of span (S) vs. crown thickness-to-span ratio (s/S) for deep arches (left) and shallow arches (right).
In the relations for shallow arches containing the radius, a value R=0.7S is taken as it is recurrent for bridges having rise-to-span ratio equal to 0.2.

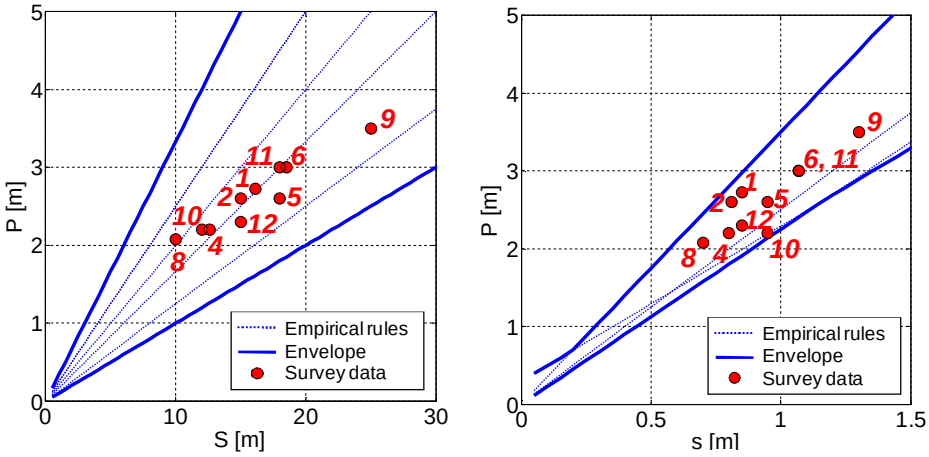

Figure 4.62. Comparison between empirical rules (single relations and envelope) and survey data in terms of span (S) (left) and vault thickness (s) (right) vs. pier top thickness (P).

Different constitutive laws (ENT, EP, Masonry01) are adopted and the results are compared to evaluate the effect of the material properties on the overall strength. The analyses with the three relations are performed by using

a fiber beam model; in addition, software RING with EP material is also adopted to make a further comparison on a wide number of cases and confirm the reliability of the developed approach. All the results of load-carrying capability analyses are collected in Table 4.10.

	Limit Analysis (LA)	Fiber Beams (FB)						
	EP	ENT	EP	Masonry01	LA^{EP}/FB^{EP}	FB^{ENT}/FB^{Mas01}	FB^{EP}/FB^{Mas01}	SF (FB^{Mas01})
#1	6180	8203	6435	4461	1.04	1.84	1.44	4.5
#2	3640	4560	3662	3213	1.01	1.42	1.14	3.2
#3	22100	26300	21494	15963	0.97	1.65	1.35	8.0
#4	3570	4119	3520	3270	0.99	1.26	1.08	3.3
#5	7210	8762	7229	6002	1.00	1.46	1.20	6.0
#6	3820	3599	4419	3084	1.16	1.17	1.43	3.1
#7	13700	22600	13200	8530	0.96	2.65	1.55	8.5
#8	4730	5955	4799	4546	1.01	1.31	1.06	4.5
#9	8400	14700	7664	4631	0.91	3.17	1.66	4.6
#10	8340	12674	8527	6644	1.02	1.91	1.28	6.6
#11	3700	3300	3766	2630	1.02	1.25	1.43	2.6
#12	10402	14293	9083	6642	0.87	2.15	1.37	6.6

Table 4.10. Bridge sample: ultimate load under LM71 rail load for different constitutive models and modelling approaches.

The comparison between fiber beam model and limit analysis reveals an extremely satisfactory agreement: in most cases the mismatch is lower than 5%, and, anyway, never higher than 16% (Table 4.10 and Figure 4.62).

The overestimate provided by the simplified constitutive assumptions peculiar of a yield design-based approach results to be, on average, equal to 86% and 36% for ENT and EP relations, respectively; the scatter of these data is quite low, as is it shown by the values of the coefficient of determination (R^2), equal to 0.81 and 0.97.

The safety factor (SF) is defined as the ultimate load divided by the exercise load (equal to 1000 kN for all the bridges, and to 2000 kN for bridge #3 that has two ways); on the whole, the surveyed bridges result to be safe since, according to the analyses performed with Masonry01 constitutive model, the values of SF range from 2.6 (bridge #11) to 8.5 (bridge #7). SF is plotted versus the bridge main geometric properties (Figure 4.63) and quite weak correlations are found. In fact, it is difficult to find a clear dependence on one parameter since several factors play an important role in the structural safety.

Firstly, bridges with larger span result to be safer, but this is probably due to the corresponding higher thickness of the vault; secondly, shallow arch bridges (low r/S) are found to be safer than deep ones; finally, no significant correlation is detected between safety and slenderness (s/S). In Figure 4.63, graph (c), it is interesting to observe that span-to-rise ratios are concentrated

around 0.2 and 0.5, indicating that these typologies were extremely more diffuse than any other ones.

The overestimate provided by ENT and EP constitutive laws is found to be higher for deep and slender arch bridges (Figure 4.64) as a consequence of the higher stresses induced on the material in these arch typologies.

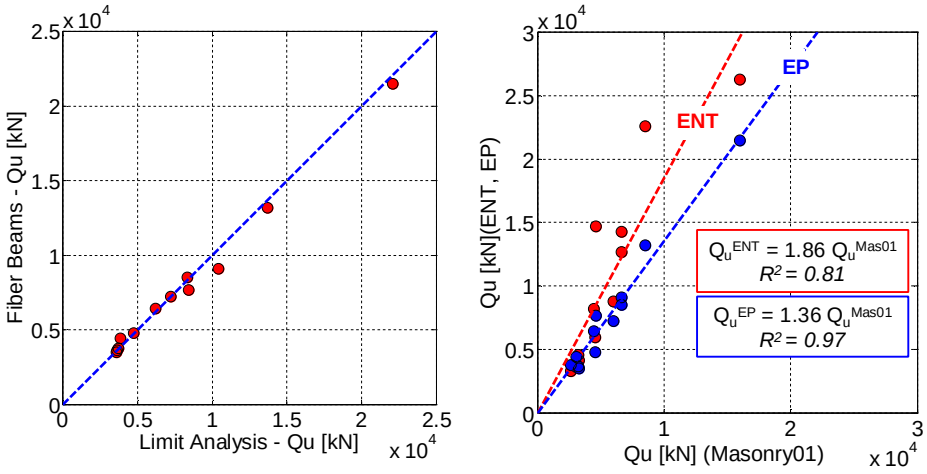

Figure 4.63. Ultimate load (Q_U): comparison between fiber beam model and limit analysis approach with EP constitutive law (left) and comparison between different material relations: ENT, EP, Masonry01 (right).

Single arch bridges and bridges with low piers show high safety factors, as it is shown by the graphs in Figure 4.65 where the dependence of SF on the number of spans and on the pier height is plotted and the failure mode is also indicated. It is seen that when one or more piers are involved in the collapse mechanism, the resulting ultimate load is lower than when the only arch fails and no interactions between arches and piers, nor between adjacent spans, occur. Moreover, SF does not decrease for a number of spans higher than 3, since, at the most, the loaded span and the two adjacent ones are involved in the failure mechanism. The safety factor globally decreases with the increase of the number of spans, with the only exception of one bridge (#12) that has the lowest rise-to-span ratio and very squat piers.

It is noteworthy that the maximum height of the pier is taken herein as the most significant parameter, and not, for example, the average value, since the weakest span is generally the one built on the highest pillars. Concerning this, it should be observed that the empirical rules do not consider any interactions, but the only arch is dimensioned regardless of the eventual presence of piers and, let alone, their height.

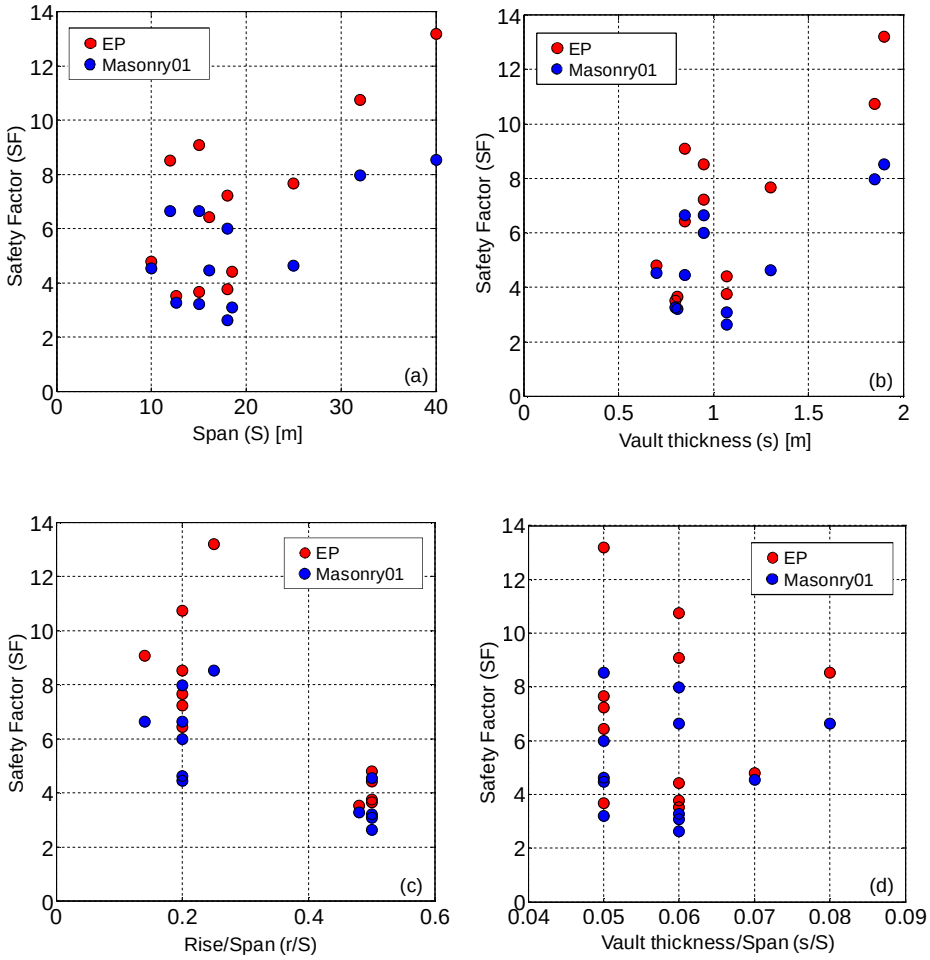

Figure 4.64. Safety factor with EP and Masonry01 constitutive laws: dependence on span (a), vault thickness (b), rise-to-span ratio (c) and thickness-to-span ratio (d).

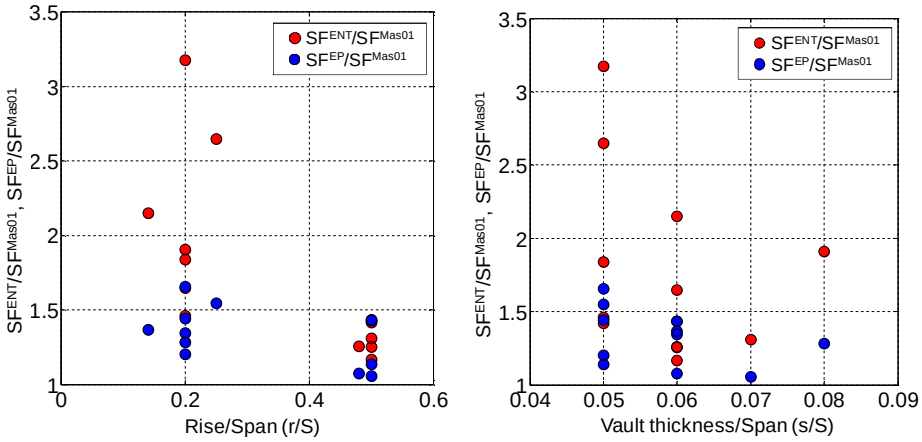

Figure 4.65. Safety factor: comparison Masonry 01 and ENT and EP constitutive laws in dependence on rise-to-span ratio (left) and thickness-to-span ratio (right).

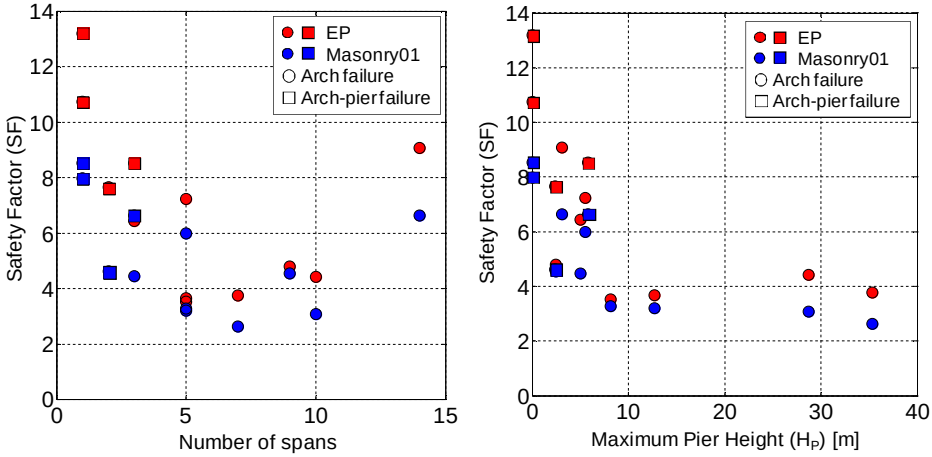

Figure 4.66. Safety factor for EP and Masonry01 constitutive laws and failure modes: dependence on number of spans (left) and maximum pier height (right).

Concluding, it has to be recalled that the proposed modelling strategy yields to an underestimate of the effective load carrying capability, since the effect of spandrels and fill in terms of stiffness and strength is not included.

On the other hand, in the model the abutments are considered as fixed, thus no interaction with the soil is accounted for. This may lead to an overestimate of the maximum load, especially for shallow arch bridges.

Moreover, when the safety of a bridge has to be assessed and interventions have to be planned the effective maintenance state of the construction has to be carefully detected together with the identification of the causes of the observed damages and of the corresponding influence on the structural response (in the static and dynamic fields) that has to be expected.

5. Seismic assessment of masonry bridges

5.1. State-of-the-art

Many of the Countries having a wide heritage of masonry bridges present also a high seismic risk, and the evaluation of the safety level towards earthquakes is hence often needed for these structures. Standard codes and guide-lines of recent issuing (Eurocode 8: CEN-EN 1998, 2005; Linee guida per la valutazione e riduzione del rischio sismico del patrimonio culturale, 2006; Nuove norme tecniche per le costruzioni, 2008; ISO, 2010) pay special attention to the seismic assessment of built constructions, but detailed instructions to perform analyses and estimate the seismic reliability of masonry bridges are still lacking.

On the other hand, the dynamic response of masonry arches is, in great measure, still unexplored. The contributions in literature devoted to this issue in the last years are either addressed to the dynamics of the arch or directly oriented to the seismic assessment of the bridge.

The dynamics of masonry arches has been primarily investigated by making use of the mechanism method (Oppenheim, 1992; Clemente, 1998; De Luca et al., 2004). The first rough estimate of the safety towards earthquakes consists in verifying that the expected peak ground acceleration is not higher than the horizontal load that turns the structure into a mechanism. Such a formulation is suitable for elegant analytical solutions and has been compared with numerical simulations performed by using distinct element models in (DeJong and Ochsendorf, 2006; De Lorenzis et al., 2007a) as well as with experimental results on small scale model arches (DeJong et al., 2008). Besides, a theoretical treatment has newly been proposed in (Sinopoli, 2010). These approaches are usually based on the classical hypotheses that the material has no tensile resistance and infinite compressive strength (Heyman, 1966).

Recently, some studies have been developed with 3-D elasto-plastic (Pelà et al., 2009) or 1-D non-linear finite elements (Resemini and Lagomarsino,

2007) to assess the global seismic safety level within a performance-based approach, coherently with the most advanced regulations.

Tridimensional models do not allow non-linear dynamic (time-step) analyses to be performed, so equivalent static analyses (push-over) are used to evaluate the safety level, and the Capacity Spectrum Method (Freeman et al., 1975; Freeman, 1998), the N2 Method (Fajfar and Gašperšič, 1996) or the Displacement Coefficient Method (FEMA-273, 1997) are applied. However, these methodologies have basically been proposed and calibrated for the design of r.c. and steel buildings and their effective reliability when applied to existing masonry bridges has to be verified.

On the other hand, an approach based on macro-elements has been proposed, through which it is possible to compare the results of non-linear static and dynamic analyses (Resemini, 2003; Resemini and Lagomarsino, 2007). Anyway, the capability of such a modelling approach in representing the effective dynamic behaviour of a masonry bridge has still to be fully proved.

Eventually, some works have been devoted to assess the vulnerability towards local mechanisms, as, for instance, the out-of-plane overturning of the spandrel walls (Rota et al., 2005).

As regards the experimental investigation, some static (Fanning and Boothby, 2001; Fanning et al., 2005) and dynamic tests (Brencich and Sabia, 2007; Mautner and Reiterer, 2007) on full-scale bridges have shown the effects of fill and spandrel walls on the dynamic response, providing the empiric basis for calibrating models with elastic 3-D finite elements (Beconcini et al., 2007); finally, in (Ramos et al., 2007) small scale models are tested in the laboratory to develop a vibration-based damage identification technique.

In the present section, the possibility of using the fiber beam-based modelling approach to simulate the seismic response of masonry bridges and perform seismic assessment is investigated. The accuracy in describing the material properties, combined to the low computational effort required for dynamic analyses, seems to guarantee the balance between the accuracy of the model of the action and that of the structure, both needed in seismic assessment.

First of all, the dynamics of a single arch under constant base acceleration is considered; the failure condition predicted by the fiber beam model is compared with the solution provided by the mechanism method, under the same assumptions on the material behaviour (ENT constitutive model). The effects induced by the variation of the arch geometry are investigated and, finally, numerical simulations are carried out considering different constitutive relations, accounting for a finite compressive strength (EP constitutive model) and a limited ductility (Masonry01 relation), to investigate how the local properties influence the overall dynamic resistance.

Then, the seismic analysis of masonry bridges is faced, starting from the description of the main damages induced by earthquakes and of the limit states to be considered within a seismic assessment. The procedures available at present time for the evaluation of the seismic response of constructions (modal, non-linear static and non-linear dynamic analyses) and for the estimate of their safety level towards earthquakes (push-over based methods) are recalled, underlining the issues needing particular attention when they are applied to masonry bridges.

Ronciglione Viaduct, already analyzed in the previous chapter, is considered as a case study; firstly, its dynamic behaviour in the elastic range is examined by means of a linear 3-D finite element model and its natural frequencies and modal shapes are compared with the results of the fiber beam model to have a further validation confirm. Non-linear push-over and dynamic analyses are then performed and their predictions are compared in terms of resultant base shear and displacement response to assess to what extent, or under what conditions, a static approach ensures an adequate reliability. Finally, some basic concepts of a framework for the performance-based seismic assessment of masonry bridges are outlined.

5.2. Collapse of masonry arches under pulse base acceleration

In this section, a single arch under pulse base acceleration is considered and its failure is evaluated by means of a finite element model built with fiber beams; the results are compared to the ones provided by the mechanism method to check the reliability of the fiber beam approach.

According to the mechanism method assumptions, masonry is considered rigid, with infinite compressive strength and no tensile resistance; moreover, no sliding between voussoirs is allowed. In the collapse configuration the structure is turned into a mechanism resulting from the formation of four hinges, and can be treated as a kinematic chain made of four bars. The solution, derived in paragraph 5.2.2., is based on displacement and velocity analyses on four-bar linkage mechanisms (Erdman and Sandor, 1984), briefly recalled in paragraph 5.2.1., and on basic principles of energetic balance, while the finite element simulations, described in paragraph 5.2.3., consist in non-linear dynamic analyses under rectangular accelerograms.

5.2.1. Displacement and velocity analyses on four-bar linkage mechanisms

A mechanism is a mechanical device that has the purpose of transferring motion and/or force from a source to an output. A linkage consists of links (or bars), generally considered rigid, which are connected by joints to form open or closed chains (or loops). Such kinematic chains, with at least one link fixed, become mechanisms if at least two other links retain mobility, or structures if no mobility remains. A mechanism permits relative motion between its rigid links, a structure does not.

If the motion exhibited by the mechanism is such that all the links move in parallel planes, it is called two-dimensional or plane. Plane rigid body motion consists of rotation about axes perpendicular to the plane of motion and translation.

The four-bar linkage is the simplest closed loop linkage and has three moving links plus one linked link and four pin joints (Figure 5.1). The link that is connected to the power source, or prime mover, is called the input link (AB). The output link connects the moving pivot (C) to ground pivot (D); finally, the coupler or floating link connects the two moving pivots (B and C), thereby coupling the input to the output link.

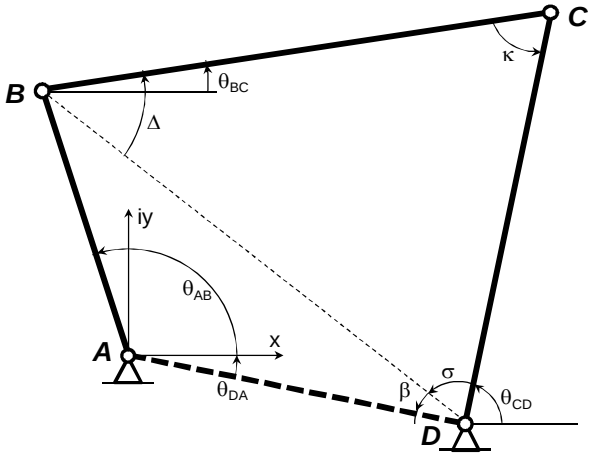

Figure 5.1. The four-bar linkage.

The four-bar linkage is a mechanism with one degree of freedom, then prescribing one position parameter (or Lagrange parameter), like, for example, the angle of the input link, will completely specify the position of the rest of the mechanism, identified by the angles of the other links (which are the dependent parameters of the system).

The length of the four links of the linkage ABCDA are identified by the segments AB, BC, CD and AD, and their angles θ_{AB}, θ_{BC}, θ_{CD} and θ_{DA} are measured counterclockwise from the horizontal; moreover the angle κ is called transmission angle, β is the angle between the link DA and the diagonal BD, and, finally, σ is the angle between CD and BD. Note that the linkage is defined in a complex reference plane (x, iy).

The relations giving these four angles are (5.1−5.4) and can be easily demonstrated by geometric considerations:

$$\cos\kappa(\theta_{AB}) = \frac{CD^2 + BC^2 - AB^2 - DA^2}{2BC \cdot CD} + \frac{AB \cdot DA}{BC \cdot CD}\cos(\theta_{AB} - \theta_{DA}) \quad (5.1)$$

$$\tan\beta(\theta_{AB}) = \frac{AB \cdot \sin(\theta_{AB} - \theta_{DA})}{DA - AB \cdot \cos(\theta_{AB} - \theta_{DA})} \quad (5.2)$$

$$\tan\sigma(\theta_{AB}) = \frac{BC \cdot \sin\kappa(\theta_{AB})}{CD - BC \cdot \cos\kappa(\theta_{AB})} \quad (5.3)$$

$$\tan\Delta(\theta_{AB}) = \frac{CD \cdot \sin\gamma(\theta_{AB})}{BC - CD \cdot \cos\gamma(\theta_{AB})} \quad (5.4)$$

Thus, the dependent angles can be written in terms of the Lagrange parameter θ_{AB}:

$$\theta_{BC}(\theta_{AB}) = \Delta(\theta_{AB}) - \beta(\theta_{AB}) + \theta_{DA} = f_1(\theta_{AB}) \quad (5.5)$$

$$\theta_{CD}(\theta_{AB}) = \pi - \beta(\theta_{AB}) - \sigma(\theta_{AB}) + \theta_{DA} = f_2(\theta_{AB}) \quad (5.6)$$

To obtain the rotational velocities ω_{BC} and ω_{CD}, given ω_{AB}, it is useful to express them in the polar form, in addition to the Cartesian one, starting from the first link AB.

The position of B considered from the origin A is given by the vector $\mathbf{R_{AB}}$, which can be written by the following expression (5.7), then derived with respect to the time to obtain the absolute linear velocity vector of point B ($\mathbf{v_{AB}}$), expressed in polar and Cartesian forms in expressions (5.8) and (5.9), respectively:

$$\mathbf{R_{AB}} = AB\cos\theta_{AB} + i\,AB\sin\theta_{AB} = ABe^{i\theta_{AB}} \quad (5.7)$$

$$\mathbf{v_{AB}} = \frac{\partial \mathbf{R_{AB}}}{\partial t} = \frac{\partial AB\, e^{i\theta_{AB}}}{\partial t} = AB\, e^{i\theta_{AB}} \frac{\partial \theta_{AB}}{\partial t} = i\,\mathbf{R_{AB}}\,\omega_{AB}$$

(polar form) (5.8)

$$\mathbf{v_{AB}} = -\sin\theta_{AB}\ \mathrm{AB}\frac{\partial\theta_{AB}}{\partial t} + \mathrm{i}\mathrm{AB}\cos\theta_{AB}\frac{\partial\theta_{AB}}{\partial t} = \quad \text{(Cartesian form)} \quad (5.9)$$
$$= \mathrm{AB}\,\omega_{AB}\left(\cos\theta_{AB} - \sin\theta_{AB}\right)$$

Note that ω_{AB} is the angular velocity of AB, with respect to the x axis, and is a scalar variable measured positive if counterclockwise.

The relative velocity of point C with respect to point B can be expressed by the difference of their velocities with respect to a third point, such as A:

$$\mathrm{v}_{\mathbf{BC}} = \mathbf{v_{AC}} - \mathbf{v_{AB}} = \frac{\partial \mathbf{R_{AB}}}{\partial t} = \mathrm{i}\,\mathbf{R_{AC}}\,\omega_{AC} - \mathrm{i}\,\mathbf{R_{AB}}\,\omega_{AB} \Rightarrow \quad (5.10)$$
$$\Rightarrow \mathbf{v_{AC}} = \mathrm{v}_{\mathbf{BC}} + \mathbf{v_{AB}} = \mathrm{i}\,\mathbf{R_{BC}}\,\omega_{BC} + \mathrm{i}\,\mathbf{R_{AB}}\,\omega_{AB}$$

Similarly, the velocity of point C can be written also with respect to D:

$$\mathbf{v_{CD}} = \mathrm{i}\,\mathbf{R_{CD}}\,\omega_{CD} \quad (5.11)$$

The rotational velocities of links BC and CD can be finally found by solving this system (made of two scalar equations) and written in terms of the Lagrange parameter of the system and its derivative with respect to time:

$$\mathrm{i}\,\mathbf{R_{AB}}\,\omega_{AB} + \mathrm{i}\,\mathbf{R_{BC}}\,\omega_{BC} = \mathrm{i}\,\mathbf{R_{CD}}\,\omega_{CD} \Rightarrow$$
$$\Rightarrow \begin{cases} \omega_{AB}\mathrm{AB}\cos\theta_{AB} + \omega_{BC}\mathrm{BC}\cos\theta_{BC} - \omega_{CD}\mathrm{CD}\cos\theta_{CD} = 0 \\ \omega_{AB}\mathrm{AB}\sin\theta_{AB} + \omega_{BC}\mathrm{BC}\sin\theta_{BC} - \omega_{CD}\mathrm{CD}\sin\theta_{CD} = 0 \end{cases} \quad (5.12)$$

$$\omega_{BC}\left(\theta_{AB},\omega_{AB}\right) =$$
$$= \frac{\mathrm{AB}\,\mathrm{Cos}\theta_{CD}\sin\theta_{AB} - \mathrm{AB}\cos\theta_{AB}\sin\theta_{CD}}{\mathrm{BC}\left(-\mathrm{Cos}\theta_{BC}\sin\theta_{CD} + \cos\theta_{CD}\sin\theta_{BC}\right)}\omega_{AB} = \tilde{f}_1\left(\theta_{AB},\omega_{AB}\right) \quad (5.13)$$

$$\omega_{CD}\left(\theta_{AB},\omega_{AB}\right) =$$
$$= \frac{-\mathrm{AB}\cos\theta_{BC}\sin\theta_{AB} + \mathrm{AB}\cos\theta_{AB}\sin\theta_{BC}}{\mathrm{CD}\left(\cos\theta_{BC}\sin\theta_{CD} - \cos\theta_{CD}\sin\theta_{BC}\right)}\omega_{AB} = \tilde{f}_2\left(\theta_{AB},\omega_{AB}\right) \quad (5.14)$$

These latter two functions can be written also in the following form:

$$\omega_{BC}\left(\theta_{AB},\omega_{AB}\right) = \tilde{f}_1\left(\theta_{AB},\omega_{AB}\right) = \frac{\partial f_1\left(\theta_{AB}\right)}{\partial\theta_{AB}}\omega_{AB} = \frac{\partial f_1\left(\theta_{AB}\right)}{\partial\theta_{AB}}\dot{\theta}_{AB} \quad (5.15)$$

$$\omega_{CD}\left(\theta_{AB},\omega_{AB}\right) = \tilde{f}_2\left(\theta_{AB},\omega_{AB}\right) = \frac{\partial f_2\left(\theta_{AB}\right)}{\partial\theta_{AB}}\omega_{AB} = \frac{\partial f_2\left(\theta_{AB}\right)}{\partial\theta_{AB}}\dot{\theta}_{AB} \quad (5.16)$$

5.2.2. Solution provided by the mechanism method

In this section, the collapse of a circular arch under impulse base motion is evaluated on the base of energetic balance principles. The structure is considered to be turned into a mechanism characterized by the formation of four plastic hinges (A, B, C and D) and is thereby treated as a four-bar linkage ABCDA (Figure 5.1). Such a mechanism is made by three mobile links (AB, BC and CD) and a fourth fixed one (DA), connecting the two constrained hinges D and A, and has only one degree of freedom. Thus, the deformed configuration, described by the rotations of the links, depends on only one of them, arbitrarily chosen as the Lagrange parameter of the system; in this case $\theta_{AB}=\theta$, that is the rotation of the driver link, is chosen. The rotations θ_{BC} and θ_{CD} and rotational velocities $\dot{\theta}_{BC}$ and $\dot{\theta}_{CD}$ of links BC (coupler) and CD (follower) are written in terms of θ and $\dot{\theta}$ through displacement and velocity analyses, as it is discussed in the previous paragraph. The rotations of the links are represented in Figure 5.2; in the initial configuration they are denoted as $\theta_{AB,0}$, $\theta_{BC,0}$ and $\theta_{CD,0}$; since link DA is fixed, θ_{DA} does not change during motion. Moreover, r_{AB}, r_{BC} and r_{CD} are the distances of the link centres of mass (G_{AB}, G_{BC}, G_{CD}) measured from hinges A, B and D, respectively; ψ_{AB}, ψ_{BC} and ψ_{CD} are their angular offsets measured from the rotations θ_{AB}, θ_{BC} and θ_{CD}. Finally, the masses of the links AB, BC and CD are named m_{AB}, m_{BC} and m_{CD}, respectively.

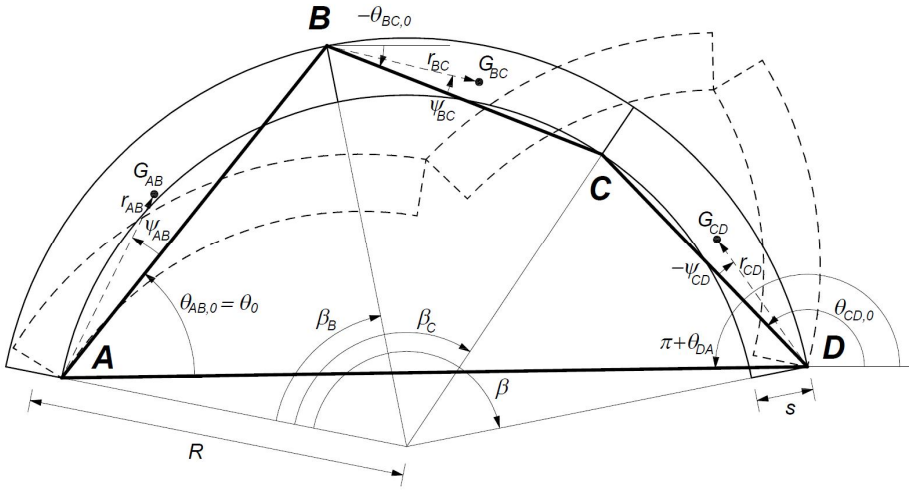

Figure 5.2. The circular arch as a four-bar linkage mechanism in its initial and deformed configurations.

The external force is an acceleration at the base (named a), constant within a time interval τ, and null for $t > \tau$, and the failure condition is

represented by the maximum sustainable acceleration for a given impulse duration.

The problem is solved only for the first half cycle of motion and the positions of the plastic hinges (identified by the angles β_B and β_C) are assumed to be equal to 62.5° and 107.5° respectively, as it is done in (Oppenheim, 1992; De Lorenzis et al., 2007a).

First of all, the potential energy of the system $V(\theta)$ is derived; it depends on θ by means of equation (5.17), being g the acceleration of gravity, and is plotted in Figure 5.3 for an arch having radius R=10m, thickness s=0.15R and angle of embrace β=157.5° (note that during motion θ decreases).

$$V(\theta) = g\left[m_{AB} r_{AB} \sin\left(\theta_{AB} + \psi_{AB}\right) + m_{BC} AB \sin\theta_{AB}\right] + \\ + g\left[m_{BC} r_{BC} \sin\left(\theta_{BC} + \psi_{BC}\right) + m_{CD} r_{CD} \sin\left(\theta_{CD} + \psi_{CD}\right)\right] \quad (5.17)$$

Starting from the initial geometry, in which $\theta=\theta(t=0)=\theta_0$, $V(\theta)$ increases until it reaches a peak value when $\theta=\theta_1$; when $\theta \leq \theta_1$, the self weight spends a negative work, since it tends to bring back the structure to its undeformed configuration. On the contrary, when $\theta > \theta_1$ it contributes to make the deformation diverge and so its work is positive. Thereby, the peak rotation can be defined as a non-recovery condition.

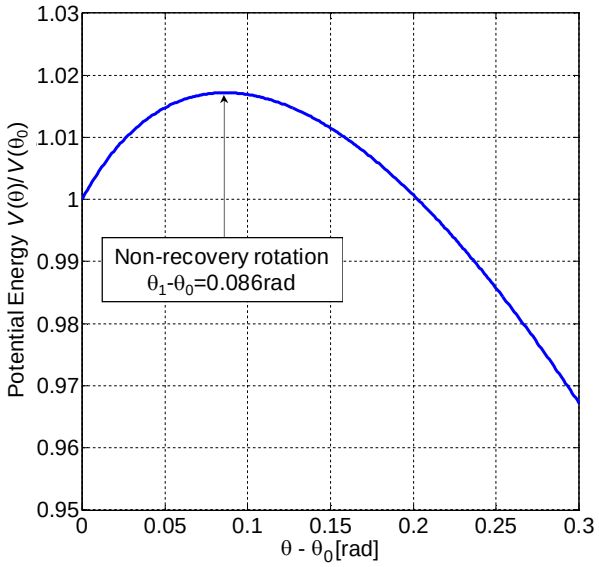

Figure 5.3. Potential energy variation for a circular arch having β=157.5° R=10m and s/R=0.15.

The arch fails as soon as the total work done by the inertial forces in the duration τ (which is a positive work) is equal to the difference in potential

energy between θ_1 and θ_0 (that is the maximum negative work the self-weight can spend). A similar procedure was developed in (Housner, 1963) to identify the overturning of a rigid block under constant base acceleration.

In the present case, the failure condition is expressed by Equation (5.18), in which v_{AB}, v_{BC} and v_{CD} are the horizontal components of the velocities of their centres of mass, stated in expressions (5.19−5.21).

$$\int_0^{\tau} a\left(m_{AB}\, v_{AB}(t) + m_{BC}\, v_{BC}(t) + m_{CD}\, v_{CD}(t)\right) dt = V(\theta_1) - V(\theta_0) \quad (5.18)$$

$$v_{AB}(t) = \frac{\partial}{\partial t}\left[r_{AB}\cos\left(\theta_{AB}(t) + \psi_{AB}\right)\right] = r_{AB}\frac{\partial \theta}{\partial t} \quad (5.19)$$

$$\begin{aligned} v_{BC}(t) &= \frac{\partial}{\partial t}\left[r_{BC}\cos\left(\theta_{BC}(t) + \psi_{BC}\right) + AB\cos\left(\theta_{AB}(t)\right)\right] = \\ &= \frac{\partial \theta}{\partial t}\sqrt{AB^2 + {r_{BC}}^2 + 2\,AB\,r_{BC}\cos\left(\theta - \theta_{BC} - \psi_{BC}\right)}\frac{\partial \theta_{BC}}{\partial \theta} \end{aligned} \quad (5.20)$$

$$v_{CD}(t) = \frac{\partial}{\partial t}\left[r_{CD}\cos\left(\theta_{CD}(t) + \psi_{CD}\right)\right] = r_{CD}\frac{\partial \theta_{CD}}{\partial t} = r_{CD}\frac{\partial \theta_{CD}}{\partial \theta}\frac{\partial \theta}{\partial t} \quad (5.21)$$

To solve (5.18), the equation of motion of the system is needed; it is expressed in terms of the unique Lagrange parameter $\theta(t)$ and can be derived starting from Hamilton's principle:

$$\frac{\partial}{\partial t}\left(\frac{\partial T}{\partial \dot{\theta}}\right) - \frac{\partial T}{\partial \theta} + \frac{\partial V}{\partial \theta} = Q \quad (5.22)$$

where $V(\theta)$ is the potential energy, $T(\theta, \dot{\theta})$ is the kinetic energy and $Q(\theta)$ is the forcing function (Oppenheim, 1992). Since the four-bar linkage has one degree of freedom, Hamilton's principle depends on the unique Lagrange parameter of the system θ.

The potential energy T is stated by expressions (5.23), in which I_{AB}, I_{BC} and I_{CD} are the centroidal moments of inertia of the links:

$$T = \frac{1}{2}\left[m_{AB}\left(r_{AB}\dot{\theta}_{AB}\right)^2 + I_{AB}\dot{\theta}_{AB}{}^2 \right] + \\ + \frac{1}{2} m_{BC}\left[\left(AB\dot{\theta}_{AB}\right)^2 + 2ABr_{BC}\cos\left(\theta_{AB} - \theta_{BC} - \psi_{BC}\right)\dot{\theta}_{AB}\dot{\theta}_{BC} + \left(r_{BC}\dot{\theta}_{BC}\right)^2 \right] + \\ + \frac{1}{2} I_{BC}\dot{\theta}_{BC}{}^2 + \frac{1}{2}\left[m_{CD}\left(r_{CD}\dot{\theta}_{CD}\right)^2 + I_{CD}\dot{\theta}_{CD}{}^2 \right] \tag{5.23}$$

The forcing function Q is a linear function of the constant acceleration a, given by (5.24):

$$Q = -a \cdot m_{AB}\frac{\partial}{\partial\theta_{AB}} r_{AB}\cos\left(\theta_{AB} + \psi_{AB}\right) - \\ - a \cdot m_{BC}\frac{\partial}{\partial\theta_{AB}}\left[r_{BC}\cos\left(\theta_{BC} + \psi_{BC}\right) + AB\cos\theta_{AB} \right] - \\ - a \cdot m_{CD}\frac{\partial}{\partial\theta_{AB}} r_{CD}\cos\left(\theta_{CD} + \psi_{CD}\right) \tag{5.24}$$

All the terms of Hamilton's principle (5.22) can be expressed in terms of θ(t) and therefore the equation of motion can be written as:

$$M(\theta)\ddot{\theta} + L(\theta)\dot{\theta}^2 + F(\theta)g = P(\theta)a \tag{5.25}$$

Equation (5.25) expresses the equality between the works associated to kinetic and potential energy (on the left side) and to the external load (on the right side) and contains four coefficients: M(θ), L(θ), F(θ) and P(θ). They depend on the geometry of the system and are strongly non-linear in θ; their expressions are reported in (5.26−5.29):

$$M(\theta) = I_{AB} + AB^2 m_{BC} + m_{AB} r_{AB}{}^2 + \\ + 2AB\, m_{BC}\, r_{BC}\cos\left(\psi_{BC} + \theta_{BC} - \theta\right)\frac{\partial\theta_{BC}}{\partial\theta} + \\ + \left(I_{BC} + m_{BC} r_{BC}{}^2\right)\left(\frac{\partial\theta_{BC}}{\partial\theta}\right)^2 + \left(I_{CD} + m_{CD}\, r_{CD}{}^2\right)\left(\frac{\partial\theta_{CD}}{\partial\theta}\right)^2 \tag{5.26}$$

$$L(\theta) = -AB\, m_{BC}\, r_{BC} \sin(\psi_{BC} + \theta_{BC} - \theta)\left(\frac{\partial\theta_{BC}}{\partial\theta} - 1\right)\frac{\partial\theta_{BC}}{\partial\theta} + \\ + \left(AB\, m_{BC}\, r_{BC} \cos(\psi_{BC} + \theta_{BC} - \theta) + \left(I_{BC} + m_{BC}\, r_{BC}^{\,2}\right)\frac{\partial\theta_{BC}}{\partial\theta}\right)\frac{\partial^2\theta_{BC}}{\partial\theta^2} + \\ + \left(I_{CD} + m_{CD}\, r_{CD}^{\,2}\right)\frac{\partial\theta_{CD}}{\partial\theta}\frac{\partial^2\theta_{CD}}{\partial\theta^2} \tag{5.27}$$

$$F(\theta) = m_{AB} r_{AB} \cos(\psi_{AB} + \theta) + \\ + m_{BC}\left(AB\cos\theta + r_{BC}\cos(\psi_{BC} + \theta_{BC})\frac{\partial\theta_{BC}}{\partial\theta}\right) + \\ + m_{CD} r_{CD} \cos(\psi_{CD} + \theta_{CD})\frac{\partial\theta_{CD}}{\partial\theta} \tag{5.28}$$

$$P(\theta) = AB\, m_{BC} \sin\theta + m_{AB} r_{AB} \sin(\psi_{AB} + \theta) + \\ + m_{BC} r_{BC} \sin(\psi_{BC} + \theta_{BC})\frac{\partial\theta_{BC}}{\partial\theta} + \\ + m_{CD} r_{CD} \sin(\psi_{CD} + \theta_{CD})\frac{\partial\theta_{CD}}{\partial\theta} \tag{5.29}$$

The expressions of the four coefficients can be simplified by writing the geometrical dimensions in terms of the radius R and of the mass density γ, and then dividing by γR^2; thus, the equation of motion does not depend on the mass density. Moreover, since M and L are proportional to R^3, while F and P are proportional to R^2, in the resulting equation of motion R multiplies the terms in $\ddot{\theta}$ and $\dot{\theta}$ and not the other ones; thereby, a size effect results to be expected in the dynamic response of the arch but not in the static one.

To determine the expression of $\theta(t)$, an initial state of rest ($\dot{\theta} = \ddot{\theta} = 0$) is imposed and instantaneous (constant) values of the coefficients are taken: $M_0 = M(\theta_0)/\gamma R^2$, $L_0 = L(\theta_0)/\gamma R^2$, $F_0 = F(\theta_0)/\gamma R^2$ and $P_0 = P(\theta_0)/\gamma R^2$. The latter assumption leads to a tangent approximation of the response inducing an approximation that is licit in the small rotations field. The equation of motion is hence recast as:

$$M_0\ddot{\theta} + L_0\,\dot{\theta}^2 + F_0\, g = P_0\, a \tag{5.30}$$

(5.30) is solved and the expression of $\theta(t)$ is found:

$$\theta(t) = \frac{M_0}{L_0} \ln\left(\cos\left(\frac{\sqrt{L_0(F_0\, g - P_0\, a)}}{M_0} t\right)\right) \tag{5.31}$$

The failure condition can now be determined by substituting in (5.18) the expression of θ(t) given by (5.31). Since no analytical (closed-form) solution of the integral in (5.18) can be found, a numerical integration is made. The solution for an arch having an angle of embrace β=157.5°, radius R=10m and slenderness ratio s/R=0.15 is plotted in Figure 5.4.

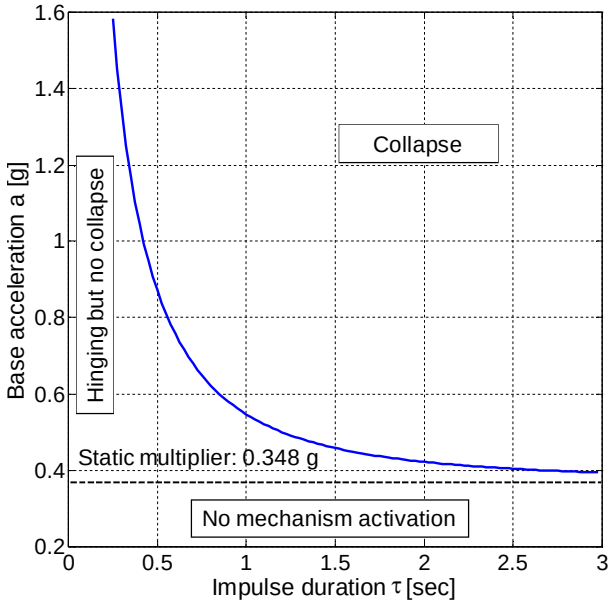

Figure 5.4. Failure domain under impulse base motion for a circular arch having β=157.5° R=10m and s/R=0.15.

It is seen that for short impulse durations high accelerations are needed to induce the structural collapse, while for $\tau \to \infty$ the curve asymptotically tends to a limit value coinciding with the static multiplier. The latter can be easily obtained as the ratio between the virtual works of horizontal and vertical loads, which is equal to F_0/P_0 as stated in Equation (5.30) if dynamic effects are neglected.

Three domains can be identified in the graph as it is pointed out in (Clemente, 1998): if the ground motion amplitude is lower than the limit value the horizontal acceleration is not even sufficient to turn the arch into a mechanism as no hinging occurs; on the contrary, when it is higher than the limit value the onset of motion takes place. If the point (τ, a) is below the failure curve it represents an impulse which does not cause the structural

collapse, i.e. there is hinging but the arch returns to its initial geometry; finally, if the couple (τ, a) identifies a point above the curve the corresponding impulse makes the arch fail.

5.2.3. Numerical simulation through fiber beams

Once the arch is modelled by using beam elements with fiber cross-section, the investigation of its failure condition under impulse base motion is made by repeated non-linear dynamic analyses carried out for several impulse durations so as to find as many collapse acceleration values. Aiming at reproducing the same assumptions of the mechanism method, no damping is considered and the material assigned to the fibers has no tensile resistance and infinite compressive strength; finally, the stiffness is high enough that the it can be considered as infinite. No plastic hinges are defined a priori as they are determined by the model. The result is found to be independent on the number of beam elements or of fibers in their cross section, provided that an adequate discretization is ensured that does not affect the geometry of the arch (inadequate number of elements) or the stress distribution within the cross-section (inadequate number of fibers).

The result of the FE simulation is represented in Figure 5.5 for an arch having mass density equal to 2 ton/m^3, R=10m, s=0.15R and β=157.5°, under an impulse with amplitude ranging from 0.73 to 0.77g and duration τ=0.60sec. The collapse is assumed to occur when the rotation of the driver link AB (Figure 5.5b) or the horizontal displacement of the crown (Figure 5.5d) diverges, i.e. does not go back to zero after the peak and so no equilibrium solution can be found any more. The failure configuration is characterized by the activation of a four-hinge mechanism (Figure 5.5a) and is correctly predicted; the positions of the hinge sections are easily identified by the peaks in the curvature diagram (Figure 5.5c), where a slight spreading is due to the continuum nature of the modelling approach. Finally, the stress field in sections A, B, C and D is plotted in Figure 5.6, pointing out the high level of partialization of the hinges where the load resultant is very close to the section edge, at the arch intrados and extrados alternatively.

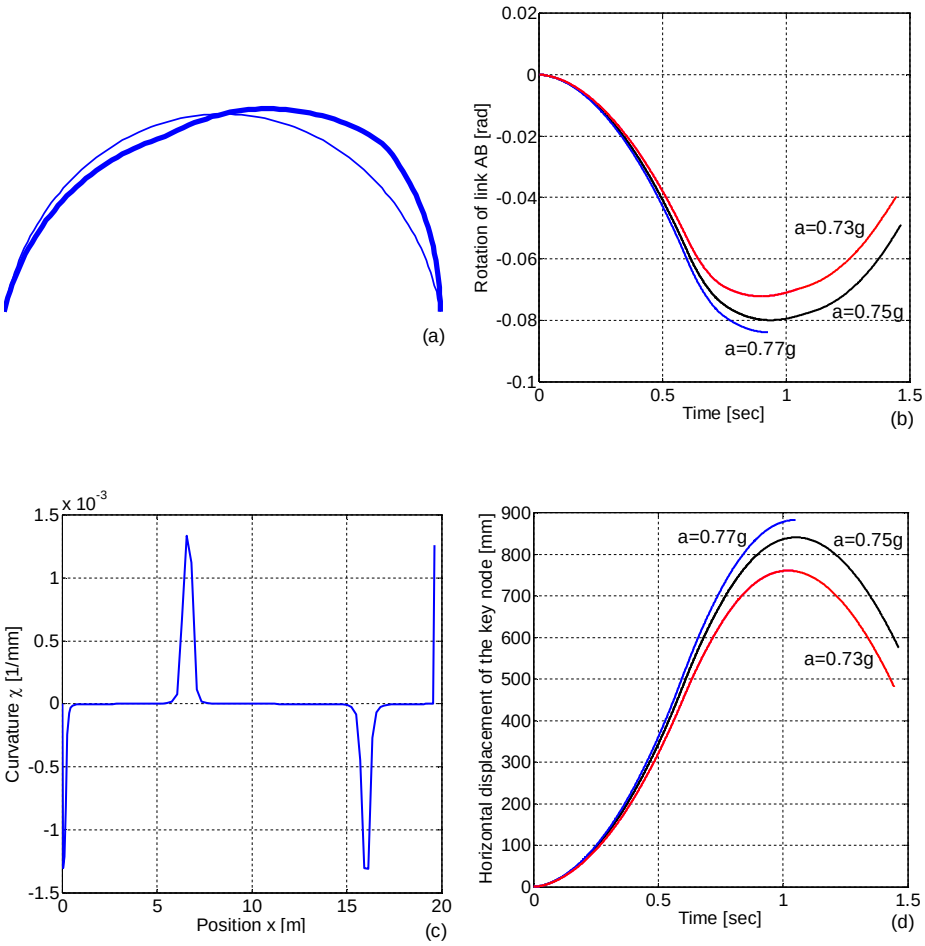

Figure 5.5. Fiber beam model results for an arch having R=10m, s/R=0.15, β=157.5° under impulse base motion with τ=0.60 sec: collapse configuration (a), driver link rotation (b) and horizontal displacement of the key node (d) for different values of base acceleration, curvature of the beam elements identifying the position of the plastic hinges (c).
In subplots a and c the impulse amplitude is a=0.75g.

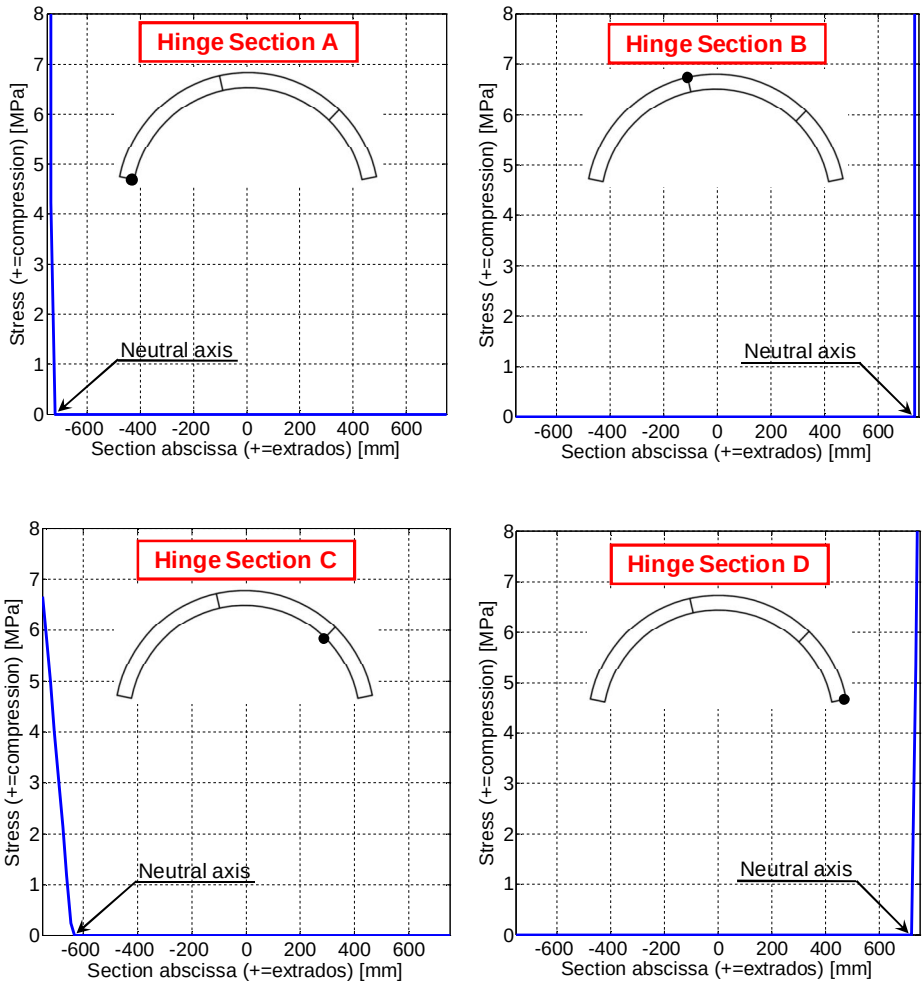

Figure 5.6. Fiber beam model results for an arch having R=10m, s/R=0.15, β=157.5° under impulse base motion with a=0.75g and τ=0.60 sec: stress field in the hinge sections.

The comparison between mechanical model and fiber beam approach is carried out for arches having constant slenderness s/R=0.15 and radius ranging from 5m to 20m (Figure 5.7) and for arches having R=10m and thickness (s) ranging from 0.12R to 0.2R (Figure 5.8). The failure condition provided by the mechanism method is plotted with solid lines, while the results of FE simulations are represented by the marks.

A very good agreement is found for all the considered configurations, even if, for very short impulses (τ<0.4sec) it can be difficult to find stable numerical solutions. Regarding the sensitivity analyses, the curves

corresponding to different values of R show an increase of resistance towards short impulses associated to the increase in the size (Figure 5.7); such a difference becomes smaller for long impulses and asymptotically tends to zero since all the arches have identical static multipliers. In fact, the static solution does not depend on the size while the dynamic one does, as discussed before about the equation of motion of the system (5.30).

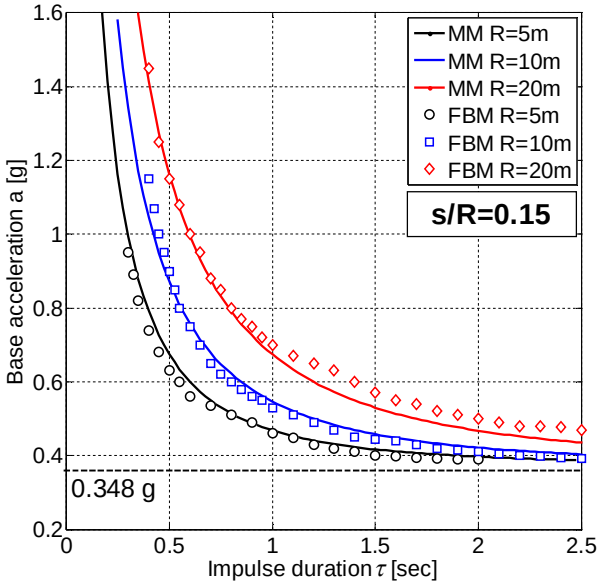

Figure 5.7. Failure domain under impulse base motion different size (R) for arches having s/R=0.15and β=157.5°: comparison between mechanism method (MM) and fiber beam model (FBM).

The variation of the aspect ratio s/R results in the variation of the arch capacity towards both dynamic actions and static loads: as the thickness increases, the resistance becomes higher for both short and long impulses, and the limit value grows, too (Figure 5.8). The positions of the plastic hinges and the non-recovery rotations depends on s/R, and not on R: a higher slenderness results in a decrease of angles β_B and β_C (Figure 5.9) indicating that the plastic hinges move towards to first one (point A), as it is found also in (Clemente, 1998). Lower s/R ratios are related to higher non-recovery rotations, since the potential energy is proportional to the link masses, as it is also shown by the curves plotted in Figure 5.10 representing the variation in potential energy $V(\theta)$ for different slenderness values. Finally, it is noteworthy that $\theta_0-\theta_1$ is a small angle for the investigated values of s/R, which are comparable, for typical span dimensions, to the section thickness

suggested in the empirical formulations proposed in classical design treatises and adopted in masonry arch bridges.

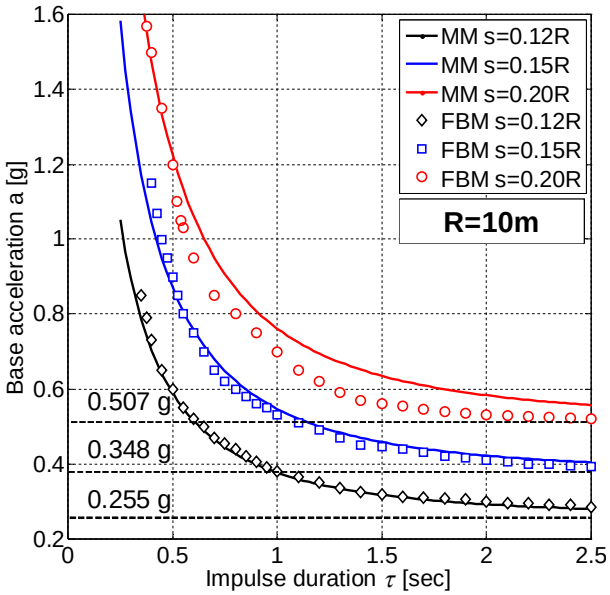

Figure 5.8. Failure domain under impulse base motion different aspect ratios s/R ratios for arches having R=10m and β=157.5°: comparison between mechanism method (MM) and fiber beam model (FBM).

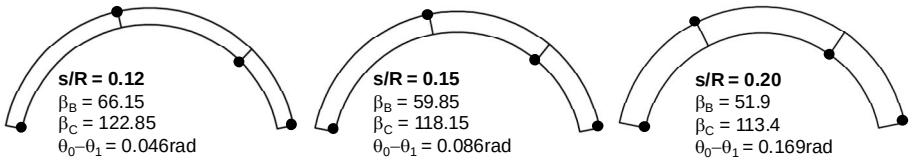

Figure 5.9. Position of the plastic hinges and non-recovery rotations for different s/R ratios.

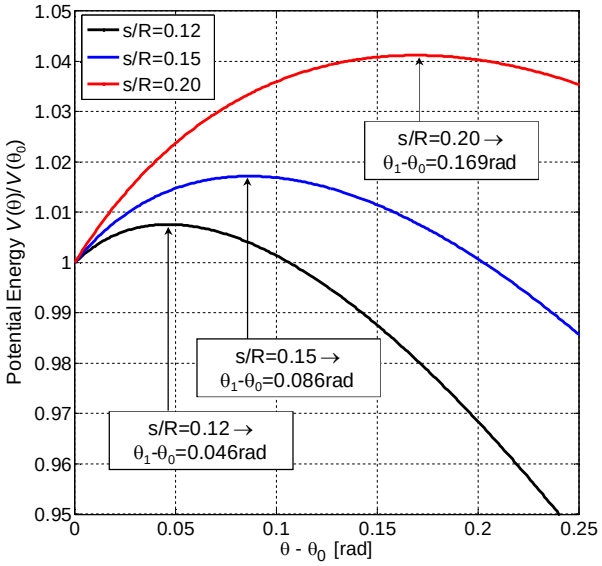

Figure 5.10. Normalized potential energy for arches having β=157.5° and different aspect ratios s/R.

5.2.4. Effect of material properties

Thanks to the agreement found between mechanism method and fiber beam approach, the latter model is used to investigate the effect of the material properties on the dynamic behaviour of the arch under acceleration pulse at the base. The same circular arch as before (R=10m, s/R=0.15, β=157.5°) is analyzed considering elasto-plastic (EP) and Masonry01 constitutive models in order to investigate how the use of a more accurate law for the material can affect the arch capability to sustain dynamic actions. The values of the parameters of the constitutive relations are the same ones assigned in the previous chapter of the Thesis for static analyses (Table 3.3).

When the assumptions of infinite strength and unlimited ductility (Heyman, 1966) are removed, passing from ENT to EP material, and from EP to Masonry01, a slight decrease of the arch resistance towards impulse base acceleration is found (Figure 5.11): the limit value passes from 0.348g to 0.336g and 0.325g. Therefore, the resistance to horizontal static loads is not strongly influenced by the material properties and the classical assumption of infinite strength appears reliable (note that the referential arch is a shallow arch and that higher differences have to be expected for deep arches).

However, as it is shown in Figure 5.11, the asymptotic value giving the resistance towards static loads is reached more rapidly if the effective

material behaviour is taken into account than if the elasto-plastic assumption is made or an infinitely resistant material is assumed. Thus, the capacity to pulse base acceleration turns to be heavily dependent on the material properties in the range of short-to-medium pulse durations. For example, for τ=1sec the base acceleration making the arch fail is equal to 0.53g, 0.44g and 0.375g for the three constitutive laws: in this case, neglecting the effective material properties provides and overestimate of the collapse pulse acceleration of about 155% and 375% for EP and ENT constitutive laws, respectively.

It appears from these results that, as for the assessment of travelling load-carrying capability, also in the case of the resistance to horizontal acceleration pulses the material properties play a non-negligible role and failing to accounting for the finite value of material strength and for the limited ductility in compression may lead to a significant overestimate of the effective arch capacity.

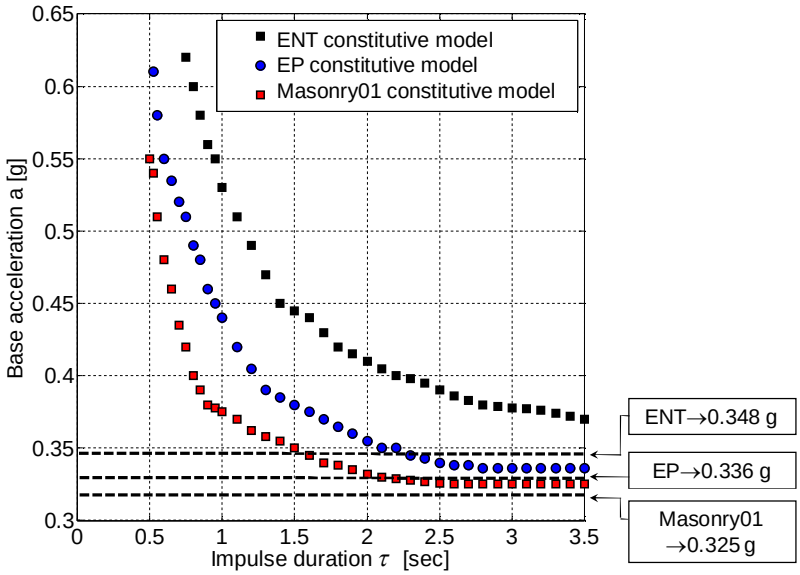

Figure 5.11. Failure domain under impulse base motion of and arch with R=10m, s/R=0.15, β=157.5°, considering different materials: Elastic-no tensile resistant (ENT), Elastic perfectly plastic (EP), Masonry01.

5.3. Behaviour of masonry arches under earthquake motion

Aiming at investigating the seismic response of a masonry arch under earthquake motion, modal analysis, push-over analysis under different load distribution and non-linear dynamic (step-integration) analysis are performed. The structure is arch considered in previous section, having radius R=10m, thickness s/R=0.15 and angle of embrace β=157.5°. The more refined constitutive relation for masonry (Masonry01 model) is adopted.

Modal analysis provides the modal frequencies, the participating factors and masses and the eigenvectors that might be used in push-over analysis. The first ten modal shapes are represented in Figure 5.12, and their periods and frequencies are collected in Table 5.1 together with the modal participating factors and masses (referred to horizontal and vertical directions). Modes #1, #4 and #5, which are clearly un-symmetric, display significant participating masses in horizontal direction, modes #2 and #7 give a very low contribution; on the contrary, the participating factors of all these modes in vertical direction are null. Modes #2, #3, #6, #8 and #9 show a symmetric shape, and their contribution is only in vertical direction; in particular, mode #3 displays the highest participating mass.

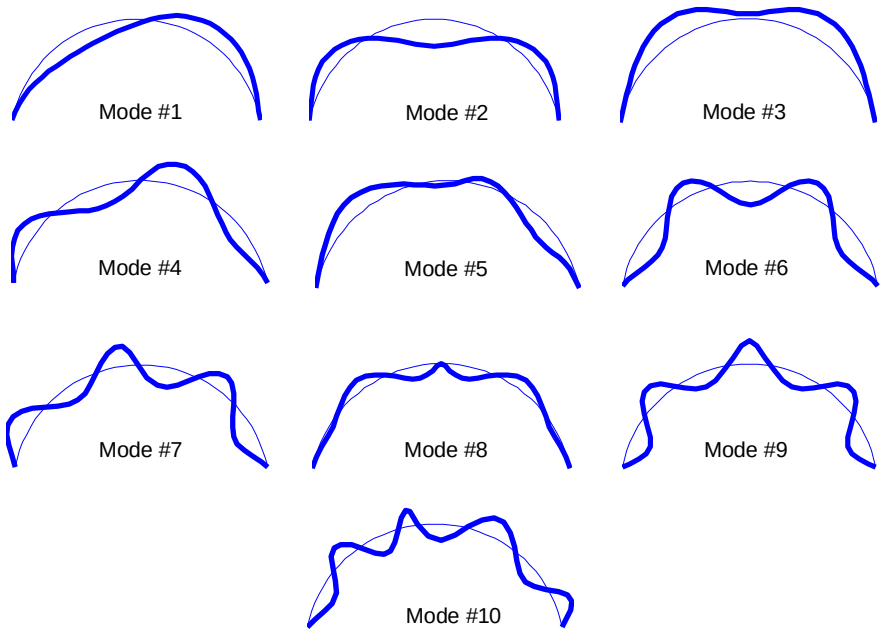

Figure 5.12. Modal analysis: first ten modal shapes.

Non-linear cyclic static analyses are then performed; forces are applied within an incremental displacement-controlled quasi-static analysis, after having applied the entire self-weight. Three distributions are used (Figure 5.13):

#1: Horizontal loads proportional to masses;

#2: Horizontal loads proportional to the product of masses and displacements of the fundamental mode (mode #1);

#3: Horizontal and vertical loads, proportional to the product of masses and displacements of the first mode. This last distribution accounts for the fact that the first eigenvector contains non-null displacements in both vertical and horizontal directions, even if the participating mass in the former direction is zero (the algebraic sum of the vertical displacements of the nodes results null).

Mode	Period T [sec]	Frequency *f* [Hz]	Horizontal direction		Vertical direction	
			Participating factor Γ	Participating mass *m*	Participating factor Γ	Participating mass *m*
1	0.44	2.25	0.26	40.4%	0.00	0.00
2	0.23	4.29	0.00	0.0%	0.12	8.5%
3	0.13	7.94	0.00	0.0%	0.25	36.3%
4	0.12	8.40	0.20	22.3%	0.00	0.00
5	0.08	13.16	0.12	8.2%	0.00	0.00
6	0.07	13.70	0.00	0.0%	0.08	3.9%
7	0.05	18.87	0.06	2.3%	0.00	0.00
8	0.05	21.28	0.00	0.0%	0.14	11.4%
9	0.04	25.64	0.00	0.0%	0.08	3.5%
10	0.03	31.25	0.07	3.1%	0.00	0.00

Table 5.1. Modal analysis: periods and frequencies, participating factors and masses of the first ten modes.

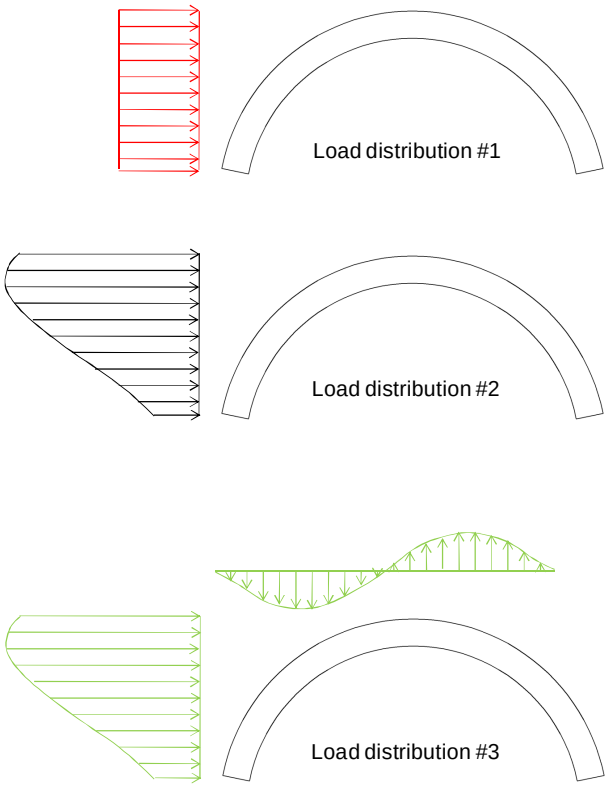

Figure 5.13. Load distributions for push-over analyses.

The capacity curves resulting from push-over analyses are represented in Figure 5.14, in which the horizontal displacement of the key node (d_k) and the resultant base shear normalized by the arch self weight (V_b/W) are on the x-axis and on the y-axis, respectively. Since the structure is symmetric, the capacity curves are symmetric, too. Moreover, it is seen that, passing from distribution #1 to #2 and #3, a reduction of both strength and stiffness is found: the ultimate load is in the order of 33%, 28% and 21% of the self-weight, respectively. The cyclic loading leads to very narrow cycles in the response, indicating a low hysteretic dissipation. Such a result is not so different from the response of a rigid block in rocking motion, pointing out the similitude between masonry arches and rigid body systems. Finally, it has to be said that numerical instabilities arise at the very beginning of the softening branch of the response curves.

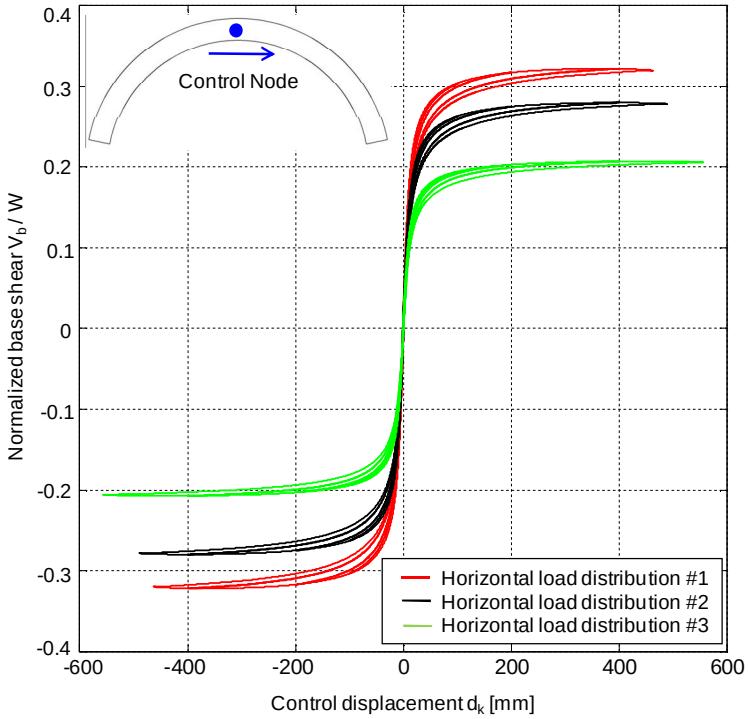

Figure 5.14. Push-over curves for different load distributions.

Non-linear dynamic analyses are performed under two natural accelerograms (Figure 5.15), with growing scaling factor (SF) ranging from 0.2 to 1.6. Dissipative phenomena are represented by means of a Rayleigh viscous damping term, whose parameters are chosen so as to achieve an equivalent damping ratio (ξ) equal to 2% at the first and fourth modal frequencies (f_1=2.25Hz and f_4=8.40Hz), which are the most significant in terms of participating mass in horizontal direction. The chosen damping ratio ξ=2% seems reasonable by looking at the cyclic capacity curves and considering that no fill soil nor spandrel walls are present in the considered structure. Analogously to push-over analyses, the horizontal displacement of the crown (d_k) and the resultant base shear V_b are recorded.

The results (shown in Figures 5.16 and 5.17 for the two input signals) are represented in terms of maximum response under the various scaling factors and whole response curve of two simulations (having SF equal to 0.8 and 1.2). The maximum response is identified by maximum displacement of the control node (the key) and corresponding (same instant) base shear, normalized by the arch self-weight W.

It is seen that both the response curve of a single simulation and the points representing the application of a record with increasing scaling factor result to be close to the capacity curve of the push-over analysis, provided that

distribution #3 is adopted. Dynamic effects, probably due to the interaction between modes, result in a slight irregular response. As regards the maximum conditions, under signal #1 the shear of the last point (SF=1.6) is a little lower than the previous one (SF=1.4), while under signal #2 the points identifying simulations with SF=0.8, SF=1.0 and SF=1.2 almost lie on the same horizontal line, representing very close values of the base shear. Concerning the whole response curves, their shape seems to indicate that the global response results from a sort of superimposing of different modes.

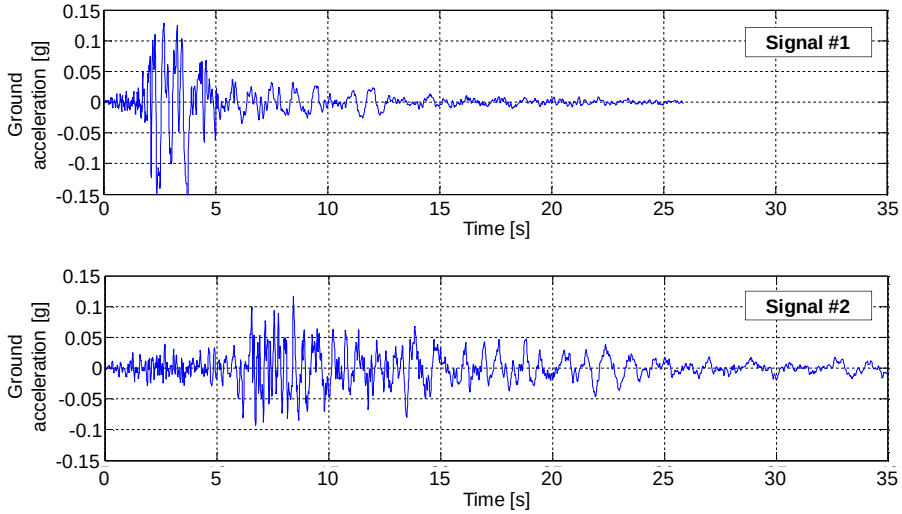

Figure 5.15. Signals used for non-linear dynamic analyses on the single masonry arch.

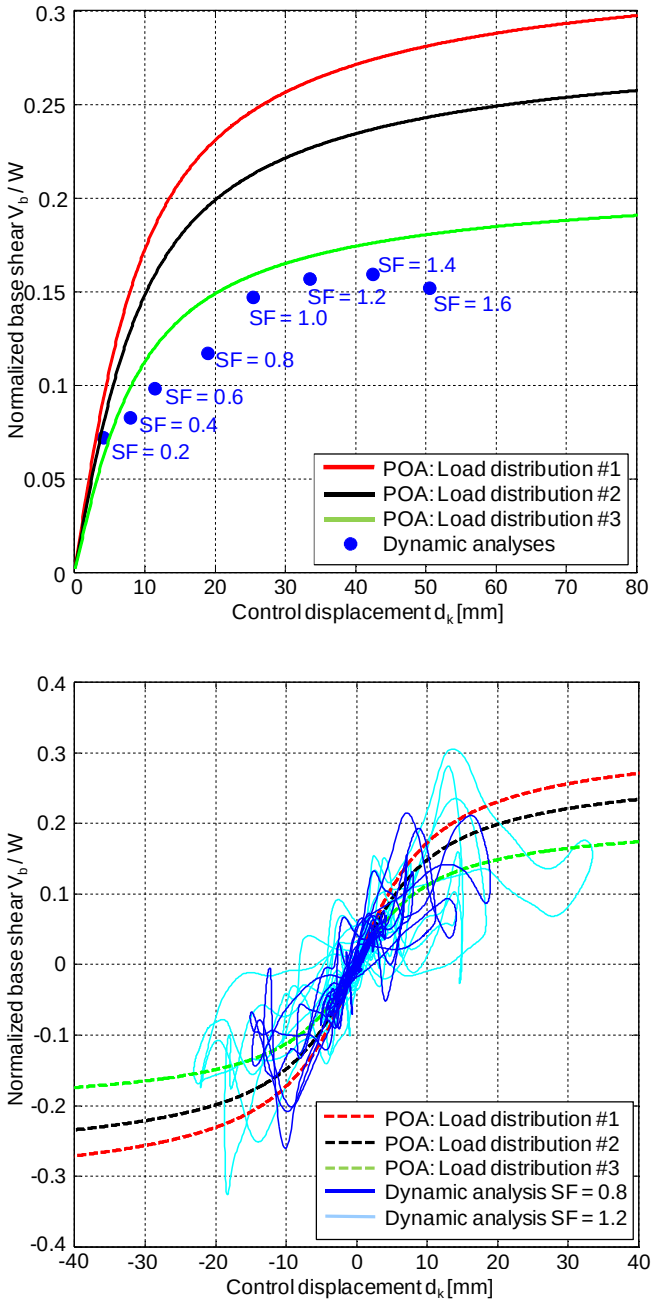

Figure 5.16. Comparison between push-over and non-linear dynamic analyses under accelerogram #1: response curves of two dynamic simulations with different scaling factors (up) and maximum conditions for all the adopted scaling factors (down).

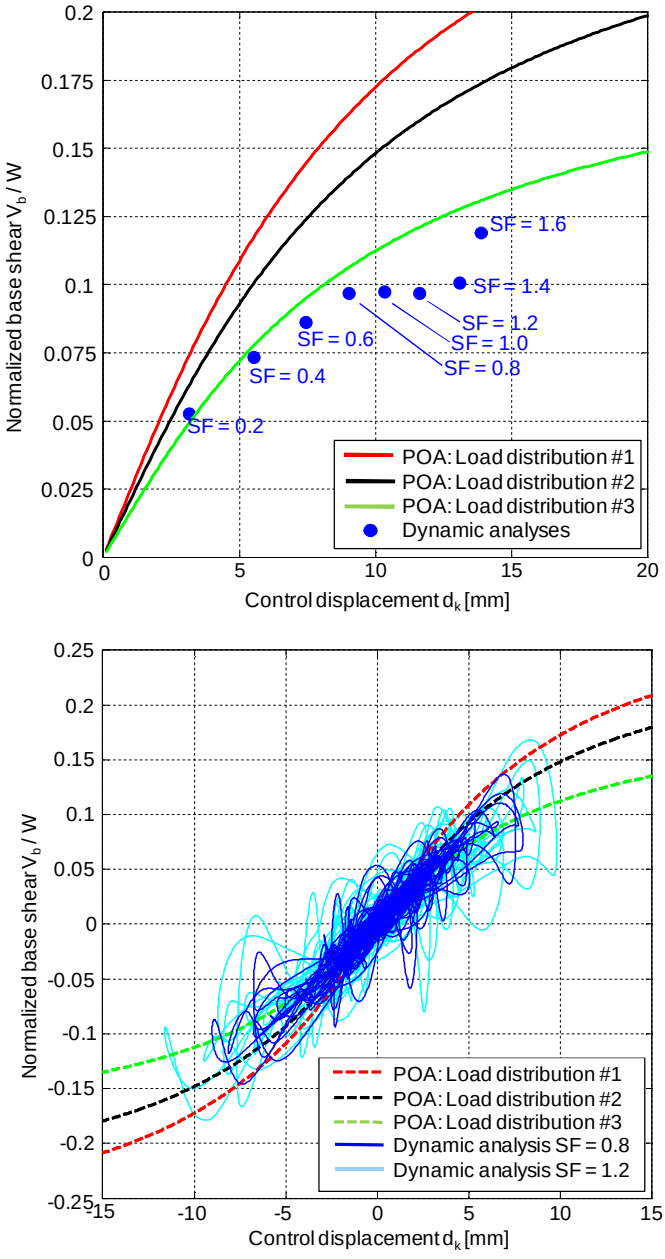

Figure 5.17. Comparison between push-over and non-linear dynamic analyses under accelerogram #2: response curves of two dynamic simulations with different scaling factors (up) and maximum conditions for all the adopted scaling factors (down).

The sensitivity to the radius R and to the aspect (span-to-radius) ratio s/R is investigated. Non-linear dynamic analyses are carried out under signals #1 and #2 and repeated for different geometries. In particular, the radius ranges from 1m to 15m and the aspect ratio ranges from 0.08 to 0.2, which are considered the interesting intervals from an engineering perspective.

For each simulation, a preliminary modal analysis is also performed, so that the equivalent damping ratio is always equal to 2% for the first and fourth frequencies, which depend, of course, on the geometry. An increase in the radius results in a linearly proportional increase in the period, while no variations in terms of participating mass is found. Diversely, when s/R changes, both the period and the participating mass change, too, even if the former decreases much more rapidly than the latter; slender arches display longer periods and slightly higher participating masses than squat ones.

The results of the sensitivity analyses under earthquake motion are plotted in Figures 5.18 and 5.19: an increase of the maximum displacement (normalized by R) is found to be substantially proportional to the arch radius, while a decrease of the maximum displacement results from the increase of s/R, indicating that large (being equal the aspect ratio) and slender arches display higher displacements than squat ones.

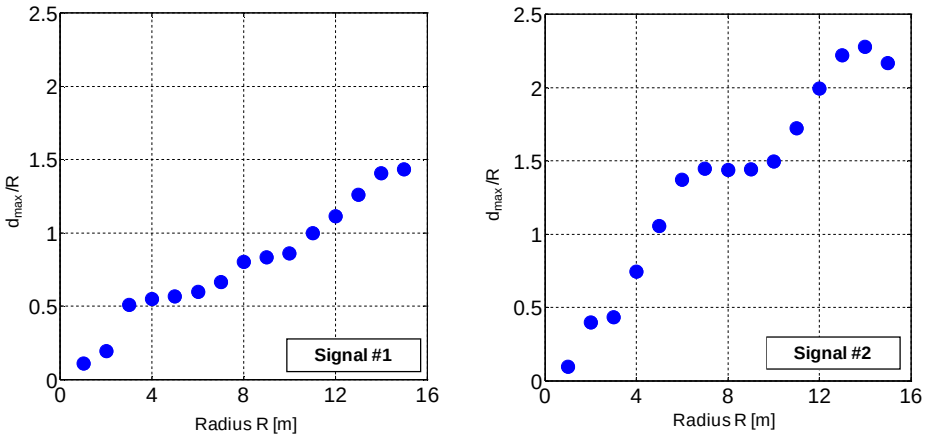

Figure 5.18. Maximum displacement in non-linear dynamic analyses: sensitivity to the radius R.

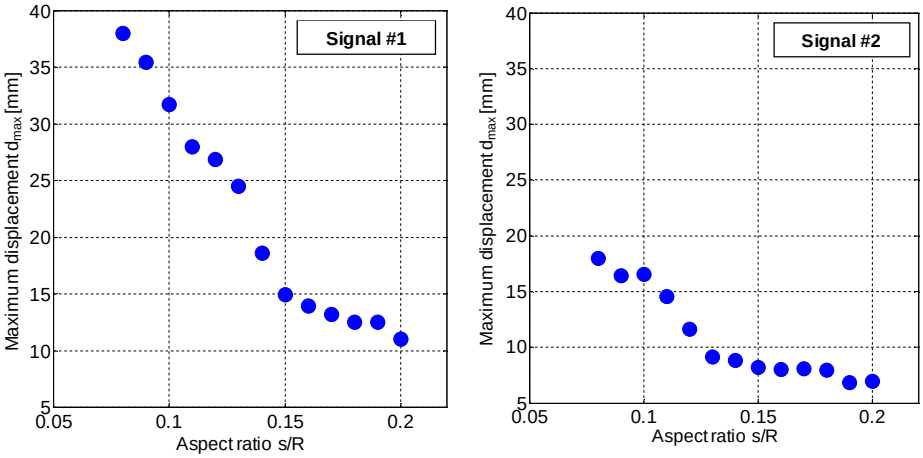

Figure 5.19. Maximum displacement in non-linear dynamic analyses: sensitivity to the aspect (span-to-radius) ratio s/R.

5.4. Seismic analysis of masonry bridges

5.4.1. Damages induced by seismic events

Very few information are available on damages or collapses induced by earthquakes on masonry bridges. From the one hand, this can be attributed to the higher attention that is paid to buildings and built-up-areas rather than on bridges; on the other hand, it may result from the low vulnerability of this structural typology towards seismic actions.

Damages caused by seismic events can be classified depending on the kind of mechanism they are associated to (the portion of the construction that is involved), or on their severity (the importance of their consequences) (Resemini, 2003; Rota, 2004; Gambarotta et al., 2006).

If the mechanism typology is considered, two main categories of damage can be defined:

– *Damages associated to local mechanisms*
  Rotation or overturning of the spandrel walls (typically occurring on small bridges made of a single, often shallow, arch or having very squat piers); moderate shear damage of piers.

– *Damages associated to global mechanisms*
  Collapse of one or more vaults, overturning of the bridge in transversal direction, flexure or shear collapse of the piers. Such damages have been observed on multi-span bridges and viaducts, having tall piers and medium to long span (>12m) deep vaults, and are typically generated by severe earthquakes.

Looking at the consequences produced by the damage state, the following distinctions can be made:

– *Damages that influence, but not compromise, the bridge serviceability*
  They are associated to local mechanisms and consist in limited but non-reversible deformations; the permanent out-of-plane rotation of the spandrel walls (in the order of 5÷10cm) has been surveyed on some structures, reducing the confining effect on the fill soil and, therefore, the load-carrying capability of the bridge; in this case, longitudinal cracks on the deck have been observed.
  Besides, on rail bridges, a residual vertical deflection of the track (induced by the deformation of the fill soil) could compromise the transitability.

– *Damages that compromise the bridge serviceability*
  They are associated to both local and global mechanisms; the former case includes slight cracks on the piers, mainly due to high compressive stresses or foundation settlements. Several examples are collected in technical literature showing the out-of-plane overturning of the spandrel walls: the collapse can involve the only wall or its external leaf, the wall and the external cover of the arch, or, in the most severe conditions, the wall and the fill soil, especially when made of loose material.
  Global mechanisms in longitudinal plane may induce a decompression of the arch and the falling of some voussoirs; the main causes are: non-synchronous ground motion at the base of the piers, large out-of-phase displacements of high slender piers, and, finally, dynamic effects on the arch. Such a disarrangement is favored by the presence of an extremely poor masonry with weak mortar; anyway, it has mainly surveyed on the only lateral stone cover of the vaults.
  Typically, these damages can be easily repaired and the serviceability restored.

– *Damages that induce the bridge collapse*
  They are extremely rare; very few case are collected in literature, in which the collapse of the whole bridge, or of a large portion of it, has occurred for overturning in transversal direction.

5.4.2. Limit states and seismic analysis methods

Analogously to buildings, at least two limit states have to be considered in the seismic analysis of masonry bridges: a damage limit state (DLS) and a ultimate limit state (ULS) (Eurocode 8: CEN-EN 1998, 2005; Linee guida per la valutazione e riduzione del rischio sismico del patrimonio culturale, 2006; Nuove norme tecniche per le costruzioni, 2008; ISO, 2010). On the base of the damages surveyed on masonry bridges after seismic events, summarized in the previous paragraph, some considerations can be made on the structural response under DLS and ULS conditions:

– *Damage Limit State (DLS)*
  It consists in the appearance of local damages compromising the serviceability of the bridge and needing a reduction of maximum weight and speed allowed, or a temporary suspension of traffic for inspection and repairing interventions.
  Under DLS conditions, local mechanisms have to be analyzed, such as the out-of-plane overturning of the spandrel walls and the ruptures of limited portions of the construction, including non-structural elements, like the parapets, the infrastructural installations and the read surface. The stress level on main structural elements (vaults and piers) has to be recorded to prevent the onset of cracks due to material crushing. Finally, the relative displacement of the arch springers has to be checked, as it can induce a misalignment of the voussoirs.

– *Ultimate Limit State (ULS)*
  It consists in the collapse of the bridge or of a large portion of it, but also in the appearance of a severe and diffuse damage state compromising the practicability of the structure.
  The global response in both longitudinal and transversal directions has to be considered; the former typically results the most vulnerable for bridges with squat piers, while the latter is often the less safe for high viaducts.
  The seismic assessment of an existing masonry bridge has to include the identification of the expected severe damages or collapses of the main structural elements (arches and piers), that can compromise the capability of the construction in sustaining even the vertical loads.

Partial models can be adopted for the evaluation of the seismic response of a limited portion of a masonry bridge and the assessment of its vulnerability towards earthquakes.

The local mechanism of out-of-plane overturning of the spandrel walls can be studied by using the rigid block model and applying an adequate base motion, derived as the earthquake motion filtered by the structure from the ground to the base of the wall (Rota et al., 2005).

Concerning piers and vaults, simplified models have been proposed in literature to determine the seismic response of limited portion of the bridge. The behaviour of a single pier is analyzed by considering it as isolated from the remaining part of the construction and by having recourse to a beam model with adequate constraint conditions. A single arch (with fixed ends) under transversal horizontal loads is instead represented by using a simplified resistant system made of equivalent diagonal rectilinear truss elements. Anyway, these approaches may lead to an excessive underestimate of the effective safety level (Gambarotta et al., 2006).

Otherwise, global models are needed to simulate the overall seismic response of a masonry bridge under earthquake motion and to evaluate its safety level towards seismic loads. The available procedures, prescribed by codes for buildings, go from linear static and linear dynamic (modal) analyses, to non-linear static analysis (push-over) and non-linear dynamic analysis (time-step integration). In the following paragraphs, they are briefly recalled and some observations about their application to masonry bridges are made.

5.4.3. Modal analysis

Modal analysis represents the most simple approach to the evaluation of the dynamic behaviour of structures. Anyway, its basic assumption that the material is linear elastic constitutes a strong simplification when applied to masonry bridges. In fact, because of the weakness of masonry in traction, the effective structural response may be significantly far from the one provided by elastic numerical simulations. Thereby, attention has to be paid to the interpretation of the results: modal shapes really make sense only when describing the dynamic response to environmental vibrations (induced for example by traffic loads or by the wind) producing small displacements. In this case, the cross-section of the structural elements, whose compression results from gravity loads, does not reach a state of partialization and the effects of self-weight and vibrations can be superposed without large errors.

As regards the elastic stiffness of the material, it should be defined so as to be representative of the effective overall stiffness under the design

scenario. Within a seismic assessment, since large displacements are expected, a secant rather than an initial tangent Young modulus should be assumed. Moreover, the elements that are expected to play a negligible role in the non-linear response (e.g. that are not compressed in the deformed configuration) should not be included in the analysis.

Clearly, an adequate representation of the structural masses is crucial for achieving a reliable description of the dynamic response of a structure; concerning this, spandrel walls and fill soil play a fundamental role in the seismic behaviour of masonry arch bridges. Anyway, their accurate modelling in FE codes requires refined strategies with 2-D or 3-D elements. Since this entails heavy computational costs, simplified representations can be achieved by means of concentrated point masses, adequately positioned and connected to the underlying vaults and piers.

Modal frequencies and eigenvectors can be taken as a preliminary indication of the main characteristics of the dynamic response of a masonry bridge: the more deformable direction (longitudinal or transversal, on the base of the periods of vibration), the expected deformed configuration (depending on the modal participating factors and on the percentages of excited masses), the input signals that may induce the most severe effects on the construction (depending on their frequency content). Finally, modal analysis provides the shape of load distributions to adopt in push-over analyses.

5.4.4. Push-over analysis-based procedures for seismic assessment

Codes and guide lines of recent issuing propose criteria for the evaluation of the safety towards earthquakes based on non-linear static approaches (push-over). Typically, they need limited computational effort (lower than non-linear dynamic analyses) but provide a more reliable estimation than linear methods of the structural response of strongly non-linear constructions like masonry bridges.

At present time, the most common non-linear static analysis-based methodologies are the Capacity Spectrum Method (Freeman et al., 1975; Freeman, 1998), adopted in the American Standard ATC-40, and the N2 Method (Fajfar and Gašperšič, 1996), included in Eurocode8 (CEN-EN 1998, 2005) and in the Italian Standard (Nuove norme tecniche per le costruzioni, 2008). Both the methods consist in the comparison of the seismic capacity of the structure and the seismic demand.

CSM and N2 method can be now considered part of the well-established usage of professional engineers for what concerns r.c. and steel buildings, but their reliability when applied to masonry bridges has still to be proved, mostly because of the strong simplifications resulting from their main basic

assumption, i.e. that the load distribution imposed on the structure during push-over analysis corresponds to the one produced by the earthquake. From this hypothesis, it follows that an adequate choice of the distribution of horizontal loads is crucial, since different distributions may lead to totally different results. Typically, forces proportional to the product of masses and modal displacements (referred to the fundamental period) are considered the most suitable to reproduce a deformed configuration that is close to the effective one; of course, this is true only when the dynamic response is mainly governed by the fundamental mode (whatever that is). When dealing with masonry bridges, attention has to be paid to modal shapes and participating masses, since higher modes may induce heavier effects than modes with longer periods, especially in longitudinal direction and in bridges with squat piers, which may display un-symmetric modal shapes or local modes involving limited portions of the construction, like the case of torsional modes of the vaults (Gambarotta et al., 2006).

The possibility for including the contribution of higher modes consists in performing modal push-over analyses (Chopra and Goel, 2002; Goel and Chopra, 2005). Assuming that the dynamic response is governed by the first mode does not even allow the effect of damage and inelastic phenomena to be accounted for. Refined methodologies have been proposed to include damage evolution during the deformation process, such as the adaptive push-over (Antoniou and Pinho, 2004). They have never been applied to masonry bridges, and, since a high computational effort is needed, they seem to be, by now, cumbersome in current use.

As regards the load distribution to be used for in-plane push-over on arch bridges, since eigenvectors usually display displacements in both horizontal and vertical directions, analyses with both horizontal and vertical loads (proportional to the product of masses and modal displacements, i.e. to inertial forces) appear to provide the most reliable estimation of the structural overall stiffness.

The N2 Method was initially proposed to achieve a satisfactory balance between required reliability and applicability for design use, and its name was chosen to state the fact that two separate mathematical models are adopted to represent capacity and demand. The capacity is obtained by a non-linear static analysis and represented by the capacity curve; the demand is described by an inelastic response spectrum derived from the elastic acceleration one. The latter is provided by the code for the site of interest and for the design earthquake scenario (hazard level), while the procedure for deriving the inelastic spectrum takes into account the cumulative damage associated to the inelastic behaviour of the structure, which is considered to be particularly important for existing (and masonry) constructions.

Seismic capacity and demand are compared in the spectral domain, defined as the plane having the spectral displacement S_d on the x-axis and the

spectral acceleration S_a on the y-axis. The capacity curve, when converted in the spectral domain, takes the name of Capacity Spectrum (CS), while the acceleration spectrum takes the name of Demand Spectrum (DS). The conversion of the push-over curve into the CS is based on the assumption that the response of the structure, which is a multi-degree-of-freedom (MDOF) system, can be represented by the response of an equivalent SDOF system.

The relation (5.32) holds between a quantity of the MDOF system (Ω) and the SDOF one ($\Omega*$):

$$\Omega = \Gamma \Omega * \tag{5.32}$$

It depends on the modal participating factor Γ, defined as stated by (5.33), being $\mathbf{M}$ the structure mass matrix, $\mathbf{\Phi}$ the eigenvector normalized so that its maximum is 1, and, finally, $\mathbf{t}$ the influence vector containing the direction cosines between the earthquake motion direction and the degrees of freedom of the system. The numerator of Γ is also called modal participating mass (m*).

$$\Gamma = \frac{\mathbf{t}^T \mathbf{M} \mathbf{\Phi}}{\mathbf{\Phi}^T \mathbf{M} \mathbf{\Phi}} \tag{5.33}$$

Thus, the CS is derived through expressions (5.34) and (5.35) from the push-over curve defined in the plane of the control displacement (d_k) and of the resultant base shear (V_b).

$$S_d = \frac{d_k}{\Gamma} \tag{5.34}$$

$$S_a = \frac{V_b}{\Gamma \cdot m*} \tag{5.35}$$

The conversion of the elastic acceleration spectrum in the spectral domain requires the deriving of the spectral displacement (S_{de}) from the period (T) and the spectral acceleration (S_{ae}):

$$S_{de} = \frac{T^2}{4\pi^2} S_{ae} \tag{5.36}$$

The intersection between CS and DD is called Performance Point (PP); it represents the behaviour of the structure under the design earthquake scenario and is used to check the seismic performance at maximum displacement. In fact, its coordinates give the maximum expected spectral acceleration and displacement in the SDOF system, from which the base shear and displacement of the MDOF system can be derived by using (5.33) and (5.34).

The definition of the inelastic response spectrum requires to represent the damping due to hysteresis and damage; the inelastic SDOF system is described by means of an equivalent bilinear, often elastoplastic, law. When the post-yield stiffness is equal to zero (EP system) the influence of moderate strain hardening is assumed to be incorporated in the demand spectrum (Fajfar, 1999).

Within the N2 Method an equivalent elastic-perfectly plastic SDOF system is defined, and a ductility factor μ is obtained. It is equal to the ratio between the ultimate displacement d_u and the yielding displacement d_y:

$$\mu = \frac{d_u}{d_y} \tag{5.37}$$

To account for the hysteretic dissipation of ductile structures, a reduction factor R_μ is also derived according to (5.38), in which T_C (often called characteristic period of the ground motion) is the transition period where the constant acceleration segment of the spectrum ends. R_μ depends on the natural period of the system, on its ductility, on its hysteretic response and related damping, as well as on the characteristics of the ground motion. Several procedures have been proposed to calibrate R_μ, mainly based on parametric investigations on different groups of records, statistical studies, empirical observations and some validation tests using non-linear time-history analyses (Vidic et al., 1994), always referring to buildings, and never to bridges nor, let alone, to masonry arch bridges.

$$R_\mu = \begin{cases} (\mu - 1)\dfrac{T}{T_C} + 1 & T < T_C \\ \mu & T \geq T_C \end{cases} \tag{5.38}$$

The inelastic demand spectrum is obtained through (5.39).

$$\begin{cases} S_a = \dfrac{S_{ae}}{R_\mu} \\ S_d = \dfrac{\mu}{R_\mu} S_{de} = \dfrac{\mu}{R_\mu} \dfrac{T^2}{4\pi^2} S_{ae} = \mu \dfrac{T^2}{4\pi^2} S_a \end{cases} \tag{5.39}$$

Since $R_\mu = \mu$ for $T \geq T_C$ the principle of equal displacement between elastic and inelastic SODF systems is assumed for high periods. Diversely from (Vidic et al., 1994) and (Fajfar, 1999; 2000) in which the elastoplastic equivalent system is defined once and for all on the base of the whole capacity curve, it seems to be preferable to build it for all the displacement values in the range of interest, so that the effectively required ductility under

a displacement condition, rather than the ultimate one, is considered. Moreover, the identification of a ultimate displacement resulting from a push-over analysis should represent the achievement of a ultimate (failure) condition, which is not always obvious, and, of course, cannot depend on the maximum displacement value before the loss of convergence in the numerical simulation.

Concerning this, it has to be added that the capacity curves of large-span masonry bridges may display so high displacements that the performance point is in the ascending branch. Thus, from the one hand, a bilinear system related to the ultimate displacement would lead to an overestimate of the effective inelastic demand; on the other hand, this also seems to indicate that the degrading behaviour of the push-over response does not significantly affect the outcome of the seismic assessment, being out of the displacement range of interest.

The equivalency between MDOF and SDOF consists in the same underlying area (energetic equivalence), the same ultimate displacement and the same stiffness of the push-over curve. Of course, other criteria can be chosen, such as the minimization of the standard deviation between capacity spectrum and bilinear law or an elastic period of the equivalent SDOF system (T*) equal to the period coming from modal analysis; T* is obtained according to (5.40) in which d_y* and f_y* are the coordinates of the yielding point in the spectral domain.

$$T^* = 2\pi\sqrt{\frac{m^* d_y^*}{f_y^*}} \tag{5.40}$$

The Capacity Spectrum Method (Freeman et al., 1975; Freeman, 1998) is substantially analogous to the N2 Method, but assumes different criteria for the definition of the inelastic spectrum. In fact, the inelastic demand is represented by an over-damped elastic response spectrum in which an equivalent viscous damping ratio ξ>5% is computed by considering the effectively dissipated energy in the cyclic response (Chopra, 2006), which is in turn estimated by means of an equivalent bi-linear system and some coefficients experimentally calibrated to evaluate the hysteretic dissipation.

5.4.5. Non-linear dynamic analysis

The most accurate way to evaluate the seismic response of a structure is represented by non-linear dynamic analyses; it allows to account for the dissipative phenomena, damage accumulation and evolution, differential earthquake motion at the constraints (multi-support excitation), without any strong basic assumed simplifications. On the other hand, it needs high

computational effort and calculus duration, an adequate representation in the model of material cyclic behaviour and of dissipative phenomena (damping), a complex pre-processing phase for choice and manipulation of signals, a careful choice of output variables to record and, finally, a delicate post-processing procedure for elaborating them.

Generally, the signals adopted for the seismic structural analysis are of three types: artificial waveforms, simulated accelerograms and natural records. Several database of natural recorded signals are available on internet (COSMOS, PEER, ISESD, ESD, USGS, ITACA) from which acceleration time-histories can be downloaded together with all the information about the corresponding seismic event. The records to be used in the analysis must be chosen so as to be representative of the ground motion at the site and must be recorded at a consistent source-site distance (Bommer and Acevedo, 2004). Different criteria can be used for the selection of the records, based on geophysical parameters (earthquake magnitude, source-to-site distance, site classification, fault characteristics) or on the matching to the elastic response spectrum (as many seismic design codes often require).

As regards the number of records to be used, it should be chosen to be efficient and sufficient: small enough to provide good results (low scatter in both the demand and the capacity estimates) but at the same time large enough to provide a complete characterization of the response (Vamvatsikos and Cornell, 2004).

In the selection process, the accelerograms can be scaled to achieve a better representation of the design earthquake scenario, which often means an improved match with the target spectrum. Generally, scalar factors can be applied to the acceleration and/or time axes of the record to obtain the desired PGA and/or duration, respectively; in the former case, the correspondence between signal and target spectra can be pursued at a specific period value (for example at the fundamental period of the structure) or on average within a period window (Bommer and Acevedo, 2004). Such a window has to include the fundamental frequencies of the structure, i.e. the ones of the modes whose contribution to the overall dynamic response is significant. High masonry bridges may display a fundamental mode in the transversal plane with high period (>1.5 sec) and participating mass (60÷70%); in this case the typically chosen window (0.15÷2.0 sec) may result to be inadequate, and a wider one should be fixed having a higher upper limit.

The issue of scaling the accelerograms to be used in non-linear dynamic analyses of structures is quite debated in literature. Sets of scaled signals are considered to be independent on the anchoring value of the code spectrum (it is easier to find a real record set that is compliant to the code spectrum) and to reduce the record-to-record variability in the response (Iervolino et al., 2008). From a physical point of view, an accelerogram depends on the magnitude of the event (M_E) and on the distance from the source (R_E) in terms

of both peak ground acceleration (PGA) and of shape (high magnitude events produce seismic waves having a high content at lower frequencies than low magnitude events). Scaled signals provide the desired PGA but correspond to events that could be significantly far from the design one. For example, a severe scenario in which the expected PGA is 0.7g could be represented by the record of a weak earthquake with PGA=0.07g that is scaled by a factor 10.

The main point is to understand how the scaling produces effects on the structural response, i.e. if the non-linear response of a multi-degree-of-freedom structural system depends on M_E and R_E beyond its dependence through the intensity level. In more formal terms, the issue is to know if the non-linear MDOF response is conditionally independent of M_E and R_E, given a spectral acceleration (Shome et al., 1998). If it is, then the selection of the set of records is greatly simplified because it can be made within a database of any M_E and R_E; on the contrary, only records corresponding to events with magnitude and distance close to the design one can be considered in the selection process.

Even if this issue is still open, recent studies suggest that scaling the amplitude of records is allowed provided that not too high scaling factors are used (Beyer and Bommer, 2007). Moreover, a linear scaling on the only accelerogram axis and the pursuing of the compatibility on average within a period interval, and not only on a single period value, seem to be preferable.

In non-linear dynamic analyses, a term representing dissipative phenomena is usually included. Damping mechanisms (viscous damping, Coulomb friction damping, radiation damping, hysteretic damping) as well as damping ratios have been widely discussed by several authors (see, among others: Chopra, 2006; Priestley et al., 2007) and the main point on which they seem to agree is that this is a very complex issue (especially for multi-degree-of-freedom systems and for unreinforced masonry structures) since it is damage dependent and poor information on it are available in literature.

Rayleigh damping is a simplified way to take into account the dissipative properties of the structure through a viscous term $\mathbf{C}$ proportional to the mass $\mathbf{M}$ and the structure stiffness $\mathbf{K_S}$ matrices (5.41).

$$\mathbf{C} = \zeta_1 \mathbf{M} + \zeta_2 \mathbf{K_s} \tag{5.41}$$

When hysteretic damping is included in the model (for example through the constitutive law assumed for the material), Rayleigh damping represents the dissipative effects induced by other phenomena which are not explicitly described, such as local inelastic deformations due to inhomogeneous distribution of the stresses at the micro-scale that can occur also in a range of average macroscopic stresses that are well below the elastic threshold. If the

fill soil is not included in the structural model, Rayleigh damping has also to describe the dissipative effects produced by its presence.

Some proposals for the equivalent viscous damping ratio to be used in dynamic analyses on masonry structures are made one the base of shaking table tests in (Benedetti et al., 1998; Juhásová et al., 2008; Mazzon et al., 2009; Elmenshawi et al., 2010); it seems that a ratio in the order of 2%÷10% could be reasonable, even if in all these works only walls or small-scale building models are considered. Moreover, according to some authors (Priestley et al., 2007), higher damping ratios should be used for severe earthquake scenarios (ultimate limit state condition), for which strong damages are expected, and for prevalence of flexural response, while lower values should be assumed when weak events (serviceability limit state condition) are of interest and the shear is expected to mainly govern the structural response.

The scalar parameters of the Rayleigh damping ζ_1 and ζ_2 should be chosen so as to get a reasonable damping value within the range of frequencies in which the spectral content of both the input signal and of the structural response is significant. High damping values can be accepted for very low frequencies (<0.2Hz) that are usually reset to zero in the filtering process of sampled recorded signals, as well as for very high frequencies (>50Hz) that can result from numerical instabilities and, anyway, have negligible importance in terms of structural dynamic response.

Finally, a certain damping allows to contain numerical instabilities and thereby can be useful in simulations, provided that, of course, it does not affect the result by introducing an error, considering also that the structural response may show strong sensitivity to small variations of the damping term.

During non-linear dynamic analyses one or more damage measures and/or structural state variables have to be monitored; generally, three choices can be made to synthetically represent the overall response (and to make comparisons with static methods): the maximum displacement of the control node and the corresponding (same time instant) resultant base shear; the maximum base shear and the corresponding displacement of the control node; the maximum displacement and the maximum resultant base shear within a time window of a certain amplitude centred in the time instant of maximum displacement (Ferracuti et al., 2008). When dealing with potentially degrading systems (showing a softening branch in the static load-displacement curve) the first choice is preferable with respect to the second one. The last possibility has instead a uncertain mechanical justification, unless it is intended as a way to account for higher modes having a non-negligible influence on the dynamic response of the MDOF system.

One case study is considered in the following section, in which the methodologies discussed in this paragraph are applied and some issues related to their employment for the seismic assessment of a multi-span bridge are underlined.

5.5. Seismic response of masonry bridges: a case study

The case study of Ronciglione viaduct, illustrated in paragraph 4.4.1 is described in this section.

5.5.1. Dynamic characterization

In a first step, the dynamic behaviour of Ronciglione Viaduct in the elastic range is investigated by a linear 3-D finite element model, in which all structural elements can be faithfully represented; the results in terms of modal shapes and natural frequencies are compared to those provided by a fiber beam model to investigate the capability of a 1-D modelling approach in representing the dynamic response of a multi-span arch bridge.

The 3-D model is made of brick finite elements with 8 nodes (Figure 5.20); a Young modulus E=750MPa and a self weight γ=1650kg/m^3 are assigned to vault brickwork, according to experimental results, while E=750MPa, γ=1500 kg/m^3, and E=200MPa, γ=1500kg/m^3 are chosen for pier tuff masonry and fill soil, respectively. Sensitivity analyses are performed to investigate how the material characteristics influence the structural response, revealing a strong dependence on the stiffness of the piers.

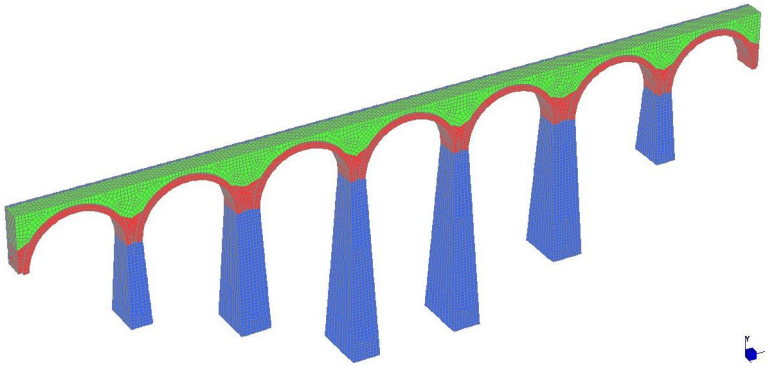

Figure 5.20. Model of Ronciglione Viaduct with brick elements.

The first ten modal shapes of Ronciglione Viaduct are represented in Figures 5.21−5.30, while periods (T), frequencies (*f*), participating factors (Γ) and masses (*m*) provided by fiber beam-based model are collected in Table 5.2. The bridge conformation, characterized by high central piers, is such that the principal modal shape is in transversal direction and nearly symmetric, with all nodal displacements of the same sign and higher for the central spans (Figure 5.21); the following three modes in ascending order of frequency are again in the transversal plane and present cross-shaped horizontal displacements (Figures 5.22−5.24), then also modes #7, #8 and #9 are in the transversal plane (Figures 5.27−5.29). The first longitudinal mode is mode #5 (Figure 5.25) and the following ones are #6 and #10 (Figures 5.26 and 5.30). On the whole, modal shapes strongly result from the height of the central piers, the stiffness of the second and fifth ones and from the stiffness of the arch, which appears high enough to produce an interaction between the spans, but not so high to make the piers move always towards the same direction.

As it is seen from Table 5.2, the modes display a significant contribution (participating factor and mass) in one only direction, while in the other one they do not participate in the dynamic response of the bridge. In particular, the fundamental modes are #6 and #1 for longitudinal and transversal planes, respectively. Their participating masses are relatively low (37% and 55%), similarly to what is found in (Gambarotta et al., 2006), in which the dynamic characterization of twenty Italian masonry bridges is presented.

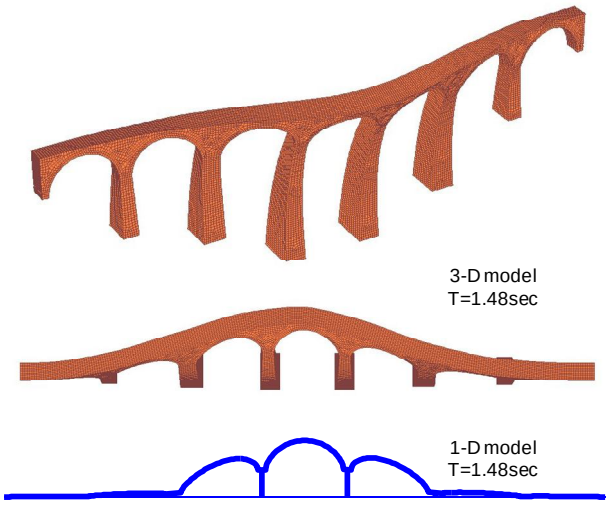

Figure 5.21. Modal shape #1: comparison between models with brick elements and fiber beams.

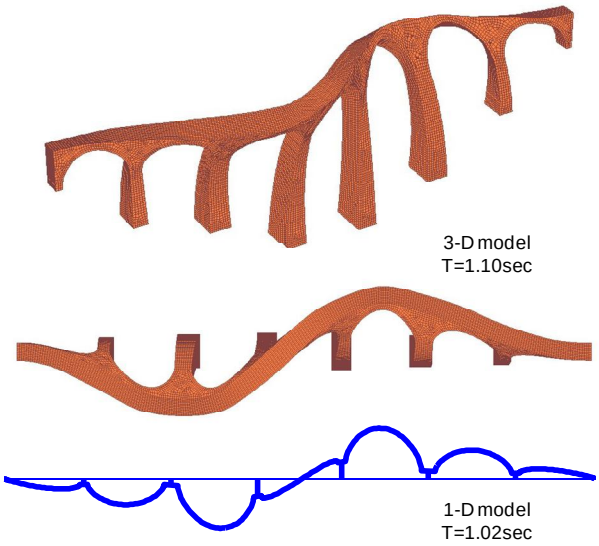

Figure 5.22. Modal shape #2: comparison between models with brick elements and fiber beams.

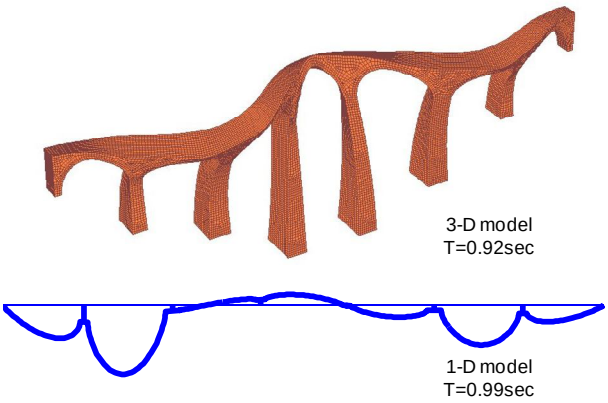

Figure 5.23. Modal shape #3: comparison between models with brick elements and fiber beams.

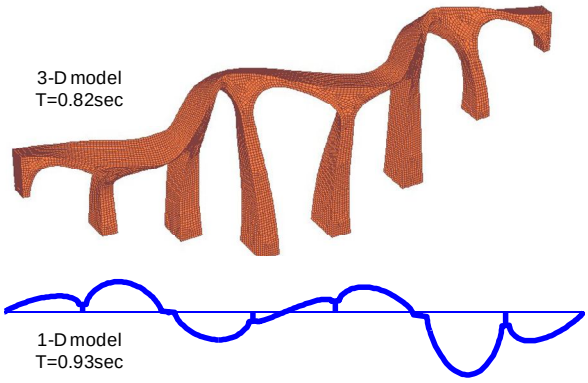

Figure 5.24. Modal shape #4: comparison between models with brick elements and fiber beams.

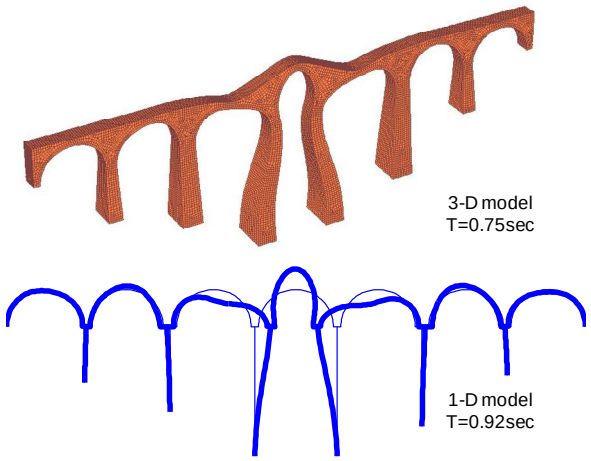

Figure 5.25. Modal shape #5: comparison between models with brick elements and fiber beams.

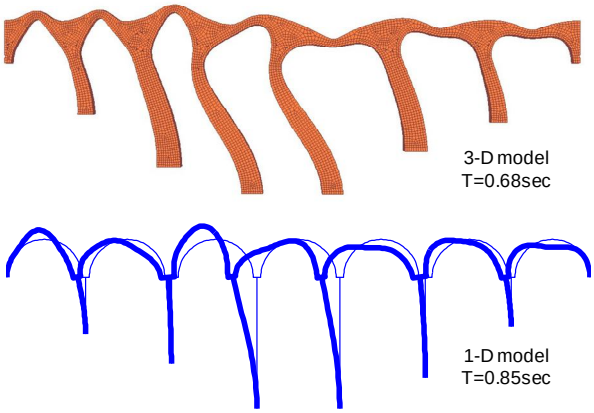

Figure 5.26. Modal shape #6: comparison between models with brick elements and fiber beams.

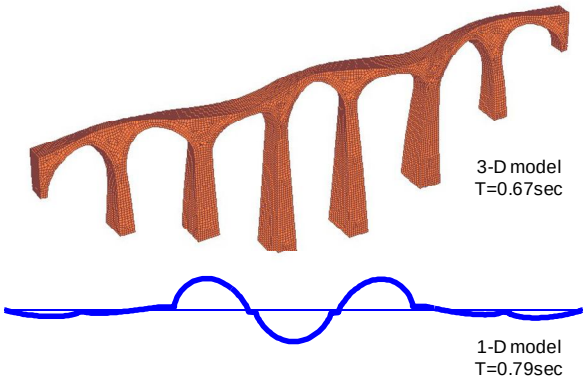

Figure 5.27. Modal shape #7: comparison between models with brick elements and fiber beams.

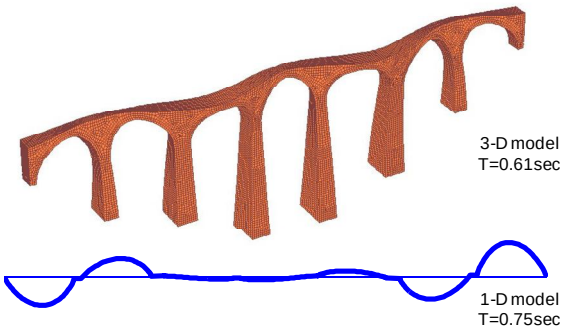

Figure 5.28. Modal shape #8: comparison between models with brick elements and fiber beams.

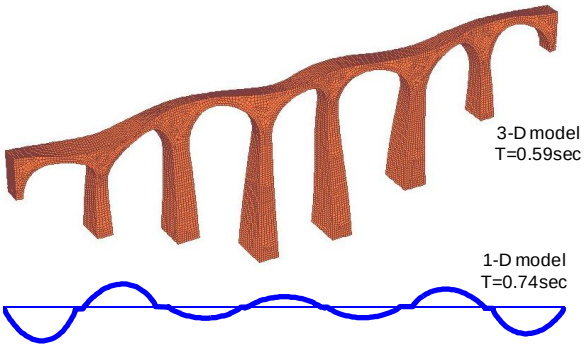

Figure 5.29. Modal shape #9: comparison between models with brick elements and fiber beams.

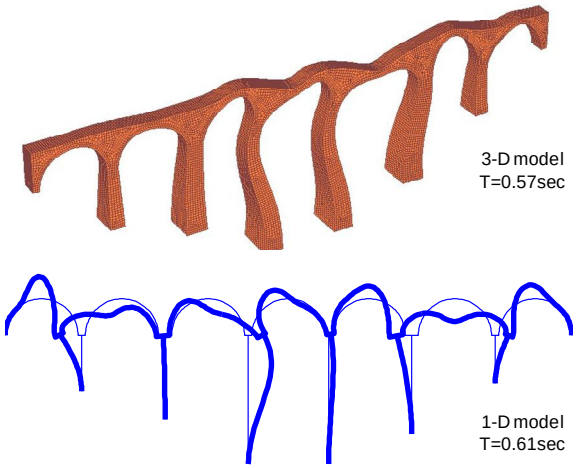

Figure 5.30. Modal shape #10: comparison between models with brick elements and fiber beams.

Mode	Period T [sec]	Frequency *f* [Hz]	Longitudinal Plane		Transversal Plane	
			Participating factor Γ	Participating mass *m*	Participating factor Γ	Participating mass *m*
1	1.477	0.676	≅ 0	≅ 0	1.73	55%
2	1.015	0.984	≅ 0	≅ 0	0.01	2%
3	0.99	1.01	≅ 0	≅ 0	0.31	15%
4	0.929	1.075	≅ 0	≅ 0	0.04	1.5%
5	0.922	1.083	0.22	2.6%	≅ 0	≅ 0
6	0.848	1.179	1.44	37%	≅ 0	≅ 0
7	0.795	1.257	≅ 0	≅ 0	0.03	0.8%
8	0.753	1.327	≅ 0	≅ 0	0.005	0.4%
9	0.749	1.334	≅ 0	≅ 0	0.12	4%
10	0.614	1.628	0.15	6%	≅ 0	≅ 0

Table 5.2. Modal analysis: periods and frequencies, participating factors and masses of the first ten modes (fiber beam model).

In the 1-D model, vaults and piers are described by using fiber beam elements, while for backing and abutments truss elements with fiber cross-section are used, as it is illustrated in the previous chapter. When the dynamic behaviour is under investigation, the representation of spandrels and fill in terms of mass results to be essential, as well as the contribution of the former ones in terms of in-plane stiffness (Fanning et al., 2001; Brencich and Sabia, 2007). Therefore, the mass of soil and spandrels is represented through point-masses connected by rigid links to the underlying vaults (Figure 5.31); the stiffening contribution of the spandrel walls (and, indirectly, the interaction between adjacent volumes of fill soil) is represented by horizontal and diagonal truss elements (Figure 5.32). The stiffness of the diagonal truss

elements is reduced to 50% in the modal analysis, since they only work as struts and not as ties.

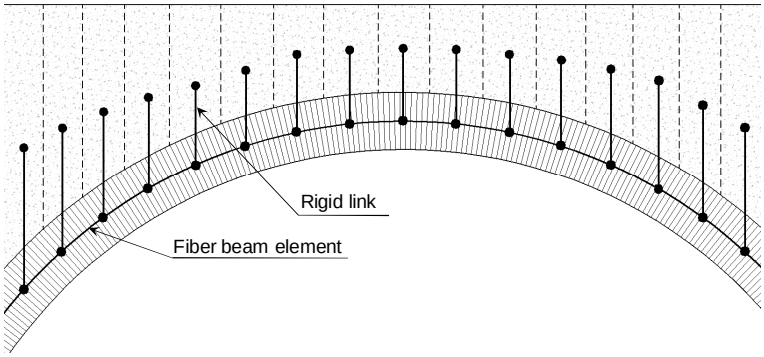

Figure 5.31. Fiber beam model: detail of the representation of fill soil.

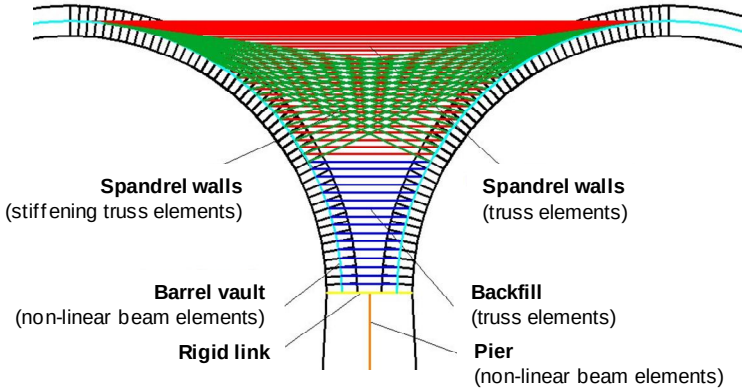

Figure 5.32. Fiber beam model: detail of the representation of backing and spandrel walls by means of non-linear truss elements.

The cross-section of vaults and piers is discretized into 100×100 fibers, while the one of truss elements representing backings, spandrels and abutments is divided into 30×30 fibers. Finally, a shear flexibility is assumed for the cross-section of piers in both the principal directions, as well as a torsion flexibility.

Within the dynamic characterization phase, the same mechanical properties adopted for the 3-D model are assigned to the fibers of the 1-D one. A satisfactory agreement is found in terms of both periods and modal shapes (Figures 5.21−5.30), especially for the modes (#1 and #6) considered to play a significant role in the seismic response; at the same time, a certain overestimate of the natural periods is observed for some higher modes.

5.5.2. Push-over analyses

Push-over analyses are carried out under in-plane and out-of-plane loads with different distributions: one (#1) is proportional to nodal masses, another one (#2) is proportional to nodal masses times horizontal displacements of longitudinal and transversal principal modes (mode #1 and mode #6) for in-plane and out-of-plane forces, respectively. Finally, a third distribution (#3) is also adopted in longitudinal direction, with horizontal and vertical loads proportional to nodal masses and displacements of mode #6. Forces are applied to nodes of arches and piers, as well as to those representing fill soil and spandrels, within an incremental quasi-static analysis which follows the application of the entire self-weight.

Material properties are described by means of the uniaxial constitutive model Masonry01 whose parameters are determined according to Table 3.3. Such a relation is assigned to the fibers of the cross-section of beam elements representing vaults and piers, and to the truss elements describing backings, spandrels and abutments.

Analyses are carried out under displacement control, adopting an energy increment-based convergence criterion and a linear geometric transformation rule. Wide load cycles are performed, with increasing positive and negative peak displacements. Resulting capacity curves are plotted in Figures 5.33 and 5.34, in which the control displacement (d_k) is on the horizontal axis and the normalized base shear on the vertical one. The control displacement is the horizontal component of displacement of the springer and of the crown of the central span for in-plane and out-of-plane analyses, respectively; it is measured, obviously, in the same direction in which loads are applied. Such a choice seems to be reasonable on the base of modal shapes found in the dynamic characterization, being these nodes the ones showing the largest displacements in eigenvectors #6 (in-plane analysis) and #1 (out-of-plane analysis). The normalized base shear is the resultant base shear V_b divided by the bridge self-weight (W).

Lower resistance and stiffness are found towards transversal forces and when a distribution proportional to the product of nodal masses and modal displacements (distribution #2) is used, since its resultant is applied in a higher position and produces a stronger bending moment at the base of the piers. Under in-plane loads, distribution #3 provides even lower stiffness and resistance. The mismatch in stiffness of the different capacity curves in both directions results from the different displacement fields produced by the imposed loads. If compared to the modal shapes, the closest deformed configuration is provided by load distribution #3 and #2 for longitudinal and transversal planes, respectively.

Similarly to the case of the single arch (Figure 5.13), the shape of all push-over curves is characterized by extremely narrow cycles, independently

of the load distribution nor of the direction of analysis, indicating that low hysteretic dissipation is expected during earthquakes.

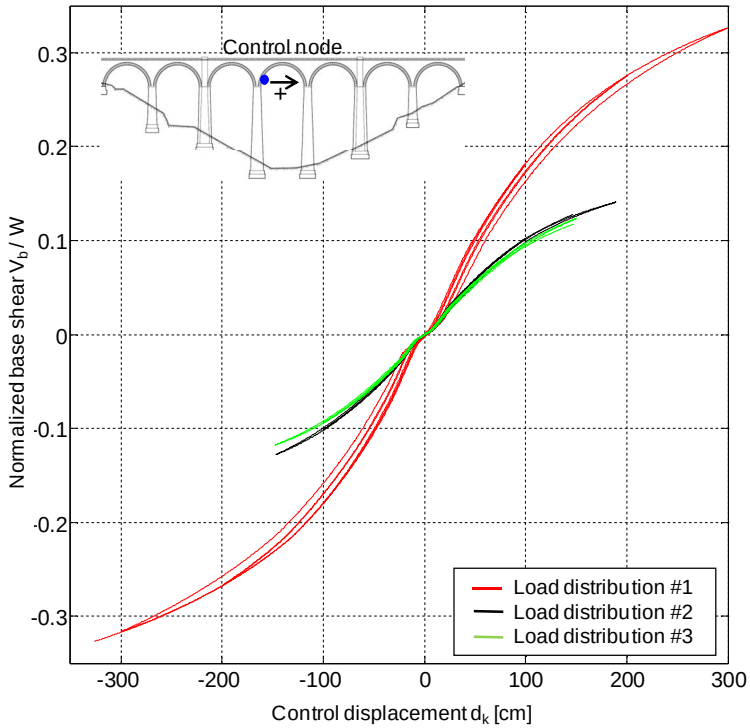

Figure 5.33. Capacity curves corresponding to different load distributions for in-plane push-over analyses.

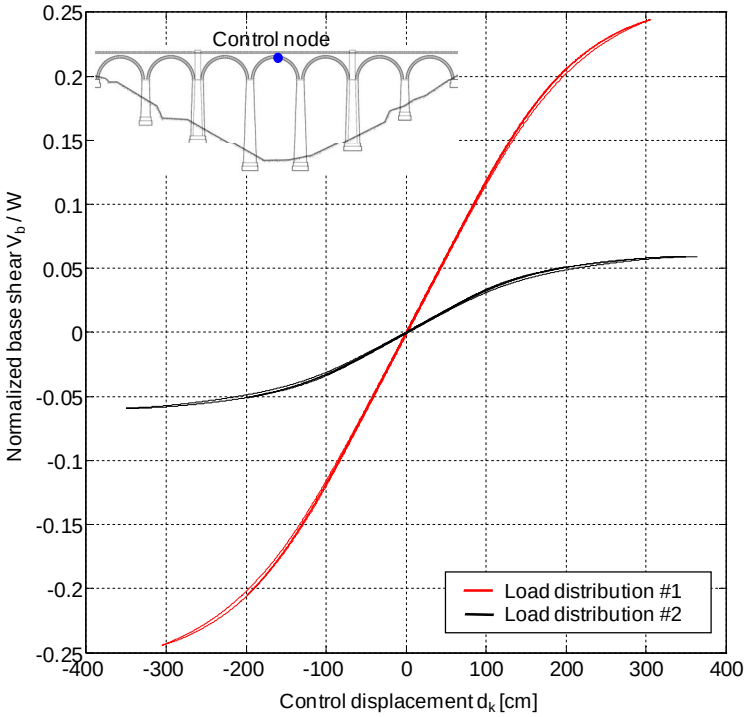

Figure 5.34. Capacity curves corresponding to different load distributions for out-of-plane push-over analyses.

Under in-plane loads, the very first branch of the capacity curves shows a low slope immediately increasing after the exceeding of a displacement of about 5cm; this has to be attributed to the progressive collaboration of the spandrel walls, which result strongly stressed under horizontal forces but do not collaborate under the self-weight. Considering the settlement process occurred on the structural elements of the bridge during its life, such a response does not reliably represent the actual state of the construction. The global stiffness provided by capacity curves has to be computed by neglecting the initial branch and considering instead the following linear phase.

Aiming at investigating the sensitivity to the variation of the mechanical properties of brickwork (compressive strength f_{cp} and ductility η) non-linear static analyses are carried out in transversal direction with load distribution #2. An increase of compressive strength results in a capacity curve with higher resistance and stiffness, while the higher is the ductility the higher is the displacement capacity, with a low corresponding strength variation (Figure 5.35).

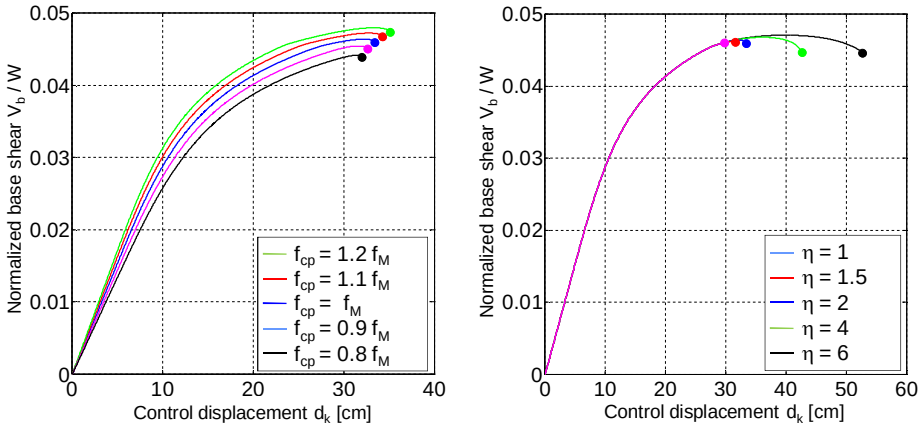

Figure 5.35. Sensitivity analyses in the transversal plane under load distribution #2: dependence of the capacity curve on the compressive strength (left) and on the ductility (right) of the material.

5.5.3. Non-linear incremental dynamic analyses (IDA) under natural accelerograms

The evaluation of the response of Ronciglione Viaduct under earthquake motion is made by means of incremental dynamic analysis (IDA) procedure (Vamvatsikos and Cornell, 2002). Such a method is becoming more and more widely adopted to estimate the response of structures under seismic loads. It consists in performing repeated non-linear dynamic analyses under accelerograms with increasing intensity level (IL), which is a monotonic scalable ground motion severity measure. The peak ground acceleration (PGA) is assumed as the intensity level measure and ranges from 0.2 to 2.0 (full application corresponds to IL=1.0).

Two different limit states are considered: the Ultimate Limit State (ULS) and the Damage Limit State (DLS); they are characterized by a probability of exceedence (p) equal to 10% and 63% respectively in the reference period V_R. The latter is defined as the product of the nominal life V_N and a coefficient C_U accounting for the functional type of the structure (i.e. its importance in case of seismic event). V_N=50 years and C_U=1.5 are assumed herein, resulting in a reference period V_R of 75 years. Return periods T_R of the considered events are then obtained by expression (5.42) and result to be equal to 712 years and 75 years for ULS and DLS, respectively.

$$T_R = -\frac{V_R}{\ln(1-p)} \tag{5.42}$$

The response spectra of the horizontal acceleration provided by Italian code (Nuove norme tecniche per le costruzioni, 2008) for the two considered limit states are represented in Figure 5.36. The initial and the maximum spectral acceleration values are 0.12g and 0.29g for ULS, and 0.07g and 0.15g for DLS.

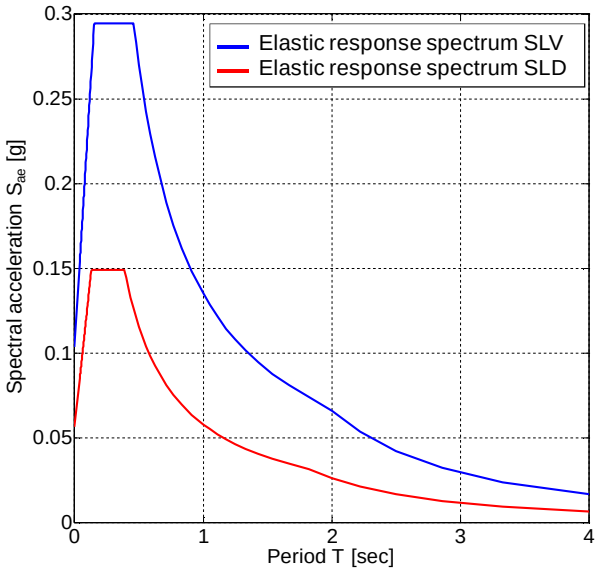

Figure 5.36. Elastic response spectrum of the horizontal component of the acceleration for ULS and DLS limit states provided by the code (Nuove norme tecniche per le costruzioni, 2008) for Ronciglione Viaduct site.

For the selection of signals software Rexel (Iervolino et al., 2009a) is used. The sets of records assumed as input signals are made of 14 accelerograms (seven events, two components each) selected from European Strong Motion Database (ESD); they are chosen and scaled to be compliant with target acceleration response spectra, i.e. to achieve a maximum spread from target spectra equal to ±10% in the 0.15÷2.50sec range; the upper bound is chosen on the base of the first period of the bridge (T_1=1.48sec).

A maximum mean scaling factor of 5 and a maximum single scaling factor of 10 are chosen to be applied to the acceleration axis; no scaling is allowed on the time axis. It has to be noted that the intensity level (IL) is applied to the selected signals and has nothing to do with the scaling factor used in the record selection.

The 14 signals are chosen among events having moment magnitude (M_E) at least equal to 6 (ULS) and 4 (DLS) and distance between the source and the recording station at least equal to 20km, to avoid weak events and near field registrations. Moreover, only signals recorded on soils having characteristics similar to the foundation soil of Ronciglione Viaduct

(classified as B according to Eurocode 8: CEN-EN 1998, 2005) are chosen. If more compliant sets are found, the one having the lowest dispersion with respect to target spectrum is chosen to restrict record-to-record dispersion of the structural response (Iervolino et al., 2009b).

The selected signals are collected in Tables 5.3 and 5.4 together with the events they correspond to, their M_E and R_E, their PGA in the two directions and the corresponding adopted scaling factors. The scaled acceleration time histories are plotted in Figures 5.37 and 5.38, for the two considered limit states, while their response spectra, the average response spectrum and the target spectrum are plotted in Figures 5.39 and 5.40.

Earthquake		Date	M_E	R_E [km]	PGA X [m/s^2]	PGA Y [m/s^2]	SF X	SF Y
#1	Campano Lucano	23/11/1980	6.9	78	0.27	0.35	3.68	2.85
#2	Kefallinia (aftershock)	23/03/1983	6.2	65	0.21	0.25	4.73	3.97
#3	Strofades (aftershock)	18/11/1997	6.0	93	0.10	0.11	9.65	8.86
#4	Manjil	20/06/1990	7.4	91	1.29	2.04	0.78	0.49
#5	Tabas	16/09/1978	7.3	68	1.00	0.85	1.01	1.19
#6	Strofades (aftershock)	18/11/1997	6.0	63	0.42	0.32	2.38	3.15
#7	Umbria Marche	26/09/1997	6.0	67	0.16	0.18	6.05	5.50
Average Values			6.54	75	0.49	0.59	4.04	3.72

Table 5.3. Selected signals for IDA on Ronciglione Viaduct under ULS limit state conditions.

Earthquake		Date	M_E	R_E [km]	PGA X [m/s^2]	PGA Y [m/s^2]	SF X	SF Y
#1	Aigion (aftershock)	15/06/1995	5.6	34	0.10	0.09	5.35	5.94
#2	Itea	05/11/1997	5.6	52	0.13	0.11	4.17	4.95
#3	Kallithea	18/03/1993	5.8	41	0.10	0.10	5.37	5.46
#4	Izmir	06/11/1992	6.0	63	0.28	0.28	1.95	1.95
#5	Kyllini	16/10/1988	5.9	51	0.11	0.12	4.99	4.51
#6	Ano Liosia	07/09/1999	6.0	20	0.85	0.76	0.64	0.72
#7	Izmit (aftershock)	11/11/1999	5.6	36	0.08	0.19	6.56	2.89
Average Values			5.78	42	0.23	0.23	4.15	3.77

Table 5.4. Selected signals for IDA on Ronciglione Viaduct under DLS limit state conditions.

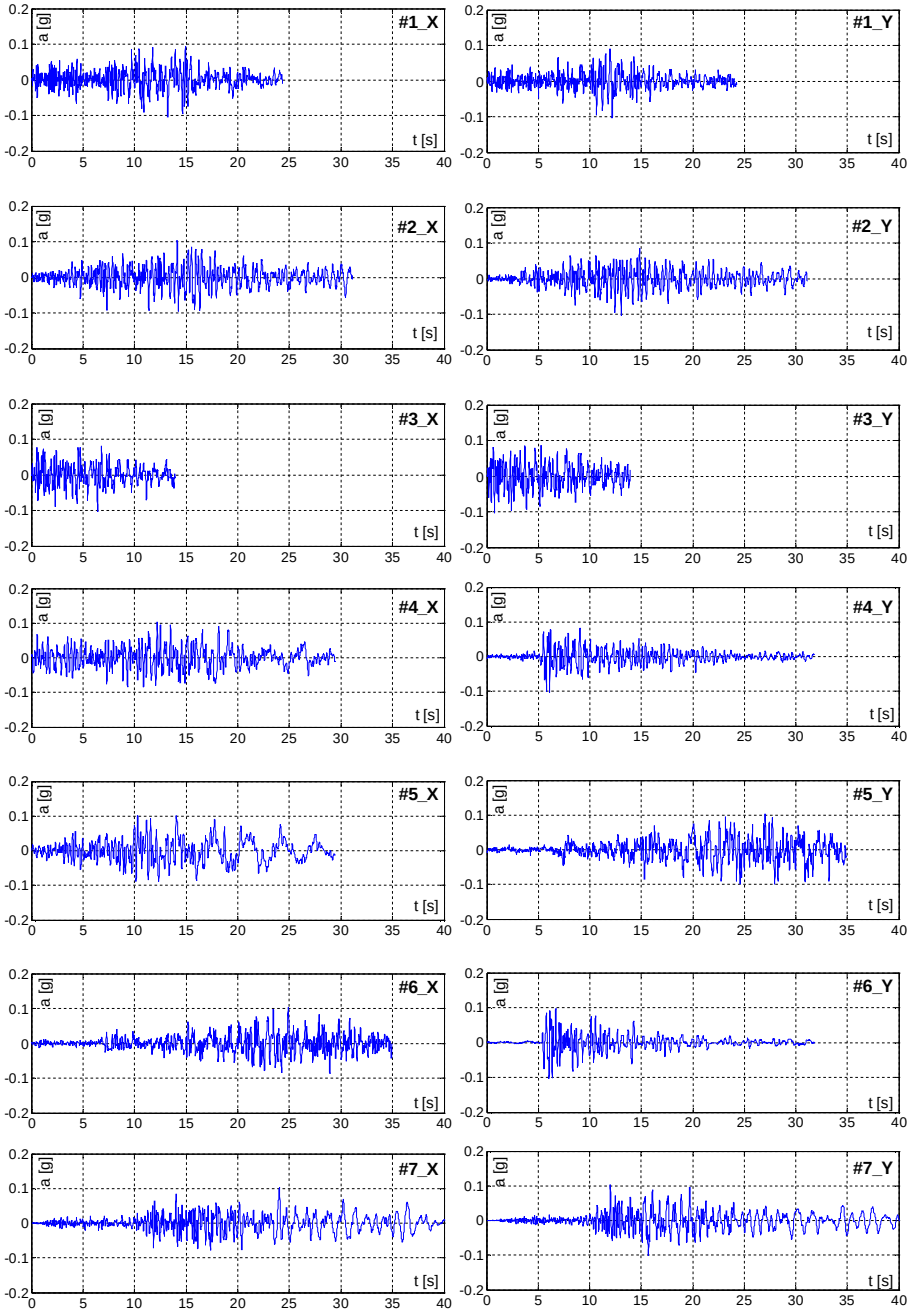

Figure 5.37. Scaled signals used for Incremental Dynamic Analysis on Ronciglione Viaduct under Ultimate Limit State (ULS) conditions.

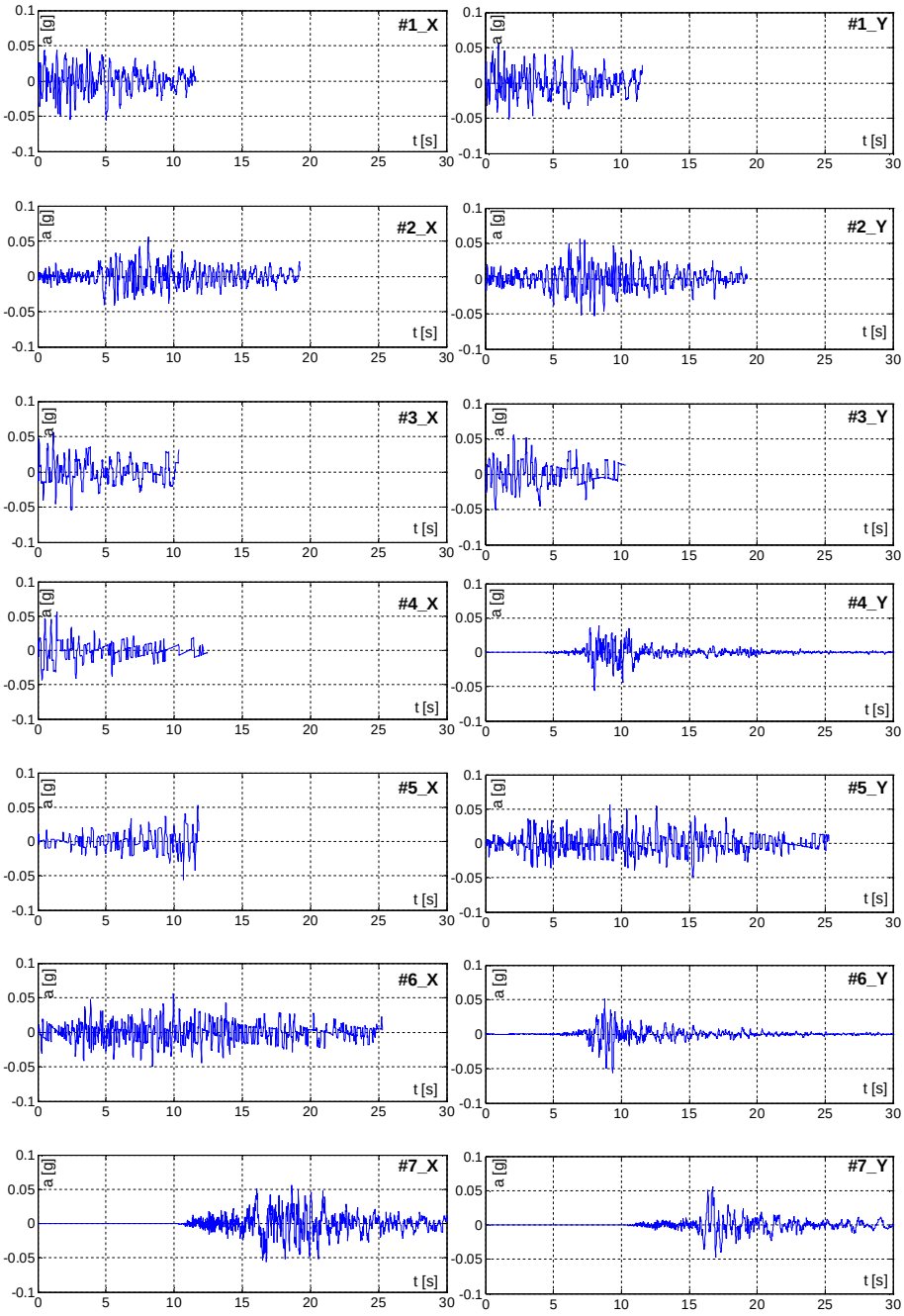

Figure 5.38. Scaled signals used for Incremental Dynamic Analysis on Ronciglione Viaduct under Damage Limit State (DLS) conditions.

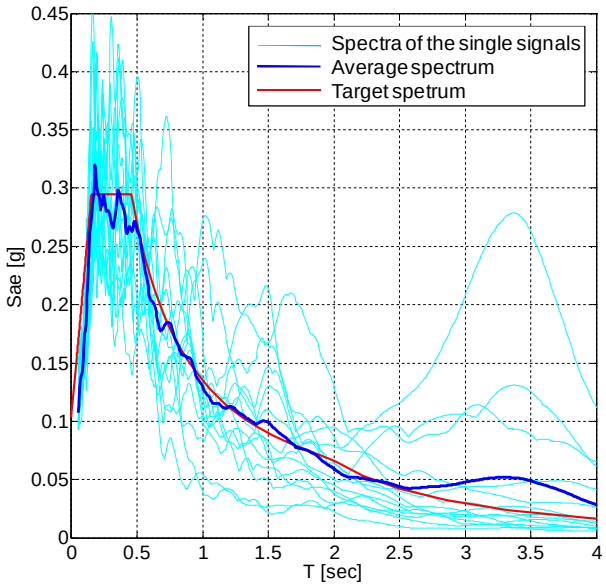

Figure 5.39. Acceleration response spectra of the selected signals, average spectrum and target spectrum for Ultimate Limit State (ULS) conditions.

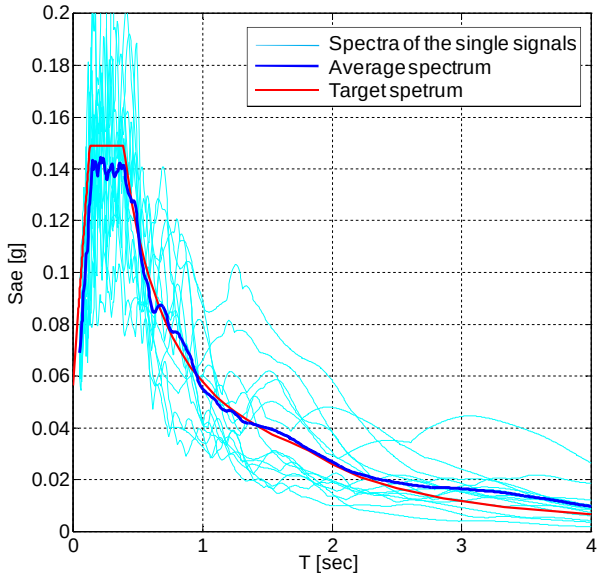

Figure 5.40. Acceleration response spectra of the selected signals, average spectrum and target spectrum for Damage Limit State (DLS) conditions.

The values ζ_1=0.2701 and ζ_2=0.0086 are assumed for the scalar parameters of Rayleigh damping; the corresponding damping ratio ξ is given

by expression (5.43) as a function of the pulsation ω (Chowdhury and Dasgupta, 2003) and is equal to 5% for the first (f_1=0.676Hz) and the sixth (f_6=1.179Hz) frequencies and anyway lower than 10% within the frequency interval in which the content of both input signal and structural response appears significant (Figure 5.41).

$$\xi(\omega) = \frac{\zeta_1}{2\,\omega} + \frac{\zeta_2\,\omega}{2} \tag{5.43}$$

The assigned damping ratio makes the comparisons between non-linear dynamic analyses and non-linear static analysis-based methods consistent, since the elastic spectrum provided by the code basically assumes a viscous damping of 5%. For this reason, the same damping constants are assumed for both ULS and DLS earthquake scenarios and no lower damping resulting from a lower expected damage is adopted for weak events, since it is considered to be included in the definition of the elastic spectrum and, therefore, in the corresponding set of compliant records.

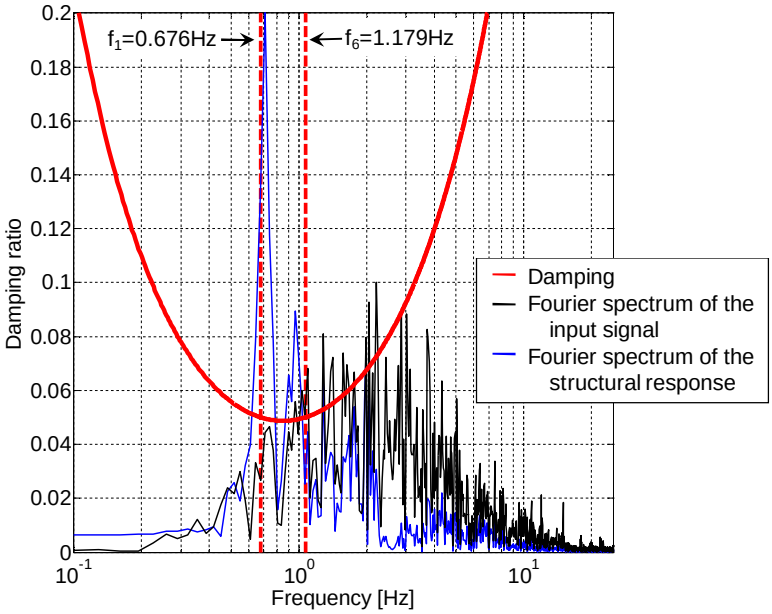

Figure 5.41. Rayleigh damping and Fourier spectrum of accelerogram #2, Y component, ULS conditions, and of the structural response (horizontal acceleration of the control node under out-of-plane analysis).

As regards the output variables, the maximum control displacement (d_k) and the corresponding (same instant) resultant base shear (V_b) are recorded for each simulation so as to obtain a set of couples (d_k,V_b), useful for the

comparison with push-over analyses. The control nodes are the springer and the crown of central span for in-plane and out-of-plane analyses, respectively, as it is done for non-linear static analyses. For each intensity level (IL) the average of displacement and base shear values resulting from the application of all the accelerograms are determined, and IDA curve is built

It is noteworthy that push-over curves are nearly symmetric and no heavy directional effect is found in time-step analyses; thus, the comparison is made in the only positive semi-plane d_k-V_b.

It is seen from Figures 5.42−5.45 that the points representing the single dynamic simulations are widely scattered (especially in transversal direction), but average IDA curves retrace with good approximation the capacity curves for both longitudinal and transversal analyses, if an adequate horizontal load distribution is applied (#3 and #2 for in-plane and out-of-plane analyses, respectively). This consideration is confirmed by the comparison between capacity curves and whole response curves of dynamic simulations, represented in Figures 5.46 and 5.47 for in-plane and out-of-plane analyses (two signals and two values of IL are chosen, as an example). A sort of macroscopic stiffness can be identified, being similar to push-over stiffness under #3 and #2 load distributions. Moreover, the contribution of more than one only mode seems to be evident from the shape of the response curves, showing wide, and slightly chaotic, cycles.

In Figures 5.42−5.45 the points on IDA curves relative to IL=1.0 represent the expected average response of the bridge under the various seismic scenarios, and is named Performance Point.

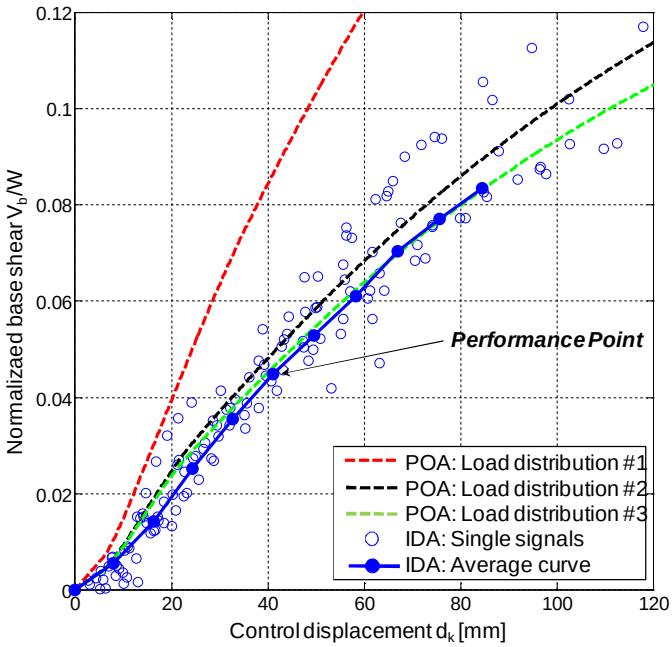

Figure 5.42. IDA curve and capacity curves for in-plane analyses and ULS conditions.

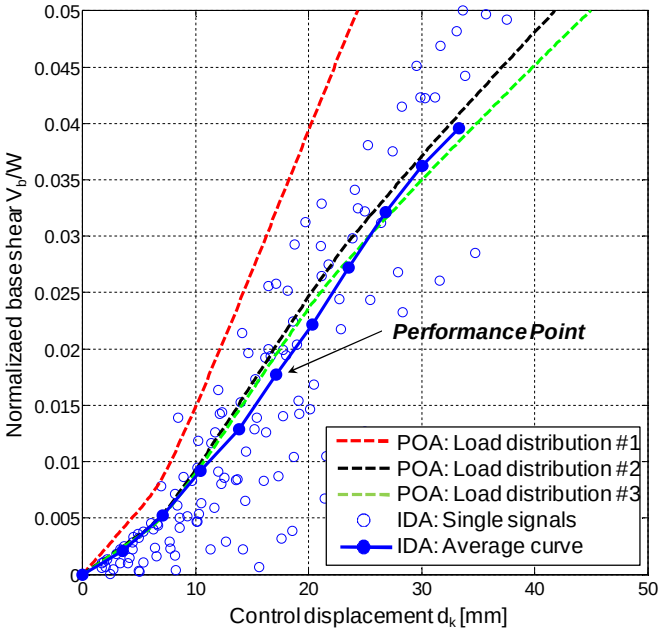

Figure 5.43. IDA curve and capacity curves for in-plane analyses and DLS conditions.

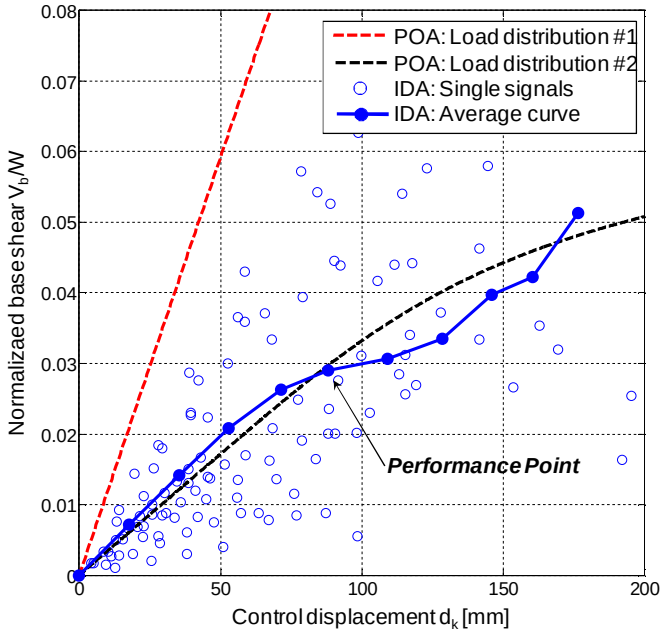

Figure 5.44. IDA curve and capacity curves for out-of-plane analyses and ULS conditions.

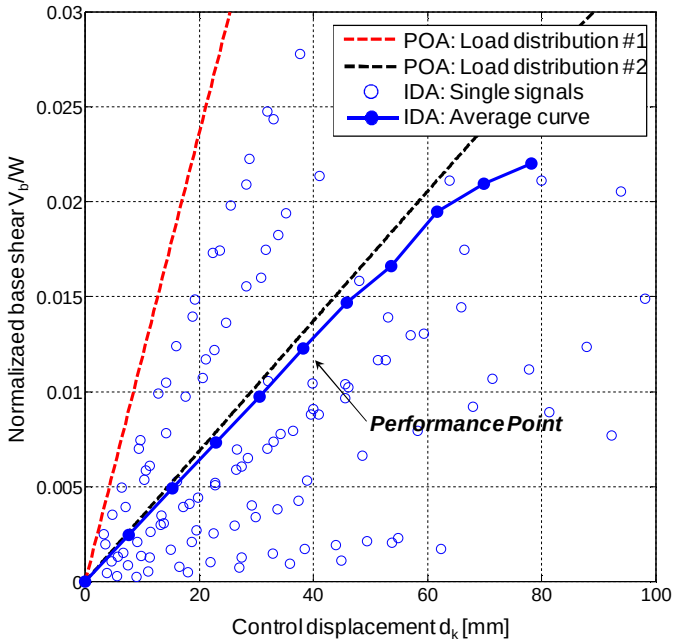

Figure 5.45. IDA curve and capacity curves for out-of-plane analyses and DLS conditions.

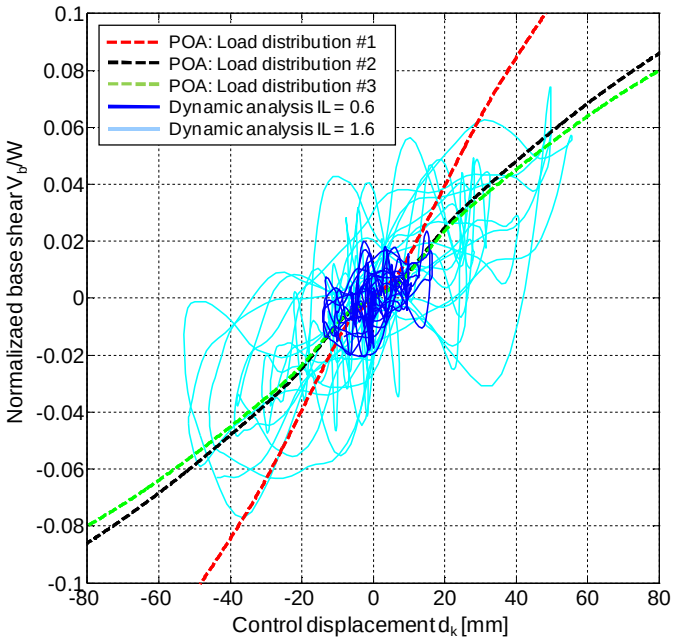

Figure 5.46. Comparison between push-over and non-linear dynamic analyses in longitudinal direction (accelerogram #3, X component).

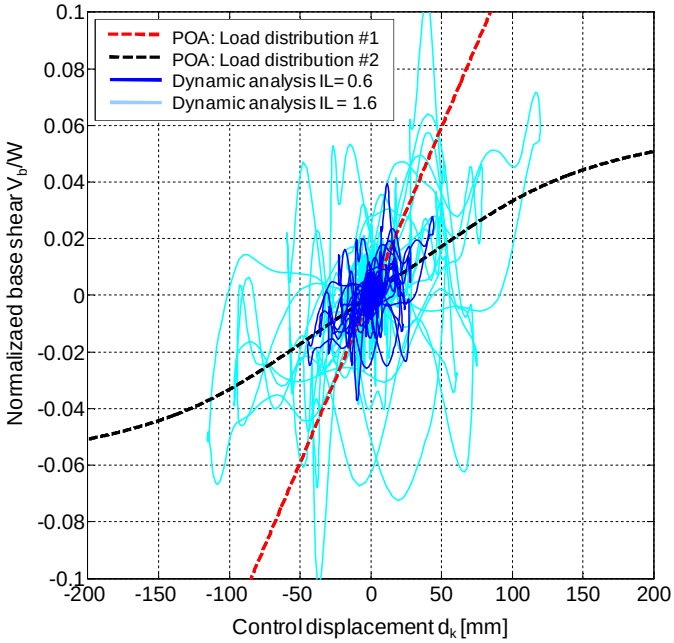

Figure 5.47. Comparison between push-over and non-linear dynamic analyses in transversal direction (accelerogram #1, X component).

A strong sensitivity to damping is found, as it is seen from Figures 5.48 and 5.49. In the former, the variation of the control displacement d_k is plotted towards the equivalent damping ratio ξ, in the wide range going from 1% to 20%. Such a variation is normalized with respect to the reference value ξ=5%. For ξ=1% d_k is equal to 110% the reference value, while for ξ=20% it reduces to about 55%.

In the latter plot the time-history of control node displacement is represented for three values of ξ (2%, 5%, 8%). Apart from the reduction in maximum displacement, it is seen that a higher damping produces a more rapid reduction of the free oscillations after the end of the signal (t=24sec). Finally, the three curves display a phase shift after the instant of maximum displacement, which tends to vanish after the end of the accelerogram.

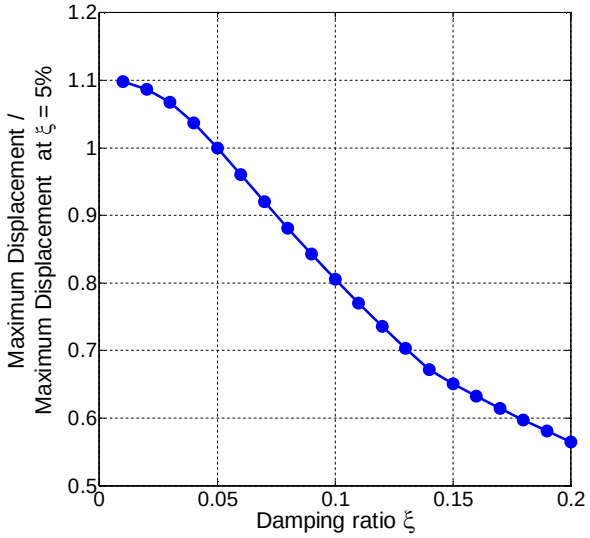

Figure 5.48. Displacement vs. Rayleigh damping ratio (Out-of-plane analysis, ULS limit state, accelerogram #1, Y component).

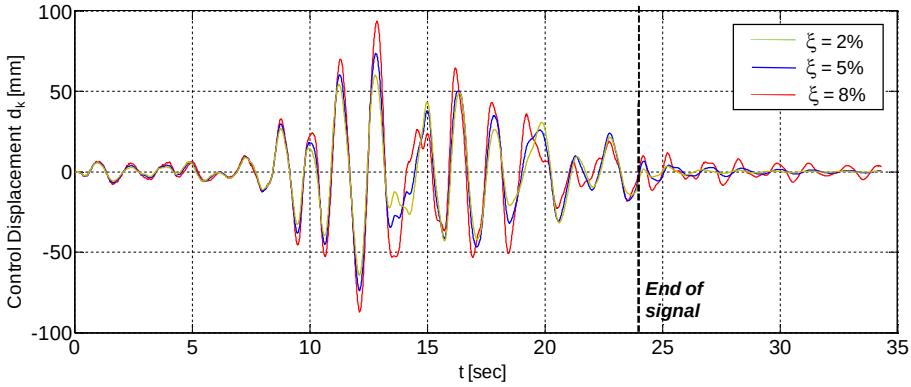

Figure 5.49. Time history of the control displacement for different damping ratios (Out-of-plane analysis, ULS limit state, accelerogram #1, Y component). Duration of the signal: 24 sec.

5.5.4. Seismic assessment by means of N2 Method

The feasibility of N2 Method when applied to masonry bridges is investigated in this section, with reference to Ronciglione Viaduct case study. In-plane and out-of-plane responses are separately analyzed, considering both ULS and DLS limit states. The parameters of the equivalent bi-linear SDOF systems are collected in Table 5.5, together with the coordinates of the Performance Point (PP) provided by non-linear dynamic analyses.

	In-plane analyses		Out-of-plane analyses	
	ULS	DLS	ULS	DLS
d*(PP)	28.6 mm	11.9 mm	50.9 mm	22.1 mm
f*(PP)	0.077 W	0.031 W	0.089 W	0.038 W
d_y*	36.6 mm	16.1 mm	41.3 mm	18.3 mm
d_u*	40.0 mm	17.1 mm	49.5 mm	20.9 mm
f_y*	0.105 W	0.046 W	0.076 W	0.034 W
μ	1.09	1.06	1.20	1.15
Γ	1.44	1.44	1.73	1.73

Table 5.5. Properties of the bi-linear equivalent systems and Performance Point coordinates provided by non-linear dynamic analyses.

The performance point identified by the N2 procedure is compared to non-linear dynamic simulations by taking the average response to each set of signals when integrally applied (IL=1.0). A significant overestimate is found for in-plane analyses (Figure 5.50), which could be attributed to the relatively low participating mass of the sixth mode (chosen as the fundamental one in the longitudinal direction), while a slight underestimate results for what concerns the out-of-plane response (Figure 5.51). Anyway, Ronciglione

Viaduct result to remain in a substantially elastic condition under the earthquake scenarios provided by the code for its construction site. This, of course, is a preliminary, anything but exhaustive, information to conclude that it is safe towards earthquakes.

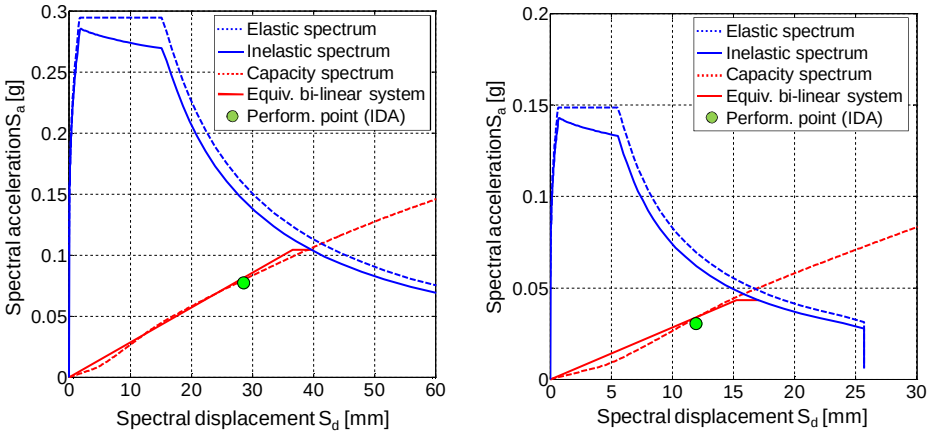

Figure 5.50. Application of the N2 Method to Ronciglione Viaduct: in-plane analyses for ULS (left) and DLS (right) limit states and comparison with IDA results.

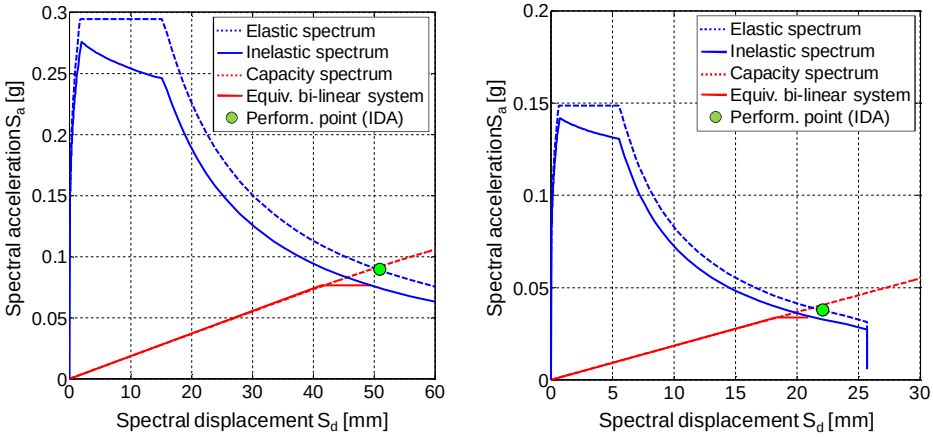

Figure 5.51. Application of the N2 Method to Ronciglione Viaduct: out-of-plane analyses for ULS (left) and DLS (right) limit states and comparison with IDA results.

Finally, an extremely severe seismic scenario (named hereafter *severe ULS*) is considered and the N2 method is applied to investigate its reliability when the response of the bridge is significantly non-linear. The assumed

elastic spectrum has an initial value of 0.29g and a maximum one equal to 0.75g. It is represented in Figure 5.52 together with the response spectrum of the 14 natural records used in non-linear dynamic analyses and their average spectrum. The accelerograms, selected and manipulated as discussed before, are collected in Table 5.6 and represented in Figure 5.53.

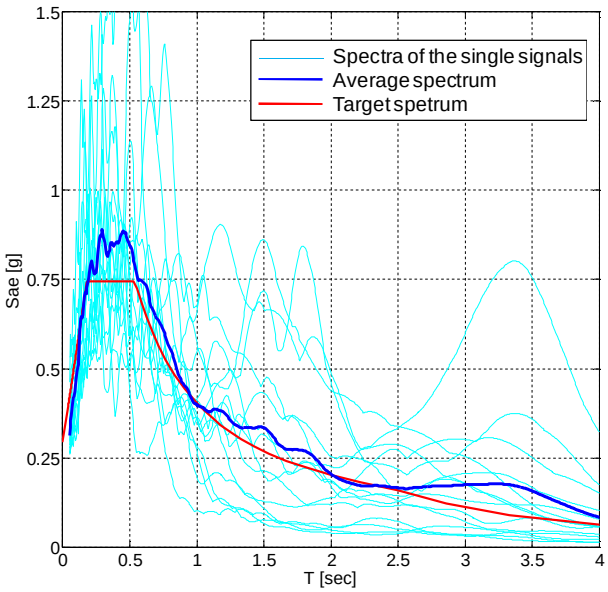

Figure 5.52. Acceleration response spectra of the selected signals, average spectrum and target spectrum.

Earthquake		Date	M_E	R_E [km]	PGA X [m/s^2]	PGA Y [m/s^2]	SF X	SF Y
#1	Izmit	17/08/1999	7.6	96	1.08	1.12	2.68	2.58
#2	Adana	27/06/1998	6.3	30	2.16	2.64	1.34	10.90
#3	Manjil	20/06/1990	7.4	91	1.30	2.05	2.23	1.41
#4	Manjil	20/06/1990	7.4	81	0.95	0.84	3.04	3.44
#5	Izmit	17/08/1999	7.6	94	1.76	1.56	1.65	1.86
#6	Racha (aftershock)	15/06/1991	6	50	0.31	0.35	9.24	8.20
#7	Izmit	17/08/1999	7.6	39	0.90	1.27	3.22	2.28
Average Values			7.1	69	1.21	1.40	3.34	4.38

Table 5.6. Selected signals for non-linear dynamic analyses on Ronciglione Viaduct under severe ULS conditions.

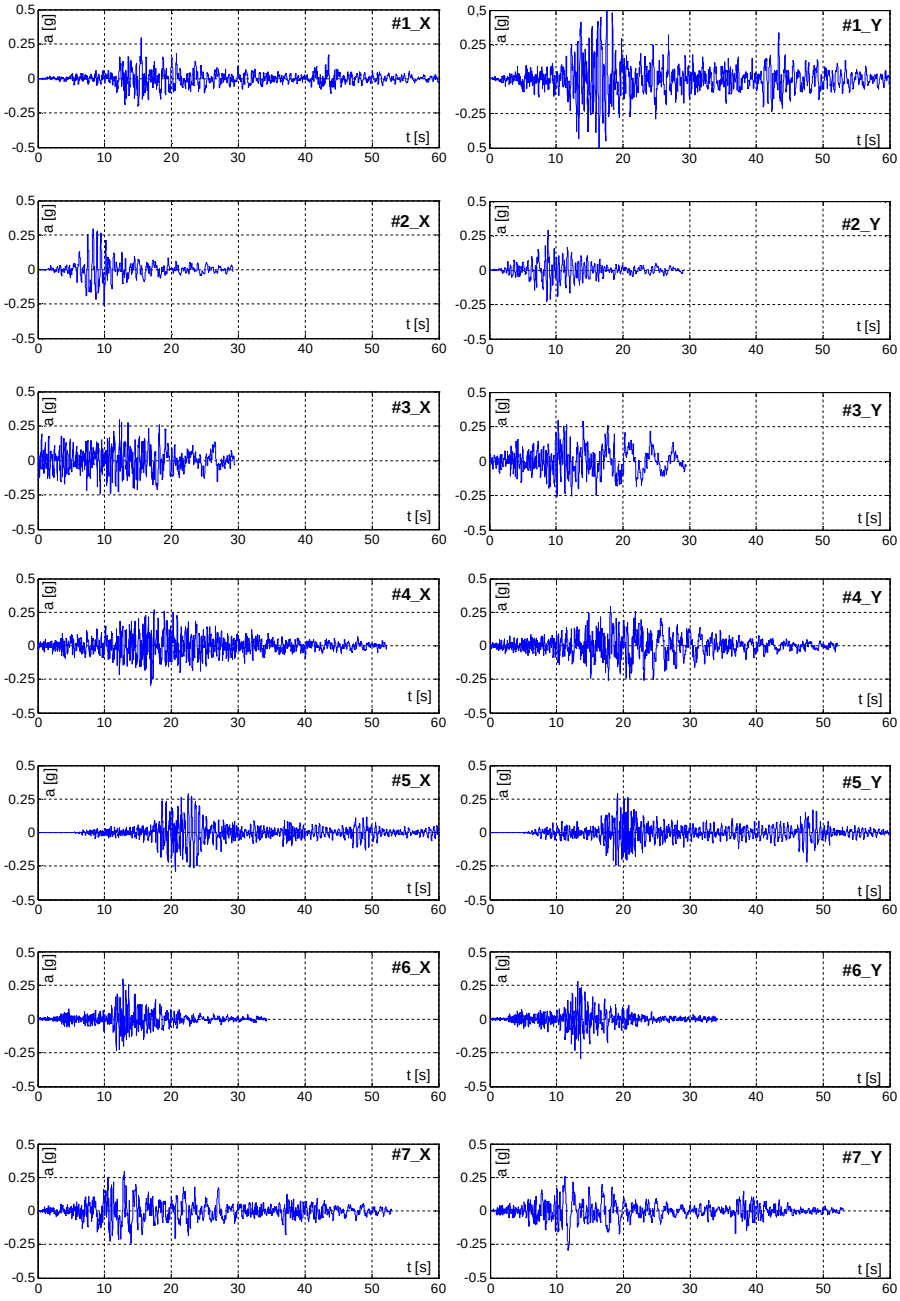

Figure 5.53. Scaled signals used for the non-linear dynamic analysis on Ronciglione Viaduct under severe ULS conditions.

	In-plane analyses	Out-of-plane analyses
d*(PP)	90.1 mm	145.1 mm
f*(PP)	0.183 W	0.131 W
d_y*	58.9 mm	82.7 mm
d_u*	118.8 mm	148.0 mm
f_y*	0.168 W	0.153 W
μ	2.02	1.79
Γ	1.44	1.73

Table 5.7. Properties of the bi-linear equivalent systems and Performance Point coordinates provided by non-linear dynamic analyses (severe ULS conditions).

The comparison between N2 method and non-linear dynamic simulations is represented in Figure 5.54 for longitudinal and transversal directions, and almost the same considerations of the previous case can be made: an overestimate (in the order of 15%) of the displacement is found for in-plane analyses, while, as regards out-of-plane response a slight underestimate (about 10%) has to be noted.

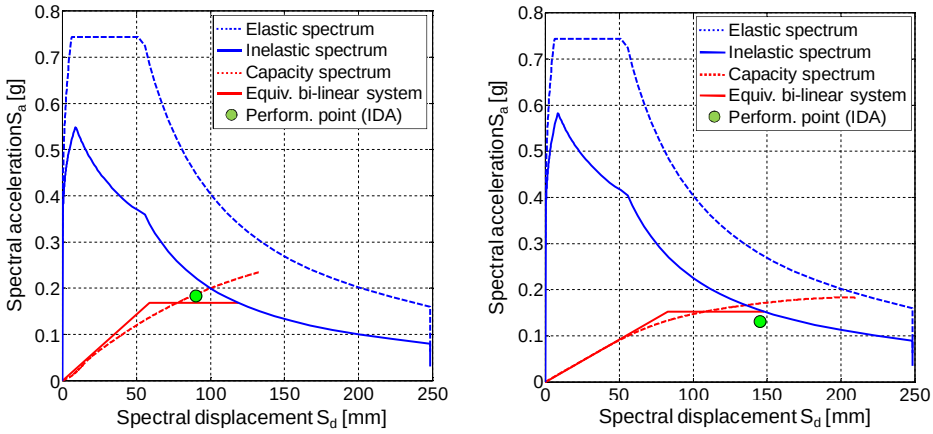

Figure 5.54. Application of the N2 Method to Ronciglione Viaduct under severe ULS limit state: in-plane (left) out-of-plane (right) analyses and comparison with non-linear dynamic analysis results.

5.6. Towards a performance-based seismic assessment

The performance-based seismic assessment (PBSA) is a general approach consisting in evaluating the performance response of a structure when subjected to a given level of seismic hazard. It has become popular in the last decades for both assessment of existing constructions and design of new ones; in fact, even if buildings conceived according to the most updated criteria performed well during strong earthquakes from a life safety perspective, their level of damage and the economic loss due to loss of use and repair were unexpectedly high.

Design for seismic resistance has met in the recent past a conceptual evolution from strength to performance (which are not considered as synonymous any more), so the idea of designing a structure having in mind some desired performance goals is not new. Anyway, the PBSA has been incorporated only in the most recently issued codes, within procedures based on push-over analysis in which the identification of damage states is made in terms of displacement thresholds. In a more general view of the PBSA framework, the performance level can be expressed in terms of stresses and loads, accelerations, displacements and drifts; the latter ones seem to be the most significant parameters, since they can be directly related to the level of damage (Ghobarah, 2001).

The PBSA has been mainly conceived and applied for r.c. and steel buildings and the scientific literature is extremely poor in application to existing masonry bridges. This is also due to the lacking of deep experimental information and surveyed data about the seismic capacity of this structural typology.

Clearly, the structural model to be adopted and the analysis to be performed for the seismic assessment depend on what phenomenon (damage, collapse) and what kind of response (global behaviour of the bridge, local response of a particular structural element) is under investigation.

As already said, the global assessment of a masonry bridge towards earthquakes requires the evaluation of the seismic response in both longitudinal and transversal directions, in which the structural behaviour may display strong differences in terms of damages, failure mechanisms, offered safety level. If a modelling approach analogous to the one proposed in this Thesis is used, some global collapse mechanisms, mainly referred to vaults and piers, can be checked within a PBSA procedure by looking at some displacement measures.

As already discussed in paragraph 5.4.1, the failure of a vault can be caused by an excessive relative displacement between the springers (in the longitudinal as well as transversal direction) or of the key with respect to the

springers, inducing distortions, loss of equilibrium and high compressive stresses, sliding between voussoirs. The failure of a pier can instead occur as a consequence of a very eccentric load resultant inducing loss of equilibrium or crushing of the material (tall piers); high shear stresses produced by excessive drifts can also induce sliding or diagonal cracks (squat piers) (Resemini, 2003; Rota, 2004).

Aiming at checking the performance level in reference of these mechanisms, some kinematic measures could be considered so as to give a synthetic description of the seismic response of a multi-span masonry viaduct (Carbone and de Felice, 2007), separately for longitudinal and transversal planes:

Longitudinal direction:

- longitudinal drift of the piers (d_L);
- relative displacement of the vault springers (v_L);

Transversal direction:

- transversal drift of the piers (d_T);
- relative displacement of the vault springers (v_T);
- transversal displacement of the key with respect to the springer (k_T).

In addition, other parameters should be checked in both directions:

- partialization of the cross section (p_L, p_T) of the vaults and of the piers, to ensure that collapse mechanisms do not occur;
- maximum compressive stress (σ_T, σ_L) in the critical sections (the ones showing maximum curvature): is has toto be lower than the material strength, to ensure that the failure is not induced by the crushing of the material.

Several other measures could also be taken as representative of particular conditions or requested performance, associated to specific needs or uses of the construction under examination. For example, the residual out-of-plane rotation of the spandrel walls and the vertical deformation of the span of a rail bridge in the longitudinal plane should be checked. The latter appear important at least with reference to an immediate use condition since it may induce a distortion of the rails and compromise the bridge practicability. However, as a general rule, residual, rather that maximum, strains and displacements should be considered (Priestley, 2000).

Four target performance levels should be considered: Serviceability limit state (SLS), Damage limit state (DLS), Ultimate limit state (ULS) and Collapse limit state (CLS), characterized by different probabilities of exceedence (p) in the reference period (V_R) equal to 81%, 63%, 10% and 5%

respectively. Under these limit states the structure is expected to remain fully operational (SLS), operational (DLS), life safe (ULS) and near collapse but not collapsed (CLS) respectively. The corresponding expected damage level is negligible, minor, moderated to extensive, very severe (Priestley, 2000).

Adequate threshold values for the response measures should be established, aiming at identifying a limited number of inequalities to verify within a seismic assessment. This is surely the most difficult step, since a wide number of experimental results, surveyed data and numerical simulations should be collected and elaborated.

The result of the assessment has finally to be represented in a capacity-demand diagram (Figure 5.55) for all the performance measures, which are evaluated my means of a push-over based method or non-linear dynamic analyses under a set of adequate records. Clearly, the former appears to be strongly preferable by professional engineers, because of the lower computational effort and time of analysis.

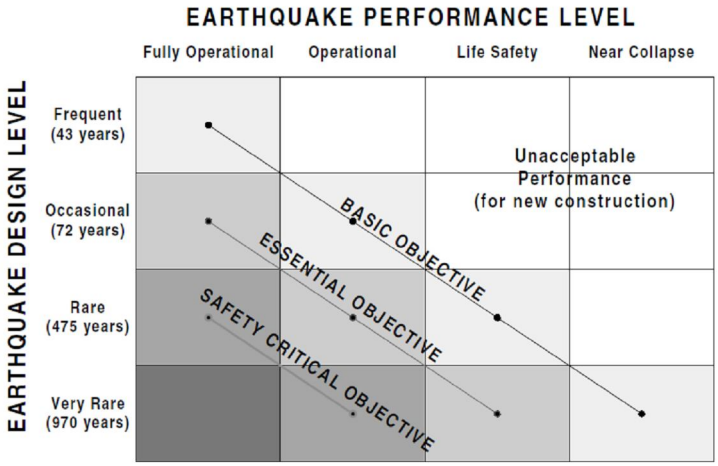

Figure 5.55. Seismic performance design objectives.
From (Bertero and Bertero, 2002).

6. Conclusions and future developments

6.1. Conclusions

The present work provides a contribution to the knowledge of the mechanical behaviour of masonry bridges, starting from the material properties, derived by means of an experimental campaign, up to the structural analysis, for which the use of a modelling approach based on fiber beam elements is adopted for load-carrying capability evaluation and seismic assessment.

In detail, the main conclusions are herewith summarized:

- The mechanical properties of historic brickwork used in the construction of arch bridges are investigated by means of cyclic compression tests under centered and eccentric loading. The compressive strength results to be between 4.5 and 7 MPa, depending on the brick arrangement, and the average stiffness is in the order of 650 MPa. A substantially linear softening phase and unloading-reloading cycles showing a negligible stiffness decrease and a low hysteretic dissipation are also found. A constitutive relation for representing the cyclic response of brickwork under compression has been defined and its parameters quantified on the base of experimental tests.

- Masonry prisms under eccentric axial load display a substantially plane cross-section behaviour, at least until severe and localized damages occur. Accordingly, a beam model with fiber cross-section is used to simulate the tests and the comparisons demonstrate its reliability in representing masonry elements under axial force and bending moment. The approach appears suitable for modelling masonry bridges, ensuring, at the same time, low computational costs and simplicity in

the determination of the parameters. The feasibility in representing the structural response of multi-span masonry bridges is demonstrated by comparisons with experimental tests and with limit analysis results.

- Structural analyses on existing bridges show that an accurate description of the material properties (crushing strength, post-peak behaviour) has important effects in terms of load-carrying capability. Totally, twelve historic rail bridges with different geometric properties are analyzed and two of them are investigated in detail, one having shallow arches and squat piers and the other one deep arches and high pillars. On the whole, the results indicate a higher load-carrying capability for bridges with shallow arches, thick vaults or low thickness-to-span ratio, and for bridges made of a single span or having squat piers. Analyses for the assessment of the load-carrying capability of multi-span masonry bridges under design loads (exercise conditions) suggest to consider only the four concentrated forces provided by the code for rail traffic, neglecting the distributed load, which may produce a load-bearing increase. Among the bridges under study, a significant overestimate of the load-carrying capacity, in the order of 35%, is found when assuming an unlimited ductility of the material, as in yield design methods.

- The dynamic response of a single arch is investigated leading to an estimate of the failure condition under impulse base motion that agrees with the one provided by the mechanism method. Sensitivity analyses reveal a dependence on the slenderness and on the size of the arch, as well as on the constitutive assumptions, especially for short impulses and high amplitude values. The response to earthquake motion, evaluated through non-linear dynamic analyses, leads to similar results and the comparison with push-over analyses, carried out under different load distributions, show that the one with both horizontal and vertical loads proportional to inertial forces provides the best agreement.

- The use of current methodologies for the seismic assessment of masonry bridges are examined with reference to an existing rail multi-span viaduct. The comparison with a 3-D finite element model reveals a good agreement in terms of natural frequencies and modal shapes, on condition that an adequate representation of pier shear deformation and spandrel wall stiffening effect is achieved. Cyclic push-over analyses under different load distributions, in both longitudinal and transversal directions, display moderate hysteretic dissipation and lower resistance and stiffness under out-of-plane forces. On the one hand, the comparison of push-over with incremental non-linear dynamic

analyses (IDA), carried out under sets of 14 natural records, shows a good agreement, provided that loads proportional to inertial forces are used; a pronounced sensitivity to damping is also found in dynamic simulations. On the other hand, the seismic assessment through the N2 method, as proposed in Eurocode 8 (CEN-EN 1998, 2005) and in Italian code (Nuove norme tecniche per le costruzioni, 2008), is not completely satisfactory. In the examined case, a slight underestimate of the displacement in transversal direction and a significant overestimate in longitudinal direction are found. Such a mismatch depends on the non-negligible contribution of higher modes, especially for in-plane behaviour, and on the difficulty in representing the bridge response by means of a bi-linear SDOF system.

6.2. Future developments

This works faces some of the most important issues in the structural analysis of masonry bridges, bringing to light the main problematic points related to these features and motivating numerous areas of continued research. Some of the available future developments of the research work presented in this Thesis are herewith indicated:

- One of the main improvements of the proposed modelling approach is represented by a more accurate description of spandrel walls and fill soil, whose contribution to the structural response is definitely non-negligible. One way could be to use 2-D multi-layered elements to describe, separately, walls and soil, treated as equivalent homogenized continua, similarly to what is proposed in (Cavicchi and Gambarotta, 2005; 2007) in the context of limit analysis.

- As regards the dynamic response of arches under earthquake motion, the achieved results should be extended to a wide number of geometric configurations and records, also including the vertical component of the seismic action. This is one of the research works currently under development by the author.

- The achievement of an accurate representation of the seismic response of multi-span masonry bridges deserves further investigation, which cannot prescind from experimental activities to

determine the effective contribution of some structural elements (like the spandrel walls) to the overall response, the damping parameters to assume in non-linear dynamic analyses and the threshold values for the structure state variables that synthetically describe the response performance.

– Finally, the methodologies and assessment criteria developed in the Thesis should be applied to a wide number of bridges in the perspective of defining detailed instructions to be included in guidelines addressed to professional engineers. An effort should be made in the field of the seismic assessment of masonry bridges on performance basis, which is definitely one of the most interesting and promising research branches for the next future.

References

Ali, S. S., Page, A. W. 1988. Finite element model for masonry subjected to concentrated loads. Journal of Structural Engineering, ASCE, 114(8):1761-1784.

AlShebani, M., Sinha, S. 1999. Stress-Strain characteristics of brick masonry under uniaxial cyclic loading. Journal of Structural Engineering, ASCE, 125(6):600-604.

Antoniou, S., Pinho, R. 2004. Development and verification of a displacement-based adaptive push-over procedure. Journal of Earthquake Engineering, 8(5):643-661.

Anziani, A., Binda, L., Mirabella Roberti, G. 2000. The effect of heavy persistent actions into the behaviour of ancient masonry. Materials and Structures, 33:251-261.

Aprile, A., Benedetti, A., Grassucci, F. 2001. Assessment of cracking and collapse for old brick masonry columns. Journal of Structural Engineering, ASCE, 127(12):1427-1435.

ATC-40. 1996. Seismic evaluation and retrofit of concrete buildings. Applied Technology Council. US Standard.

Auric, A. 1911 Ponts en maçonnerie (calculs et construction). O. Doin et fils: Paris, France. [in French].

Barbi, L., Briccoli Bati, S., Ranocchiai, G. 2002. Mechanical properties of ancient bricks: statistical analysis of data. In Proc. of 7th International Seminar on Structural Masonry for Developing Countries, Belo Horizonte, Brazil.

Baronio, G., Binda, L., Tedeschi, C., Tiraboschi, C. 2003. Characterization of the materials used in the construction of the Noto Cathedral. Construction and Building Materials, 17:557-571.

Beconcini, M. L., Buratti, G., Croce, P., Mengozzi, M., Orsini, P., Luise, M. 2007. Dynamic characterization of a five spans historical masonry arch bridge. In Proc. of ARCH'07, 5th International Conference on Arch Bridges, Madeira, Portugal.

Belidor, B. F. 1729. La Science des ingénieurs dans la conduite des travaux de fortification et d'architecture civile. Paris: Claude Jombert: Paris, France. [in French].

Benedetti, D., Carydis, P., Pezzoli, P. 1998. Shaking table tests on 24 simple masonry buildings. Earthquake Engineering and Structural Dynamics, 27:67-90.

Bertero, R. D., Bertero V. V. 2002. Performance-based seismic engineering: the need for a reliable conceptual comprehensive approach. Earthquake Engineering and Structural Dynamics, 31:627-652.

Beyer, K., Bommer, J. J. 2007. Selection and scaling of real accelerograms for bi-directional loading: a review of current practice and code provisions. Journal of Earthquake Engineering, 11:13-45.

Binda L., Baronio, G., Tiraboschi, C., Tedeschi, C. 2003. Experimental research for the choice of adequate materials for the reconstruction of the Cathedral of Noto. Construction and Building Materials, 17:629-639.

Binda, L., Fontana, A., Frigerio, G. 1988. Mechanical behaviour of brick masonries derived from unit and mortar characteristics. In Proc. of 8th International Brick/Block Masonry Conference, Dublin, Ireland.

Bommer, J. J., Acevedo, A. B. 2004. The use of real earthquake accelerograms as input to dynamic analysis. Journal of Earthquake Engineering, 8(1):43-91.

Boothby, T. E. 1997. Elastic plastic stability of jointed masonry arches. Engineering Structures 19(5):345-351.

Boothby, T. E. 2001. Load rating of masonry arch bridges. Bridge Engineering, 6(2):79-86.

Brencich, A., Colla, C. 2002. The influence of construction technology on the mechanics of masonry railway bridges. In Proc. of Railway Engineering 2002, 5th International Conference and Exhibition, London,

Brencich, A., Corradi, C., Gambarotta, L. 2006. Strength of eccentrically compressed brickwork pillars: a theoretical and experimental analysis. In Proc. of 7th International Masonry Conference, London, UK.

Brencich, A., Corradi, C., Gambarotta, L., Mantegazza, G., Sterpi E. 2002. Compressive strength of solid clay brick masonry under eccentric loading. In Proc. of 6th International Masonry Conference, London, UK.

Brencich, A., de Felice, G. 2009. Brickwork under eccentric compression: experimental results and macroscopic models. Construction and Building Materials, 23:1935–1946.

Brencich, A., De Francesco, U. 2004a. Assessment of multi-span masonry arch bridges. Part I: A simplified approach. Journal of Bridge Engineering, ASCE, 9:582-590.

Brencich, A., De Francesco, U. 2004b. Assessment of multi-span masonry arch bridges. Part II: Examples and applications. Journal of Bridge Engineering, ASCE, 9:591-598.

Brencich, A., De Francesco, U., Gambarotta, L. 2004. Non linear elasto-plastic collapse analysis of multispan masonry arch bridges. Journal of Bridge Engineering, 9(6):582-590.

Brencich, A., Gambarotta, L. 2005. Mechanical response of solid clay brickwork under eccentric loading. Part I: Unreinforced masonry. Materials and Structures, 38:257-266.

Brencich, A., Gambarotta, L., Sterpi, E. 2007. Stochastic distribution of compressive strength: effects on the load carrying capacity of masonry arches. In Proc. of ARCH'07, 5th International Conference on Arch Bridges, Madeira, Portugal.

Brencich, A., Morbiducci, R. 2007. Masonry arches: historical rules and modern mechanics. International Journal of Architectural Heritage, 1(2):165-189.

Brencich, A., Sabia, D. 2007. Tanaro bridge: dynamic tests on a couple of spans. Bridge Engineering, 12(5):662-665.

Breymann, G. A. 1926. Trattato di costruzioni civili. Vallardi: Milan, Italy. [in Italian].

Brookes, C. L. 2008. Assessment and strengthening masonry arch bridges. In Proc. of SAHC'06, 6th International Conference on Structural Analysis of Historic Constructions, Bath, UK.

Brooks, J. J., Abdullah, C. S., Forth, J. P., Bingel, P. R. 1997. The effect of age on the deformation of masonry. Masonry International, 12(2):51-55.

Brooks, J. J., Abu Baker B. H. 2004. Shrinkage and creep of masonry mortar. Materials and Structures, 37:117-183.

Brooks, J. J., Abu Baker, B. H. 1998. The modulus of elasticity of masonry. Masonry International, 12(2):58-63.

Campanella, G. 1928. Trattato generale teorico pratico dell'arte dell'ingegnere civile, industrial ed architetto: ponti in muratura. Vallardi: Milan, Italy. [in Italian].

Carbone, I., de Felice, G. 2007. Fragilità di ponti ad arco in muratura sotto azioni sismiche longitudinali. In Proc. of XII Convegno di Ingegneria Sismica ANIDIS, Pisa, Italy. [in Italian].

Cavalieri, L., Failla, A., La Mendola, L., Papia, M. 2005. Experimental and analytical response of masonry elements under eccentric vertical loads. Engineering Structures, 27:1175-1184.

Cavicchi, A., Gambarotta, L. 2005. Collapse analysis of masonry bridges taking into account arch-fill interaction. Engineering Structures, 27:605-615.

Cavicchi, A., Gambarotta, L. 2007. Lower bound limit analysis of masonry bridges including arch-fill interaction. Engineering Structures, 29:3002-3014.

CEN - EN 1991. 2005. Eurocode 1: Actions on structures. European Standard.

CEN - EN 1998. 2005. Eurocode 8: Design of structures for earthquake resistance. European Standard.

Chang, G., Mander, J. 1994. Seismic Energy Based Fatigue Damage Analysis of Bridge Columns: Part I – Evaluation of Seismic Capacity. NCEER Technical Report 94-6.

Chopra, A. K. 2006. Dynamics of structures. Prentice Hall: Upper Saddle River, NJ, USA.

Chopra, A. K., Goel, R. K. 2002. A modal push-over analysis procedure for estimating seismic demands for buildings. Earthquake Engineering and Structural Dynamics, 31:561-582.

Chowdhury, I., Dasgupta, S. P. 2003. Computation of Rayleigh damping coefficients for large systems. The Electronic Journal of Geotechnical Engineering, 8(C).

Clemente, P. 1998. Introduction to dynamics of stone arches. Earthquake Engineering and Structural Dynamics, 27(5):513-522.

Clemente, P., Buffarini, G., Rinaldis, D. 2010. Application of limit analysis to stone arch bridges. In Proc. of ARCH'10, 6th International Conference on Arch Bridges, Fuzhou, China.

Clemente, P., Occhiuzzi, A., Raithel, A. 1995. Limit behaviour of stone arch bridges. Journal of Structural Engineering, 121(7):1045-1050.

Curioni, G. 1874. L'arte del fabbricare, ossia corso complete di istituzioni teorico-pratiche. Negro: Torino, Italy [in Italian].

Da Porto, F., Franchetti, P., Grendene, M., Ranzato, L., Valluzzi, M., Modena, C. 2007. Structural capacity of masonry arch bridges to horizontal loads. In Proc. of ARCH'07, 5th International Conference on Arch Bridges, Madeira, Portugal.

de Felice, G. 2001. Overall elastic properties of brickwork via homogenization. In Structural Engineering, Mechanics and Computation, Zingoni Editor, Elsevier: Amsterdam, 1:411-418.

de Felice, G. 2007. Load-carrying capacity of multi-span masonry arch bridges having limited ductility. In Proc. of ARCH'07, 5th International Conference on Arch Bridges, Madeira, Portugal.

de Felice, G. 2009. Assessment of the load-carrying capacity of multi-span masonry arch bridges using fibre beam elements. Engineering Structures, 31(8):1634-1647.

de Felice, G., Carbone, I. 2006. Experimental investigation on historic brickwork subjected to eccentric axial loads. In Proc. of SAHC'06, 5th International Conference on Structural Analysis of Historic Constructions, New Delhi, India.

De Lorenzis, L., DeJong, M., Ochsendorf, J. A. 2007a. Failure of masonry arches under impulse base motion. Earthquake Engineering and Structural Dynamics, 36:2119-2136.

De Lorenzis, L., Dimitri, R., La Tegola, A. 2007b. Reduction of the lateral thrust of masonry arches and vaults with FRP composites. Construction and Building Materials 21:1415–1430.

De Luca, A., Giordano, A., Mele, E. 2004. A simplified procedure for assessing the seismic capacity of masonry arches. Engineering Structures, 26:1915-1929.

DeJong, M. J., De Lorenzis, L., Adams, S., Ochsendorf, J. A. 2008. Rocking stability of masonry arches in seismic regions. Earthquake Spectra, 24(4):847-865.

DeJong, M., Ochsendorf, J. A. 2006. Analysis of vaulted masonry structures subjected to horizontal ground motion. In Proc. of SAHC'06, 5th International Conference on Structural Analysis of Historic Constructions, New Delhi, India.

Department of Transport. 1997. Design manual for roads and bridges. Vol. 3, Sec. 4, Part 4, The assessment of highway bridges and structures. London, UK.

Ding, D. 1997. Studies on brick masonry under compression. Materials and Structures, 30:247-252.

Domède, N., Sellier, A. 2010. Numerical analysis of masonry arch bridges: benefits and limits of damage mechanics. In Proc. of ARCH'10, 6th International Conference on Arch Bridges, Fuzhou, China.

Drosopoulos, G. A., Stavroulakis, G. E., Massalas, C. V. 2007. FRP reinforcement of stone arch bridges: Unilateral contact models and limit analysis. Composites: Part B, 38: 144–151.

Drysdale, R. G., Hamid, A. A. 1982. Effect of eccentricity on the compressive strength of brickwork. Journal of the British Ceramic Society, 30:102-108.

Dupuit, J. 1870. Traité de l'équilibre des routes et de la construction des pontes en maçonnerie. Dunod: Paris, France. [in French].

Elmenshawi, A., Sorour, M., Mufti, A., Jaeger, L. G., Shrive, N. 2010. Damping mechanisms and damping ratios in vibrating unreinforced stone masonry. Engineering Structures, 32:3269-3278.

Erdman, A., Sandor, G. 1984. Mechanism Design. Analysis and Synthesis. Prentice-Hall: Englewood Cliffs, NJ, USA.

Ewing, D. E., Kowalsky, M. J. 2004. Compressive behavior of unconfined and confined clay brick masonry. Journal of Structural Engineering, ASCE, 130(4):650-661.

Fajfar, P. 1999. Capacity spectrum method based on inelastic demand spectra. Earthquake Engineering and Structural Dynamics, 28:979-993.

Fajfar, P., Gašperšič, P. 1996. The N2 method for the seismic damage analysis of RC buildings. Earthquake Engineering and Structural Dynamics, 25:31-46.

Fanning, P. F., Boothby, T. E. 2001. Three-dimensional modelling and full-scale testing of stone arch bridges. Computers and Structures, 79:2645-2662.

Fanning, P. J., Sobczak, L., Boothby, T. E., Salomoni, V. 2005. Load testing and model simulations for a stone arch bridge. Journal of Bridge Engineering, ASCE, 1(4):367-378.

FEMA-273. 1997. NEHRP guidelines for the seismic rehabilitation of buildings. FEMA Publication 273. National Earthquake Hazards Reduction Program. Federal Emergency Management Agency. US Standard.

Ferracuti, B., Pinho, R., Savoia, M. 2008. Statistical validation of nonlinear push-over methods by incremental dynamic analyses. Valutazione e riduzione della vulnerabilità sismica di edifici esistenti in cemento armato. Polimetrica: Milano, Italy.

Ferrovie dello Stato. 1907. Modalità da adottarsi per la compilazione dei progetti dei manufatti, muri e gallerie. Grafica Editrice Politecnica: Torino [in Italian].

Foraboschi, P. 2004. Strengthening of masonry arches with fiber-reinforced polymer strips. Journal of Composites for Construction Construction, ASCE, 8(3):191-202.

Francis, A. J., Horman, C. B., Jerrems, L. E. 1971. The effect of joint thickness and other factors on the compressive strength of brickwork. In Proc. of 2nd International Brick/Block Masonry Conference, Stoke on Kent, UK.

Freeman, S. A., 1998. Development and use of capacity spectrum method. In Proc. of 6th US National Conference on Earthquake Engineering, Seattle, WA, USA.

Freeman, S. A., Nicoletti, J. P. Tyrell, J. V. 1975. Evaluations of existing buildings for seismic Risk. A case study of Puget Sound Naval Shipyard, Bremerton, Washington. In Proc. of 1st US National Conference on Earthquake Engineering, Berkeley, CA, USA.

Gambarotta, L., Brencich, A., Cavicchi, A., Sterpi, E. 2006. Vulnerabilità sismica dei ponti in muratura. Rapporto di Ricerca, Progetto RELUIS 2005-2008, Linea di Ricerca n.3, U. R. 3 (Valutazione e riduzione del rischio sismico dei ponti esistenti, Ponti in muratura). [in Italian].

Gauthey, E. C. M. 1809. Traité de la construction des ponts. Didot: Paris, France. [in French].

Gautier, H. 1716. Traité des ponts. Cailleau: Paris, France. [in French].

Gay, C., 1924. Ponts en Maconnerie. Encyclopedie de génie civil et des travaux publics. J. B. Bailliére et fils: Paris, France. [in French].

Ghobarah, A. 2001. Performance-based design in earthquake engineering: state of development. Engineering Structures, 23:878-884.

Gilbert, M. 2005. Ring, theory and modelling guide. University of Sheffield, Sheffield, UK.

Gilbert, M., Melbourne, C. 1994. Rigid-block analysis of masonry structures. Structural Engineering, 72(21):356-361.

Gilbert, M., Nguyen, D.P., Smith, C.C. 2007a. Computational limit analysis of soil-arch interaction in masonry arch bridges. In Proc. of ARCH'07, 5th International Conference on Arch Bridges, Madeira, Portugal.

Gilbert, M., Smith, C. C., Wang, J., Callaway Ph. A., Melbourne, C. 2007b. Small and large-scale experimental studies of soil-arch interaction in masonry bridges. In Proc. of ARCH'07, 5th International Conference on Arch Bridges, Madeira, Portugal.

Goel, R. K., Chopra, A. K. 2005. Role of higher-mode push-over analysis in seismic analysis of buildings. Earthquake Spectra, 21(4):1027-1041.

Harvey, W. J. 1988. Application of the mechanism analysis to masonry arches. The Structural Engineer, 66(5):77-84.

Harvey, W. J., Smith, F. W. 1991. The behaviour and assessment of multi-span arches. The Structural Engineer, 69(24):411-417.

Harvey, W. J., Tomor, A. K., Simon, J. 2001. Application of Moire photography for internal load distribution in arches and walls. The Structural Engineer, 79(3):14-18.

Harvey, W. J., Tomor, A. K., Smith, F. 2005. A three dimensional model for arch bridge behaviour. Structural Engineering International, 2:101-104.

Heyman, J. 1966. The stone skeleton. International Journal of Solids and Structures, 2(2):249-279.

Heyman, J. 1982. The masonry arch. Ellis Horwood: London, UK.

Hilsdorf, H. K. 1969. Investigation into the failure mechanism of brick masonry loaded in axial compression. In Designing Engineering and Construction with Masonry Products. Johnson F. B. Editor (Gulf Publishing): Huston, Texas, US.

Hoffmann, G., Schubert, P. 1994. Compressive strength of masonry parallel to the bed joints. In Proc. of 10th International Brick/Block Masonry Conference, Calgary, Alberta, Canada.

Housner, G. W. 1963. The behaviour of inverted pendulum structures during earthquakes. Bulletin of the Seismological Society of America, 53(2):403-417.

Hughes, T. G., Blackler, M. J. 1997. A review of the UK masonry arch assessment methods. In Proc. of Institute of Civil Engineering, 122:305-315.

Hughes, T. G., Pritchard, R. 1998. In situ measurement of dead and live load stresses in a masonry arch. Engineering Structures, 20:5-13.

ICOMOS/ISCARSAH. 2003. Recommendations for the analysis, conservation and structural restoration of architectural heritage.

Iervolino, I., Galasso, C., Cosenza, E. 2009a. REXEL: computer aided record selection for code-based seismic structural analysis. Bulletin of Earthquake Engineering, 8:339-362.

Iervolino, I., Maddaloni, G,. Cosenza, E. 2008. Eurocode 8 compliant real record sets for seismic analysis of structures. Journal of Earthquake Engineering, 12:54-90.

Iervolino, I., Maddaloni, G,. Cosenza, E. 2009b. A note on selection of time-histories for seismic analysis of bridges in Eurocode 8. Journal of Earthquake Engineering, 13:1125-1152.

Iervolino, I., Manfredi, M., Cosenza, E. 2006. Ground motion duration effects on nonlinear seismic response. Earthquake Engineering and Structural Dynamics, 35:21-38.

ISO 13822. 2010. Bases for design of structures - Assessment of existing structures. International Standard.

Jorini, A. F. 1918. Teoria e pratica della costruzione dei ponti. Ulrico Hoepli Editore: Milano, Italy. [in Italian].

Juhásová, E., Sofronie, R., Bairrão, R. 2008. Stone masonry in historical buildings - Ways to increase their resistance and durability. Engineering Structures, 30:2194-2205.

Kent, D. C., Park, R. 1971. Flexural members with confined concrete. Journal of the structural division ASCE, 97(7):1969-1990.

Lagomarsino, S., Galasco, A., Penna, A. 2002. Pushover and dynamic analysis of URM buildings by means of a non-linear macro-element model. In Proc. of the

International Conference Earthquake Loss Estimation and Risk Reduction, Bucharest, Romania.

Lemos, J. V. 2007. Discrete element modelling of masonry structures. International Journal of Architectural Heritage, 1(2):190-213.

Léon, J., Espejo, S. R. 2007. Load test to collapse on the masonry arch bridge at Urnieta. In Proc. of ARCH'07, 5th International Conference on Arch Bridges, Madeira, Portugal.

Léon, J., Martinez, J. L., Martin-Caro, J. A. 2004. Widening, strengthening and repair of a masonry bridge in Ponteceso (Galicia, Spain). In: Arch Bridges IV, Advances in Assessment Structural Design and Construction (Roca, P. and Molins, C.). CIMNE: Barcelona, Spain.

Linee guida per la valutazione e riduzione del rischio sismico del patrimonio culturale. 2006. Ministero per i beni e le attività culturali. Gangemi Editore: Roma, Italy. Italian Standard. [in Italian].

Litewka, A., Szojda, L. 2006. Damage, plasticity and failure of ceramic and cementitious composites subjected to multi-axial state of stress. International Journal of Plasticity, 22:2048-2065.

Lourenço, P. B. 1994. Analysis of masonry structures with interface elements: theory and applications. Report No. 03-21-22-0-01, Delft University of Technology, Delft, the Netherlands.

Lourenço, P. B. 1998. Experimental and numerical issues in the modelling of the mechanical behavior of masonry. In Proc. 2nd SAHC'98 International Conference on Structural Analysis of Historical Constructions, Barcelona, Spain.

Lourenço, P. B., Hunegn, T., Medeiros, P., Peixinho, N. 2010. Testing and analysis of masonry arches subjected to impact loads. In Proc. of ARCH'10, 6th International Conference on Arch Bridges, Fuzhou, China.

Ma, M. Y., Pan, A. D., Luan, M., Gebara, J. M. 1995. Stone arch analysis by the DDA method. In: Arch Bridges (Melbourne, C.). Thomas Telford ed.: London, UK.

Mann, W., Betzler, M. 1994. Investigations on the effect of different forms of test samples to test the compressive strength of masonry. In Proc. of 10th International Brick/Block Masonry Conference, Calgary, Alberta, Canada.

Mautner, M., Reiterer, M. 2007. Measurements of dynamic deformation behaviour of masonry arch bridges. In Proc. of ARCH'07, 5th International Conference on Arch Bridges, Madeira, Portugal.

Mazzon, N., Valluzzi, M., Aoki, T., Garbin, E., De Canio, G., Ranieri, N. Modena, C. 2009. Shaking table tests on two multi-leaf stone masonry buildings. In Proc. of 11th Canadian masonry symposium, Toronto, Ontario, Canada.

McNary, W. S., Abrams, D. P. 1985. Mechanics of masonry in compression. Journal of Structural Engineering, ASCE, 114(4):857-870.

Melbourne, C., Gilbert, M., Wagstaff, M. 1997. The collapse behaviour of multispan brickwork arch bridge. The Structural Engineer, 75(17):297-305.

Melbourne, C., Tomor, A. 2006. Application of acoustic emission for masonry arch bridges. Strain, International Journal for Strain Measurement, 42(3):165-172.

Melbourne, C., Tomor, A. K. 2004. Fatigue performance of composite and radial-pin reinforcement on multi-ring masonry aches. In Proc. of ARCH'04, 4th International Conference on Arch Bridges, Barcelona, Spain.

Melbourne, C., Tomor, A.K., Wang, J. 2007. A new masonry arch bridge assessment method (SMART). Bridge Engineering, ICE, 160(2):81-87.

Melbourne, C., Wagstaff, M. 1993. Load tests to collapse of three large-scale multi-span brickwork arch bridges. In Bridge management. Vol. 2, Inspection, maintenance assessment and repair. Thomas Telford: London, UK.

Mery, E. 1840. Sur l'equilibre des voutes en berceau. Annales des Ponts et Chaussées (XIX). [in French].

Middendorf, B., Hughes, J. J., Cakkebaut, K., Baronio, G., Papayianni, I. 2005. Investigative methods for the characterisation of historic mortars. Materials and Structures, 38:761-769.

Mojsilović, N. 2005. A discussion of masonry characteristics derived from compression tests. In Proc. of 10th Canadian masonry symposium, Banff, Alberta, Canada.

Mojsilović, N., Marti, P. 1997. Strength of masonry subjected to combined loads. ACI Structural Journal, 94(6):633-42.

Mojsilović, N., Marti, P. 2002. Eccentric shear and normal forces in structural masonry. In Proc. of 6th International Masonry Conference, London, UK.

Molins, C., Roca, P. 1998. Capacity of masonry arches and spatial structures. Journal of Structural Engineering, ASCE, 124(6):653-663.

Nuove norme tecniche per le costruzioni (Decreto del Ministero delle Infrastrutture 14/01/2008) e circolare esplicativa (Circolare 617/C.S.LL.PP. 02/02/2009). Italian Standard. [in Italian].

Oliveira, D. V., Lourenço, P. B., Lemos, C. 2010. Geometric issues and ultimate load capacity of masonry arch bridges from the northwest Iberian Peninsula. Engineering Structures, 32(12):3955-3965.

Oliveira, D. V., Costa, V. M., Sousa, J. F., Lourenço, P. B.. Diagnosis and repair of a historic stone masonry arch bridge. In Proc. of ARCH'10, 6th International Conference on Arch Bridges, Fuzhou, China.

Oliveira, D. V., Lourenço, P. B., Roca, P. 2006. Cyclic behavior of stone and brick masonry under uniaxial compressive loading. Materials and Structures, 39(2):219-227.

Olivito, R. S., Stumpo, P. 2001. Fracture mechanics in the characterization of brick masonry structures. Materials and Structures, 34: 217-223.

Oppenheim, I. J. 1992. The masonry arch as a four-link mechanism under base motion. Earthquake Engineering and Structural Dynamics, 21:1005-1017.

Orakcal, K., Massone, L., Wallace, J. 2006. Analytical modeling of reinforced concrete walls for predicting flexural and coupled shear-flexural responses. PEER Report 2006/07.

Page, A. W. 1978. Finite element model for masonry. Journal of the Structural Division, ASCE, 104(8):1267-1285.

Page, A. W. 1981. The biaxial compressive strength of brick masonry. In Proc. of the Institution of Civil Engineers, 71(2):893-906.

Page, A. W. 1983. The strength of brick masonry under biaxial compression-tension. International Journal of Masonry Construction, 3:26-31.

Page, J. 1987. Load tests on two arch bridges at Preston, Shropshire and Prestwood, Staffordshire. Research report 101, Transport and road research laboratory, Department of Transport, Crowthorne, England, UK.

Pelà, L., Aprile, A., Benedetti, A. 2009. Seismic assessment of masonry arch bridges. Engineering Structures, 31(8):1777-1788.

Perronet, J. R. 1788. Construire des ponts au XVIII siecle. Ecole Royal des Ponts et Chaussées: Paris, France. [in French].

Prentice, D. J., Ponniah, D. A. 1994. Testing of multi-span model of masonry arch bridges. In Proc. of Centenary Year Bridge Conference, Cardiff, UK.

Priestley, M. J. N. 2000. Performance based seismic design. In Proc. 12WCEE, 12th World Conference on Earthquake Engineering, Auckland, New Zealand.

Priestley, M. J. N., Calvi, G. M., Kowalsky, M. J. 2007. Displacement-based seismic design of structures. IUSS Press: Pavia, Italy.

Ramos, L. F., Lourenço, P. B., De Roeck, G., Campos-Costa, A. 2007. Progressive damage analysis based on vibration signatures: an application to a masonry arch. In Proc. of ARCH'07, 5th International Conference on Arch Bridges, Madeira, Portugal.

Resemini, S. 2003. Vulnerabilità sismica dei ponti ferroviari ad arco in muratura. Ph.D. Thesis. Università degli Studi di Genova, Italy. [in Italian].

Resemini, S., Lagormarsino, S. 2007. Displacement-based methods for the seismic assessment of masonry arch bridges. In Proc. of ARCH'07, 5th International Conference on Arch Bridges, Madeira, Portugal.

Roberts, T. M., Hughes, T. G., Dandamundi, V. R., Bell, B. 2006. Quasi-static and high cycle fatigue strength of brick masonry. Construction and Building Materials, 20:603-614.

Robinson, J. I., Ponniah, D. A., Prentice, D. J. 1997. Soil pressure measurements on a multi-span brick arch. In Proc. of 7th International Conference on Structural Faults and Repair, Edinburgh, UK.

Rofflaen, E. 1881. Traité théorique et pratique sur la résistance des matériaux dans les constructions. Se éd.: Paris, France. [in French].

Rondelet, G. 1802. Traité theorique et pratique de l'art de bâtir. Didot Frères Fils et Cie Ed.: Paris, France.

Ross, A. D. 1937. Concrete creep data. The Structural Engineer, 15(8):314-326.

Rosson, B. T., Soyland, K. 1998. Inelastic behavior of sand-lime mortar joint masonry arches. Engineering Structures, 20(1-2):14-24.

Rota, M. 2004. Seismic vulnerability of masonry arch bridge walls. MSc Dissertation. Rose School, Pavia, Italy.

Rota, M., Pecker, A., Bolognini, D., Pinho, R. 2005. A methodology for seismic vulnerability of masonry arch bridge walls. Journal of Earthquake Engineering, 9(2):331-353.

Sakai, J., Kawashima, K. 2000. Un unloading and reloading stress-strain model for concrete confined by tie reinforcements. In Proc. 12WCEE, 12th World Conference on Earthquake Engineering, Auckland, New Zealand.

Sala, E., Giustina, I., Plizzari, G. A. 2008. Lime mortar with natural pozzolana: historical issues and mechanical behavior. In Proc. of SAHC'06, 6th International Conference on Structural Analysis of Historic Constructions, Bath, UK.

Scott, B., Park, D. R., Priestley, M. J. N. 1982. Stress-strain behaviour of concrete confined by overlapping hoops at low and high strain rates. Structural Journal of the ACI, 79(1):13-27.

Séjourné, P. 1913. Grandes voutes. Imprimerie Veuve Tardy: Bourges, France

Shi, G. H. 1988. Discontinuous deformation analysis. A new numerical model for statics and dynamics of block systems. PhD Thesis, University of California, Berkeley, CA, USA.

Shome, N., Cornell, C. A., Bazzurro, P., Carballo, J. E. 1998. Earthquakes, records and non linear responses. Earthquake Spectra, 14(3):469-500.

Shrive, N. G. 1985. Compressive strength and strength testing of masonry. In Proc. of 7th International Brick/Block Masonry Conference, Melbourne, Australia.

Shubert, P. 1988. Compressive and tensile strength of masonry. In Proc. of 8th International Brick/Block Masonry Conference, Dublin, Ireland.

Sima, J. F., Roca, P., Molins, C. 2008. Cyclic constitutive model for concrete. Engineering Structures, 30:695-706.

Sinopoli, A. 2010. A semi-analytical approach for the dynamics of the stone arch. Engineering and Computational Mechanics, ICE, 163(3):167-178.

Società italiana per le strade ferrate del Mediterraneo. 1894. Ferrovia Roma-Viterbo con diramazione per Ronciglione. [in Italian].

Società italiana per le strade ferrate del Mediterraneo. 1906. Relazione sugli studi e lavori eseguiti dal 1897 al 1905 con 74 tavole. Tipografia Squarci: Roma, Italy. [in Italian].

Spacone, E., Filippou, F. C., Taucer, F. F. 1996. Fiber beam-column model for non-linear analysis of R/C frames. Part 1: formulation. Earthquake Engineering and Structural Dynamics, 25:711-25.

Taucer, F. F., Spacone, E., Filippou, F. C. 1991. A fiber beam-column element for seismic response analysis of reinforced concrete structures. Report No.

UCB/EERC-91/17, Earthquake Engineering Research Center College of Engineering University of California, Berkeley.

Tomor, A. K., Melbourne, C. 2007. Condition monitoring of masonry arch bridges using acoustic emission technique. Structural Engineering International, 17(2):188-192.

Tomor, A., Wang, J. 2010. Fracture development process for masonry under static and fatigue loading. In Proc. of ARCH'10, 6th International Conference on Arch Bridges, Fuzhou, China.

UNI 8942-3. 1986. Elementi per muratura di laterizio (Brick products for masonry structures). Italian Standard [in Italian].

UNI EN 1015-11. 1999. Methods of test for mortar for masonry. Determination of flexural and compressive strength of hardened mortar. European Standard.

UNI EN 772-1. 2000. Methods of test for masonry units. Determination of compressive strength. European Standard.

Valluzzi, M. R., Binda, L., Modena, C. 2005. Mechanical behavior of historic masonry structures strengthened by bed joints structural repointing. Construction and Building Materials, 19:63-73.

Valluzzi, M. R., Valdemarca, M., Modena, C. 2001. Behavior of brick masonry vaults strengthened by FRP Laminates. Journal of Composites for Construction, ASCE, 5(3):163–169.

Vamvatsikos, D., Cornell, C. A. 2002. Incremental dynamic analysis. Earthquake Engineering and Structural Dynamics, 31:491-514.

Vamvatsikos, D., Cornell, C. A. 2004. Applied incremental dynamic analysis. Earthquake Spectra, 20(2):523-553.

Venu, Madhava Rao, K., Venkatarama Reddy, B. V., Jagadish, K. S. 1997. Strength characteristics of stone masonry. Materials and Structures, 30:233-237.

Vermeltfoort, A. 1994. Compression properties of masonry and its components. In Proc. of 10th International Brick/Block Masonry Conference, Calgary, Alberta, Canada.

Vidic, T., Fajfar, P., Fischinger, M. 1994. Consistent inelastic design spectra: strength and displacement. Earthquake Engineering and Structural Dynamics, 23:507-521.

Wang, J., Melbourne, C., Tomor, A. K. 2010. The theoretical basis of the MEXE method for masonry arch assessment. In Proc. of 8th International Masonry Conference, Dresden, Germany.

Yassin, M. Y. 1994. Nonlinear analysis of prestressed concrete structures under monotonic and cyclic loads. Ph.D. Dissertation, Department of Civil Engineering, University of California, Berkeley.

Zheng, Y., Taylor, S., Robinson, D. 2010. Nonlinear finite element analysis of masonry arch bridges reinforced with FRP. In Proc. of ARCH'10, 6th International Conference on Arch Bridges, Fuzhou, China.

Related publications by the Author

De Santis S, de Felice G. 2010. Evaluation of the seismic response of masonry arch bridges modelled using beam elements with fiber cross-section. In Proc. of ARCH'10, 6th International Conference on Arch Bridges, Fuzhou, China.

de Felice G., De Santis S. 2010. Experimental and numerical response of arch bridge historic masonry under eccentric loading. International Journal of Architectural Heritage, 4:115-137.

de Felice G., De Santis S. 2009. Si possono modellare elementi murari pressoinflessi come travi a fibre? In Proc. of Convegno WonderMasonry, Ischia, Italy. [in Italian].

de Felice G., De Santis S. 2009. Valutazione della risposta sismica di ponti ad arco in muratura attraverso il modello di trave a fibre. In Proc. of XIII Convegno di Ingegneria Sismica ANIDIS, Bologna, Italy. [in Italian].

de Felice G., De Santis S. 2008. Experimental investigation and numerical modelling of eccentrically loaded historic brickwork for railway arch bridge assessment. In Proc. of. HMC'08, International Historical Mortar Conference, Lisbon, Portugal.

Carbone I., De Santis S., Mauro A., de Felice G. 2005. Prove Sperimentali per la caratterizzazione meccanica della muratura di ponti ferroviari. Rapporto Finale, Progetto PRIN 2003/05 (Sicurezza, conservazione e gestione dei ponti in muratura). [in Italian].

Address correspondence to:
Stefano De Santis
Roma Tre University
Department of Structures (DiS)
Via Corrado Segre, 4-6
00146 Rome, Italy
sdesantis@uniroma3.it